# The Impact of Degradation Reactions on Aprotic Metal-$O_2$ Battery Performance

by

Robert Black

A thesis
presented to the University of Waterloo
in fulfillment of the
thesis requirement for the degree of
Doctor of Philosophy
in
Chemical Engineering

Waterloo, Ontario, Canada, 2016

## Author's Declaration

I hereby declare that I am the sole author of this thesis. This is a true copy of the thesis, including any required final revisions, as accepted by examiners.

I understand that my thesis may be made electronically available to the public.

_____

Robert Black

# Abstract

The need for new portable energy storage technologies places increasing demand on the development of new batteries beyond Li-ion. Potential candidates to fill this necessity are the class of metal-$O_2$ batteries. In particular, Li-$O_2$ batteries offer a theoretical energy density of ~ 3,000 Wh/kg; a huge leap in energy storage beyond that of today's traditional batteries. The energy is derived from the electrochemical reaction of $Li^+$ with gaseous oxygen, $O_2$, to form $Li_2O_2$, which is stored on the positive electrode surface. Current-day aprotic Li-$O_2$ batteries cannot reach these high theoretical energy densities, however, because they are plagued with pitfalls, including poor capacity retention, low rate capabilities, and high voltage inefficiencies. This is a result of electrode and electrolyte degradation reactions that occur during normal cell operation. This thesis explores the source of these inefficiencies, and focuses on the electrode and electrolyte degradation reactions that arise during cell operation. To support this thesis, the following is presented:

1. Methods for screening the stability of electrolytes and electrode materials towards the highly nucleophilic $O_2^-$/$Li_2O_2$.
2. The impact of electrolyte instability and by-product formation has on the Li-$O_2$ oxygen reduction reaction (ORR) and oxygen evolution reaction (OER) catalytic activity, along with a discussion of the validity of a $Li_2O_2$ OER catalyst.
3. The design, development, and construction of an on-line mass spectrometer for quantitative analysis of the metal-$O_2$ chemistry.
4. The importance of quantifying the ORR/OER efficiency, demonstrated through the use of mass spectrometry, where understanding the actual metal-$O_2$ chemistry is crucial to form proper conclusions.

5. A study on the stability of various cell components in the Na-$O_2$ battery to contrast the viability of the Na-$O_2$ battery as a potential candidate moving forward.

To better understand the stability of various cell components against the highly nucleophilic $O_2^-$/$LiO_2$ species, it is necessary to determine the stability of various cell components in the absence of any electrochemical processes that may occur during cell operation. Taking this precaution decouples parasitic reactions that are electrochemical in nature from those that are chemical in nature. *Section 3* presents such a chemical method that can probe the reactivity of $O_2^-$/$LiO_2$ towards cell components, such as electrode materials and electrolytes. This technique utilizes $KO_2$ with 18-crown-6 ether as a chemical source of $O_2^-$. Upon addition of a Li-based salt (such as $LiPF_6$), the $O_2^-$ reacts with $Li^+$ to form $LiO_2$. This further undergoes disproportionation to form $Li_2O_2$, much like what occurs in an actual electrochemical cell. In the presence of carbon black, a common positive electrode material, the carbon acts as a nucleation site for $O_2^-$/$LiO_2$ formation and prevents the highly crystalline formation of $Li_2O_2$. The formation of semi-amorphous $Li_2O_2$ via this chemical method is also in contrast to $Li_2O_2$ formed on electrochemical discharge from an Li-$O_2$ cell. A solution-based mechanism is proposed for the formation of $Li_2O_2$ under low-current driven formation, which gives rise to the formation of >500 nm toroid-like structures.

With the validation that this $KO_2$ mechanism mimics the expected chemistry of a Li-$O_2$ cell, electrode materials and various aprotic electrolytes commonly used in the Li-$O_2$ cell are tested for chemical stability. Polyvinylidene fluoride (PVdF), a common Li-$O_2$ positive electrode binder, is not stable to $O_2^-$/$LiO_2$. Hydrogen abstraction by $O_2^-$ from the PVdF backbone occurs, which in turn causes the release of a fluorine anion $F^-$ as the PVdF forms a double-bonded structure. This is evident through discoloration of the PVdF and the

appearance of LiF and KF in the crystalline diffraction pattern of the collected solid products. Another by-product of this reaction is $H_2O_2$. This $H_2O_2$, in the presence of popular ORR/OER catalysts such as $MnO_2$, decomposes to form $H_2O$. The $H_2O$ reacts with $Li_2O_2$ to form LiOH. This process can be avoided through the use of a more stable binder material, such as lithiated nafion, which is proven with the above mentioned $KO_2$ reactions to be completely stable to superoxide attack. Apart from positive electrode materials, this $KO_2$ probe also demonstrates the instabilities of popular electrolyte solvents like propylene carbonate and TEGDME towards $O_2^-/LiO_2$ formation.

In *Section 4*, an attempt to minimize the discharge/charge overpotentials in the Li-$O_2$ cell is made with the use of an ORR/OER catalyst. $Co_3O_4$ on reduxed graphene oxide (RGO) is used as a catalyst material, and its catalytic properties for $Li_2O_2$ oxidation are explored with evidential support of fundamental electrochemical studies coupled with full cell measurements. Compared to a pure carbon positive electrode, the $Co_3O_4$/RGO composite exhibits a decreased charge overpotential for $Li_2O_2$ oxidation by nearly 400 mV (compared to carbon electrodes without $Co_3O_4$/RGO). Yet, unlike traditional electrocatalysts which lower the activation energy via electron transfer, the $Co_3O_4$/RGO acts as an oxidation "promoter" through the enhanced surface transport of the $Li_2O_2$ species. This is determined from cyclic voltammetry measurements, as well as comparing the onset of oxidation with linear sweep voltammetry. Furthermore, the $Co_3O_4$ catalyst exhibits improved capacity retention on cycling when the available surface that reacts with $Li_2O_2$ is limited, hence minimizing the formation of decomposition products. However, while the oxidation "promoter" activity of $Co_3O_4$ is evident and improves cell performance, decomposition product formation from parasitic reactions involving the electrolyte and $O_2^-/LiO_2$ species

limits the positive electrode activity to only the first few cycles. With the aid of TOFSIMS, it is clear that the accumulation of decomposition products block $Co_3O_4$/RGO active sites after the initial stages of $Li_2O_2$ oxidation. Hence, without a method during cell operation to remove these insoluble decomposition products, the catalytic activity of various new positive electrode materials cannot be fully realized.

To better understand the Li-$O_2$ chemistry and determine how positive electrode activity affects cell performance, mass spectrometry is highly recommended to be utilized. *Section 5* outlines the design process behind the construction and optimization of a mass spectrometer to analyze the discharge/charge chemistry of the Li-$O_2$ cell. From quantitative evaluation of gas evolution during cell oxidation, the efficiency of $Li_2O_2$ oxidation, as well as the presence of positive electrode/electrolyte based side reactions, can be determined. This provides a metric to compare various positive electrode materials for their $Li_2O_2$ oxidation activity. Then, with pre-loaded $Li_2O_2$/active material positive electrodes, mass spectrometry is used to evaluate the activity of $Li_2O_2$ oxidation in the absence of any degradation products that would normally form on cell discharge. The reactivity of $Li_2O_2$ with a carbon surface clearly inhibits efficient oxidation of $Li_2O_2$ due to the formation of $Li_2CO_3$ layers at the positive electrode/$Li_2O_2$ interface. This reaction can be circumvented through a positive electrode material that is more stable to $Li_2O_2$ oxidation, such as TiC. Furthermore, the stability of popular Li-$O_2$ battery electrolytes, such as TEGDME and DMSO, and their impact on $Li_2O_2$ oxidation, is presented. Finally, a discussion on the importance of analyzing the Li-$O_2$ cell chemistry outside of pure galvanostatic cycling analysis is put forth. This is evident with the use of $Mo_2C$ as a positive electrode material, which despite demonstrating remarkably low charge overpotentials, produces almost no $O_2$ evolution on charge due to the

formation of $Li_xMoO_3$ upon reactivity of $Li_2O_2$.This consumes the positive electrode in the process, making this a non-reliable electrode material. Hence, as occurs in abundance within the literature, the activity of various positive electrode materials cannot be concluded based on electrochemistry alone.

With clear decomposition product formation confirmed, which is a major detriment to Li-$O_2$ battery performance, *Section 6* analyzes the accumulation of decomposition products during Na-$O_2$ cell operation. In the Li-$O_2$ cell, the large charge overpotential for $Li_2O_2$ oxidation is a result of insulating Li-carboxylate products. The Na-$O_2$ cell, despite operating in similar conditions as the Li-$O_2$ cell, and generating similar carboxylate side-products, does not exhibit such large charge overpotentials. Decomposition products present in the Na-$O_2$ cell are evaluated and quantified in an ether-based electrolyte. It is clear that the main source of decomposition in the Na-$O_2$ cell is from the highly nucleophilic $O_2^-$/$NaO_2$ . In contrast to the Li-$O_2$ battery, the low overpotential associated with $NaO_2$ does not promote further formation of decomposition products. The fact that $NaO_2$, unlike $Li_2O_2$, is able to be oxidized at low overpotentials, even in the presence of decomposition products that form on discharge, implies the oxidation of $NaO_2$ and $Li_2O_2$ are fundamentally different. The facilitation of $NaO_2$ oxidation by a proton phase transfer catalyst is discussed and contrasted to the oxidation of $Li_2O_2$. $NaO_2$ in contact with the ether-electrolyte is proven to eventually be fatal to the Na-$O_2$ battery, for its continued reactivity with the electrolyte, even in the absence of any electrochemistry, produces insoluble Na-carboxylate products which terminate electron transfer.

## Acknowledgements

I would first like to extend my utmost gratitude to my supervisor, Dr. Linda F. Nazar, for her guidance and help throughout my graduate career. While the metal-$O_2$ field has been very rough at times, I feel I have acquired a great deal of knowledge that I can apply to many electrochemical storage fields in the future. Without her constant pressure, I may have given up earlier in my career. Furthermore, I would like to thank my committee members: Dr. Zhongwei Chen, Dr. Eric Prouzet, and Dr. Pavle Radovanovic. I would also like to thank my external committee member, Dr. Lynden Archer.

I would like to thank Dr. Si Hyoung Oh for his tremendous help in the development of many of the concepts presented in *Section 3*. This work was started near the beginning of my graduate career, and without his help, the research in this area would have never been pursued.

I would like to acknowledge and give thanks to Dr. Jin Hyon Lee for his extensive contributions in *Section 4* of this thesis. Dr. Lee is responsible for the initial synthesis of the RGO and RGO/$Co_3O_4$, as well as early electrochemical measurements. I would also like to thank Dr. Charles Mims and Dr. Rana Sodhi from Surface Interface Ontario (University of Toronto) for all their work involving sample preparation, operation, and data analysis involved with the TOFSIMs measurements.

The design and calibration of the mass spectrometry equipment as outlined in *Section 5* would not have been possible without the help of Dr. Petr Novak and Dr. Erik Jaemstrop Berg from the Paul Scherrer Institute. There guidance and willingness to assist with early measurements of mass spectrometry, plus assist in the design and construction of the mass

spectrometer presented was invaluable. Furthermore, I would like to thank Dr. Dipan Kundu for his role in the work presented on $Mo_2C$. Dr. Kundu is responsible for the synthesis of $Mo_2C$, and much of the electrochemical analysis and XPS measurements.

For the work presented in *Section 6*, I would like to thank Abhinandan Shyamsunder and Dr. Graham Murphy. Both individuals contributed a great deal to discussions of electrolyte decomposition pathways. Abhinandan Shyamsunder also performed the NMR experiments. I would also like to thank Dr. Dipan Kundu for his assistance in performing the iodometric titrations. Parvin Adeli also deserves thanks for her assistance in electrochemical cell assembly.

## Table of Contents

## List of Figures

## List of Tables

## Abbreviations

**AN –** Acceptor Number (Electrolyte property)

**Ar –** Argon (inert gas)

**CA –** Chronoamperometry (type of electrochemical experiment)

**CDEM –** Continuous Dynode Electron Multiplier (detector for mass spectrometer)

**Diglyme –** Diethylene Glycol Diethyl Ether (solvent for Na-$O_2$ electrolyte)

**DME** – Dimethoxyethane (solvent for Li-$O_2$ electrolyte)

**DMSO** – Dimethyl sulfoxide (solvent for Li-$O_2$ electrolyte)

**DN** – Donor Number (electrolyte property)

**EDX –** Energy Dispersive X-Ray (analytical technique)

**FC** – Faraday Cup Detector (detector for mass spectrometer)

**HRTEM –** High Resolution Transmission Electron Microscopy (Instrument)

**IOC** – Inverse Opal Carbon (positive electrode material)

**KB –** Ketjen Black (high surface area carbon powder used for positive electrodes)

**LSV** – Linear Sweep Voltammetry (electrochemical experiment)

**MeCN** – Acetonitrile (solvent for Li-$O_2$ electrolyte)

**NaOTf –** Sodium Triflate (salt for Na-$O_2$ batteries)

**NPG** – Nanoporous Gold (positive electrode material)

**OER** – Oxygen evolution reaction

**OCV –** Open Circuit Voltage (rest potential of electrochemical cell)

**OEMS** – Online Electrochemical Mass Spectrometry (Instrument)

**ORR** – Oxygen reduction reaction

**PC** – Propylene Carbonate (solvent for Li-$O_2$ electrolyte)

**PS** – Polystyrene (positive electrode material)

**PTC –** Phase Transfer Catalyst (cell additive)

**PTFE –** Polytetrafluorethylene (positive electrode binder)

**PVdF –** poly(vinylidene difluoride) (positive electrode binder)

**RGO** – Reduced Graphene Oxide (positive electrode materials)

**SEM –** Scanning Electron Microscopy (instrument)

**TEGDME** – Tetraethylene glycol dimethyl ether (solvent for Li-$O_2$ electrolyte)

**TEM –** Transmission Electron Microscopy (instrument)

**TOF-SIMS** – Time of Flight Secondary Ion Mass Spectrometry (Analysis technique)

**UHV** – Ultra High Vacuum

**XRD** – X-ray diffraction

# 1.0 - Introduction

## 1.1 – Battery (Electrochemical Energy Storage) Terminology

A battery is an electrochemical energy storage device that converts chemical energy into electrical energy. The chemical energy is contained within the battery material, known as electrodes, with no external fuel source necessary as is the case with combustion engines or fuel cells. Hence, batteries are ideal for portable energy storage. The chemical energy is converted into electrical energy from the electrochemical reduction/oxidation reactions (redox) of the battery's active materials. In typical battery terminology, one redox couple is known as an electrochemical cell. A battery consists of one or more of these cells in various configurations in order to meet the energy requirements of the desired application. For the purposes of this dissertation, cell and battery will be used interchangeably, as all studies and performance metrics presented throughout are based on a single redox couple configuration (cell).

A typical cell is comprised of three main components: *i)* positive electrode, *ii)* negative electrode, and *iii)* electrolyte. The components of a Li-ion battery are depicted in **Figure 1.1**. Reduction of the active material occurs at the positive electrode, where electrons are accepted from the external electric circuit. The negative electrode liberates electrons during operation and undergoes *oxidation*. In typical battery nomenclature, the positive electrode is referred to as the *cathode*, being the site where free cations in solution migrate to undergo reduction. The negative electrode is referred to as the *anode*, where anions in solution migrate to undergo oxidation. This nomenclature is generally accepted within the battery community, and is accurate of a primary cell that is not reversible. On cell discharge, the electrons flow from the negative electrode (anode - oxidation) to the positive electrode

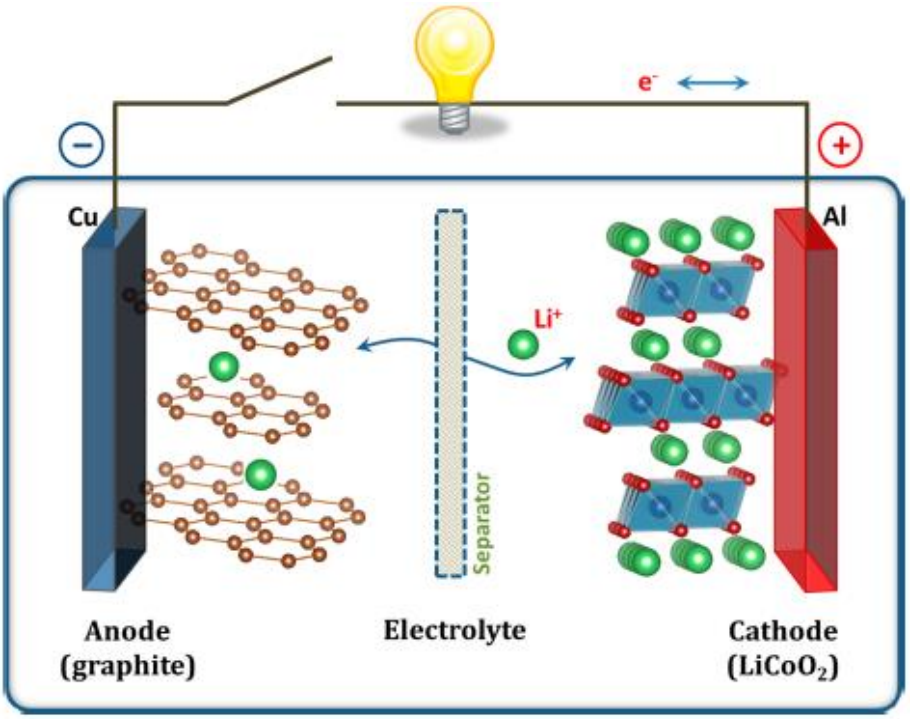


**Figure 1-1 -** Schematic of a typical Li-ion battery. Lithium ions are shuttled between the negative electrode (graphite) and positive electrodes ($LiCoO_2$) during operation through an ion conducting electrolyte. The components depicted here represent the fundamental configuration of all electrochemical batteries.[1]

(cathode - reduction) via an external circuit. With secondary batteries, the cell can also be charged through the reverse flow of electrons. This changes the nomenclature of the electrodes. For the purpose of this dissertation, in order to avoid confusion, the term positive electrode and negative electrode will be used throughout. The final cell component of an electrochemical cell, the electrolyte, is an ionic conducting medium which allows for the transfer of charge between the two electrodes. The electrolyte is typically a salt dissolved in a variety of aqueous or organic solvents (battery dependant). Solid ionic conductors can also serve as the electrolyte. Together, the positive electrode, negative electrode, and electrolyte comprise an electrochemical cell.

The combination of positive electrode and negative electrode active materials determines the storage characteristics of the cell. Two metrics are used to determine the total amount of work (energy) that can be harnessed from a cell: the cell voltage and capacity. The free energy of a cell is given by *equation 1-1* below:

$$\Delta G = -nFE^\circ \qquad \textit{(equation 1-1)}$$

where *F* is Faraday's constant (96,485 C/mol), *n* is the number of electrons involved in the redox reaction, and *E*° is the standard potential of the cell (V). *E*° is also known as the electromotive force (emf) of the cell. The standard potential is determined through the relation in *equation 1-2*, which is defined as the difference in the reduction and oxidation potentials of the positive and negative electrodes, respectively.

$$E^\circ = E_{Red} - E_{Ox} \qquad \textit{(equation 1-2)}$$

Treatment of the cell potential in this manner is misleading because the true cell voltage is also dependent on factors such as electrolyte salt concentration and temperature. The relationship to determine the true cell potential is known as the *Nernst equation*. This allows for the theoretical treatment of the potential of an electrical half-cell that deviates from the standard state. This relationship is given in *equation 1-3*:

$$E = E^\circ - \frac{RT}{nF} ln Q \qquad \textit{(equation 1-3)}$$

where R is the ideal gas constant, and *Q* is the reaction quotient (in this case, Q = [reduction species]/[oxidation species]). Hence, the actual cell voltage is a function of the cell temperature, the standard potentials of the redox couples, and the concentration of the reduction and oxidation species.

The theoretical capacity is an important metric of cell performance, for the capacity of a cell is defined as the total quantity of electrons (charge) that are passed during operation. The typical unit for capacity is ampere-hours (Ah). This capacity can be represented as a gravimetric capacity (Ah/g), volumetric capacity ($Ah/cm^3$), or simply as a unit of charge (Ah). The obtainable cell capacity and the actual cell voltage governs the total energy of the battery:

$$\text{Total Energy (Wh)} = \text{E (V)} \times \text{Capacity (Ah)} \qquad \textit{(equation 1-4)}$$

The representation of the total energy from a battery is dependent on its application. For example, typical Li-ion batteries are represented as a gravimetric energy density Wh/kg, where the energy is based on the mass of the total cell configuration. For other applications, total cell volume is important, so the energy is represented as a volumetric energy density (Wh/L). Regardless, the definition of total cell energy is universal for all electrochemical energy storage systems, and serves as a benchmark to compare multiple electrochemical energy storage technologies across all applications.

## 1.2 – Li-$O_2$ Batteries

The lithium-oxygen (Li-$O_2$) battery has recently garnered a great deal of attention due to the promise of an extremely high energy density that eclipses current-day and next generation electrochemical storage technologies.[1,2] **Table 1-1** compares both the theoretical and practical gravimetric and volumetric energy densities of the Li-$O_2$ battery to other popular electrochemical storage systems. In terms of energy per mass of the final products, the Li-$O_2$ cell has a very high theoretical energy density of 3,458 Wh/kg. This is greater than any current day battery technology and surpasses promising next-generation

electrochemical storage technologies such as Li-S. For this reason, the Li-$O_2$ cell is of great interest from both academic and industrial perspectives

**Table 1-1 –** Comparison of the practical and theoretical energy densities of commercial and in-development battery technologies.[**Error! Bookmark not defined.**]

| System | Gravimetric Energy (Wh/kg) | | Volumetric Energy Density (Wh/L) | |
|---|---|---|---|---|
| | **Calculated** | **Practical** | **Calculated** | **Practical** |
| **Li-$O_2$** | 3,458 | **?** | 6,170 | **?** |
| **Li/S** | 2,566 | 350 | 4,260 | 350 |
| **Zn/Air** | 1,086 | 180 | 6,091 | 208 |
| **C/$LiCoO_2$** | 387 | 100 | 1,105 | 150 |
| **M-H/NiOOH** | 180 | 63 | | 142 |
| **Pb/$PbO_2$** | 171 | 60.6 | 370 | 108 |

Another comparison of the Li-$O_2$ battery technology to other electrochemical energy storage systems is shown in **Figure 1-2**.[**Error! Bookmark not defined.**] This figure compares the capabilities of different electric vehicle technologies. While the Li-$O_2$ cell is currently still in the research and development phase, a vehicle utilizing an Li-$O_2$ cell could potentially achieve a driving distance of over 500 km per charge; nearly three times greater than current day electric vehicle technology based on Li-ion batteries (assuming the theoretical energy density can be achieved). Other prospects for the application of the Li-$O_2$ cell in the automotive industry are extremely positive, with an outlook of being able to travel over 800 km on a single charge by the year 2020.[3]

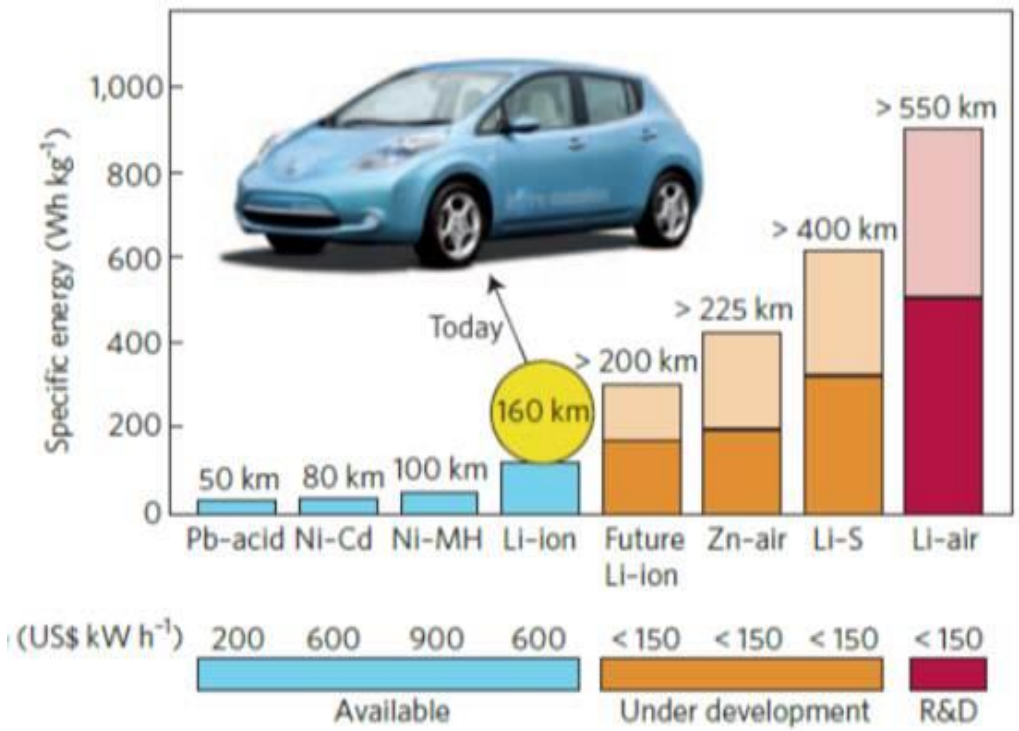


**Figure 1-2 -** Practical specific energy values for various electrochemical storage technologies. Estimated driving distance from a single discharge/charge is based on current technology in the Nissan Leaf. Monetary values for technologies under development and in R&D stages are targets set forth by the US Advanced Battery Consortium.[1]

Commercialization of Li-$O_2$ battery technology will have major implications for the portable electronics and automotive industry if it is applied in the same manner as today's successful Li-ion batteries. Multiple complications that exist for the Li-$O_2$ cell, however, prevent the development of a practical and commercially viable battery. This includes, but is not limited to, slow rate capabilities, poor cycling retention, chemically unstable cell components, and safety concerns with the use of a metallic Li-metal negative electrode. In order for the Li-$O_2$ cell to be commercially viable, research must focus on the development of stable electrolytes and positive electrode materials. Improvements must also be made in

the areas of $Li_2O_2$ storage, efficient oxygen reduction reactions (ORR) and oxygen evolution reactions (OER), as well as limitation of the side reactions that negatively impact cell performance. The following sections will briefly outline progress that has been made in the metal-$O_2$ battery field towards addressing these problems, and provide an overview of the current performance issues that are key areas for current research and future improvements.

### 1.2.1 – Chemistry of the Li-$O_2$ Battery

A typical aprotic Li-$O_2$ cell is comprised of a lithium metal negative electrode, a porous composite positive electrode, and an ionically conducting organic medium as the electrolyte. **Figure 1.3a** illustrates the a typical Li-$O_2$ cell during discharge. The negative electrode undergoes oxidation to release $Li^+$ into solution. In conjunction, the

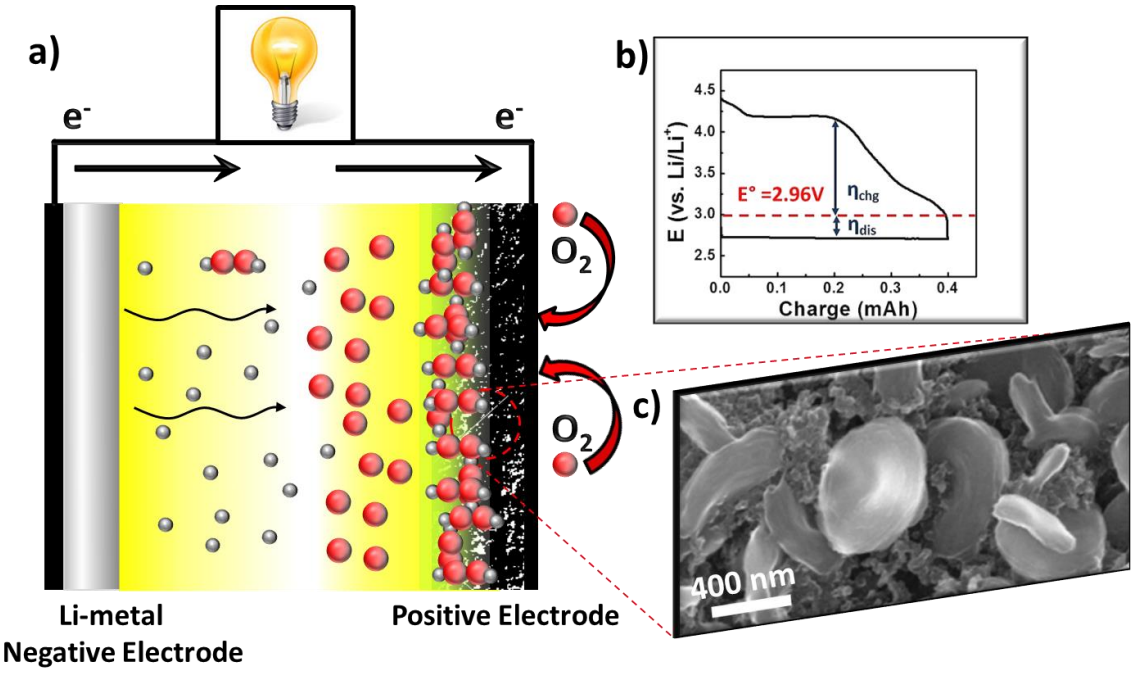


**Figure 1-3 – (**a) Depiction of the discharge process of a typical aprotic Li-$O_2$ battery, and (b) associated discharge/charge electrochemical voltage profile under a constant applied current. (c) An SEM micrograph of the discharge product, $Li_2O_2$.

gaseous oxygen at the positive electrode undergoes oxidation to form $O_2^-$, which reacts with $Li^+$ to form $LiO_2$. This species is not thermodynamically stable and undergoes disproportionation to form the final product, $Li_2O_2$. The theoretical voltage for this reaction is 2.96 V, with only a minor discharge overpotential observed in practice (**Figure 1.3b)**.[1] The $Li_2O_2$ deposits as small crystalline toroids onto the electrode surface, evident from SEM micrographs of discharged positive electrodes (**Figure 1.3c**). It is necessary for the positive electrode to have a high degree of porosity so that dissolved $O_2$ can access all active sites for ORR/OER and store a large volume of insoluble and electrically insulating $Li_2O_2$. The capacity of the Li-$O_2$ battery is ultimately determined by the total volume of $Li_2O_2$ able to be stored on and within the electrode surface.

The exact mechanism for $Li_2O_2$ production was the primary focus of early reports on Li-$O_2$ batteries, with competing results over whether the discharge process was primarily driven in solution or on the electrode surface.[4,5,6] From these early reports, it has been speculated that the production of $Li_2O_2$ follows a 3-step process, as shown in *equations 1-5* & *1-6* below.

$$O_2 + Li^+ + e^- \rightarrow LiO_2 \quad E° = 3.0\ V\ vs.\ Li/Li^+ \qquad \textit{(equation 1-5)}$$

*Followed by either:*

$$2LiO_2 \rightarrow Li_2O_2 + O_2 \qquad \textit{(Chemical Process)} \qquad \textit{(equation 1-6a)}$$

$$LiO_2 + Li^+ + e^- \rightarrow Li_2O_2 \qquad E° = 2.96\ V\ vs.\ Li/Li^+ \qquad \textit{(equation 1-6b)}$$

Experimental work from McCloskey [4] et. al provides evidence that equations *(1-6a)* and *(1-6b)* are the main reactions on cell discharge. Recent publications have taken a more thorough investigation into these processes and confirm that process *(1-5)* and *(1-6a)* are indeed likely to occur, with the possibility of $Li_2O_2/LiO_2$ mixed states in the final

product.[5,6] Another possibility is the production of $Li_2O$, but authors that have explored this product have stated its extreme difficulty to oxidize compared to $Li_2O_2$.[7] Regardless of the mechanism on discharge, a cell void of contamination and side reactions will produce $Li_2O_2$ as the primary discharge product. The $Li_2O_2$ takes on a toroidal morphology, shown in **Figure 1.3c.** This distinct shape is not universal, for the current rate has a profound impact on the toroid morphology. Smaller toroids, and even amorphous "film" structures, result at higher discharge rates.[8,9] This is demonstrated in **Figure 1.4** below, along with the impact that the current rate has on the obtainable discharge capacity. This effect on discharge capacity can be understood based on the insulating nature of the $Li_2O_2$. At high current rates, the formation of a thin conformal film creates high impedance layers that block active sites for $O_2$ reduction on the electrode surface. Low current rates allow for a more controlled $O_2^-$ /$LiO_2$ nucleation process. The formation of $Li_2O_2$ toroids also allows more of the surface to be exposed, leading to more $Li_2O_2$ host sites and hence a larger capacity.

In recent reports, it has been shown that the effect of solvent additives, in particular $H_2O$, influence the formation of $Li_2O_2$ toroids on discharge, as well as impact the final discharge capacity. A report from Aeturki *et. al*. reveals that small amounts of water, of the levels that can easily contaminate any aprotic Li-$O_2$ cell unless extreme precaution was used to prevent this, are responsible for the growth of these $Li_2O_2$ toroids.[10] It appears that there are two distinct pathways for the growth of $Li_2O_2$ on the positive electrode surface. One pathway, in the absence of $H_2O$, involves nucleation and growth of $Li_2O_2$ on the positive electrode surface, which results in conformal film coatings. This film growth is self-limiting due to the insulating nature of the $Li_2O_2$ preventing further electron mobility, and hence blocks active sites on the positive electrode from further oxygen reduction. The second

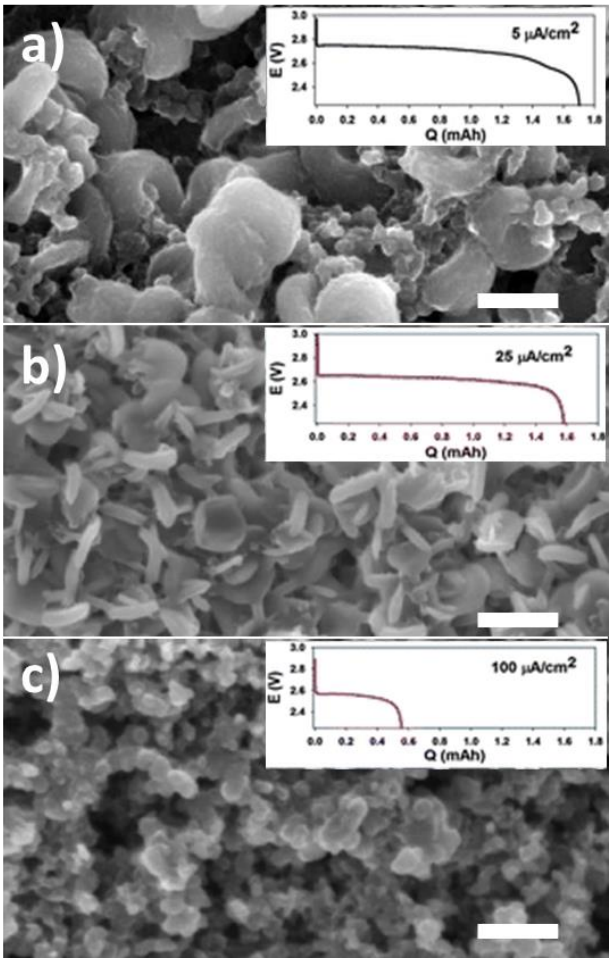


**Figure 1-4 -** SEM micrographs and corresponding electrochemical discharge profile of carbon electrodes with a discharge current rate of (a) 5 uA/cm$^2$, (b) 25 uA/cm$^2$, and (c) 100 uA/cm$^2$. The lower current rate results in the formation of larger toroids, coupled with a greater capacity compared to a high current rate. At high current rates a small capacity is exhibited with a thin conformal film of $Li_2O_2$.[8]

reduction pathway is a solution based mechanism, made possible due to the enhanced solubilization of $O_2^-$ and $LiO_2$ from the high donor (DN) and accepter number (AN) additives in the electrolyte. These are present as residual $H_2O$, or other proton sources (such as methanol, benzoic acid etc.). $O_2^-$ is easily solubilized by these additives, and causes the solution based formation of $LiO_2$. The disproportionation reaction proceeds on the surface of the electrode, or nucleates on existing $Li_2O_2$ particles at the solid/solution interface to grow

the observed toroidal crystals. The growth occurs on [0001] oxygen-rich terminated surfaces of the $Li_2O_2$, which are the lowest energy and most abundant surfaces.[11] In reality, both surface and solution based growth of $Li_2O_2$ occurs, as outlined in **Figure 1.5**.

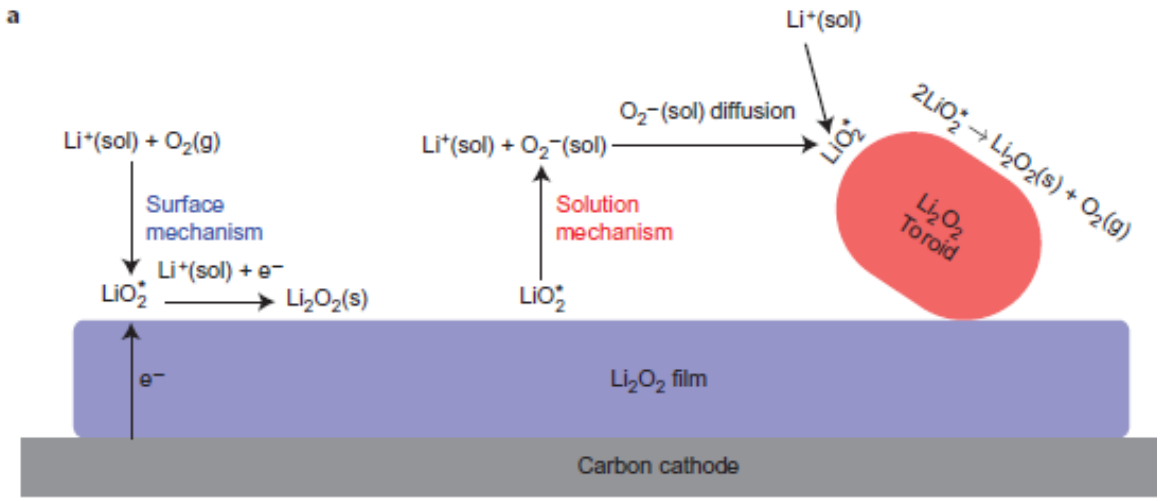


**Figure 1-5 -** Schematic of the two possible mechanisms for $Li_2O_2$ production. After $O_2$ reduction at the electrode surface, and subsequent reaction to form $LiO_2$, the species can either become solvated in solution to eventually form $Li_2O_2$ toroids (right side of mechanism), or can stay surface bound where a concerted mechanism gives rise to $Li_2O_2$ (left mechanism).[10]

It has been demonstrated that through proper selection of electrolyte and the use of electrolyte additives, the proportion of $O_2^-/LiO_2$ solubility, and hence the solution-driven growth of $Li_2O_2$, can be controlled.[12] Thermodynamics dictates the production and decomposition of $Li_2O_2$ occurs at 2.96 V. In practice, overpotentials limit the voltage efficiency of the Li-$O_2$ cell. The overpotential on discharge, $\eta_{dis}$, is ~0.2 V when moderate current rates are used. Investigations into the origin of this discharge overpotential reveal that it arises due to iR potential loss from the resistance of cell components, and can be minimized through better electrical contacts and low current rates.[8,13]

However, one of the main concerns of the Li-$O_2$ battery is the large charge overpotential, $\eta_{chg}$, for $Li_2O_2$ oxidation. On cell charge, the $Li_2O_2$ is oxidized to evolve $O_2$ and liberate $Li^+$ ions back into the electrolyte. This oxidation occurs with a very large overpotential, as shown previously in **Figure 1.3b**. The oxidation of $Li_2O_2$ follows a lithium deficient solid solution reaction, different than that of the discharge reaction pathway (reduction via a soluble $LiO_2$ intermediate) which will be an important distinction in subsequent sections of this dissertation.[14] A report by fellow colleagues has determined the charge mechanism of $Li_2O_2$ through the use of *operando* X-ray diffraction.[14] The oxidation of $Li_2O_2$ occurs in two stages and gives rise to the experimentally observed two-step voltage profile. Initially, amorphous and small nanocrystals of $Li_2O_2$ are oxidized at relatively low potentials (~3.2 V) (**Figure 1.6a**). This results in the creation of Li-vacancies and the formation of a small amount of $Li_{2-x}O_2$. As the potential increases to the region between 3.4 – 3.9 V, the oxidation of crystalline $Li_2O_2$ occurs through a surface driven process, proceeding in two steps to oxidize $Li_2O_2$ completely to $Li^+$ and $O_2$:

$$Li_2O_2 \rightarrow Li_{2-x}O_2 + xLi + xe^- \qquad \textit{(equation 1-7)}$$

$$Li_{2-x}O_2 \rightarrow (2-x)Li^+ + (2-x)e^- + O_2 \qquad \textit{(equation 1-8)}$$

The small $Li_2O_2$ platelets preferentially oxidize first, followed by the larger platelets at the end of charge. This is confirmed via X-ray diffraction and microscopic observation (**Figure 1-6b).** Other researchers have attempted to elucidate the origin of this charge overpotential with theoretical models and experimental practices, as well as recent experimental investigations that provide hints of the complex chemistry that occurs.[15,16]

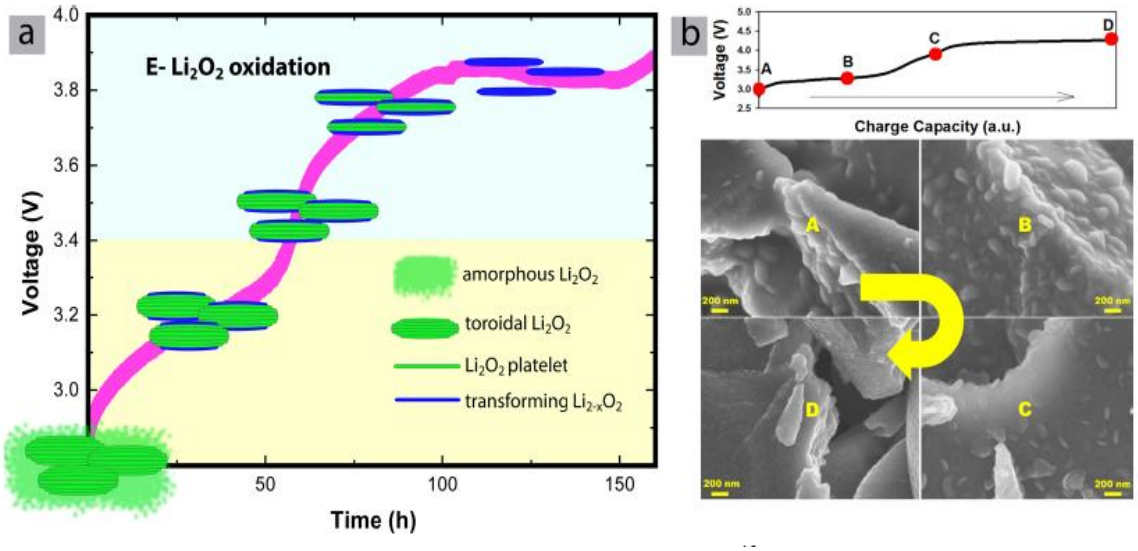


**Figure 1-6 – (**a) Schematic of the charge profile for oxidation of $Li_2O_2$ that was electrochemically discharged on a carbon cathode. (b) SEM images at specific points of charge to show the morphological changes of the $Li_2O_2$ toroids. [15]

However, apart from inherent $Li_2O_2$ oxidation inefficiencies, evidence suggests a contribution to this overpotential is impedance caused by Li-carboxylate decomposition products. It is the presence of these decomposition products that underlie the main limitations of the Li-$O_2$ battery. This will be discussed in great detail throughout the body of this dissertation.

### 1.2.2 – Positive Electrodes for the Li-$O_2$ Battery

The positive electrode plays a very critical role in determining the capacity and cycling efficiency of the Li-$O_2$ cell. The overall cell capacity is determined by the positive electrodes ability to store insoluble $Li_2O_2$. Many theoretical studies have reported that the maximum capacity limitation of a Li-$O_2$ cell is due to mass and electron transport issues that arise from accumulation of $Li_2O_2$.[9,17,18,19] Electron transport becomes inhibited as the positive electrode surface becomes covered with electrically insulating $Li_2O_2$. Computational

results summarize the increase in discharge overpotential necessary to maintain the reduction current (**Figure 1-7)**.[20] As the thickness of the $Li_2O_2$ layer increases, large amounts of potential bias are necessary to achieve the same charge transport current. Ultimately, it is the accumulation of this $Li_2O_2$ layer and the limitation of charge transport that causes discharge termination. Other reports have shown a similar limitation in $Li_2O_2$ growth based on the reduced mass transport of $O_2$ to active sites on the positive electrode.[17] The accumulation of solid $Li_2O_2$ at the positive electrode/electrolyte interface occludes $O_2$ from reaching further depths of the electrode surface, thus limiting further production of $Li_2O_2$. This issue is further exacerbated when decomposition products are generated, for they are more difficult to remove, and thus the regeneration of accessible active surface area becomes problematic over multiple cycles. One approach to circumvent this issue and obtain high gravimetric and

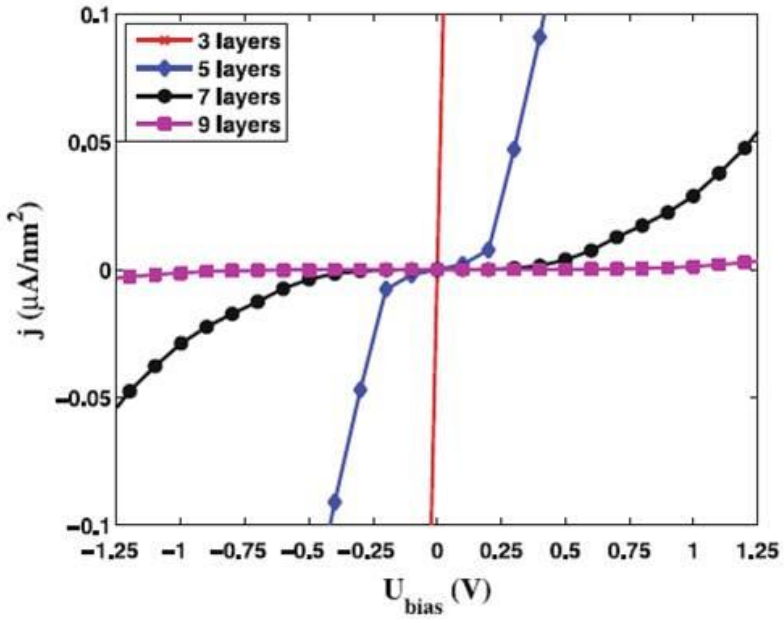


**Figure 1-7 -** Calculated current-bias curves as a function of the $Li_2O_2$ thickness. As the layer thickness increases, the necessary bias for charge transport increases due to the accumulation of $Li_2O_2$ layers. [20]

volumetric energy densities is through the design and use of positive electrode architectures that allow for full utilization of pore structure and efficient charge transport at all stages of cell operation.[17] Another approach is through the use of cell additives. The use of $O_2^-/LiO_2$ solubilizing additives assists in the formation of $Li_2O_2$ from the surface regime to the solution regime, as alluded to previously. This helps to alleviate the capacity restriction imposed by the growth of surface coverage impedance layers, and allows for a larger capacity to be obtained due to minimal occlusion of the positive electrode active sites.

Another necessity of the Li-$O_2$ positive electrode is stability towards aggressive reactants during cell operation. From the early stages of Li-$O_2$ cell development, carbon was primarily the positive electrode material of choice.[4,9,14,21] This is due to a variety of factors, such as carbon's low density, low cost, ease of availability, and the variety of different morphologies that are commercially available. Carbon is also active for ORR/OER in the Li-$O_2$ cell, making it an excellent candidate as a standard positive electrode. It is evident, however, that pure-carbon electrodes suffer from issues such as corrosion in the presence of $Li_2O_2$, and promotion of electrolyte decomposition on discharge.[**Error! Bookmark not defined.**,19,23,24] *Equations 1-9 & 1-10* below show probable mechanisms for the direct reaction of $Li_2O_2$ with the carbon surface to form $Li_2CO_3$. $Li_2CO_3$ covers active sites for ORR/OER and remains until these products can be electrochemically oxidized, which requires a high potential.[24] This oxidation also produces $CO_2$, which is poisonous to the Li-$O_2$ chemistry.[25]

$$Li_2O_2 + C + 1/2O_2 \rightarrow Li_2CO_3 \qquad \Delta G = -542\ kJ/mol \qquad \textit{(equation 1-9)}$$

$$2Li_2O_2 + C \rightarrow Li_2O + Li_2CO_3 \qquad \Delta G = -533\ kJ/mol \qquad \textit{(equation 1-10)}$$

The production of $Li_2CO_3$ at the $Li_2O_2$/carbon interface is exacerbated on cell charge, and leads to further production of $Li_2CO_3$.[4] **Figure 1.8** displays the evolution of $CO_2$ at different stages of cell discharge and charge on a $^{13}C$ carbon electrode. With the use of a $^{13}C$ labeled positive electrode, the $CO_2$ evolution is determined to evolve from oxidation of electrolyte-based $Li_2CO_3$, or carbon-source (electrode) based $Li_2{}^{13}CO_3$.[23] It is apparent that the issues with carbon electrode materials are two-fold. On both discharge and charge, the carbon positive electrode promotes the decomposition of the electrolyte to form

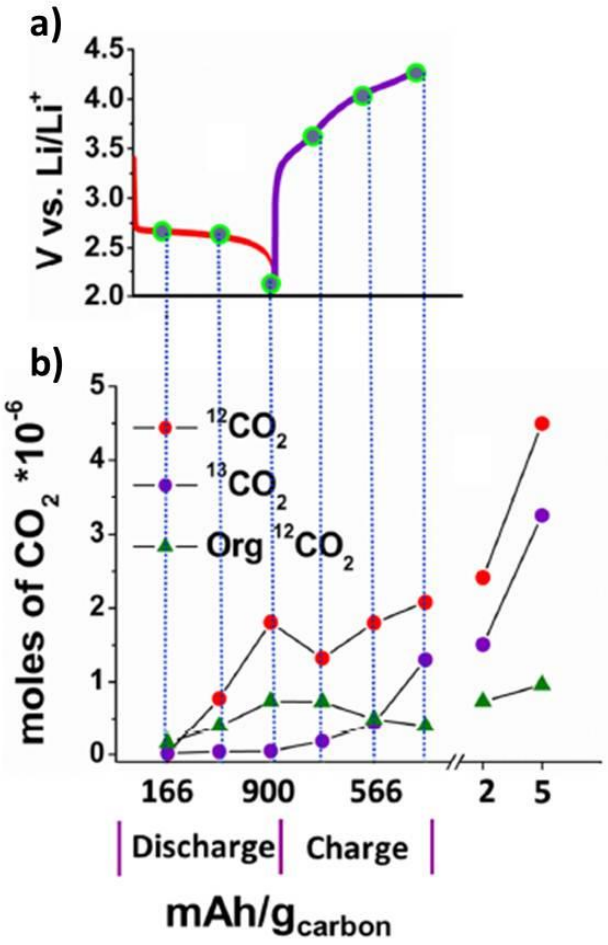


**Figure 1-8 -** Analysis of the carbonate amount at different stages of cell discharge/charge of a carbon positive electrode in a ether-electrolyte. Carbonate amount was determined by treatment of the cathode with acid to signal $Li_2CO_3$, and Fenton's reagent to signal the Li-carboxylate.[23]

Li-carboxylates. Full electrochemical oxidation of these products requires a cell potential > 4 V. The carbon positive electrode is not stable above charge potentials over 3.5 V, however, where it undergoes oxidation as evident from the evolution of $^{13}CO_2$. Hence, while the formation of decomposition products from both the positive electrode and the electrolyte occur at relatively low voltages, the high voltage necessary to oxidize these products results in carbon oxidation, and causes further parasitic reactions. These products contribute to the large polarization that is observed on charge over numerous cycles, which ultimately limits the capacity retention and cycling capabilities of the Li-$O_2$ cell.

One solution to the issue of carbon reactivity is the use of non-reactive positive electrode materials. While some claim these materials as "catalysts" for the Li-$O_2$ chemistry due to the lowering in voltage overpotential and improvement in cycling capabilities that are typically exhibited, research suggests that these alternative materials do not catalyze the Li-$O_2$ chemistry in the same manner as traditional electrocatalysts.[26] One example is titanium carbide (TiC). TiC in both TEGDME and DMSO-based electrolytes exhibits a lower charge overpotential compared to a pure carbon positive electrode, as shown in **Figure 1-9** below.[27] The cycling capabilities are also drastically improved, for 100 cycles are obtainable with very minimal loss in capacity. This improved performance is proposed to be due to the lack of parasitic reactions. TiC does not react with $Li_2O_2$ to form Li-carbonates or other carboxylate species, and it is argued that DMSO is completely stable to superoxide attack. Specifically, the use of TiC as a positive electrode material substantially improves cell performance and enhances cycling capabilities. The benefit of TiC as a positive electrode material is evident through closer examination of its properties in the presence of $Li_2O_2/O_2^-$

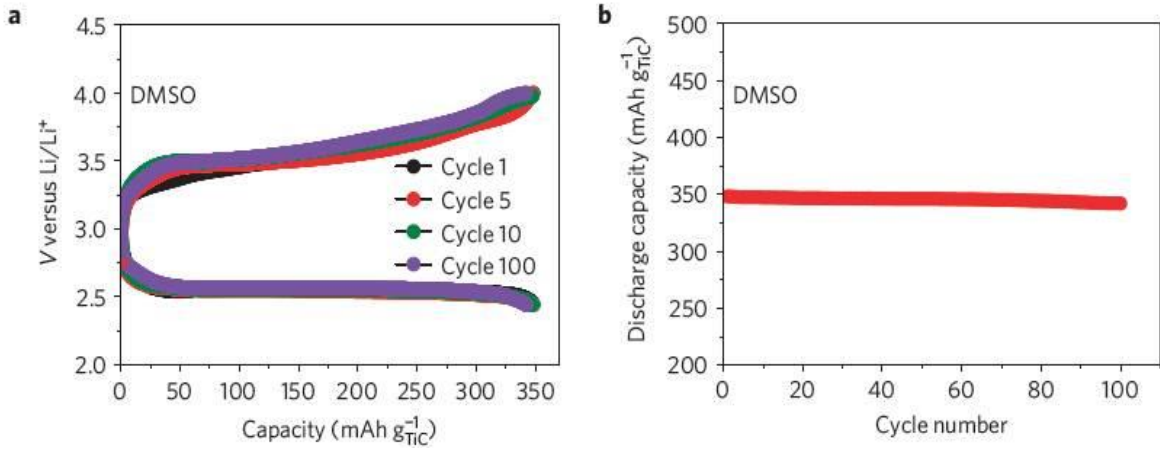


**Figure 1-9 -** (a) Electrochemical profile and (b) cycling profile as a function of discharge capacity of TiC in 0.5 M $LiClO_4$/DMSO.[27]

Upon exposure to $Li_2O_2$, the surface of TiC reacts to form nanometer thick $TiO_{2-x}$ layers.[28] These layers protect the bulk TiC from further oxidation while being thin enough to allow for electron transport. If this $TiO_{2-x}$ passivation layer is too thick, the electrochemistry is completely inhibited.[28] The complete removal of a 100% carbon positive electrode, in conjunction with the use of an electrochemically stable electrolyte, has the capability to greatly improve the Li-$O_2$ battery performance.

Such results lend credibility to the cell stability issues discussed above. Additionally, many other reports have investigated different positive electrode materials, from nanoporous gold [29], ruthenium-based positive electrode materials [30], and other carbide materials. [31,32] Thus, the need for an ORR/OER active material that is stable to the Li-$O_2$ chemistry, or that has the necessary activity to oxidize decomposition products at low overpotentials, is a crucial requirement for commercialization of the Li-$O_2$ battery.

However, in order to ensure ORR/OER activity is maintained during the entirety of cell operation, not only does the positive electrode have to be stable to $Li_2O_2/O_2^-$ attack, but the surface of the positive electrode must also remain ORR/OER active. This leads to the

second major crux of aprotic Li-$O_2$ batteries, which is that solid decomposition products form as a result of electrolyte decomposition. Therefore, before the true activity of Li-$O_2$ positive electrodes can be realized, the accumulation of electrolyte decomposition products that result from parasitic reactions during discharge and charge must be prevented.

### 1.2.3 – Electrolytes for the Li-$O_2$ Battery

While the development of new positive electrode materials is crucial to obtain a large energy density and facilitate a more efficient ORR/OER reaction, the electrolyte is very important for long-term cell stability. To maximize the performance of the Li-$O_2$ battery, the electrolyte must possess a high ionic conductivity, high $O_2$ solubility, and high $O_2$ diffusivity. This is necessary to achieve high rate capabilities and exceptional mass transport. Furthermore, if the Li-$O_2$ battery is to be commercially viable, the electrolyte should be cost efficient and non-hazardous. For commercial purposes and long-term stability, the volatility of the electrolyte must be minimal to prevent termination of ion transport as a result of complete electrolyte evaporation, especially if the Li-$O_2$ battery is (eventually) operated in the open atmosphere. The most imperative requirement for the Li-$O_2$ battery electrolyte, however, is chemical and electrochemical stability. As will become evident in subsequent sections, the long-term operation of the Li-$O_2$ battery is dependent on the electrolyte stability towards both $O_2^-$ and $Li_2O_2$, as well as stability within the electrochemical potential window of operation. The following section explores the common electrolytes that have been utilized in Li-$O_2$ batteries and discusses their limitations.

Early reports of the Li-$O_2$ cell used carbonate-based electrolytes such as propylene carbonate (PC), a popular electrolyte for Li-ion batteries.[33] This was initially thought to be suitable based on the observed oxygen ORR/OER electrochemistry.[34,35] However, it

became apparent that the observed electrochemistry was not the decomposition and oxidation of $Li_2O_2$, but that of $Li_2CO_3$.[36,37 The formation of $Li_2CO_3$ as the primary discharge product, as opposed to $Li_2O_2$, results from the oxidation of the carbonate solvent from the highly nucleophilic $O_2^-$. These products accumulate on the positive electrode surface during cycling, forming impedance layers which deactivate the positive electrode surface. Furthermore, upon oxidation of the discharge product, the carbonate solvent decomposes to form propionic acid, which polymerizes on the metallic lithium negative electrode to form a thick insulating gel. A thorough discussion and analysis of carbonate instability in the Li-$O_2$ cell can be found in a pioneering report by Freunberger *et. al.* [38]

Another class of electrolytes worthy of discussion are ether-based (or glyme) electrolytes. To this day, ether-based electrolytes are the most popular electrolytes used in Li-$O_2$ batteries. Initially, ether-based electrolytes were considered excellent candidates due to their high stability towards $O_2^-$ based on hard-soft acid-base (HSAB) theory, as identified by O'Laire *et. al.*[39] In contrast to carbonate-based electrolytes, ether-based electrolytes do not interfere with the production of $Li_2O_2$. However, extensive studies demonstrate that while ethers are suitable electrolytes for Li-$O_2$ cells, a non-trivial degree of decomposition occurs on both discharge and charge. Many reports have outlined the mechanism for glyme decomposition (specifically, dimethoxyethane (DME) and derivatives), and have identified that both the terminal methyl groups and methylene groups are subject to hydrogen abstraction by the superoxide anion $O_2^-$. [39,40] **Figure 1.10** summarizes the decomposition of DME. Such decomposition leads to the formation of various Li-carboxylates such as Li-formate, Li-carbonates, and dimethyl oxalate.

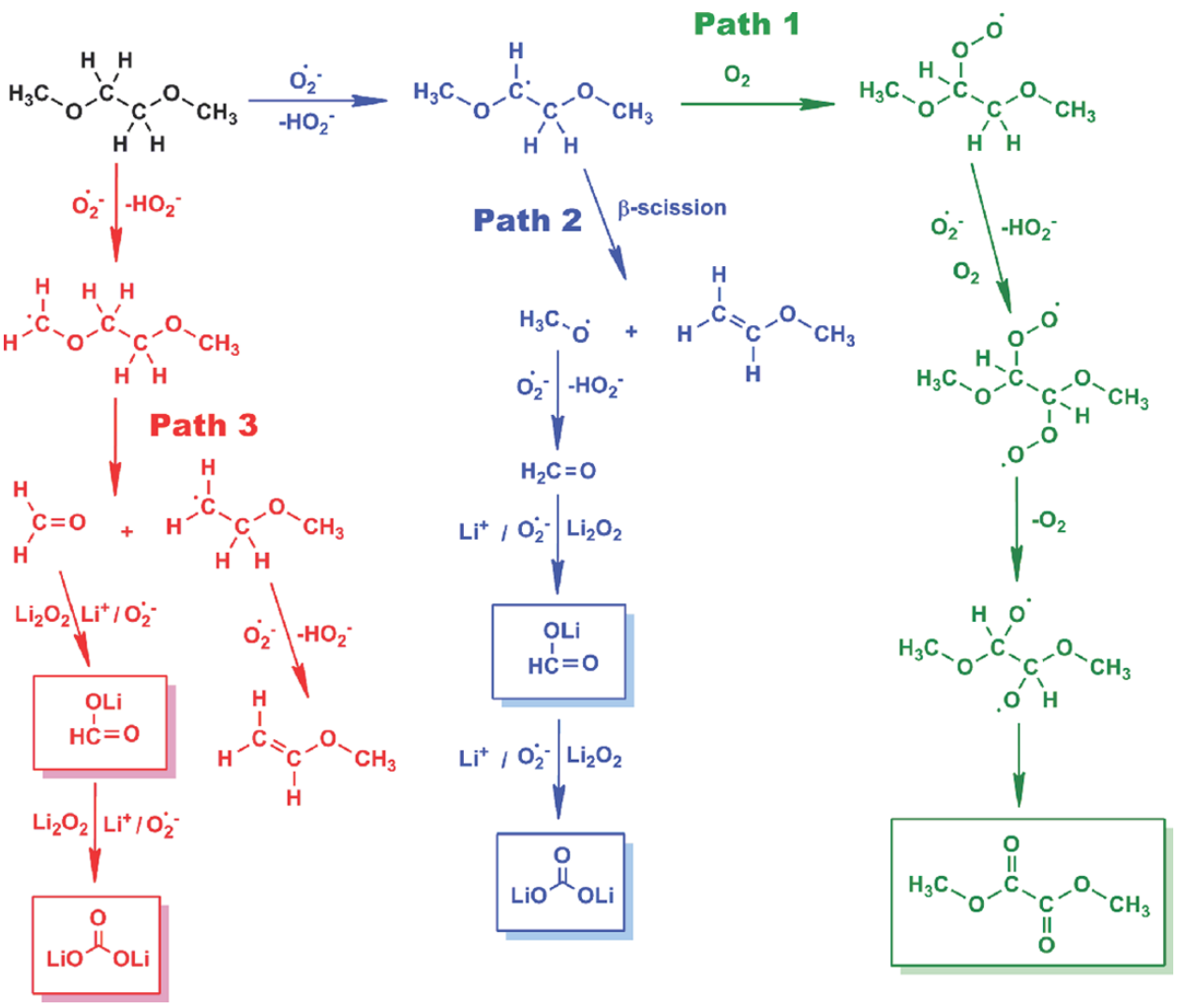


**Figure 1-10 -** Decomposition reactions of glyme-based electrolytes in the Li-$O_2$ cell as a result of $O_2^-$. The abstraction of the hydrogen by $O_2^-$ leads to the formation of a wide variety of carboxylate products, including Li-formate, Li-carbonate, and dimethyl oxalate.[43]

Apart from hydrogen abstraction, ether electrolytes are also not stable to the discharge product itself, $Li_2O_2$. Like $O_2^-$, $Li_2O_2$ is capable of hydrogen abstraction in the same manner as $O_2^-$, which causes decomposition product formation on the surface of the $Li_2O_2$ particles.[41] Furthermore, ether decomposition is accelerated during discharge in the presence of carbon, giving rise to Li-carboxylate products on the positive electrode surface, as mentioned previously.[23] Jointly, these factors together make ether-based electrolytes

unsuitable for long-term use in the Li-$O_2$ battery. Attempts to mitigate the degree of hydrogen abstraction from the glyme structure, and in turn reduce the degree of decomposition product formation, were attempted through substitution of the terminal methyl groups with more protective silane groups.[42] Another report details the successful substitution of the methylene hydrogens on the glyme backbone with methyl groups as a means to protect the glyme backbone from $O_2^-$/$Li_2O_2$ attack.[43] This method has proven to substantially reduce the degree of decomposition in the cell, and is an effective method to mitigate the degree of hydrogen abstraction. However, this backbone substitution drastically alters the electrolyte properties to become very viscous and unsuitable for higher current applications that are demanded of the Li-$O_2$ battery, and hence this electrolyte is impractical.

The main contributors to the identification and understanding of electrolyte decomposition in the Li-$O_2$ cell are from A. C. Luntz, and B. D. McCloskey. With precise mass spectrometry experiments coupled with various spectroscopic techniques, they quantified the degree of chemical instability of ether-based electrolytes (in particular DME) and the impact these instabilities have on electrochemical performance.[44] In typical Li-$O_2$ cells, a 100% efficient discharge/charge process corresponds to a 2 $e^-/O_2$ oxygen consumption (ORR) or evolution (OER). Under typical operating conditions in ether-based electrolytes, the oxygen evolution from $Li_2O_2$ oxidation, which is a measure of the charge efficiency, measures between 2.60 – 3.20 $e^-/O_2$ (values are highly dependent on operating conditions).[4,17,39,43] This is a direct result of the formation of Li-carboxylate species (parasitic reactions) in tandem with the desired $Li_2O_2$ formation and oxidation. The presence of these carboxylate species is evident at potentials > 4.0 V, at which point their oxidation produces $CO_2$. **Figure 1-11** demonstrates the impact that Li-carboxylates have on the

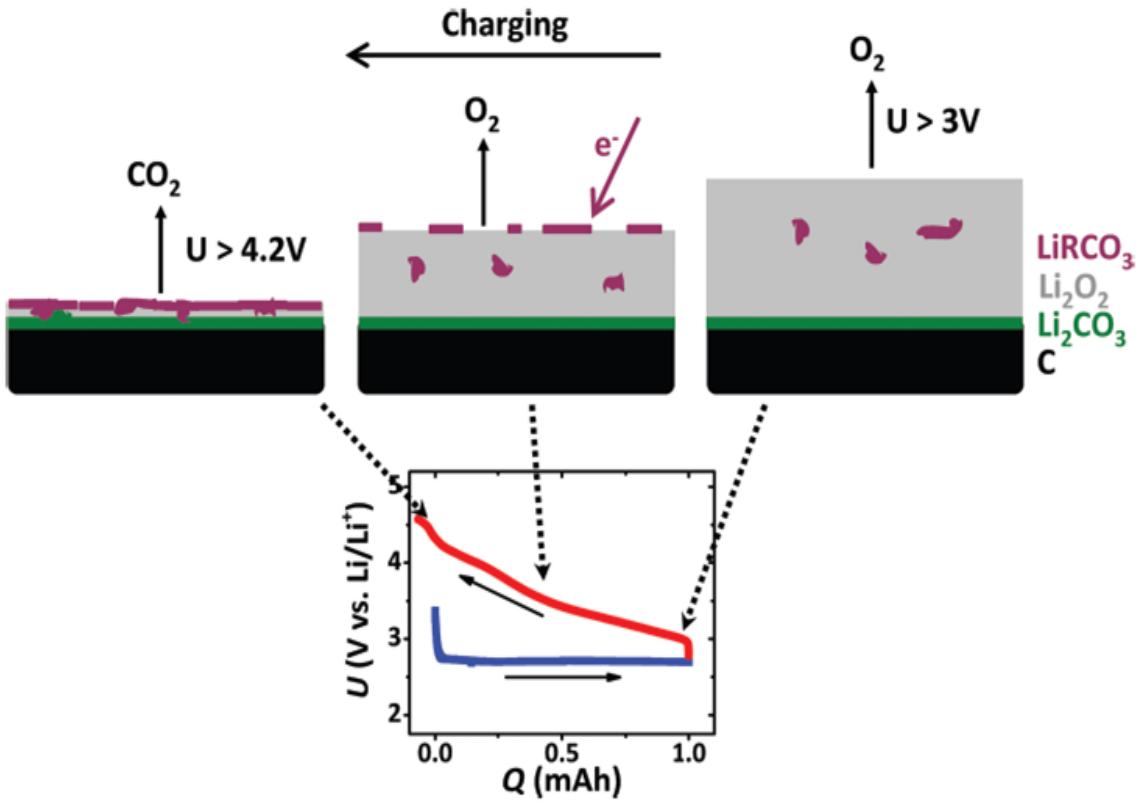


**Figure 1-11 -** Schematic showing the origin of the charge overpotential in Li-$O_2$ batteries operated in ether-based electrolytes. At the start of charge, $Li_2O_2$ is oxidized at a low potential, as it is the bulk constituent on the cathode surface. As the $Li_2O_2$ oxidizes, the fresh $Li_2O_2$ surface reacts with electrolyte to form Li-carboxylate decomposition products. This insulating product creates impedance layers, resulting in an increase of the cell potential to oxidize the remaining $Li_2O_2$. The end of oxidation occurs at a high potential, when the $Li_2O_2$ is removed and the Li- carboxylates (formed from both the $Li_2O_2$/electrolyte interface and $Li_2O_2$/carbon interface) are oxidized at U > 4.2 V.[18]

oxidation chemistry of $Li_2O_2$.[18] The major product formed on discharge is $Li_2O_2$, along with non-trivial amounts of Li-carboxylate species. Initially, $Li_2O_2$ is oxidized at low overpotentials, but the potential gradually increases throughout the entirety of oxidation. This results from two occurrences: the formation of Li-carboxylates at the $Li_2O_2$ surface, and the removal of the $Li_2O_2$, which increases the proportion of carboxylates to $Li_2O_2$. Consequently, as $Li_2O_2$ is removed and the presence of carboxylates begins to dominate, the potential must increase in order to maintain a constant galvanostatic charge rate. Eventually, all $Li_2O_2$ is

consumed and only the surface of $Li_2CO_3$ and other Li-carboxylate decomposition products remain, which requires large potentials (> 4.2 V) to electrochemically oxidize. Some of this product cannot be electrochemically oxidized, and will remain present during subsequent discharge cycles.[18]

The impact of these decomposition products on the energy efficiency of the Li-$O_2$ battery can be understood through quantification of the decomposition products. In a study by McCloskey *et. al*, iodometric titration coupled with mass spectrometry identifies the efficiency of $Li_2O_2$ formation and oxidation, as well as the quantity of decomposition products that form during cell operation.[44] In this report they demonstrate that on discharge, the maximum purity of the $Li_2O_2$ obtained is approximately 91% of the discharge capacity, noting that ~10% of the current passed goes into the formation of Li-carboxylate products. This of course is a function of operating conditions, with variance greatly dependent on cell materials used as well as the electrochemical conditions employed. The formation of Li-carboxylates originates from reactivity of $Li_2O_2$ with the glyme electrolyte. A majority of the Li-carboxylate products ($Li_2CO_3$, Li-formate, as well as Li-methoxide and ethoxide) form on charge. $CO_2$ accompanies the evolution of oxygen at high potentials, as shown in **Figure 1-12.** At these high potentials, the production of Li-carboxylate species accelerates. This work demonstrates the major problem with the Li-$O_2$ battery and the effect that decomposition products have on the cell inefficiencies. Currently, with ether-based electrolytes, there is no practical approach to remove these carboxylate products during cycling in a manner that will allow for stable performance over numerous cycles.

In an effort to circumvent these ether-based electrolyte issues, research has shifted towards the use of other aprotic media in the Li-$O_2$ cell. Of the other electrolytes explored in

the Li-$O_2$ battery, dimethoxy sulfone (DMSO) has shown great promise as a stable electrolyte for the Li-$O_2$ battery. As mentioned previously, a fully functional cell with DMSO as the electrolyte and TiC as the positive electrode was created by Thotiyl *et. al*.[27] The author claims that DMSO is very stable towards superoxide and $Li_2O_2$ reactivity, and thus exhibits excellent cycling capabilities (**Figure 1-9** previously) with clear elimination of decomposition products. However, these results are not reproducible, as further research has demonstrated. The reactivity of DMSO with $O_2^-$ produces sulphoxide and sulphone-based decomposition products.[45,46] The cause for this discrepancy among reports is not known.

Other electrolyte media has been explored, with investigations of amides [47], sulphones [48], and a variety of ionic liquids [49,50,51] ultimately proving unsuccessful as a

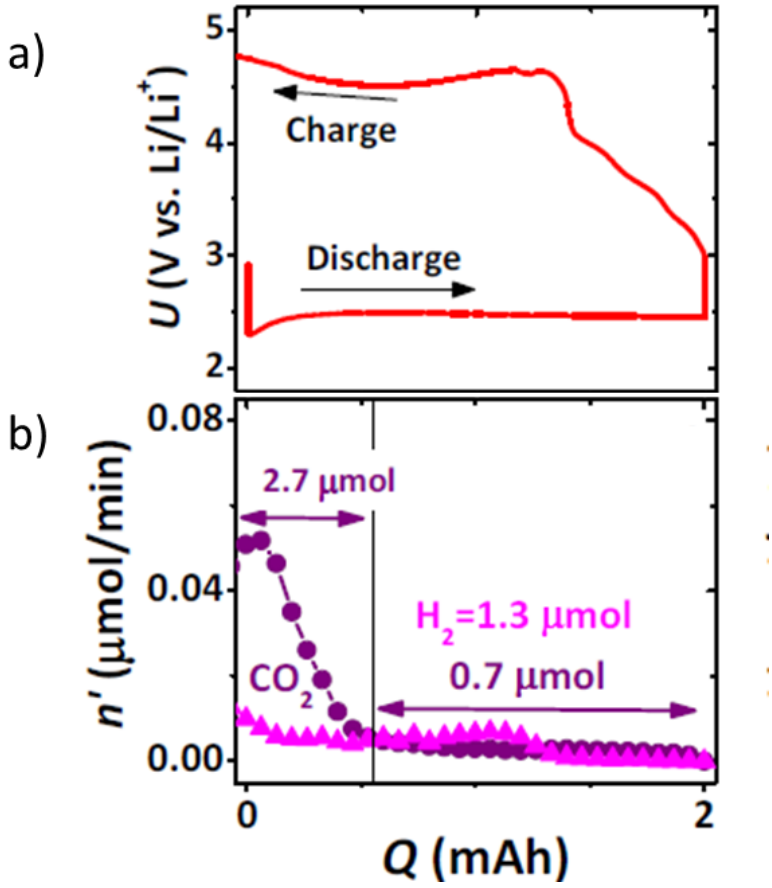


**Figure 1-12 –** (a) Electrochemical charge curve and (b) corresponding $CO_2$ evolution of a P50 carbon positive electrode operated in 1M LiTFSI/DME electrolyte. [44]

more stable electrolyte system. Furthermore, theoretical studies have screened the stability of multiple different electrolytes, as a means to explore potential candidates for experimental studies. Bryantsev *et. al*, have proposed a variety of potential electrolyte candidates by screening solvents based on their stability to $O_2^-$ attack and $O_2/O_2^-$ electrochemical reversibility.[52] Unfortunately, there is no known electrolyte that is completely stable to $O_2^-$ /$Li_2O_2$ oxidation which can also be practically used in a Li-$O_2$ cell, and thus avoiding electrolyte decomposition in current Li-$O_2$ cells is near impossible. Other reports demonstrate that the Li-salt also decomposes, and salt products, such as LiF, comprise a small amount of the final discharge products.[53]

Not mentioned in this section, but which are still a very real concern, is the issue of metallic lithium and the safety concerns that arise with its use as the negative electrode.

Overall, it is clear that many issues must be overcome before commercialization of the Li-$O_2$ battery can be realized. Even if the Li-$O_2$ battery were to be rid of these stability issues and achieve stable cycling with low overpotentials, the practical use of the Li-$O_2$ battery still remains suspect. Given the stringent requirements for ultra-pure $O_2$ (since $Li_2O_2$ is easily contaminated with $CO_2$ and other products in the atmosphere [54]), as well as the concerns for the large volume of oxygen that will be necessary for practical use, giving rise to an unacceptable volumetric capacity [55], the commercialization of Li-$O_2$ battery technology is problematic.

## 1.3 – Na-$O_2$ Batteries

One appealing alternative to Li-$O_2$ batteries are a similar class of metal-$O_2$ batteries that utilize $Na^+$ as the cation source. A comparison of the electrochemical performance of Na-$O_2$ vs. Li-$O_2$ batteries is shown in **Figure 1-13**, which displays representative voltage

profiles for a single cell cycle. Compared to the Li-$O_2$ battery, the voltage profile of the Na-$O_2$ battery exhibits a much improved voltage efficiency, as well as other desirable properties as will be discussed in subsequent sections. The first report of an Na-$O_2$ battery demonstrated a fully working cell comprised of molten metallic sodium operated at 100°C.[56] Following this, the first room temperature studies of the Na-$O_2$ battery were reported by Hartmann *et. al.*[57] This report demonstrates that the Na-$O_2$ battery operates under the same principles as the Li-$O_2$ battery, but with key differences that makes the Na-$O_2$ cell an appealing alternative to the currently troublesome Li-$O_2$ system. The ORR in Na-$O_2$ batteries follows a 1 $e^-$ reduction of $O_2$ to form $O_2^-$, which reacts with $Na^+$ to form $NaO_2$. Unlike $LiO_2$, $NaO_2$ does

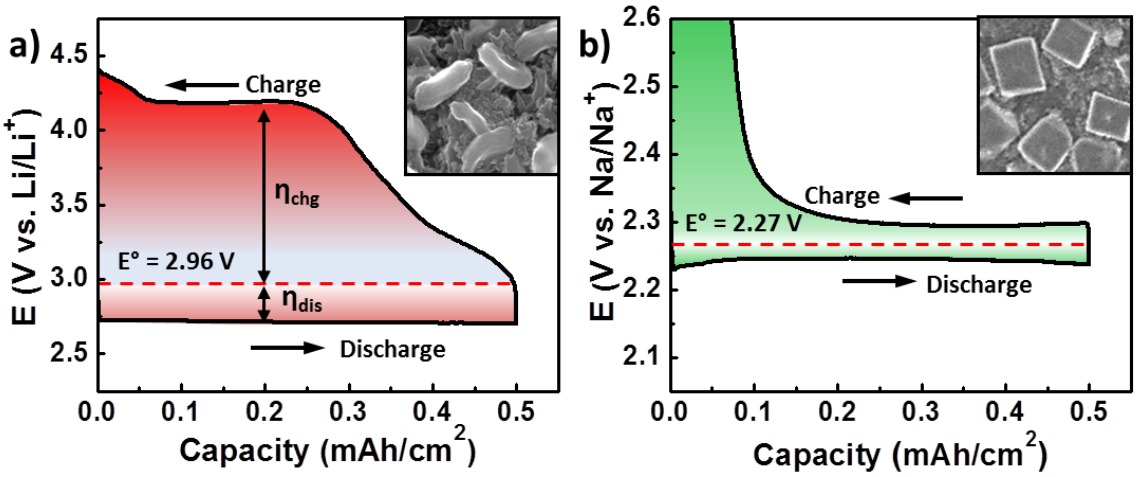


**Figure 1-13 -** Comparison of (a) a typical aprotic Li-$O_2$ battery and (b) typical aprotic Na-$O_2$ battery. The Na-$O_2$ battery exhibits much better voltage efficiency, as well as a significant difference in the chemical composition ($Li_2O_2$ vs. $NaO_2$) and morphology of the discharge product.

not undergo disproportionation and is thermodynamically stable. This product is formed at a theoretical potential of 2.27 V vs. $Na/Na^+$. Given that it is a one electron process, as well as the atomic mass of sodium being heavier than lithium, the overall gravimetric energy density of the Na-$O_2$ battery is less than that of the Li-$O_2$ battery (1100 vs. 3458 Wh/kg).

Thermodynamically, $Na_2O_2$ should be the more favourable discharge product ($E° = 2.33$ vs. $Na/Na^+$), albeit only by a small difference in the energy of formation (-2.00 eV/Na vs. -2.31 eV/Na, respectively).[58] These values correspond to the bulk phases of $NaO_2$ and $Na_2O_2$, however, with the lower surface energy of nanoparticulate deposits that initially nucleate on the positive electrode surface favouring the formation and growth of $NaO_2$.[59] Many reports have surfaced which obtain $Na_2O_2$ as the discharge product. Compared to $NaO_2$, the oxidation of $Na_2O_2$ is much more difficult, with charge overpotentials similar to that $Li_2O_2$ of oxidation.[60,61,62] The cause of this discrepancy among researchers is not known, despite the same experimental conditions being used.

$NaO_2$ forms as large cubic structures and deposits on the positive electrode surface, as depicted in the inset of **Figure 1-13b**. Similar to the Li-$O_2$ battery, the amount of $NaO_2$ that is able to be stored on the positive electrode determines the total obtainable capacity. The growth of these large $NaO_2$ cubic crystals occurs with a fairly low overpotential, as shown in **Figure 1-13b**. Much like the Li-$O_2$ battery, two mechanisms of $NaO_2$ formation have been proposed. One mechanism is solution based growth, based on soluble $NaO_2$ species nucleating onto pre-existing $NaO_2$ surfaces to form the observed cube structures. The second mechanism is surface transport of electrons on the conductive $NaO_2$ surface, which leads to the direct reduction of oxygen and $NaO_2$ formation onto already existing cube surfaces.[62] Evident from the voltage profile in **Figure 1-13b**, the oxidation of $NaO_2$ exhibits a low charge overpotential compared to that of the Li-$O_2$ battery. **Table 1-2** below further compares the Li-$O_2$ and Na-$O_2$ battery based on electrochemical performance, as well as economic factors associated with the use of lithium over sodium. What the Na-$O_2$ system lacks in gravimetric energy density, it makes up for with a much lower charge overpotential,

facile cell charging, and better cycling capabilities compared to the Li-$O_2$ cell. Based on these properties, the Na-$O_2$ cell is a very attractive system to study for electrochemical storage applications.

It is clear that in the absence of any electrolyte additives (in this case, $H_2O$) or impurities, the growth of $NaO_2$ occurs via a surface based mechanism.[57] This surface based mechanism is kinetically sluggish, as evident through a large discharge overpotentia1

**Table 1-2 –** Comparison of the performance of the Li-$O_2$ battery vs. the Na-$O_2$ battery. Values given are for typical ether-based electrolyte systems.

| | **Li-$O_2$** | **Na-$O_2$** |
|---|---|---|
| **Theoretical Energy Density** | 3458 Wh/kg | 1100 Wh/kg |
| **Charge Overpotential** | Poor ( > 1 V) | Excellent (< 0.2 V) |
| **Negative electrode Stability** | Poor | Very Poor |
| **Charge efficiency ($e^-/O_2$) [63]** | 2.60 | 1.10 |
| **Discharge efficiency ($e^-/O_2$) [58]** | 2.01 | 1.01 |
| **OER/ORR[55]** | 0.78 | 0.93 |
| **Earth Abundance of metal[1] [64]** | 0.0065% | 2.05% |

[1] Earth's crust composition in mass percent

and small achievable capacity when the $H_2O$ is absent in the electrolyte (0 ppm) (**Figure 1-14a)**. However, with only small additions of $H_2O$ (> 5 ppm), the $NaO_2$ growth proceeds via a solution based mechanism. Apart from a difference in capacity, the presence of small concentrations of $H_2O$ leads to the formation of $NaO_2$ cubes (**Figure 1.14b**) instead of thin

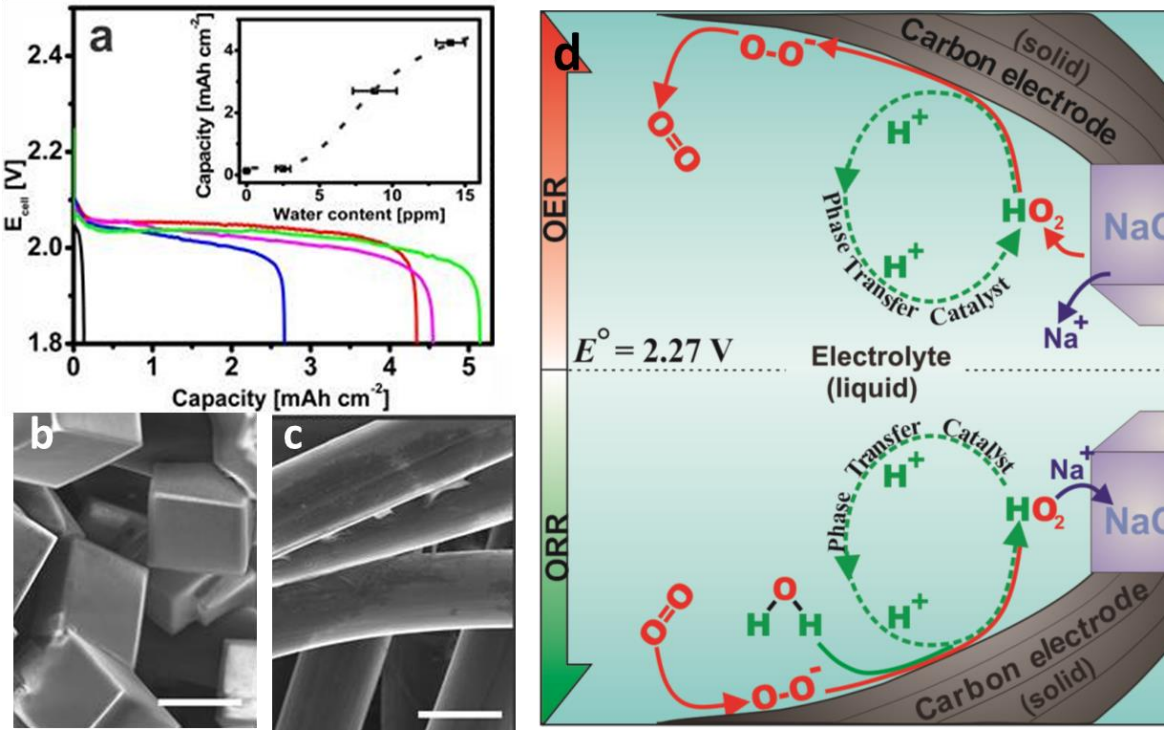


**Figure 1-14 -** The effect of water concentration on the discharge capacity can be seen in (a), where addition of $H_2O$ in amounts of 0 ppm (black line), 8 ppm (blue line), 14 ppm (red line), 10 ppm benzoic acid (magenta) and 10 ppm acetic acid (green). (b) The formation of $NaO_2$ cubes occurs with 10 ppm added $H_2O$, and (c) in the absence of any $H_2O$ (0 ppm) forms a thin surface film of $NaO_2$. The addition of $H_2O$ (or another proton source) acts to mediate the discharge/charge solubility of the $O_2^-/NaO_2$ species to allow for a much more efficient discharge/charge process via the mechanism shown in (d). [65]

$NaO_2$ films in the absence of any residual $H_2O$ (**Figure 1-14c)**. Much akin to similar studies of a solvation mediator for the formation of $Li_2O_2$ [10], the presence of a proton phase transfer catalyst (PTC) in the Na-$O_2$ cell facilitates the dissolution of $O_2^-$ and $NaO_2$ via an $HO_2$ intermediate.[65] The $HO_2$ undergoes a metathesis reaction with $Na^+$ to form $NaO_2$, which then deposits on the electrode (or existing $NaO_2$) surface. The PTC activity towards $NaO_2$ reduction/oxidation is summarized in **Figure 1-14d**. It is clear that a PTC is crucial for both the formation and decomposition of $NaO_2$, and the importance of a solution based mechanism for efficient ORR and OER.

Overall, Na-$O_2$ batteries are new and exciting avenues of research within the field of metal-$O_2$ batteries. With its many benefits compared to Li-$O_2$ batteries, such as the increased solubility of the $NaO_2$ species with a PTC eliminating the need for a solid catalyst, the Na-$O_2$ battery is set to increase in popularity in the very near future. The exploration of Na-$O_2$ batteries has just begun, in much the same manner and excitement during the advent of the Li-$O_2$ battery. Other issues, such as stability (and safety) of the metallic sodium metal negative electrode, are other areas worth investigation, which will not be discussed here.[66] It will be important to utilize what is known about the Li-$O_2$ battery and use this to understand some of the current limitations of the Na-$O_2$ battery (which will be discussed in *Section 6.0* of this dissertation), and how to overcome them.

## 1.4 – Thesis Overview

This thesis features four separate sections, each identifying a specific problem of metal-$O_2$ battery systems, and the research that was conducted to better understand these problems and identify possible solutions.

In *Section 2*, a brief description of each major characterization technique is presented. This is meant to provide the reader with a glimpse of the theory and practices used in the characterization techniques throughout this report. Furthermore, important preparation procedures and standards are discussed. While each chapter of this thesis holds its own experimental section, there are some common practices, such as electrolyte preparation, that are common to all sections of this thesis.

*Section 3* details the use of chemically generated $O_2^-$ in solution as a means to screen the stability of various Li-$O_2$ cell components. The experimental procedure is given in detail,

and validated through the production of the desired product $Li_2O_2$. The chemical production of $Li_2O_2$ is compared to electrochemically formed $Li_2O_2$. The reactivity of $O_2^-$ towards Li-$O_2$ battery components, such as the binder (PVdF), as well as common electrolyte solvents such as PC and TEGDME, is identified and investigated. This work has been published:

R. Black, S. H. Oh, J. H. Lee, T. Yim, B. Adams, L. F. Nazar. "Screening for superoxide reactivity in Li-$O_2$ batteries: effect on $Li_2O_2$/LiOH crystallization." *J. Amer. Chem. Soc.* vol.134, pp. 2902-2905, 2012. **DOI:** 10.1021/ja2111543.

*Section 4* focuses on the use of a catalyst for the Li-$O_2$ battery. The catalyst of interest is $Co_3O_4$ supported on RGO. Compared to a pure carbon positive electrode, the use of $Co_3O_4$/RGO demonstrates various benefits such as a reduced charge overpotential, larger discharge capacity, and improvement in capacity retention on cycling. A discussion is presented on the source of this improved performance, with supporting electrochemical measurements. However, as evident from the use of time of flight secondary ion mass spectrometry (TOF-SIMS), the formation of decomposition products proves to limit any positive electrode activity beyond the first few cycles. This work has been published under:

R. Black, J. H. Lee, B. Adams, C. A. mims, L. F. Nazar. "The role of catalysts and peroxide oxidation in lithium-oxygen batteries." *Angew. Chem. Int. Ed.* vol. 125, pp. 410-414, 2013. **DOI:** 10.1002/ange.201205354.

*Section 5* outlines the development and testing of a new tool to explore and quantify the efficiency of metal-$O_2$ batteries. This technique is online electrochemical mass spectrometry (OEMS). In this section, the design of the mass spectrometer instrument and its interface with a metal-$O_2$ cell are presented. The design requirements that are necessary to

ensure accurate quantification of the gas evolution on charge are discussed. The benefits of mass spectrometry to investigate the oxidation activity of various positive electrode materials are demonstrated through the use of pre-loaded $Li_2O_2$/active material composite positive electrodes. Finally, the difference between the oxidation of electrochemically generated $Li_2O_2$ and that of commercial $Li_2O_2$ powder is investigated with mass spectrometry to demonstrate the major inefficiencies of electrolyte decomposition on cell performance. The work presented here, as well as other publications where mass spectrometry has been utilized, are listed below:

B. Adams, R. Black, C. Radtke, Z. Williams, B. Mehdi, N. Browning, L. F. Nazar. "The importance of nanometric passivating films on positive electrode for Li-air batteries." *ACS Nano*. vol. 8, pp. 12483-12493, 2014. **DOI:** 10.1021/nn505337p.

B. Adams, R. Black, Z. Williams, R. Fernandes, M. Cuisinier, E. Jamstorp Berg, P. Novak, G. K. Murphy, L. F. Nazar. "Towards a stable organic electrolyte for the lithium oxygen battery" *Adv. Energy Mat.* vol. 5, pp. 1400867, 2013. **DOI:** 10.1002/aenm.201400867.

D. Kundu, R. Black, E. Jamstorp Berg, L. F. Nazar. "A highly active nanostructured metallic oxide positive electrode for aprotic Li-$O_2$ batteries." *Energy Environ. Sci*. vol. 8, pp. 1292-1298, 2015. **DOI:** 10.1039/C4EE02587C.

D. Kundu, R. Black, B. Adams, K. Harrison, K. Zavadil, L. F. Nazar. "Nanostructured metal carbides for aprotic Li-$O_2$ batteries: new insights into interfacial reactions and positive electrode stability." *J. Phys. Chem. Lett.* vol. 6, pp. 2252-2258, 2015. **DOI:** 10.1021/acs.jpclett.5b00721

*Section 6* focuses on degradation reactions in the Na-$O_2$ battery. Specifically, with the use of mass spectrometry, $^1$H NMR, and iodometric titration, the decomposition reactions in the aprotic Na-$O_2$ battery are investigated. It is identified that decomposition reactions in the Na-$O_2$ battery primarily occur as a result of $O_2^-$ and the highly reactive $NaO_2$ discharge

product. There is little contribution to the formation of decomposition products as a result of $NaO_2$ oxidation, which is in contrast to the Li-$O_2$ battery. The performance of Na-$O_2$ batteries vs. Li-$O_2$ batteries is understood through investigation of these decomposition reactions. This work is currently under revisions for ChemSusChem based on reviewer comments.

This dissertation also has three appendices. Appendix A is related to *Section 5*, and shows the gas quantification script that was created in Matlab. Using this script, it allowed for quantification of the gas evolution (based on the ion current) within seconds. Appendix B shows further data for *Section 5.3* – $Mo_2C$ positive electrode. Specifically, the XPS analysis of the $Mo_2C$ positive electrode during different stages of a cell cycle. This data further supports the conclusions that are presented in *Section 5.3*. Appendix C is an entirely separate section that focuses on the study of an inverse opal carbon positive electrode as a means to obtain a maximum energy density in the Li-$O_2$ battery. While it is demonstrated that on a single discharge, the gravimetric energy density is improved with the use of an inverse opal carbon (IOC) electrode architecture, ultimately the electrode, as is, is not useable in a Li-$O_2$ cell due to the many electrolyte and positive electrode decomposition reactions that occur. Ultimately, because of this, the inverse opal carbon work is incomplete, and further development of stable electrolytes is necessary before the benefits of different electrode architectures can be realized on a practical level.

# 2.0 - Preparation and Characterization Techniques

## 2.1 – Electrolyte Purification and Distillation

As will be evident in subsequent chapters of this thesis, the electrolyte is a vital component to the overall performance of metal-$O_2$ batteries, as it is the medium for $O_2$ dissolution and free migration of ions between electrodes. Any impurities in the electrolyte will negatively affect the final discharge product composition, and will have a large impact on the cell electrochemistry. Hence, before any cell preparation can take place, it is crucial that the organic solvents used in electrolytes be distilled, and void of any contaminants. Here I will discuss the distillation and drying procedure for solvents and salts used as a metal-$O_2$ battery electrolyte.

The solvent, as received, is poured into a round bottom flask with added sodium metal. The sodium metal removes $H_2O$ in the electrolyte *via* the surface reaction $2Na + 2H_2O \rightarrow 2NaOH + H_2$. An apparatus consisting of a fractionating column, a water condenser, and a receiving flask is assembled, as shown in **Figure 2-1**. The round bottom flask is heated to the desired temperature to bring the liquid to a boil. The solvent evaporates up the fractionating column to eventually condense in the condenser column and flows into the receiving flask. Using this method, the solvent of interest can be separated from contaminates based on its boiling temperature. A thermometer at the top of the fractionating column indicates the temperature of the boiling solvent. This is used to ensure that the distillate is the desired solvent. Typically, 10-15 mL of the initial distillate is collected and discarded, and the distillation is stopped when ~20 mL of solvent remains in the round bottom flask.

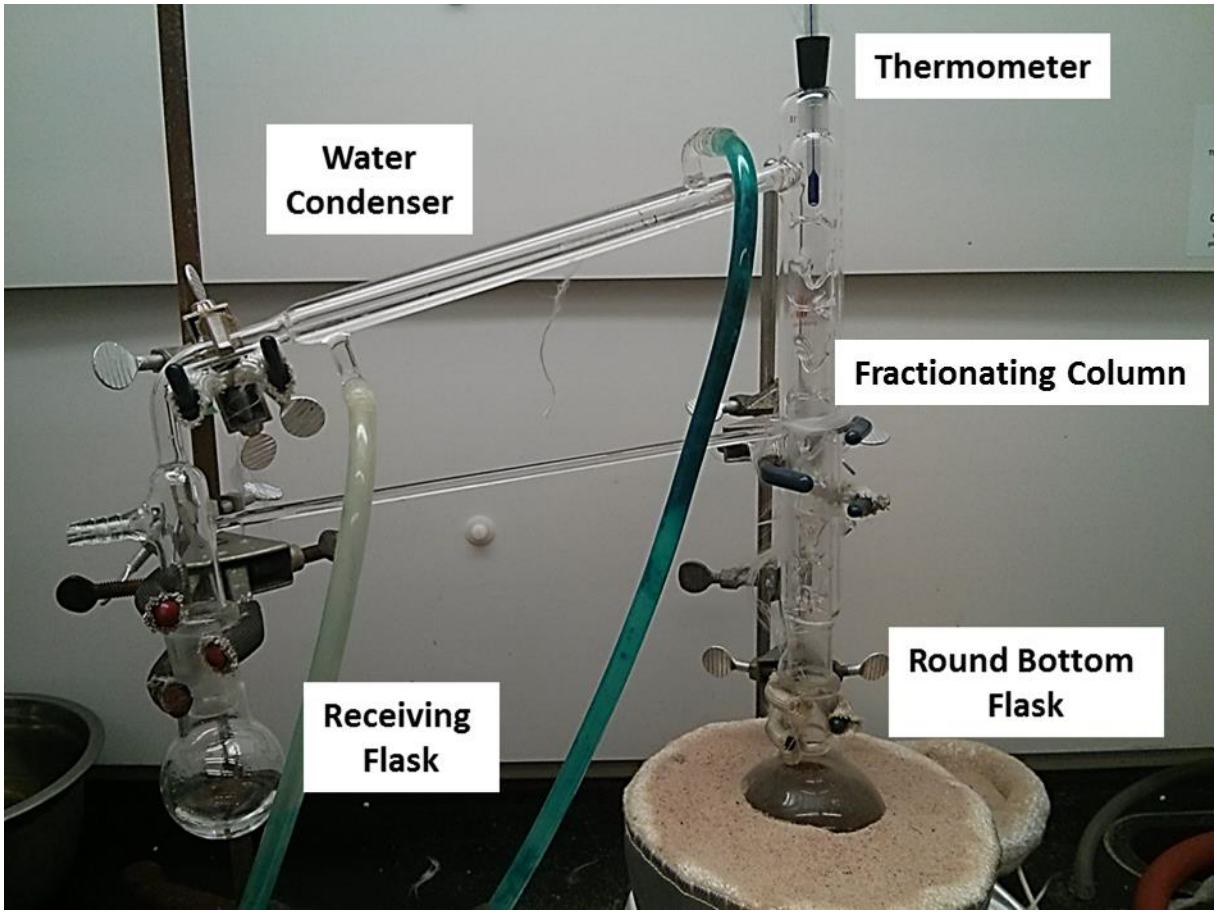


**Figure 2-1 –** Typical distillation apparatus.

Following this procedure, the newly distilled solvent is stored under Ar. A purification column is assembled from a typical chromatography column filled with activated alumina. The column is packed tight in a roughly 1:1 volume of solvent:activated alumina. The solvent is poured through the activated alumina, and the top sealed with a pressurized $N_2$ headspace. This forces the elution of the solvent through the activated alumina. This alumina removes any ether peroxides that are formed due to the high temperature required for distillation. The contents are collected over hot molecular sieves. Once the elution is complete, the solvent is stored in an Ar glovebox over molecular sieves until it is ready to be used. Ideally, the solvent is left to sit on

molecular sieves for 3 days as to fully remove residual $H_2O$. After this time period, the water content is typically < 5 ppm.

Metal-salts, such as LiTFSI and NaOTf, are dried at 150 °C under vacuum for ~2 days prior to use. This removes any residual water. The salts are brought into the glovebox without air exposure and added to the freshly distilled/purified solvent in the desired molar ratio. Following this procedure creates highly pure electrolytes that can typically be stored for 2 weeks before fresh electrolyte is produced again.

## 2.2 - Electrochemical Studies

Galvanostatic cycling monitors the change in voltage as a function of an applied constant current, and is one of the most standard electrochemical tests to determine the activity of various electrode materials in a full-battery configuration. In metal-$O_2$ batteries, this voltage response is a direct indication of the ORR/OER activity of the positive electrode material, and hence galvanostatic cycling is used to determine the performance of the battery. Important performance metrics such as coulombic efficiency and capacity, discussed in *Section 1.0*, can be determined from galvanostatic cycling.

A second electrochemical test performed in various parts of this thesis is chronoamperometry. This is a current transient technique that monitors the current response of a system to an abrupt change in the potential. Typically, the positive electrode is held at an initial potential (either the open circuit voltage (OCV) or a specified starting point of interest), and then changed to a potential where either ORR or OER occurs. The current variation is recorded as a function of time. Typical uses of chronoamperometry within the electrochemical energy storage field are to analyze the kinetic behaviour of insertion materials in Li-ion

batteries.[1] For the purpose of the Li-$O_2$ battery, chronoamperometry measures the kinetics of oxygen reduction and formation of $Li_2O_2$ on the positive electrode surface. Thus, it is a great tool to measure the kinetics of oxygen reduction and correlate this result to the galvanostatic cycling measurements.

Cycling Voltammetry (CV) and linear sweep voltammetry (LSV) are techniques where the potential is linearly scanned over a period of time, and the current response monitored at the working electrode. This can be performed with a single voltage sweep (LSV), or through numerous anodic and cathodic scans in succession (CV). The magnitude of the current response and the potential at which this response occurs provides information about the redox reactions in the Li-$O_2$ cell. Specifically, the catalytic activity of oxygen reduction and evolution reactions are deduced from changes in the onset voltage of ORR/OER. Furthermore, any additional redox chemistry, such as parasitic reactions that occur during cell operation, can be easily observed with this measurement. An example voltammogram for oxygen reduction on a glassy carbon surface is shown in **Figure 2-2** below.[2] The two peaks correspond to the one-step reduction and oxidation of $O_2$ for the formation and oxidation of $Li_2O_2$. The onset of ORR/OER in relation to the OCV gives an indication of the overpotential associated with such a reaction.

All of the above mentioned electrochemical characterization techniques were performed with an Arbin system galvanostat/potentiostat and a Biologic VMP-3.

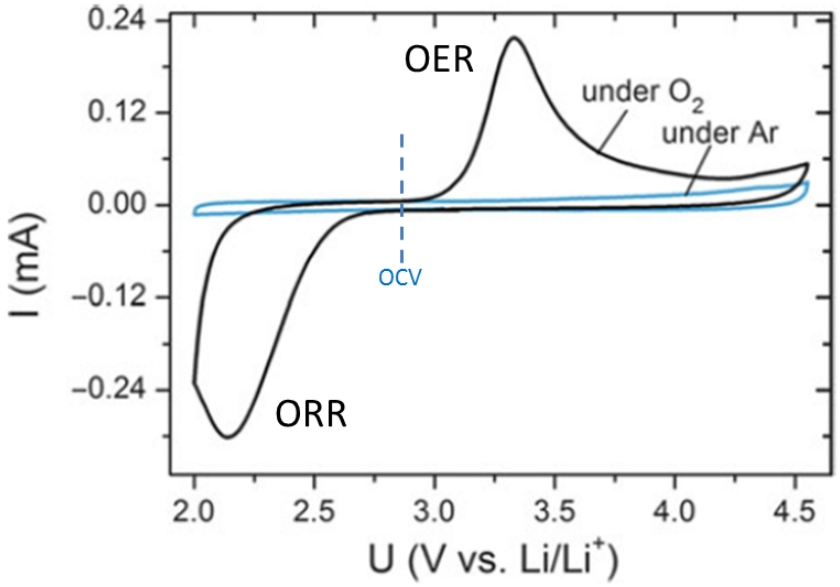


**Figure 2-2** - Cyclic voltammogram of $O_2$ redox chemistry on glassy carbon in 1M LiTFSI/DME.[2]

## 2.3 - X-Ray Diffraction

X-Ray diffraction is an excellent technique for probing the crystal structure of a material. All crystalline materials, and to an extent amorphous materials, have periodicity in their atomic structure. The specific arrangement of the atoms, also known as the crystal lattice, can be identified through the constructive interference of diffracted X-rays based on *Bragg's law* below:

$$n\lambda = 2dsin\theta$$

where λ is the incident X-ray wavelength, *d* the interplanar spacing of the crystalline planes, and θ the incident angle. Thus, Bragg's law is the relationship between the incident radiation diffraction angle and the material's interplanar spacing. **Figure 2-3** illustrates how Bragg's law is satisfied.[3] Incoming X-ray radiation of a known wavelength is incident on the crystal

surface and swept at various angles (θ). When Bragg's law is satisfied such that the path length of the scattered radiation ( $\overline{\mathrm{ABC}} = 2dsin\theta$ ) is equivalent to an integral number of the wavelength (nλ), the scattered X-rays from multiple planes are in phase and undergo constructive interference. If Bragg's law is not satisfied, the diffracted X-rays undergo destructive interference and do not reach the detector. Hence, across the entire range of incident angles, reflections will occur that correspond to the spacing of specific crystal planes.

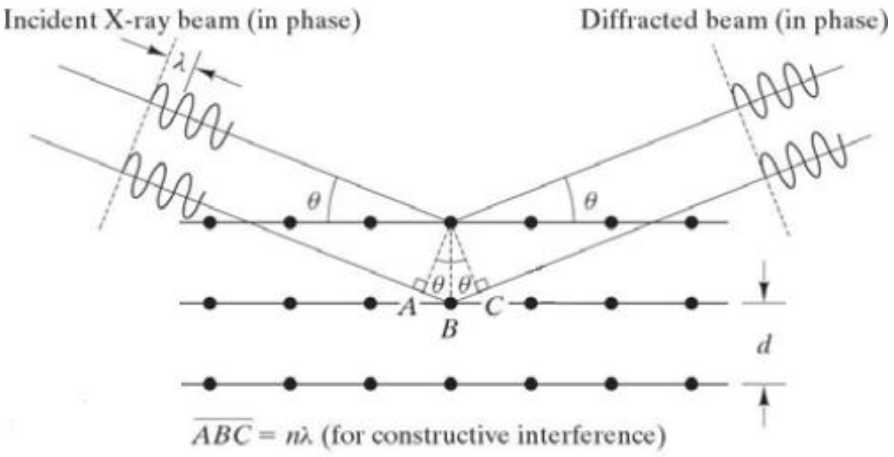


**Figure 2-3 -** Representation of X-ray diffraction and satisfaction of the Bragg equation.[3]

For this thesis, X-ray diffraction is primarily used as an identification tool. The major discharge products for the both the Li-$O_2$ battery ($Li_2O_2$) and the Na-$O_2$ battery ($NaO_2$) exhibit a high degree of crystallinity. The reflections corresponding to these products are very apparent in a powder diffraction pattern and confirm the identity of the discharge product on the positive electrode surface. However, as mentioned, X-ray diffraction is only effective for the identification of crystalline products. Amorphous products show very weak (or no) reflections, and hence cannot be identified from this measurement. While effective for the identification of

primary discharge products, other techniques must be used if amorphous discharge products are to be identified.

## 2.4 - Scanning Electron Microscopy

Scanning electron microscopy (SEM) is a valuable tool for studying the surface features of a specimen. Imaging with SEM provides excellent resolution with a large depth of field and requires minimal sample preparation compared to other electron microscopy techniques such as transmission electron microscopy. SEM operates first through subjecting the specimen to an incident beam of electrons that are typically generated via either thermionic emission (from heating a tungsten tip), or generated from a field emission source. The electrons are focused into a highly collimated beam of a very narrow spot size with the use of magnetic lenses. This beam is then raster scanned over the surface of the specimen. The depth to which the incident electrons interact with the sample surface is dependent on both the energy of the incoming electrons (accelerating voltage) and the inherent specimen properties.

This depth of interaction is known as the interaction volume. The production of three sources of radiation occurs from this volume: secondary electrons, backscattered electrons, and X-rays. In brief, secondary electrons are generated from the surface of the interaction volume and are typically low energy electrons that reveal a great deal of information about the surface topography of the specimen. Backscattered electrons, which are elastically scattered electrons with high energy, are excellent at providing elemental contrast. The formation of X-rays occurs deep within the interaction volume. The energy of the X-rays is a function of the energy difference in electron orbitals of the element from which the X-rays originated. Hence, the energy and abundance of X-rays provide a quantitative signature of the elements present in the

specimen. This is known as energy dispersive X-Ray (EDX) For this report, only secondary electrons and EDX are used for characterization.

For this dissertation, SEM was primarily used to image the discharge products on the positive electrode surface. This was extremely helpful in the identification of amorphous products that could not be clearly observed with X-ray diffraction, which would then warrant further tests to determine the identity of these products.

## 2.5 - Thermogravimetric Analysis

Thermogravimetric analysis (TGA) is a technique that measures the changes in a material's physical and chemical properties as a function of temperature. This is done by measuring the losses or gains in a material's absolute mass over a specific temperature range. The changes in the mass of a material can represent either decomposition of a specific phase or component, oxidation of the material, or a state change of the material (specifically, from a solid/liquid to the gas phase). Heat is applied to the material at a specific rate, and the mass recorded over the desired temperature range. An inert gas flows overtop the sample to remove any volatile species that are generated during heating. The change in mass is correlated to exact temperatures to pinpoint the temperature which these reactions occur.

For the work presented in this thesis, TGA was primarily used as an identification tool for electrode material composition. For composite electrode materials that comprise a specific amount of support, binder, and catalyst materials, TGA was used to identify the mass loading of each component to within 0.2%. This allowed for accurate representation of gravimetric capacity and gravimetric current rate, where necessary.

## 2.6 - Time of Flight Secondary Ion Mass Spectrometry (TOF-SIMS)

Time of flight secondary ion mass spectrometry (TOF-SIMS) is a complex analytical surface method. Secondary ion bombardment is used to generate secondary ion particles from the sample of interest, coupled with time of flight mass spectrometry to determine the identity of the secondary particles. In a typical measurement, a pulsed primary ion beam bombards the material surface. This ion beam transfers its energy to the target atoms via atomic collision, which starts a "collision cascade".[4] This energy transfer causes a fraction of the surface atoms to overcome their binding energy within the lattice and escape into vacuum, becoming secondary particles. A small portion of these secondary particles will be ejected with a positive or negative charge. A high voltage potential extracts these secondary ions from the surface, and funnels them into a secondary particle analyzer. The time required for the secondary ions to leave the surface and reach the detector is dependent on both the mass of the particle and its charge (m/z). Hence, the secondary particle can be filtered and identified from this unique signature. The total population of secondary particles can be separated based on their m/z values and displayed as a spectrum. Information about the distribution, composition, and molecular components of the material surface can be obtained from the survey spectrum.

TOF-SIMS is a survey technique, and is capable of analyzing secondary particles from m/z = 1 ($H^+$) up to m/z = 10,000 with the proper equipment. Furthermore, apart from bulk material chemical composition, a two-dimensional composition map can be generated, allowing for visualization of the chemical composition across a surface. However, limitations of TOFSIMS include that it is primarily a qualitative technique, and quantitative analysis (absolute value) can only be performed within appropriate and stringent sample standards. Furthermore, this technique is extremely surface sensitive. Both contaminants and rough

surface topography can lead to erroneous results. The system also requires the use of an ultra-high vacuum, so the sample of interest must be vacuum compatible. For the purposes of the work presented in this thesis, TOFSIMS is utilized as a tool to compare the surface constituents of a positive electrode surface at different stages of discharge/charge. In particular, common fragments of Li-$O_2$ decomposition products from glyme-based electrolytes, such as $Li_2CO_3$, can be identified and compared across multiple samples. As will be discussed in *Section 4.0* of this thesis, this technique is not recommended for quantitative analysis. Other methods such as online electrochemical mass spectrometry offer a much more in-depth analysis of the Li-$O_2$ chemistry and electrolyte decomposition that plagues metal-$O_2$ batteries.

## 2.7 - Iodometric Titration

Iodometric titration is a quantitative technique to determine the amount of metal-$O_2$ discharge product (both $Li_2O_2$ and $NaO_2$) is on the positive electrode surface (as well as in the electrolyte). Chemical reactions involved in the overall quantification process are following:

$$Li_2O_2 + 2H_2O \rightarrow 2LiOH + H_2O_2$$

--OR--

$$2NaO_2 + 2H_2O \rightarrow 2NaOH + H_2O_2 + O_2$$

$$H_2O_2 + 3I^- + 2H^+ \leftrightarrow 2H_2O + I_3^-$$

$$I_3^- + 2Na_2S_2O_3 \rightarrow Na_2S_4O_6 + 2NaI$$

In a chemical reaction involving $H_2O_2$ and $I^-$ (2), the former is reduced to water and the latter is oxidized to iodine, which can then be titrated using standard thiosulfate solution to quantify the peroxide concentration.

This reaction is slow without a catalyst but can be quite fast in the presence of catalysts such as Mo(VI) and excess $I^-$ that forces the reaction to proceed to the right resulting in the formation of $I_3^-$. The $I_3^-$ is titrated using thiosulfate based on the following reaction:

$$I_3^- + 2Na_2S_2O_3 \rightarrow Na_2S_4O_6 + 2NaI$$

In a standard iodometric estimation of $H_2O_2$, it is reacted with excess iodide in an acidic media, but acid is known to cause chemical disproportionation of peroxide to water and oxygen. Furthermore, iodide is prone to areal oxidation at acidic pH. Both these processes are likely to introduce significant error in the peroxide quantification. Therefore, in the work throughout this thesis, we have adopted a modified iodometric method employing a pH neutral iodide-phosphate buffer reaction media that maintains a steady supply of protons for the peroxide-iodide reaction, while maintaining a constant pH. Neutral pH suppresses peroxide disproportionation besides decelerating the areal oxidation of iodide. The inhibition of areal oxidation of iodide was evident from the unchanged color of the post titration solution (colorless) even days after the titration. In a standard iodometric procedure, the post titration solution turns blue very quickly from the oxidation of $I^-$ to $I_2$ that bind to starch to give the blue color.

## 2.8 - Mass Spectrometry

This section will briefly go over the theory behind mass spectrometry, as it was a large component of the analysis performed throughout this thesis. See *Section 5.1* for the design and construction of the mass spectrometer used for analysis throughout this thesis. Mass spectrometry is an analytical tool that separates, identifies, and analyzes the various gases that comprise a given volume. It does this through the ionization of the gas species, separation of

the ion species based on mass and charge (*m/z ratio)*, and detection of these ions via a detector. The system used for analysis is a Stanford Research Systems RGA 200 quadrupole mass spectrometer. This mass spectrometer is comprised of three components: *(i)* Ionization Region *(ii)* Quadrupole (filter region), and *(iii)* Detector. A representative figure of each region is shown in **Figure 2-4**.[5] To understand how a mass spectrometer operates, each region will be described below in more detail.

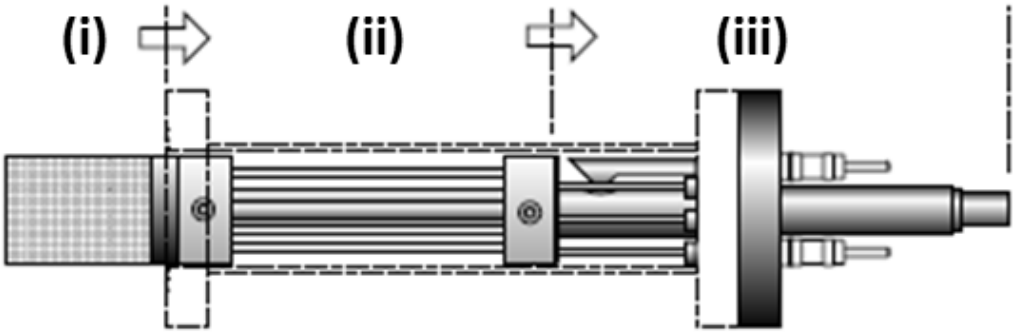


**Figure 2-4 -** Figure of a typical quadrupole mass spectrometer. The labeled regions correspond to *(i) ionization region, (ii) quadrupole mass separator, (iii) ion detector*.[5]

*(i) Ionization Region*. The ionization region is the first contact point for the gas upon entrance into the vacuum chamber. The ionizer is made of a filament, typically tungsten or thoriated $IrO_2$, depending on the oxidizing nature of the gases being analyzed. Thermionic emission causes electrons to escape from the surface of the filament. The ionizer is surrounded by a repeller grid to prevent electrons from escaping, and thus the electrons are contained within a finite volume known as the ionization volume, and undergo constant acceleration and deceleration. The electrons interact with any gas molecules within this region through electron impact ionization:

$$\mathrm{AB} + e^- \rightarrow AB^+ + 2e^-$$

The amount of ions generated within this region is dependent on the ionization efficiency, and this efficiency is a function of the electron energy. In order for impact ionization to occur in an efficient manner, the vacuum range must typically be kept below 1 x $10^{-5}$ torr. Typically, the ionization yield is between 0.01% to 0.0001%. Beyond the ionizer is a focus plate. This focus plate is kept at a negative potential relative to ground, and pulls the generated ions within the ionization volume into the quadrupole, where ion filtration occurs.

*ii) Quadrupole*. The filter region is comprised of four pristine cylindrical stainless steel rods of opposing polarity, as shown in **Figure 2-5**. These poles are operated with a combination of DC and RF voltages. During operation, ions enter along the z-axis, as shown, and oscillate along the x- and y- directions. Lateral forces resulting from the applied electric potentials cause the ions to separate based on their *m/z* value. Tuning of the DC and RF voltages causes only the ions of interest to traverse across the entire length of the quadrupole and reach the ion detector.

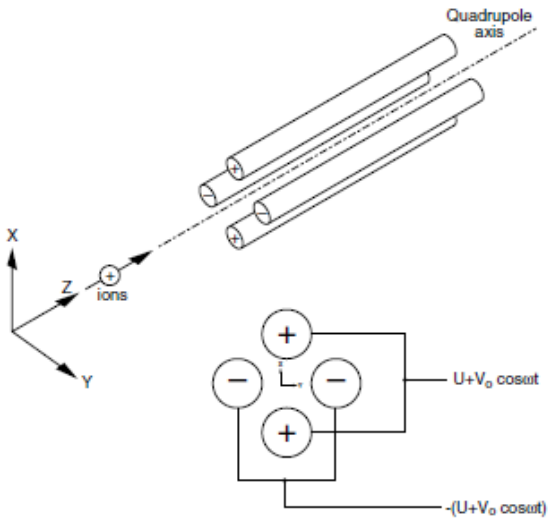


**Figure 2-5 -** Quadrupole (ion filter) for the mass spectrometer. [5]

The greater number of oscillations the ions are subjected too as they traverse the length of the quadrupole, the greater the degree of mass separation, and hence greater the resolution. This mass selectivity offers an extremely high resolution. Through varying the DC and RF voltages simultaneously, one is able to then obtain an *m/z* spectrum.

Both the ionizer and the quadrupole affect the resolution of the mass spectrometer. The user is able to tune the parameters of the ionizer (ion energy, focus plate bias) and the quadrupole (pole bias) to maximize ion transmission. However, some inherent resolution limiting factors, such as the accuracy of the pole dimensions, and the stability of the DC and RF pole bias, as well as cleanliness of the quadrupole chamber can have an impact on mass resolution. These factors become very important when quantification of the analyzed gases is necessary, and these factors must be accounted for with calibration gases in order to make accurate measurements.

*(iii) Ion Detector*. A typical mass spectrometer either makes use of a Faraday cup detector (FC) or a continuous dynode electron multiplier (CDEM). For this discussion, I will only talk about the CDEM since the CDEM has much greater resolution than the FC, and is the necessary detector to use to monitor the trace gas amounts that are generated from a metal-$O_2$ battery. A CDEM detector is highly efficient that is capable of very large gains (~$10^8$) per ion detected, which ultimately allows for detection limits in the range of 5 x $10^{-14}$ torr partial pressures (< single ppm range). This detector operates through a 4-channel tube of resistive material with an electrically conducting cone attached to the front end. This cone is biased with a very large negative voltage (1.5 kV for our operation). During operation, the positive ions that are filtered through the quadrupoles are accelerated upon entrance into the detector due to the large negative bias. This collision at high velocity generates secondary electrons, which are

accelerated down the 4-channel tube and produce more secondary electrons. These secondary electrons are then detected by the grounded plate (negative electrode) at the end of the 4-channel tube. The typical gain in this detector is approximately $10^7$ electrons for every ion. The final output is the conversion of the electrical current into ion current, based on a conversion that is determined through calibration. The gain of the CDEM can be adjusted to improve the sensitivity of the mass spectrometer, but, as a result, limits the lifetime of the detector. Furthermore, as with all mass spectrometer components, care must be taken in handling and operating the detector to ensure an extended lifetime, as well as proper operation of the instrument to obtain trustworthy results.

## 3.0 - Screening for Superoxide Reactivity in Li-$O_2$ Batteries

### 3.1 - Introduction and Stability Issues in the Li-$O_2$ Cell

In nonaqueous Li-$O_2$ batteries, the first step of ORR is the formation of $O_2^-$, which quickly undergoes a reaction in the presence of $Li^+$ to form $LiO_2$.[1] $LiO_2$ then undergoes disproportionation to form $Li_2O_2$ ($2LiO_2 \rightarrow Li_2O_2 + O_2$).[2] Due to the highly nucleophilic behaviour of $O_2^-$ and $LiO_2$, the formation of $Li_2O_2$ is accompanied with parasitic reactions.[3,4,5,6] Propylene carbonate (PC), for example, is subject to ring opening attack that produces a variety of organic lithium carboxylates.[7] Salts such as lithium bis(oxalato)borate and LiTFSI are decomposed to produce lithium oxalate and LiF respectively.[8,9] Ether-based electrolytes, as will be discussed, are also reactive to these nucleophilic species, producing a variety of Li-carboxylate decomposition products.[10] DMSO, an electrolyte solvent that displays remarkable discharge/charge performance when coupled with non-carbon positive electrode materials,[11,12] has also been shown to react with $O_2^-$ to form $DMSO_2$. [13,14] Other electrolyte systems have demonstrated the same fate, with solvents such as DMA [15], functionalized trimethylsilane (1NM3) [16], and ionic liquids [17] being unstable to superoxide attack. These reactions with $O_2^-$/$LiO_2$ not only lead to depletion of the electrolyte, but also form side-products other than the desired $Li_2O_2$, which fundamentally changes the nature of the Li-$O_2$ oxidation chemistry. In light of this, an initial probe of the interaction of $O_2^-$/$Li_2O_2$ towards a variety of cell materials is critical to screen for chemical stability. The reaction of $O_2^-$ with various cell components is the main source of cycling inefficiencies and non-stoichiometric amounts of $O_2$ evolution on charge. Furthermore, the presence of insulating decomposition products on the electrode surface

controbute to the large charge overpotential observed for $Li_2O_2$ oxidation, which in turns lead to further electrochemical decomposition processes.[18]

This section discusses a chemical screening method that utilizes $O_2^-$ from $KO_2$ to determine the stability of various Li-$O_2$ cell components. The use of $O_2^-$ is validated through the production of $Li_2O_2$ when $KO_2$/crown-ether is mixed with Li-salt. The decomposition of typical Li-$O_2$ cell components is confirmed through subjection of positive electrode materials (active material and binder) and solvents to the chemically generated $O_2^-$/$LiO_2$. The identification of decomposition products (or lack thereof) demonstrates that chemically generated $O_2^-$ from $KO_2$ is an excellent tool for screening Li-$O_2$ battery materials.

### 3.2 - Chemical Generation of $O_2^-$

To properly test the reactivity of $O_2^-$ against various cell components, the $O_2^-$ itself must be generated chemically in solution, and in abundance so that the conditions replicate, as closely as possible, the discharge reaction of a real Li-$O_2$ cell. This is done through the liberation of $O_2^-$ from $KO_2$ via a chelation agent. The known reaction of $KO_2$ with dicyclohexyl-18-crown-6 (crown ether) was used for the generation of $O_2^-$ in solution.[19] **Figure 3-1** shows a schematic detailing the different stages of this procedure. The crown ether acts as a hexadendate ligand to small cations, with a strong affinity for the potassium cation $K^+$.[20] Upon addition of the crown ether to a dissolved solution of $KO_2$ in organic media, the crown-ether complexes with $K^+$ to liberate $O_2^-$. The addition of any cell components at this stage will react with $O_2^-$ directly. In the presence of an added lithium salt, a metathesis reaction occurs to form solvated $LiO_2$ *in-situ*. This $LiO_2$ undergoes disproportionation to form $Li_2O_2$ and gaseous $O_2$, the latter of which is visible in the solution upon immediate addition of the lithium salt. The solution is left to stir for a period of 12

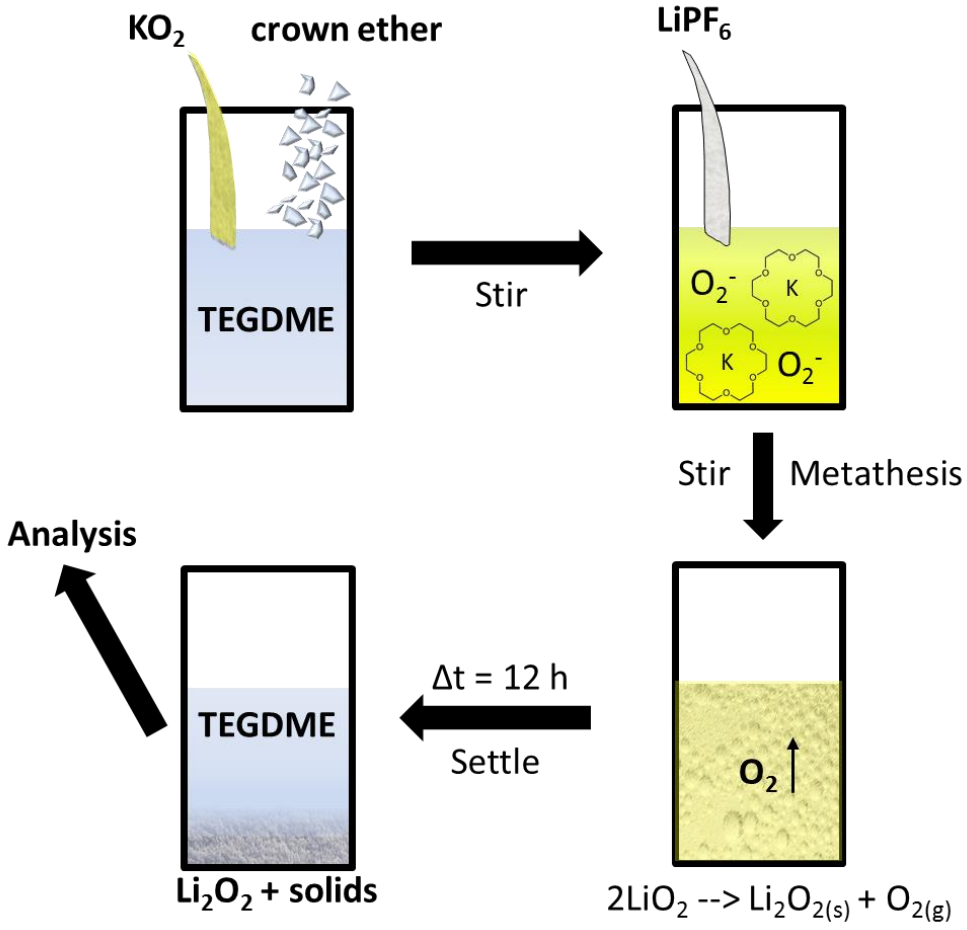


**Figure 3-1 -** Outline of procedure for $O_2^-$ reactivity test. The initial step is chelation of $KO_2$ to form $O_2^-$. Lithium salt is added to produce $LiO_2$, which undergoes disproportionation to form $Li_2O_2 + O_2$. Cell components of interest are added prior to the addition of $LiPF_6$. The contents are left to react for an extended period of time, after which the solid contents are collected for analysis.

hours. Upon completion of the reaction, the solution turns clear as all the $KO_2$ is consumed, and the solid contents settle. The solid and liquid are removed for analysis.

With the use of this technique, the stability of common materials used in a Li-$O_2$ cell is determined. The stability of carbon black, poly(vinylidene difluoride) (PVdF) or Nafion binder, and a common ORR/OER catalyst (α-$MnO_2$) [21] were investigated. As will become clear throughout this section, the presence of cell materials impacts the first stages of ORR in

the Li-$O_2$ cell through reactivity with $O_2^-$, and affects the nature and morphology of the products that are formed.

## 3.3 - Experimental

### 3.3.1 - Positive Electrode Preparation

To fabricate electrodes for full cell studies, Ketjen Black (KB), $MnO_2$ (where applicable), and Kynar 2801 (PVdF) binder are mixed in the mass ratio of 1:1:2.4, and ground with a mortar and pestle. The contents were stirred with acetone and dibutyl phthalate (DBP) for approximately 6 hours, after which the contents were cast onto a flat ceramic plate with a doctored blade. Positive electrodes of approximately 1 $cm^2$ were punched and placed into diethyl ether for 20 mins to completely remove the DBP. Following this, the positive electrodes were dried at 90 °C under vacuum for 12 hours prior to analysis.

The synthesis of the high surface area α-$MnO_2$ nanowires used in this study was based on an already reported synthesis procedure.[22] 1 mmol of $KMnO_4$ and 1 mmol $NH_4Cl$ were dissolved in 50 mL of distilled $H_2O$.The solution was stirred for 1 hour until the contents were fully dissolved. Following this, the entire contents were placed into a 60 mL Teflon autoclave that was housed inside of a stainless steel body. The autoclave was put in an oven at 140 °C for 24 hours. The autoclave was then removed and cooled. The solid brown precipitate was filtered through filter paper and washed thoroughly with an ethanol/water mixture. The formed nanowires naturally bundled into a strong mat. The mat was ground with a mortor and pestle to break up the nanowires and make them into a coarse powder.

### 3.3.2 - Cell Assembly

Electrochemical experiments were performed in a Li–$O_2$ cell of modified Swagelok design with 1 M $LiPF_6$ (battery grade, dry, 99.99% trace metals basis, Techno Semichem, Korea) in TEGDME (<20 ppm $H_2O$, Sigma-Aldrich) as the electrolyte. Cells were assembled in an Ar filled glovebox with a lithium metal negative electrode, three porous separators (Millipore glass fibre), and a porous carbon membrane supported on 316-stainless steel mesh functioning as the current collector which served as the positive electrode. The separators were presoaked in electrolyte, and an additional 80 μL of electrolyte was added during cell assembly. The cells were encased in a glass housing, purged for 10 minutes with $O_2$ (99.994% pure $O_2$, Praxair, $H_2O$ < 2 ppm), and subsequently sealed to the ambient atmosphere. The amount of oxygen available to the $O_2$ electrode in the Li–$O_2$ cells within the 270 ml glass housing was at least 50 fold higher than that required for discharging to a capacity of 5000 mAh/g. The cells were rested at open circuit for 6 h before testing. The Li–$O_2$ cells were tested galvanostatically using a current density of 140 mA $g^{-1}$ (normalized to the weight of the carbon) from open circuit to a lower voltage cutoff of 2.0 V vs. $Li/Li^+$.

Tetraethylene glycol dimethyl ether (TEGDME, Aldrich), and propylene carbonate (PC, Aldrich) were distilled and placed over activated 4A molecular sieves prior to use. All experiments were conducted in an Ar-filled glove box with < 0.5 ppm $H_2O$ and <1 ppm $O_2$. $KO_2$ and 18-crown-6 (crown ether) (Sigma-Aldrich) were added (1:1 molar ratio) to 5 ml of TEGDME and were stirred for 12 hours to ensure complete chelation of the $KO_2$ by the crown ether. A 1 M solution of $LiPF_6$ in TEGDME was added in a 2:1 molar ratio with $KO_2$ to form the lithiated oxide, $LiO_2$. Simultaneously, and in different experiments, typical materials used in Li-air cells (*ie*., poly(vinyldene difluoride) (PVdF; Sigma Aldrich); Ketjen

Black carbon; α-$MnO_2$) were added to the mixture to evaluate their reactivity. Specific investigation of electrolyte decomposition utilized a 1:2 molar ratio of $KO_2$:TEGDME and 1:5 molar ratio of $KO_2$:PC, with excess $KO_2$ relative to an amount of $LiPF_6$ sufficient to ensure enough $O_2^-$ for adequate electrolyte decomposition. All reactions were stirred for 24 hours in an inert atmosphere, and the solid was collected and washed with $CH_3CN$ multiple times. The solid products were collected by centrifugation and dried to analysis. Lithiated Nafion™ (IonPower) was dried thoroughly before use.

### 3.3.3 - Detection of Hydrogen Peroxide

To prove that hydrogen abstraction from the PVdF binder by the superoxide radical results in the formation of $H_2O_2$, we used a simple gasometric method to detect the peroxide. In a typical experiment, PVdF (100 mg) was reacted with 0.1 M $KO_2$ + 0.3 M 18-crown-6 in TEGDME for 12 hours. The supernatant was collected from the resultant black coloured product without the addition of any additional solvent. Approximately 1 mL of the supernatant was added to 10 mg of α-$MnO_2$ at room temperature. Large volumes of $O_2$ gas were observed, indicative of catalytic $H_2O_2$ decomposition which is a well-known reaction for manganese dioxides. The same experiment using lithiated Nafion™ instead of PVdF produced no gas evolution.

### 3.4 - Reactivity of $O_2^-$ and the Impact of Carbon

To first ensure $O_2^-$ is generated from the chelation of $KO_2$, Li-salt was added to validate the presence of $Li_2O_2$ as the reaction product. The production of $Li_2O_2$, confirmed from reflections corresponding to the hexagonal phase $Li_2O_2$ with X-ray diffraction shown in **Figure 3-2**, demonstrates the reliability of this method to produce $O_2^-$. This formation of

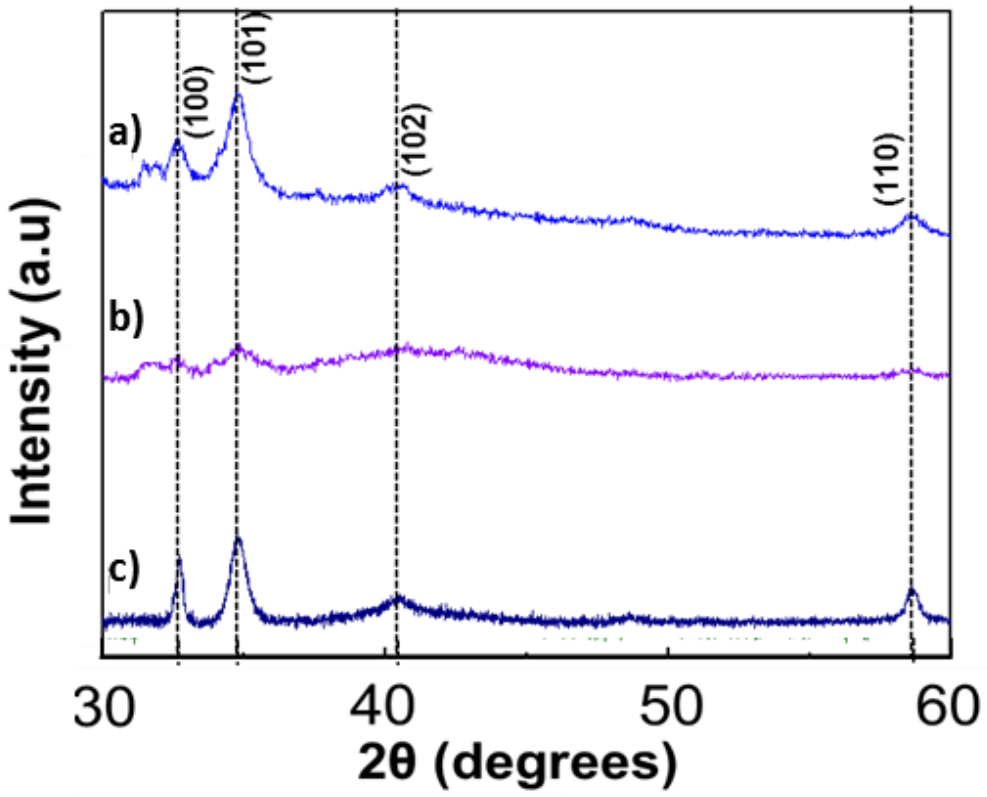


**Figure 3-2 -** Reflections corresponding to $Li_2O_2$ after the combination of (a) $LiPF_6/KO_2$/TEGDME, (b) $LiPF_6/KO_2$/TEGDME/KB, and separately (c) an electrochemically discharged Ketjen Black positive electrode in 1M $LiPF_6$/TEGDME.

$Li_2O_2$ must first occur through the reaction of $O_2^-$ with $Li^+$ to form $LiO_2$. Following this, the $LiO_2$ undergoes a dismutase reaction to form $Li_2O_2$ as shown in *equation 3.1 & 3.2*. The formation of $Li_2O_2$ from this solution based method indicates that $LiO_2$ has some limited solubility in solution.

$$KO_{2(s)} + LiPF_{6(s)} \rightarrow LiO_2 + [K^+/\text{crown ether}]PF_6^-{}_{(s)} \quad \textit{(equation 3.1)}$$

$$2LiO_{2(s)} \rightarrow Li_2O_2 + O_{2(g)} \quad \textit{(equation 3.2)}$$

These reactions are confirmed through the identification of the $[K^+/\text{crown ether}]PF_6^-{}_{(s)}$ species via single crystal diffraction, shown in **Figure 3-3,** along with the visible appearance of $O_2$ gas evolution upon immediate addition of the crown-ether to $KO_2/LiPF_6$ dissolved in the TEGDME solvent.

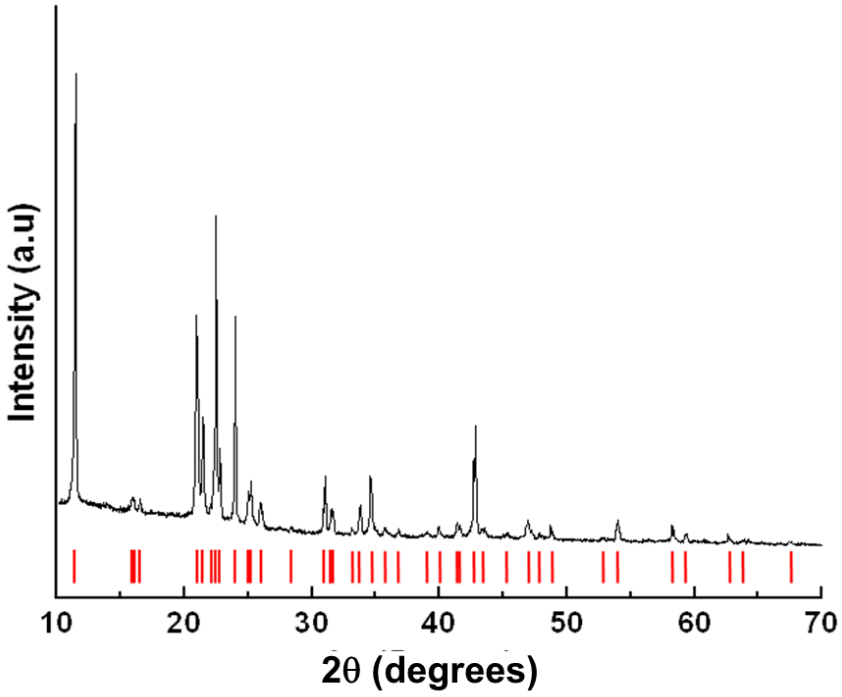


**Figure 3-3 -** XRD pattern of the recrystallized salt, $[K^+(\text{crown-ether})]PF_6^-$ , extracted from the reaction of $KO_2$ + 18-crown-6-ether + $LiPF_6$ in TEGDME with acetone, ($C_{12}H_{24}F_6KO_6P$; *Pnnm* (#58); *a* = 7.9683 (6) Å; *b* = 10.8592 (8) Å; *c* = 11.4068 (8) Å; *V* = 987.02 (12) $Å^3$. Red markers show the predicted powder pattern reflection positions based on a single crystal refinement.

To probe the reactivity of the positive electrode materials, Ketjen Black (KB - high surface area carbon powder) was added to the reaction mixture. KB is a very popular positive

electrode material used in Li-$O_2$ batteries, for the highly porous carbon framework acts as both a conducting pathway for electrons, as well as houses the insoluble $Li_2O_2$ in a lightweight framework. Upon simultaneous addition of KB with $LiPF_6$, the expected metathesis and disproportionation reaction of $Li_2O_2$ occurs. However, much less gas evolution occurs compared to the $O_2$ evolution observed in the absence of KB, as determined by visual inspection. Powder X-ray diffraction analysis of the washed solid products, shown in **Figure 3-2b**, reveals $Li_2O_2$ as the only crystalline product. The X-ray reflections are far weaker and extensively broadened compared to those of $Li_2O_2$ formed in the absence of carbon. The KB carbon powder is characterized by a large surface area (1400 $m^2g^{-1}$), and a very high fraction of surface functional groups.[23] The greatly reduced crystallinity of $Li_2O_2$ suggests that the carbon must strongly interact with the superoxide radicals which physisorb onto the surface, thus suppressing the dismustase reaction of $Li_2O_2$. This supports observations that the surface chemistry of the carbon electrode substrate strongly influences the discharge products.[24] Another possibility is the reactivity of the $Li_2O_2$ with the carbon powder, which is a well-documented source of decomposition products.[25,26] The reactivity of the carbon positive electrode with $Li_2O_2$ is thermodynamically favourable, and is shown in *equation 3.3* and *equation 3.4* below:

$$Li_2O_{2(s)} + C_{(s)} + 1/2O_2 \rightarrow Li_2CO_3 \qquad (equation\ 3.3)$$

$$2Li_2O_{2(s)} + C_{(s)} \rightarrow Li_2O + Li_2CO_3 \qquad (equation\ 3.4)$$

Furthermore, a wide variety of organic carbonates and epoxy groups form on the carbon surface as a result of surface attached $LiO_2$ species.[26] These studies utilized a variety of highly sensitive techniques such as mass spectrometry and XPS; techniques which were not

utilized for this work involving the $KO_2$ reaction. Hence, while we demonstrate a lower degree of crystallinity for $Li_2O_2$ in the presence of carbon, it is only speculation that this is due to both suppression of the dismutase reaction, and reactivity of the carbon with the generated $LiO_2$/$Li_2O_2$ species, as supported by other literature. Further discussion of the reactivity between $Li_2O_2$ and carbon is presented in *Section 5.0*.

In an electrochemical cell, the carbon also functions as surface sites for the initial step of ORR. It serves as both the active site for $Li_2O_2$ formation, as well as the host for its accumulation. **Figure 3-2c** shows the reflections corresponding to electrochemically generated $Li_2O_2$ produced with KB as the positive electrode, and 1M $LiPF_6$/TEGDME as the electrolyte. Compared to chemically formed $Li_2O_2$ ($KO_2$ reaction) described above, the electrochemically generated $Li_2O_2$ is much more crystalline. The coherence length is approximately 15-20 nm for the electrochemically formed $Li_2O_2$, as determined from Scherrer analysis, but the line broadening is so severe for the chemically formed $Li_2O_2$ that an accurate estimate of primary particle size is not possible in this case. This contrast is also reflected in the SEM micrographs of the respective products. The chemically produced $Li_2O_2$ exhibits an amorphous, ill-defined morphology (**Figure 3-4a,** and inset), in contrast to the well-defined toroids formed by electrochemically generated $Li_2O_2$ in the absence of a catalyst (**Figure 3-4b)**. Closer inspection reveals the toroids are aggregates comprised of nanocrystalline $Li_2O_2$ rods with dimensions in accord with those measured from XRD analysis (see inset, **Figure 3-4b**), approximately 15 nm x 80 nm. These aggregates form homogeneously sized toroidal macrostructures approximately 600-800 nm in diameter. As mentioned in *Section 1.2,* it is now known that the formation of $Li_2O_2$ is a surface-mediated reaction that becomes solution-mediated in presence of high DN additives, such as $H_2O$.[27]

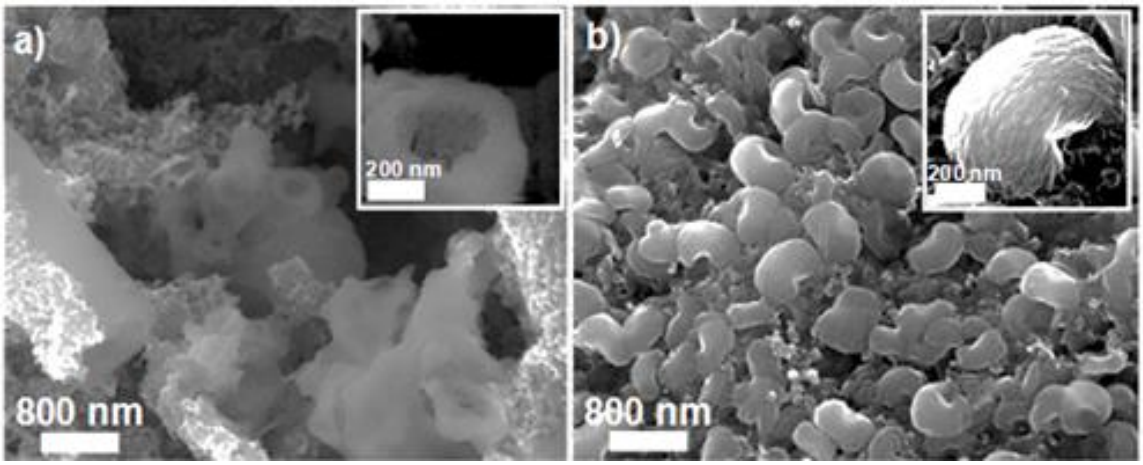


**Figure 3-4 -** SEM micrographs of $Li_2O_2$ formed from (a) the addition of $KO_2$/crown-ether/$LiPF_6$/carbon in TEGDME, and (b) electrochemically formed $Li_2O_2$ from a full cell with a carbon electrode discharged in 1M $LiPF_6$/TEGDME.

At the time of this study, the electrolytes were distilled and dried. The presence of large toroids after electrochemical discharge ensures that their formation was solution mediated by residual water that was likely introduced during electrolyte synthesis. Extreme care was not taken to completely remove water from the cell (a practice we now have much more control over, see *Section 2.1*). The production of these toroids appears only at the surface of the electrode that faces the oxygen flow; the remaining positive electrode area is bare.

The difference the chemical and electrochemical formation of $Li_2O_2$ has on the products morphology is based on two factors. The first factor is that the kinetics of the chemical formation favours rapid dismutation and precipitation due to high $LiO_2$ concentrations. In contrast, the electrochemical production of $LiO_2$ is current limited, thus crystalline $Li_2O_2$ is formed via a slow electrochemical nucleation process. The second factor is the strong cathodic polarization of the carbon surface in the electrochemical cell, which diminishes the binding of the generated $O_2^-$ to the substrate. This would be expected to

enhance diffusion of the solvated superoxide molecules away from the surface into solution, and favour peroxide formation by disproportionation via a solution-based mechanism. In either case, the formation of the large toroidal aggregates on the surface suggests a short diffusion path, followed by nucleation and crystallization of $Li_2O_2$ very close to sites where the superoxide is generated. A mechanism that could account for the growth of the toroids is shown in **Figure 3-5**. At the time of this work our proposed solution-based mechanism failed to identify the importance of additives that solubilize $O_2^-/LiO_2$ species. Other reports have

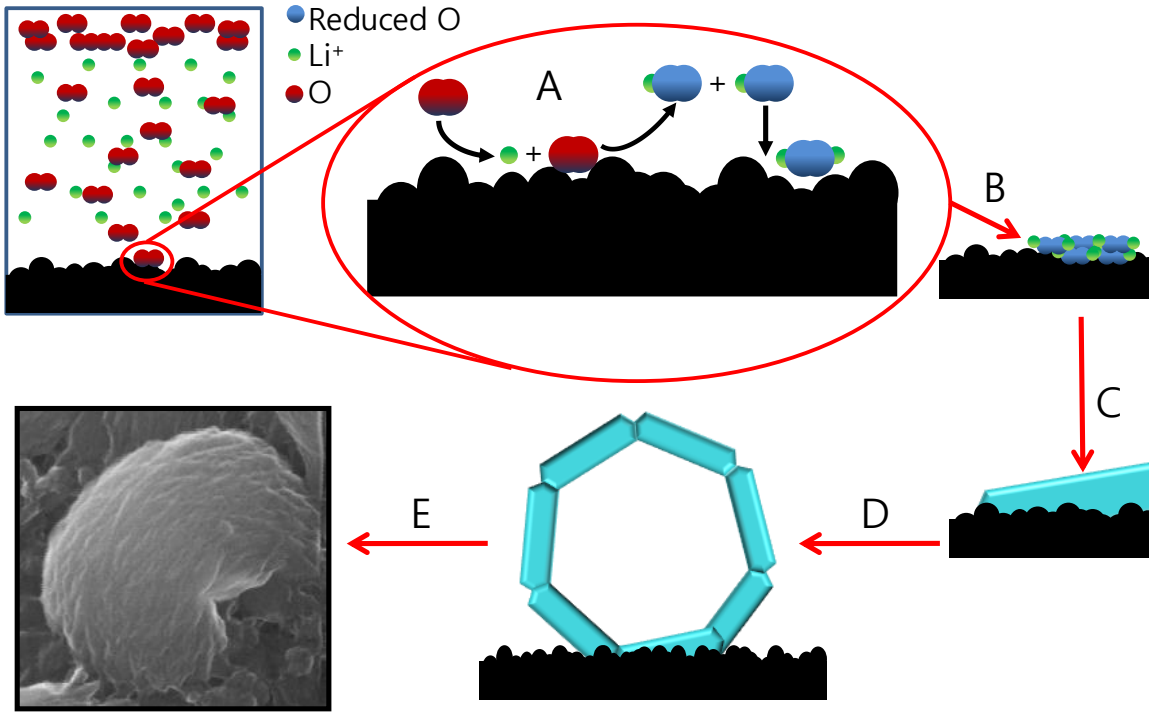


**Figure 3-5 -** Solution-driven growth of $Li_2O_2$ and possible mechanism for the production of $Li_2O_2$ toroids. Initially, A) $O_2$ is reduced on the carbon surface to form $O_2^-$ which binds with $Li^+$ to form $LiO_2$. The $LiO_2$ can either desorb by solvation and undergo reaction to form $Li_2O_2$ by disproportionation, or undergo further reduction on the surface with $e^-/Li^+$ to form $Li_2O_2$. At a critical concentration (B), nucleation of the $Li_2O_2$ forms small elongated hexagonal nanocrystallites (C). We suggest that the hexagonal crystal structure of $Li_2O_2$ (P63/mmc, the same space group as that of ice which tends to form similar rhomboid crystallites) and preferred nucleation on the prismatic crystal faces could give rise to the observed toroid aggregates for $Li_2O_2$ as simplified in (D). In a real system (E) toroid formation is undoubtedly more complicated

surfaced (rather recently) that support the concept of a solution-based $Li_2O_2$ growth mechanism driven by the presence of additives (or trace impurities, such as $H_2O$) that solubilize the $O_2^-/LiO_2$ species, so it is important to note the inclusion of these trace impurities and the impact they have on $Li_2O_2$ toroid formation.[27]

The initial oxygen reduction to form $O_2^-$ is current driven, and hence is the limiting step of the discharge reaction. Following this oxygen reduction, the $O_2^-$ is solubilized. The solvation of $O_2^-$ and its stability in solution is related to the Gutman donor number (DN) and acceptor number (AN) of the electrolyte. The presence of trace impurities of water helps to solubilize the $O_2^-$, for it has a greater AN than anhydrous DME (55 vs. 10).[27] Hence, it is the presence of $H_3O$ that allows for improved solvation of the $O_2^-$, and in turn enhances solubilization of $LiO_2$. The $LiO_2$ undergoes disproportionation to form $Li_2O_2$, which has minimal solubility in solution and deposits on the positive electrode surface, as shown in **Figure 3-5**. The growth of $Li_2O_2$ occurs on existing particles of $Li_2O_2$ which act as nucleation sites for further $LiO_2$ (solvated) disproportionation reactions. The specific toroidal shape, and nucleation/growth of $Li_2O_2$ has been an area of extensive study, and many hypotheses and models have been proposed to better understand the Li-$O_2$ ORR.[27,28,29 ]

### 3.5 – Reactivity of $O_2^-$ with PVdF

Apart from the carbon positive electrode, the chemically produced $O_2^-$ was used to explore the stability of various positive electrode binders and catalysts. Specifically, at the time of this work, poly(vinyldene difluoride) (PVdF) has been used as a binder material in a variety of other studies on the Li-$O_2$ battery system.[2,10] This is due to its solubility in a variety of solvents, which makes for easy electrode preparation that produces excellent cohesive membranes.[30] To determine if the binder itself is stable towards $O_2^-$, PVdF

powder was added to a solution of $KO_2$/crown-ether/$LiPF_6$/TEGDME. Upon addition of the PVdF, gas evolution occurred for approximately 20 seconds, after which the solution changed from light yellow to a light brown colour. This is in sharp contrast to what was observed in the absence of PVdF. The brown colour deepened as the reaction continued. After 24 hours, the solids were collected and analyzed via X-ray diffraction (**Figure 3-6a)**. There is little presence of crystalline $Li_2O_2$. In fact, the only observed crystalline products are LiF and KF implying that decomposition of PVdF occurs upon subjection to $O_2^-$. It is known that PVdF undergoes extensive defluorination in the presence of organic and alkaline bases, such as LiOH, to yield unsaturated products with polyene structures.[31,32] These strong

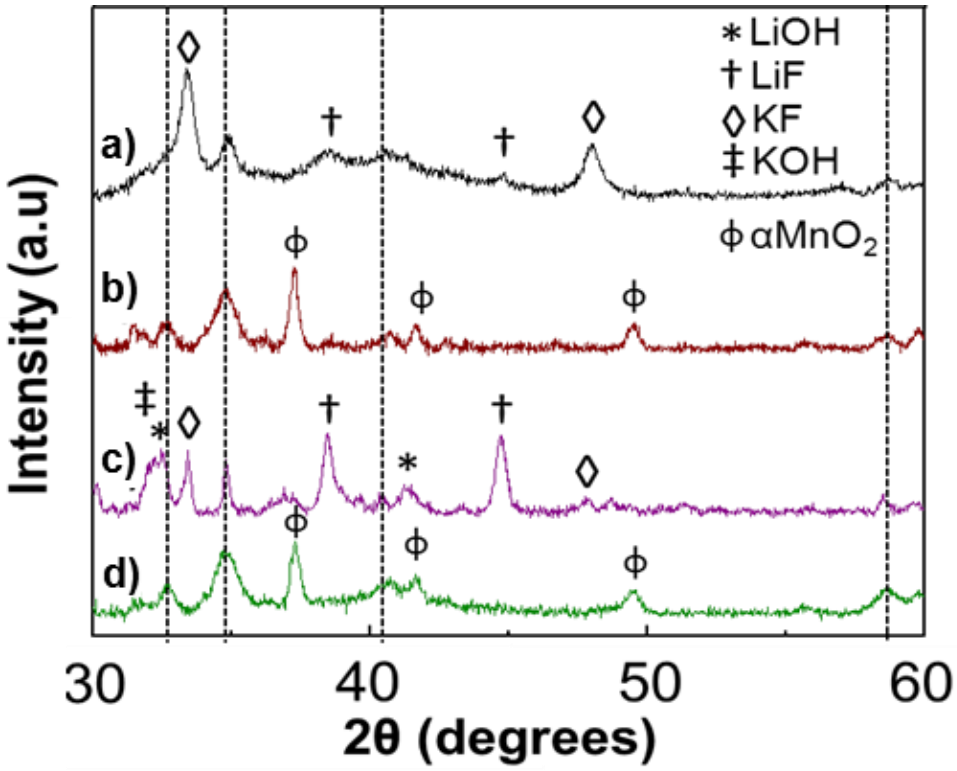


**Figure 3-6 -** Diffraction pattern of washed products for chemical reactions of $KO_2$/crown ether/$LiPF_6$ in TEGDME with added positive electrode components of (a) PVdF only, (b) α-$MnO_2$ only, (c) PVdF + α-$MnO_2$, and (d) α-$MnO_2$ + Li-Nafion. The dashed vertical black lines on all patterns indicate $Li_2O_2$.

bases of $O_2^-$ and $LiO_2$ abstract protons from the PVdF backbone, which causes a release of $F^-$ to form a conjugated double bond. This gives rise to extreme discoloration, which is in agreement with the colour change that is observed shortly after the addition of $KO_2$. $O_2^-$ is a much stronger base than $OH^-$,[33] hence, the $O_2^-$ itself acts as the hydrogen abstraction agent, resulting in the reaction shown in *equation 3-5*:

$$Li(O_2^-)_{(s)} + -(CH_2 - CF_2)_{(s)} \rightarrow HO_2 + -(CH{=}CF)^-_{(s)} + LiF_{(s)} \qquad (equation\ 3\text{-}5)$$

Such a reaction produces $HO_2$, which undergoes disproportionation to produce the additional products of $O_2$ and $H_2O_2$ shown in *equation 3-6*:

$$2HO_2 \rightarrow H_2O_2 + O_{2(g)} \qquad (equation\ 3\text{-}6)$$

Thus, the production of $O_2$ results in the observed gas evolution, while the solution discolouration is a result of the newly created $(CH{=}CF)^-$ product.

The presence of these double-conjugated by-products from PVdF decomposition was determined with $^{13}$C-NMR, as shown in **Figure 3-7**. This brown/black product exhibited peaks that correspond to the =C-H bond (71 ppm) and =C-F bond (170 ppm).[34] Further characterization of the solid products was performed with FTIR (**Figure 3-8)**. Prominent signals are present at 1522 $cm^{-1}$ and 1620 $cm^{-1}$, which corresponds to absorption of the C=C double bond and C=C-F bond respectively.[35] The proposed reactions in *equation 3-6* are further confirmed by the presence of $H_2O_2$. $MnO_2$ is highly catalytic towards the decomposition of $H_2O_2$ into $H_2O$ and $O_2$.[36] Upon addition of $MnO_2$ to the resulting supernatant of the $KO_2$/$LiPF_6$/PVdF reaction, vigorous gas evolution occurred. This confirms the existence of $H_2O_2$ as a by-product of the decomposition of PVdF. Further reports succeeding this work have confirmed the decomposition of PVdF within the Li-$O_2$ cell with

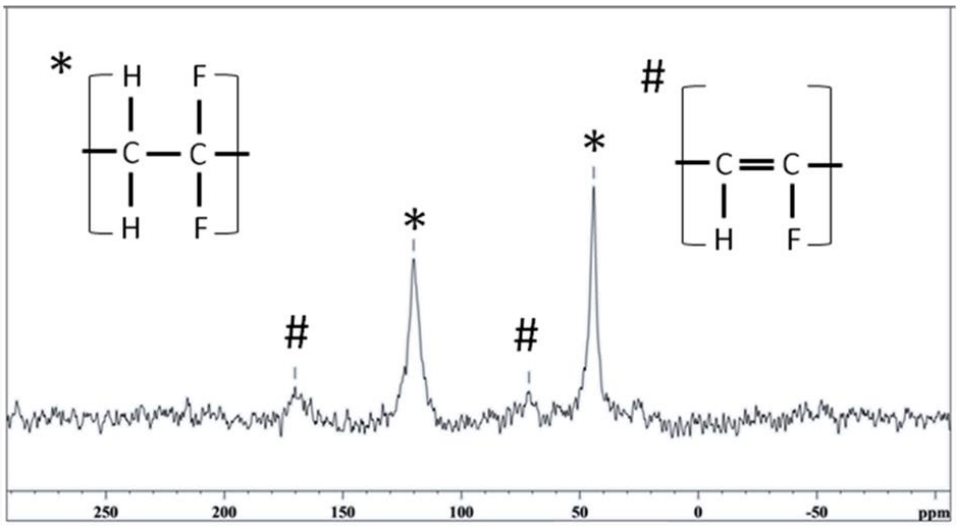


**Figure 3- 7 -** Solid state MAS $^{13}$C-NMR spectrum (500 MHz, adamantine reference) of the solid product from the chemical reaction $KO_2$ + 18-crown-6 + $LiPF_6$ + PVdF in TEGDME, after wash with acetonitrile. The more prominent signals at 44.6 ppm and 121.8 ppm are assigned to -$CH_2$- and -$CF_2$- groups in the PVDF backbone, respectively.[34] Dehydrofluorination of PVdF due to superoxide attack $O_2^-$ results in the appearance of resonances [#] at 71 ppm and 170 ppm assigned to partial conjugation of the polymer backbone owing to their characteristic downfield shift.

the use of XPS, and demonstrate that apart from PVdF instability towards $O_2^-$, contact with $Li_2O_2$ can cause the defluorination of the PVdF and the formation of the $H_2O_2$ and double-conjugated by-products.[37]

PVdF decomposition does not completely inhibit the production of $Li_2O_2$, however, implying that the superoxide radical reacts competitively with both $Li^+$ and the PVdF. In a Li-$O_2$ positive electrode prepared with PVdF, access to the binder and its relative content will determine the extent of reactivity. The side reactions of $LiO_2$ reduce the quantity of $Li_2O_2$ that is formed on discharge, and therefore limit the charge capacity of the cell. On cycling, the conjugated bond will progressively rigidify the porous membrane structure. Furthermore, the *in-situ* formation of $HO_2$ from the decomposition of the PVdF can result in H-atom abstraction from the methylene carbons on the ether (TEGDME), which will act as a radical

initiator for decomposition leading to the formation of electrolyte decomposition products as has been discussed previously.

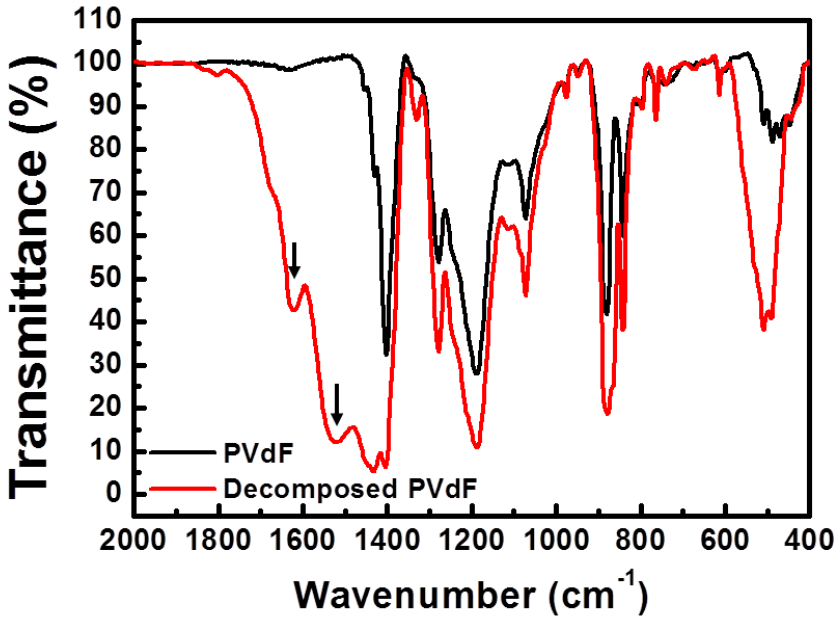


**Figure 3-8 -** FT-IR spectra of pure PVdF and the product from the reaction $KO_2$ + PVdF in TEGDME. As indicated, the IR spectrum of the latter shows two additional peaks at 1680 $cm^{-1}$ and 1540 $cm^{-1}$ (arrows), which are absent from the pure PVdF spectrum. These signature peaks correspond to hydrogen and fluorine atoms bonded to a conjugated carbon backbone as a result of the deprotonation and subsequent defluorination of the PVdF polymer chain due to the reaction with $O_2^-$.

### 3.6 – Reactivity of $O_2^-$ in the Presence of a Catalyst

This $KO_2$ probe was further used to demonstrate the effect of a catalyst on the ORR process. Specifically, α$MnO_2$ catalysts were investigated due to the prominence of $MnO_2$ and its polymorphs as highly effective ORR and OER catalysts for the Li-$O_2$ chemistry.[38] However, in these reports, the final discharge product is not solely $Li_2O_2$, but a mixture comprised of almost equal components LiOH and $Li_2O_2$. This is in contrast to a cell discharged in the absence of $MnO_2$, which produces $Li_2O_2$ only. To elucidate the process that

generates LiOH, $\alpha MnO_2$ was added to the $KO_2/LiPF_6$/TEGDME reaction mixture and the contents analyzed. These results are shown in **Figure 3-6(b-d)**. When $\alpha MnO_2$ is the only additional component added (**Figure 3-6b**), $Li_2O_2$ is the only observable crystalline product. However, upon addition of both $\alpha MnO_2$ and PVdF to the reaction mixture, the final solid product contains both $Li_2O_2$ and LiOH. LiOH Production is attributed to the $\alpha MnO_2$ catalytic activity towards $H_2O_2$. Determined earlier, $\alpha MnO_2$ catalyzes the oxidation of $H_2O_2$ to form $H_2O$. This $H_2O_2$ is clearly present as a result of $O_2^-$ attack on the PVdF backbone. With $\alpha MnO_2$ being a highly effective peroxide decomposition catalyst, the presence of $\alpha MnO_2$ in a solution of both $H_2O_2$ and $Li_2O_2$ enables the conversion of $Li_2O_2$ to LiOH via the following mechanism in *equation 3-7* and *equations 3-8*:

$$H_2O_2 \rightarrow H_2O_{(l)} + \tfrac{1}{2}O_{2(g)} \qquad (\textit{equation 3-7})$$

$$Li_2O_{2(s)} + 2H_2O_{(l)} \rightarrow 2LiOH_{(s)} + H_2O_2 \qquad (\textit{equation 3-8})$$

The generation of $H_2O$ from the oxidation of $H_2O_2$ via catalysis converts the $Li_2O_2$ to LiOH. This explains why LiOH is only observed when $\alpha MnO_2$ and PVdF are present simultaneously in the company of $O_2^-$, and not when $\alpha MnO_2$ or PVdF are present independently. Furthermore, in the presence of $O_2^-$ and PVdF, the $MnO_2$ appears to be consumed, as is evident from its absence in the diffraction pattern of **Figure 3-6c**. The consumption of $MnO_2$ upon reactivity with $H_2O_2$ has been shown to occur within the literature.[39] Further proof of this concept is shown in the solid product resulting from a $KO_2$ reaction involving $\alpha MnO_2$ with a different binder, such as Li-Nafion. In the presence of Li-Nafion and $MnO_2$, the resultant product from the $KO_2$ reaction is only $Li_2O_2$, with no

LiOH observed **(Figure 3-6d)**. Furthermore, $\alpha MnO_2$ remains and is observed in the diffraction pattern and is not consumed as it does not take part in any side reactions.

The formation of LiOH is undesirable because it can be a significant source of capacity fading in non-aqueous Li-$O_2$ cells. This is due to the tendency of the hydroxide to form a film on the positive electrode surface **(Figure 3-9)**, which blocks the catalytic active sites of ORR. Furthermore, the electrochemical oxidation of LiOH is not facile and requires an extremely high potential to charge in TEGDME.[40].

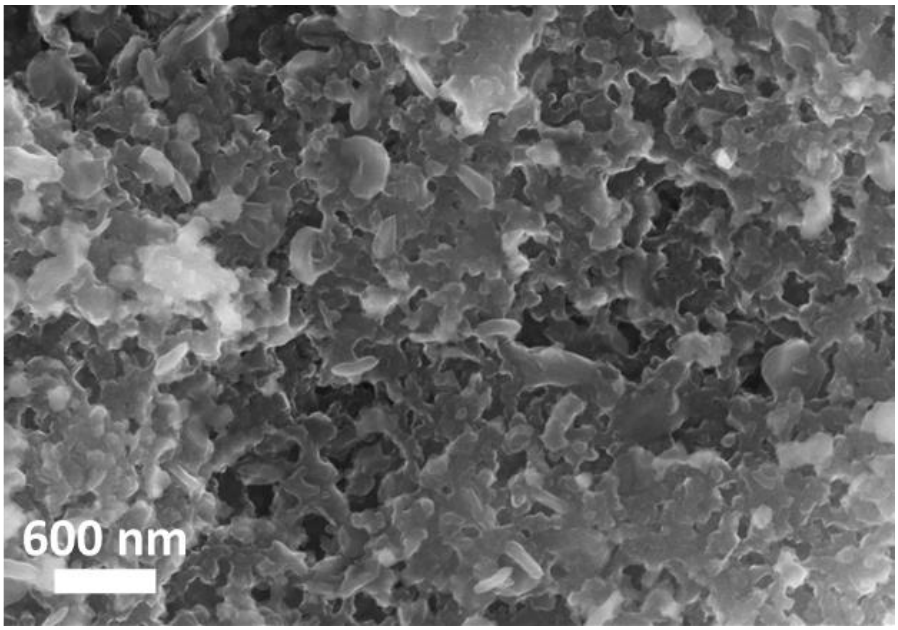


**Figure 3-9 -** SEM micrograph of the discharge product from an electrochemical cell with carbon + $\alpha MnO_2$ + PVdF binder as the positive electrode run in 1M $LiPF_6$/TEGDME. Note the mixture of toroidal like structures ($Li_2O_2$) embedded in an amorphous material that covers the surface (LiOH).

## 3.7 – Stability of PC and TEGDME

Apart from being able to prove the stability of positive electrode components, the chemical generation of $O_2^-$ allows one to probe the reactivity of $O_2^-$ towards specific solvents. Given the highly nucleophilic nature of the $O_2^-$ and $Li_2O_2$, electrolyte decomposition is an unavoidable process that occurs as part of the Li-$O_2$ cell discharge/charge chemistry. To investigate, the reactivity of two common Li-$O_2$ battery solvents, PC and TEGDME, is probed. PC, mixed with common Li-salts such as $LiPF_6$, was a common solvent used during the advent of Li-$O_2$ battery research.[1,2,3] PC has low volatility, a large electrochemical operating window, and is stable vs. metallic lithium, which makes it an ideal electrolyte for the Li-$O_2$ cell. However, PC undergoes decomposition in the presence of $O_2^-$ to produce a variety of Li-carboxylates as the primary discharge product (as opposed to the desired $Li_2O_2$).[3,7] To confirm this reactivity, the $^1$H NMR spectra in **Figure 3-10** was obtained from the solid product of PC/$KO_2$/crown-ether/$LiPF_6$ reaction. The presence of formate, acetate, and propylene glycol are very clear. This confirms the instability of PC towards $O_2^-$, and further validates the use of this $KO_2$ probe as a screening method to determine the stability of other electrolytes of interest.

TEGDME was studied due to its apparent greater stability towards $O_2^-$ compared to that of PC. While PC appears to be completely unstable to $O_2^-$ during cell discharge, the discharge product formed in TEGDME is $Li_2O_2$, as demonstrated with the previously shown diffraction patterns in **Figure 3-2**, implying, at minimum, a quasi-stability towards $O_2^-$. Upon exposure of $O_2^-$ to TEGDME, $^1$H NMR spectra were collected on the solids, and the presence of decomposition products was evident as seen in **Figure 3-11.** Formates, acetates, and methoxy(oxo)acetic anhydride derivatives exist in conjunction with $Li_2O_2$. Thus,

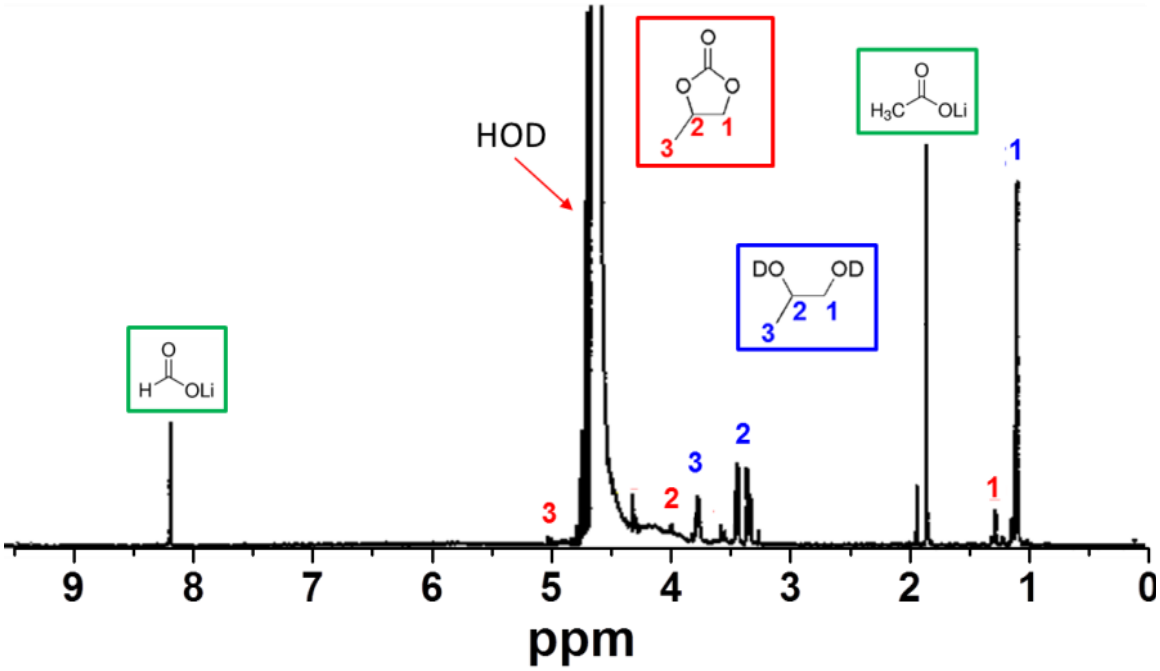


**Figure 3-10 -** $^{1}$H-NMR spectrum of the solid product of $KO_2$ + 18-crown-6 + PC, washed with acetonitrile and dissolved in $D_2O$. In addition to PC (red numbers), the $^{1}$H-NMR spectra reveal peaks of acetate ($\delta$ = 2.08 ppm) and formate ($\delta$ = 8.44 ppm), in addition to the characteristic peaks of propylene glycol in blue ($\delta$ = 3.88-3.95, 3.58-3.45 and 1.13 ppm), all of which are formed by the nucleophilic attack of superoxide on PC with $KO_2$ as reported in the literature.[7]

while TEGDME may produce $Li_2O_2$ as the discharge product, the presence of these Li-carboxylate products confirms the reactivity of TEGDME towards $O_2^-$. A mechanism for the formation of these ether-based electrolyte decomposition products was shown previously in **Figure 1-10.**

A brief comment should be made about the results presented here for TEGDME. A report by Takechi *et. al* [41] demonstrated with the use of Raman spectroscopy that a large variety of decomposition products exist in TEGDME after subjection to $O_2^-$. This is in agreement with our own results. In another report by Schwenke *et. al*.[42], a more thorough investigation of the $O_2^-$ reactivity in ether-based electrolytes was conducted. Specifically, they investigated the stability of different chain-length glyme solvents vs. $O_2^-/LiO_2$.

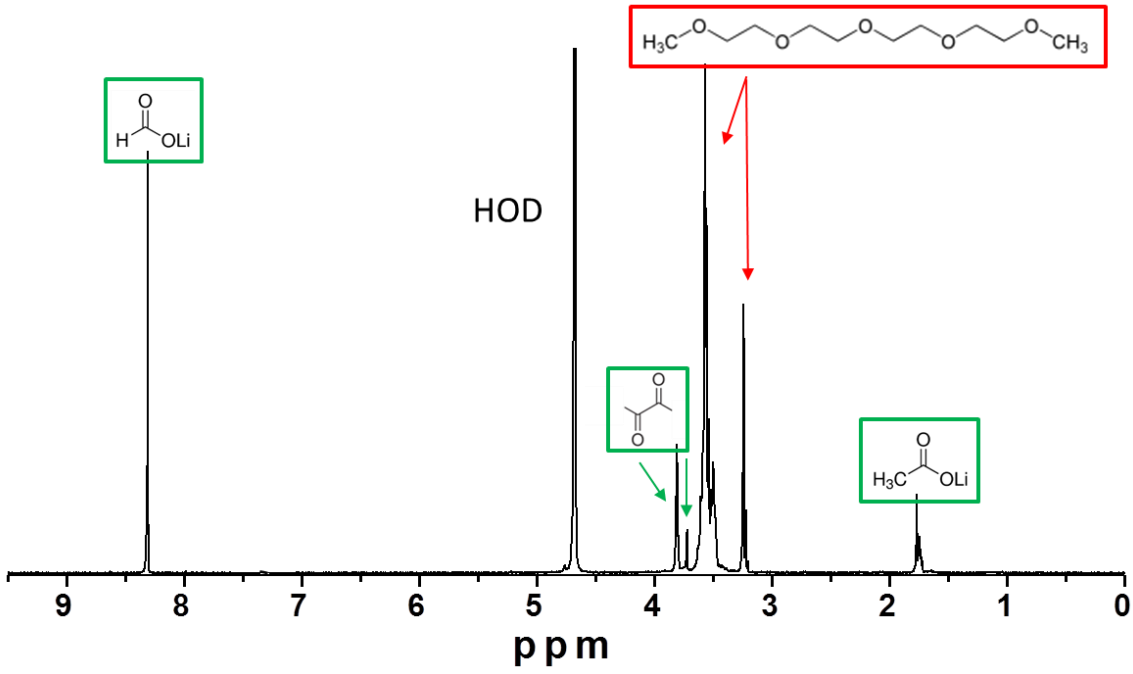


**Figure 3-11** - $^{1}$H- NMR of TEGDME solids after being subject to $KO_2$ + $Li_2O_2$. The NMR peaks of the decomposition products correspond to Li-formate (δ = 8.3 ppm), oxalates and derivatives (δ = 3.7 – 3.8 ppm), and Li-acetate (δ = 1.8 ppm).

From this study, they found that the decomposition products as a result of superoxide attack do not necessarily originate from the glyme itself, but from the impurities present within the solvent. They demonstrate this through comparison of *as-received* TEGDME electrolyte versus freshly distilled TEGDME. The *as-received* electrolyte, upon being subjected to $O_2^-$ via a $KO_2$ reaction, produced a large amount of decomposition products. The freshly distilled TEGDME, however, showed no signs of degradation. Hence, with extremely pure glyme-electrolyte, the solvent yields fewer decomposition products after being subjected to $O_2^-$. However, completely removing the impurities from TEGDME, as well as keeping the TEGDME completely free of impurities during storage, is rather difficult. This is problematic for long-term stability of the Li-$O_2$ battery, so for all practical purposes, the stability of TEGDME as a Li-$O_2$ solvent remains a critical issue. Furthermore, this type of $KO_2$ analysis

only probes the electrolyte stability towards chemically generated $O_2^-$, and does not take into account decomposition products or impurities that may form due to the electrochemical processes that occur during discharge and charge.

## 3.8 – Conclusions and Final Thoughts

In summary, generation of $O_2^-$ by chemical means is an effective tool to easily identify the reactivity of $O_2^-$ with materials used in Li-$O_2$ cells. Crystallization of $Li_2O_2$ in the absence of binder and catalyst is governed by its rate of nucleation/precipitation from $LiO_2$, its low solubility, and its interaction with the carbon surface. The electrochemical reduction of $O_2$ (where the reduction rate is current controlled), generates nanocrystalline $Li_2O_2$ that aggregates to form uniformly sized ~ 800 nm toroids. Superoxide readily reacts with PVdF resulting in dehydrofluorination to make a conjugated bond polymer, along with formation of $H_2O_2$. In the presence of a good hydrogen peroxide decomposition catalyst, $H_2O$ is produced internally in the cell and reacts with $Li_2O_2$ to form LiOH. In an electrochemical Li-$O_2$ cell, the hydroxide coats the porous positive electrode surface to form a film which blocks further catalytic activity. Hence, PVdF should not be used as a binder in any type of metal-$O_2$ battery. Other binders such as lithiated Nafion are stable against $O_2^-$, and should be used in the Li-$O_2$ cell instead. Furthermore, the activity of a catalyst towards the formation/oxidation of decomposition products is clear, and has a profound effect on the final products formed. Given this, care should be taken to understand the activity of catalysts within the Li-$O_2$ battery and how they impact cell performance. As will be demonstrated in *Section 5.0,* the effects of different catalyst materials can have a profound impact on the overall Li-$O_2$ chemistry. Knowledge of this activity towards $Li_2O_2$ and/or parasitic reactions is very important, and the demonstrated $KO_2$ probe is an excellent diagnostic tool to understand how

different active materials will impact the sensitive (and extremely reactive) $O_2^-/LiO_2$ chemistry in the Li-$O_2$ cell.

The $KO_2$ probe is also a very beneficial diagnostic tool to screen for the stability of various electrolytes. While the development of new stable electrolytes will be key to the long term stability of the Li-$O_2$ battery, this $KO_2$ probe can recognize and test the stability of new and promising candidates. In the future, this $KO_2$ probe can be used to explore electrolytes based on sulphoxides and/or amides (and many other compositions), and potentially new catalyst materials to ensure stability against $O_2^-/LiO_2$.

# 4.0 - The Role of Catalysts and Peroxide Oxidation in Li-$O_2$ Batteries

## 4.1 - Introduction

It is clear that the Li-$O_2$ battery offers a high energy density alternative to today's commercial electrochemical energy storage devices, and that a great leap forward in the world's energy storage capabilities will be realized if it can be applied. However, the large overpotential on charge along with poor capacity retention makes the use of Li-$O_2$ batteries impractical for commercial applications. In particular, the large charge overpotential (> 1 V) makes the cell extremely energy inefficient.[1] Furthermore, accompanying this large charge overpotential are parasitic reactions that greatly limit the lifetime of the battery. The lowering of this charge overpotential and facilitation of a more efficient $Li_2O_2$ oxidation pathway is tantamount to the future success of the Li-$O_2$ battery.

One approach to reduce this charge overpotential involves the use of an OER catalyst. These catalysts work to lower the activation energy of the oxygen evolution reaction, or in this case, the oxidation of $Li_2O_2$ to its constituents $Li^+$ and gaseous $O_2$. Prior to the work presented here, several types of catalysts have been employed in the Li-$O_2$ battery, such as α-$MnO_2$, EMD, $Co_3O_4$, $Fe_2O_3$, $Mn_3O_4$, and PtAu with varying levels of success.[2,3,4] Spinel-based $CoMn_2O_4$ and $Co_3O_4$ catalysts supported on graphene were reported to be promising bifunctional ORR and OER catalysts in aqueous media.[5,6] Moreover, reports have surfaced that bring into question the efficacy of $Li_2O_2$ oxidation catalysis.[7] As shown in **Figure 4-1** below, the presence of noble metal and metal oxide catalysts appear to have no significant improvement of the $Li_2O_2$ oxidation potential and $O_2$ evolution in DME-based electrolytes. With the addition of Pt and $MnO_2$, the amount of oxygen evolved is less than that of pure carbon, indicating that the presence of a catalyst can promote parasitic reactions and lead to

charge inefficiencies.[7] The work presented here is aimed at addressing these issues, and ultimately attempts to determine the role of the active material in the Li-$O_2$ cell with the use of nanocrystalline $Co_3O_4$ grown on reduced graphene oxide ($Co_3O_4$/RGO) as a positive electrode material for the Li-$O_2$ battery. The use of this material results in a significant reduction of the charge potential (~ 400 mV), and improved cycling stability. It is determined that this material acts as a promoter, rather than as a classic electron transfer catalyst, for the oxidation of $Li_2O_2$.

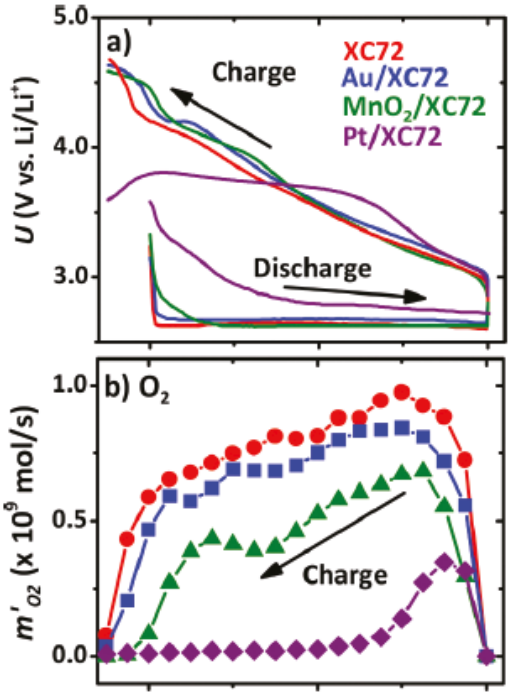


**Figure 4-1 – (**a) Electrochemical profile and (b) corresponding oxygen evolution profile for the charge reactions of different metal and metal oxide catalysts mixed with carbon. Each cell was run in DME-based solvent.[7]

## 4.2 – Experimental and Procedures

### 4.2.2 - Synthesis and Characterization of $Co_3O_4$/RGO

The $Co_3O_4$/RGO catalyst composite material was synthesized using a procedure modified from a previous report.[8] In two separate round bottom flasks, 100 mg of graphene oxide was added to 50 mL of deionized $H_2O$ (Solution A) and 100 mg of cobalt (III) pthalocyanine (CoPc) (Sigma Aldrich, 97%) was added to 50 mL of a 25% $NH_4OH$ (Solution B). Both solutions were stirred and sonicated for 3 hours. Solution B was added to the constantly stirred solution A using a pipette. Following this, 33.4 mL of 35 wt% $N_2H_4$ in water was added dropwise. The solution was heated to 40 °C and left to react for 48 hours. The contents were then collected by centrifugation and washed five times using a 50:50 water/ethanol mixture. The remaining solid was then dried overnight at 95 °C. The CoPc/graphene composite was pyrolyzed at 800 °C (10 °C/min heating ramp) for 2 hours under Ar atmosphere. After cooling, the material was exposed to air, and then subjected to a second heat treatment at 400 °C (10 °C/min heating ramp) for 2 hours under air.

The final product was characterized by powder X-ray diffraction. The reflections index to the cubic spinel $Co_3O_4$ (**Figure 4-2**). Thermogravimetric analysis (TGA) shows that the fraction of $Co_3O_4$ as part of the $Co_3O_4$/graphene composite is ~55% (**Figure 4-2 inset**). The absence of any graphene oxide peaks prove that the carbon sheets are in a substantially exfoliated state, and do not restack during the reduction and oxidation process. High resolution transmission electron microscopy (HRTEM) images depicted in **Figure 4-3** reveal that 8 - 10 nm $Co_3O_4$ particles litter the surface of the graphene sheets (also shown in the low resolution TEM, **Figure 4-3b** inset). The selective area electron diffraction (SAED) pattern

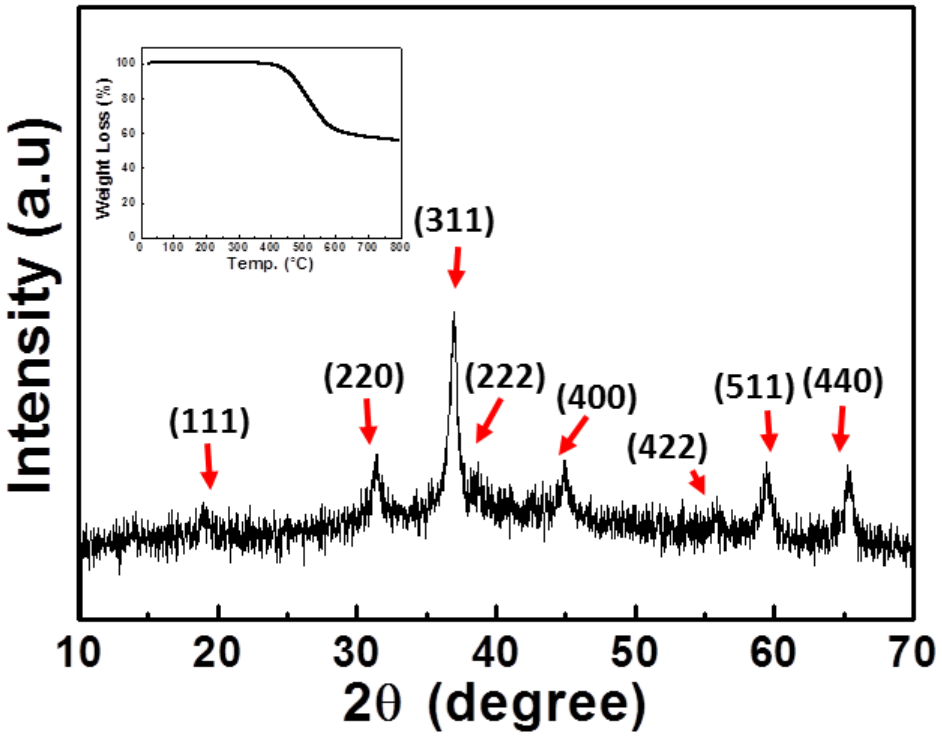


**Figure 4-2** - XRD pattern of $Co_3O_4$/RGO product with cubic spinel reflections indicated. Inset shows corresponding TGA analysis, demonstrating a mass loading of ~55 wt%.

further confirms the presence of nanocrystalline $Co_3O_4$ with a cubic spinel structure. Since some graphene/graphene oxides have been shown to be quite effective for ORR,[9] the high metal oxide content was chosen so that the $Co_3O_4$ nanocrystals cover a majority of the graphene oxide surface. This permits the properties of the oxide catalyst to be investigated independently, with the graphene acting primarily as a conductive layer to support the high metal oxide dispersion.

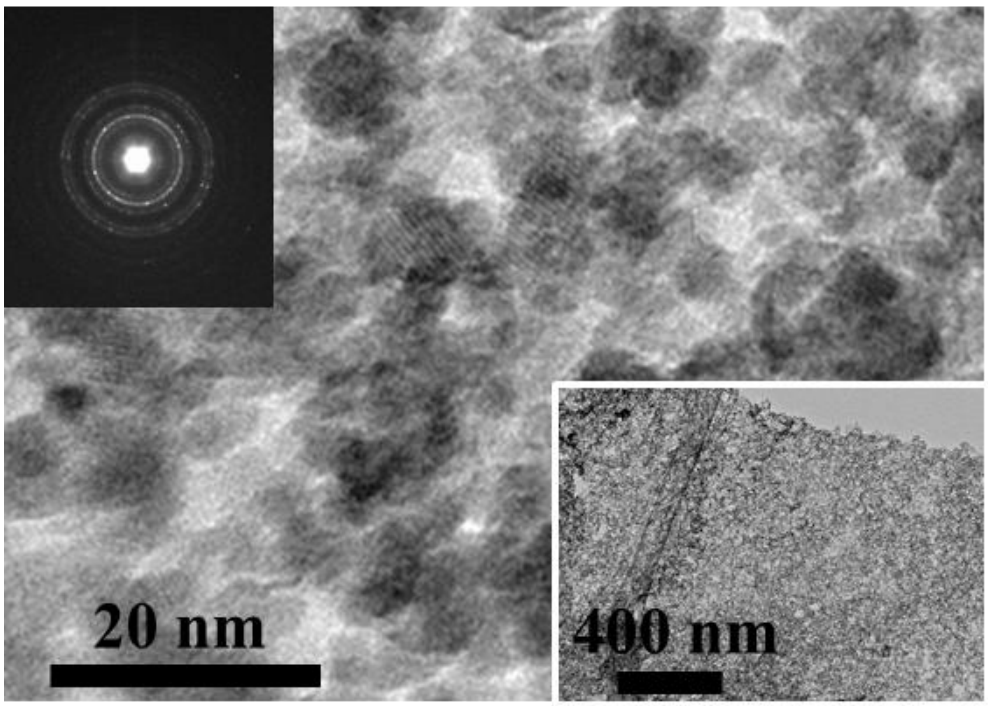


**Figure 4-3 -** TEM micrograph of $Co_3O_4$/RGO. Inset shows electron diffraction pattern of $Co_3O_4$.

## 4.3 – Activity as a Li-$O_2$ Battery Positive Electrode

### 4.3.1 – Electrochemical Performance

The electrochemical performance of Li-$O_2$ cells using 1M $LiPF_6$/TEGDME as the electrolyte, constructed with gas diffusion positive electrodes comprised of either $Co_3O_4$/RGO mixed with 70 wt% KB, or KB alone, is shown in **Figure 4-4**. All cells were run versus a metallic lithium metal counter electrode. In **Figure 4-4a** a single discharge-charge

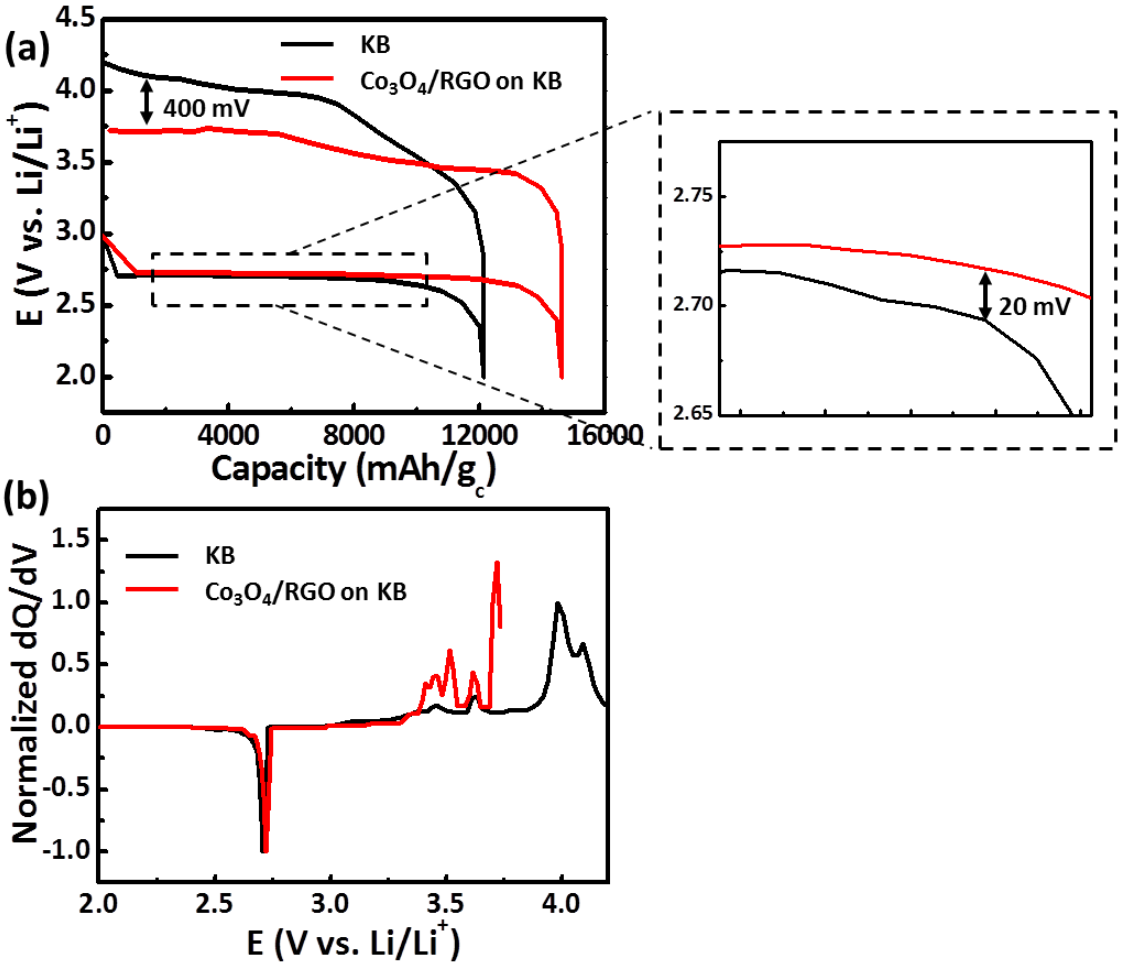


**Figure 4-4** – (a) First discharge–charge profile for Li-$O_2$ cells with Ketjen Black or $Co_3O_4$/RGO/KB at a current rate of 140 mA/g. (b) Derivative curve of (a) plotted vs. cell potential on both discharge and charge.

voltage profile for $Co_3O_4$/RGO/KB is compared to KB. Both cells exhibited similarly large capacities of 12,000-14,000 mAh/$g_c$ (1.2 – 1.4 mAh total capacity) when allowed to reach full discharge (with a voltage limitation of 2.0 V). This is accompanied by a 20 mV decrease in the ORR overpotential with the use of a $Co_3O_4$/RGO positive electrode. This difference in discharge potential cannot be explained by an increase in electronic conductivity values for the pure carbon and the $Co_3O_4$/RGO on carbon electrodes (5,000 Ω/sq, and 15,000 Ω/sq, respectively). Most importantly, however, is the large change in OER voltage exhibited by

the $Co_3O_4$/RGO positive electrode. The $Co_3O_4$/RGO positive electrode exhibits a charge plateau at ~ 3.7 V, a near 400 mV decrease in the charge potential compared to a pure carbon positive electrode. **Figure 4-4b** shows the dQ/dV curve of the discharge and charge process. This representation of the data displays the derivatives of the potential against capacity and highlights the differences in the onset of ORR/OER. Both positive electrode materials display similar onsets for $Li_2O_2$ oxidation at approximately 3.25 V. The main oxidation activity for the $Co_3O_4$/RGO positive electrode occurs at approximately 3.7 V, in contrast to the KB electrode where the potential gently slopes upon initial oxidation until reaching a flat plateau that begins at 4.0 V.

The lowering of the charge potential with the use of $Co_3O_4$/RGO is in keeping with the properties of the metal oxide as first reported by Abraham *et al*.[10] To confirm that this observed charge overpotential is from $Li_2O_2$ oxidation, a pre-filled positive electrode with $Li_2O_2$ deposited onto the $Co_3O_4$/RGO/KB surface was used. This $Li_2O_2$ was deposited from $Li_2O_2$ formed via the $KO_2$ reaction outlined in *Section 3.2*.[11] This allows $Li_2O_2$ to be grown directly onto the positive electrode material, ensuring inherent contact between the active material and $Li_2O_2$ particles. This artificially ”discharged” electrode is then subjected to electrochemical oxidation in a cell, which avoids complications from possible parasitic reactions that occur during prolonged electrochemical discharge. The $Co_3O_4$/RGO electrode exhibits a low charge overpotential compared to that of carbon (**Figure 4-5)**, and is very similar to the oxidation of electrochemically deposited $Li_2O_2$. Hence, the observed catalytic activity is directly related to the oxidation of $Li_2O_2$.

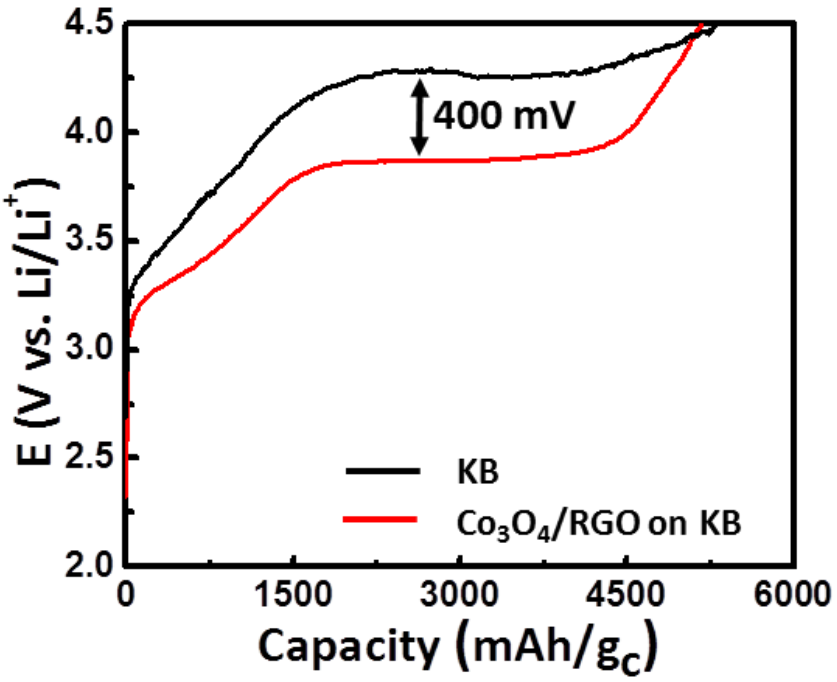


**Figure 4-5 -** Charge profile of a positive electrode prefilled with chemically produced $Li_2O_2$. Electrodes were prefilled with $Li_2O_2$ to observe the charge potential in the absence of any decomposition product formation on discharge. The disparity in the charge overpotential between prefilled vs. electrochemically formed $Li_2O_2$ is due to the large difference in size and morphology of chemical vs. electrochemically formed $Li_2O_2$.

To determine if this enhanced OER activity of $Co_3O_4$/RGO is a result of differences in the $Li_2O_2$ product, the $Li_2O_2$ morphology and crystalline structure was compared with SEM and XRD to a pure KB discharged positive electrode. The micrographs and diffraction patterns in **Figure 4-6** demonstrate that nanocrystalline $Li_2O_2$ is the only crystalline product regardless of the positive electrode material, with dimensions between 18-20 nm based on Scherrer analysis. There is no significant difference in morphology between the toroids

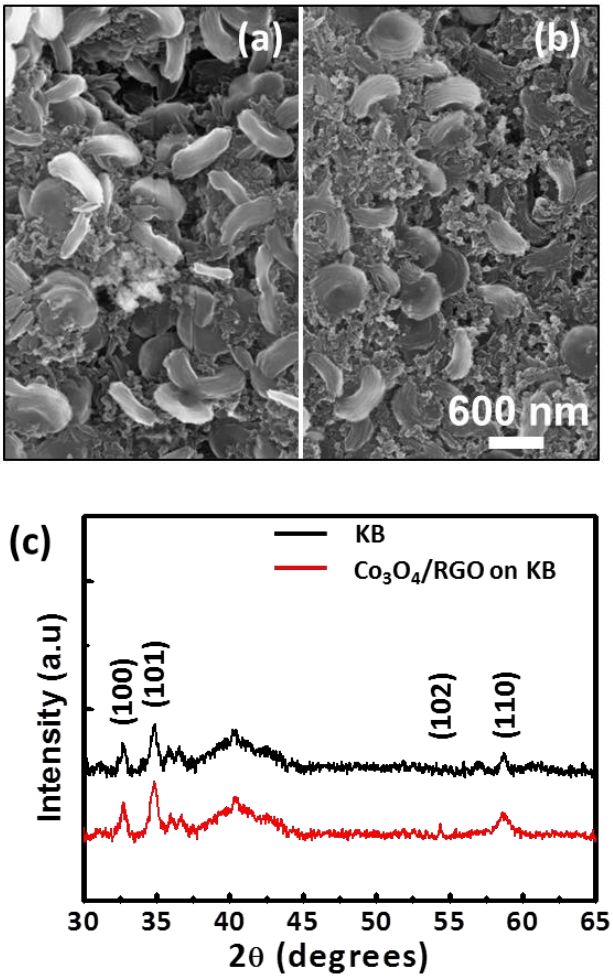


**Figure 4-6 -** SEM micrographs of recovered (a) $Co_3O_4$/RGO and (b) Ketjen Black positive electrodes after full capacity discharge. (c) Corresponding X-ray reflections of each positive electrode. Reflections of $Li_2O_2$ are indexed.

produced in the presence or absence of the $Co_3O_4$/RGO. This indicates that the carbon positive electrode component is responsible for the reduction of oxygen to $O_2^-$, which then proceeds to form $Li_2O_2$ via the previously discussed solution-based mechanism. If the production of $Li_2O_2$ were a surface-mediated process, the presence of $Co_3O_4$/RGO would most likely have an influence on the shape and size of the final product.

To further probe the activity of the $Co_3O_4$/RGO positive electrode and better understand its OER performance, chronoamperommetry (CA) and linear sweep voltammetry (LSV) were utilized with a thin layer of KB with RGO/$Co_3O_4$ deposited on a glassy carbon electrode. To determine the cathodic activity, the potential was held at 2.25 V in $O_2$ atmosphere for one hour. The corresponding current response for both KB/$Co_3O_4$/RGO and KB is shown in **Figure 4-7**. The cathodic current response of $Co_3O_4$/RGO on KB is 1.5 mA/$m^2$, double that of the KB electrode current response of 0.75 mA/$m^2$. Given the small amount of $Co_3O_4$/RGO added to the KB and its comparatively low surface area, the difference in ORR performance cannot be attributed to surface site population.

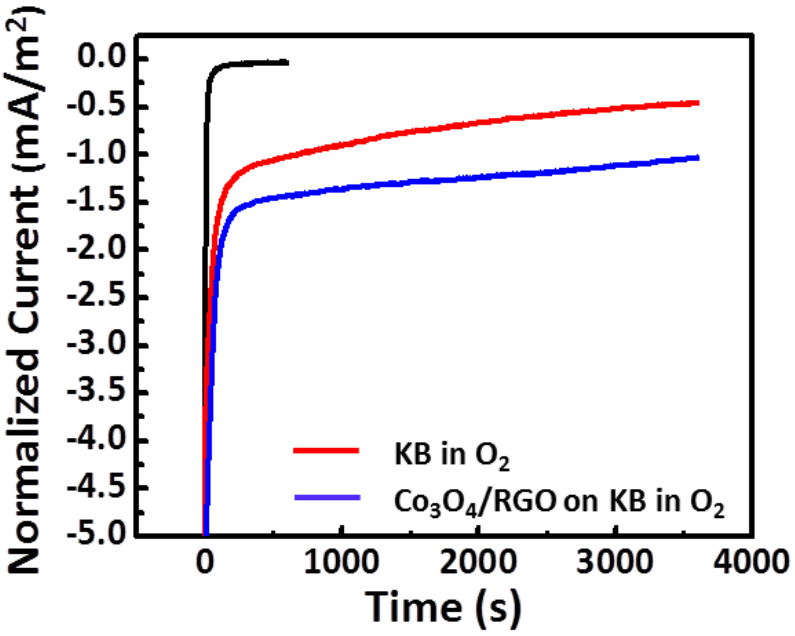


**Figure 4-7** - Current response of either KB (red) or $Co_3O_4$/RGO (blue) on a glassy carbon electrode surface held at a potential of 2.25 V vs. $Li/Li^+$. The electrolyte was 0.1 M $LiPF_6$ in TEGDME saturated with $O_2$. Both electrodes were used in $O_2$ atmosphere. The black line shows the current response of the RGO/$Co_3O_4$/KB electrode in Ar atmosphere, where no electrochemical activity is observed.

LSV studies were conducted by first holding the voltage at 2.25 V for 10 minutes in $O_2$ atmosphere to accumulate an abundance of $Li_2O_2$ on the electrode surface, followed by a sweep of the voltage to 4.7 V at a rate of 10 mV/s (**Figure 4-8**). Similar to the CA reduction studies, the response current for oxidation is greater for the $Co_3O_4$/RGO films, in part because more $Li_2O_2$ is deposited during the 10 min hold owing to better kinetics. The onset of OER is same for both KB and $Co_3O_4$/RGO, which occurs just above 3.0 V (as expected for the thermodynamics of the reaction $Li_2O_2 \rightarrow O_2 + Li$, $E° = 2.96$ V), although it is slightly less for the cobalt oxide. This is in agreement with full cell measurements in **Figure 4-4**,

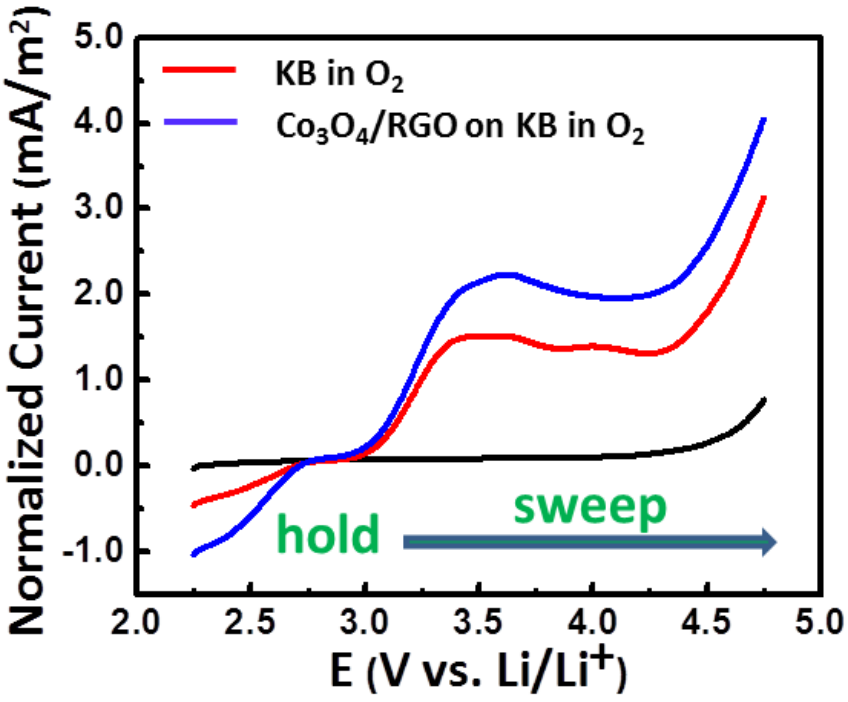


**Figure 4-8 -** Linear sweep voltammetry – current response of KB (red) and $Co_3O_4$/RGO on KB (blue) on the sweep of the voltage from 2.25 V to 4.7 V after being held to accumulate $Li_2O_2$ for 1 hour prior to sweep. The electrolyte used was 0.1M $LiPF_6$/TEGDME. Experiments were run in $O_2$ atmosphere with a sweep rate of 10 mV/s.

where the onset charge potential is similar for both KB and $Co_3O_4$/RGO electrodes. However, throughout the voltage sweep to 4.7 V, the current response exhibits similar behaviour. The findings from these LSV experiments are in accord with reports from McCloskey *et. al* on the efficacy of electrocatalysis in aprotic media, which shows no difference in the charge potential among various electrode materials.[7] The discrepancy between these results and the full cell studies can be attributed to the experimental conditions. For these LSV experiments, very little $Li_2O_2$ is deposited. This is the same with the studies from McCloskey *et. al*, where full cell studies were run with small capacities (< ~ 500 mAh/g). At these capacities, the surface of the positive electrode is expected to be only minimally covered with $Li_2O_2$. In the full cell studies presented in **Figure 4-4**, a much greater amount of $Li_2O_2$ is deposited, and fully covers the electrode surface (See **Figure 4-6**). At this surface coverage, the change in charge overpotential is observed. In short, at low levels of peroxide deposition when the carbon and peroxide are in contact on the nanoscale, OER occurs at a consistent potential irrespective of the metal oxide.

### 4.3.2 – $Li_2O_2$ Oxidation "Promoter"

The results obtained from these fundamental studies suggest that $Co_3O_4$/RGO does not act as a conventional catalyst that lowers the activation energy *via* electron transfer reactions. Rather, the hybrid catalyst reduces the binding energy of $Li_xO_2$ species in both forward and reverse electrochemical processes to enhance surface transport. This hypothesis is based on two factors. Studies on alkene oxidation reactions demonstrate the presence of mobile surface oxygen species (superoxide and peroxide) on 14-15 nm nanocrystallites of $Co_3O_4$ supported on $CeO_{2-x}$.[12] The second is the finding detailed in *Section 3.4* that $Li_2O_2$ produced from the deposition of lithium superoxide from solution ($2LiO_2 \rightarrow Li_2O_2 + O_2$)

onto high surface area carbon via $KO_2$ is much less crystalline than in the absence of carbon.[12] This can be attributed to the strong binding of superoxide with carbon defect sites that inhibits the disproportionation reaction of $LiO_2$. Metal oxide surfaces are considered to be less "sticky" than carbon surfaces with an abundance of defects and dangling bonds. Thus, they can better facilitate mass transport of $O_2^-/LiO_2$ species that are generated at the positive electrode surface, and hence have a weaker bind on these oxygen species compared to high surface area carbons alone. These factors are particularly critical at high capacities, where the surface becomes covered with insulating $Li_2O_2$ species, and access to the electrode surface for efficient formation of $O_2^-/LiO_2$ species is vital for further capacity increase.

One important point of discussion is how this "catalyst" promoter affects the oxidation of $Li_2O_2$, given the very large ~700 nm toroidal aggregates that are formed on discharge. Visual examination of SEM images taken at different periods of an entire cell cycle for the $Co_3O_4$/RGO electrode, in combination with analytical studies using XRD and TOFSIMS, provides a hint of this oxidation process. The $Li_2O_2$ toroids that are deposited on the surface on discharge to 6000 mAh/g (point D, **Figure 4-9**) immediately start to disintegrate when 10% of oxidation is reached (point C1, **Figure 4-9**). This C1 point corresponds to the onset of the first plateau at 3.3 V. This discrete onset potential that is observed is the same as that reported elsewhere for $O_2$ release.[7] Remnants of the nanocrystalline $Li_2O_2$ toroidal aggregates are still visible, but many have collapsed and filled in the voids between the electrode particles. An SEM image taken on completion of the transition (at a charge capacity of 25% or 1500 mAh/g at point C2), shows that the disintegrated toroids form an aggregate film which covers the electrode surface. XRD

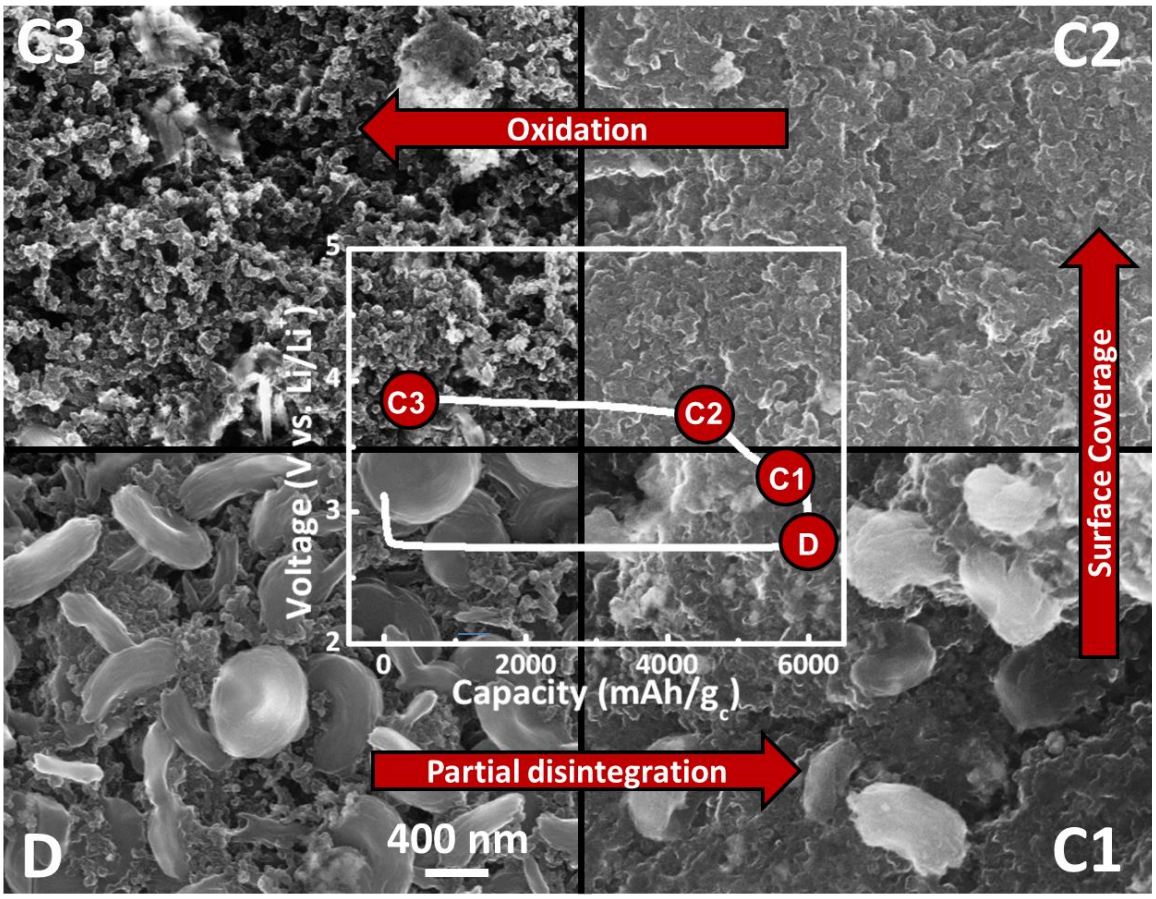


**Figure 4-9 -** SEM micrographs of the physical change of $Li_2O_2$ during cell charge. Remnants of the nanocrystalline $Li_2O_2$ toroidal aggregates are still visible, but many have collapsed and filled in the voids between the electrode particles. The electrode surface on completion of the transition (at a charge of 25% or 1500 mAh/g at point $C_2$), reveals disintegrated toroids form an agglomerate film.

analysis confirms this material is amorphous. We propose that surface transport of $Li_xO_2$ species on OER is facilitated by close proximity to the $Co_3O_4$/RGO. The majority of the subsequent oxidation (75% of the total charge) takes place at a voltage plateau (up to point C3) which is lower than the potential where electrodes that have been deliberately constructed from $Li_2CO_3$ evolve significant $CO_2$ (~ 4.3 V).[13] Thus it is primarily $Li_2O_2$ that is being oxidized at the 3.9 V plateau. Full charge to the equivalent discharge capacity results in removal of the $Li_2O_2$ to produce a relatively clean carbon surface, although a small

amount of residual $Li_2O_2$ remains as evident from the diffraction pattern of a fully charged positive electrode (**Figure 4-10)**. There appears to be no apparent change in the crystal structure of the $Co_3O_4$ catalyst particles after one cycle, confirmed with powder X-ray diffraction.

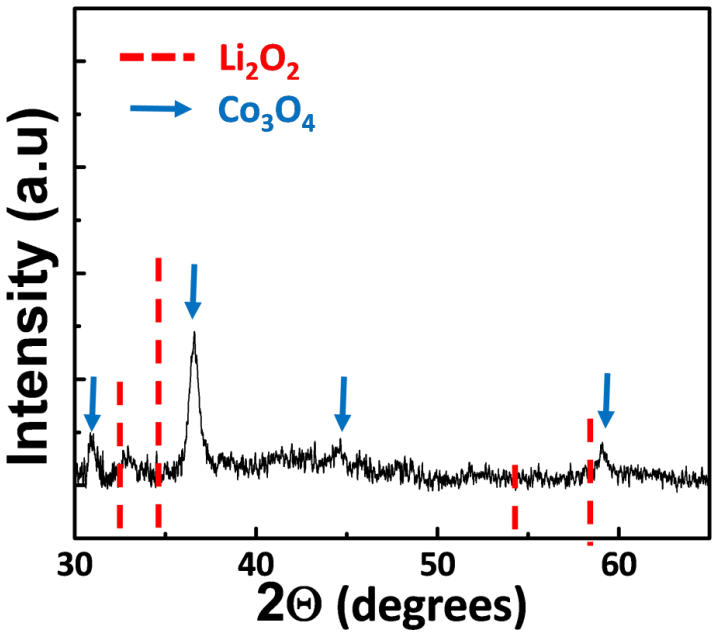


**Figure 4-10** - XRD pattern of a $Co_3O_4$/RGO on KB electrode that has been discharged to 6,000 mAh/$g_c$, and then fully charged (1 cycle). Only those reflections corresponding to the crystalline $Co_3O_4$ on the metal oxide/graphene composite catalyst are visible. The absence of reflections from crystalline $Li_2O_2$ and other possible crystalline by-products from electrolyte decomposition imply full removal of products from the carbon surface after the first cycle.

## 4.4 – Impact of Degradation Reactions on Catalytic Activity

### 4.4.1 – Time of Flight Secondary Ion Mass Spectrometry (TOFSIMS) Analysis

TOFSIMS analysis of the decomposition products on the electrode surface at the points indicated by D → $C_3$ are summarized in **Figure 4-11**. The normalized intensity of the secondary-ion $Li_3CO_3^+$ fragment (mass = 81, normalized to $Li^+$) is shown as a function of the cycle stage. This fragment is highly characteristic of alkali carbonates, as reported in the literature and as shown by our own data for a $Li_2CO_3$ standard (**Table 4-1).**[14] This

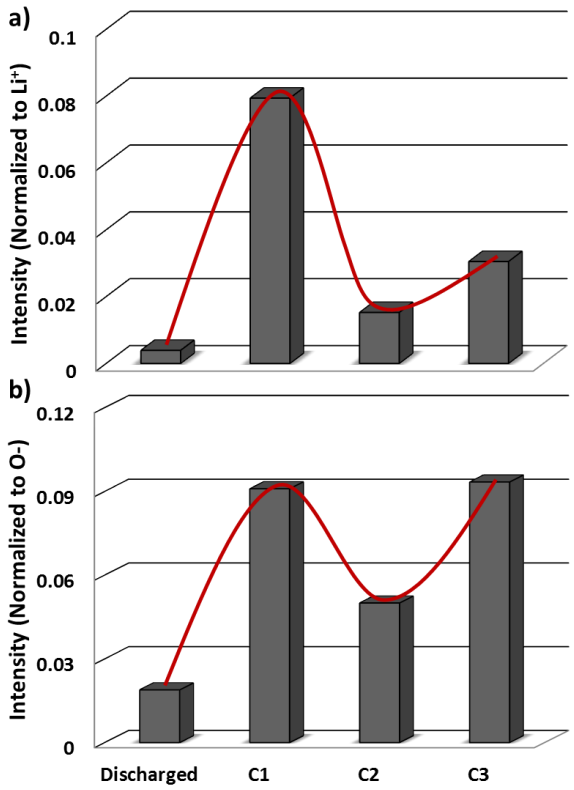


**Figure 4-11 -** Ion intensity from TOFSIMS measurements of recovered electrodes after discharge/charge to specified capacity limitations. The points of Discharged, C1, C2, and C3 correspond to the points in **Figure 4-9**. (a) $Li_3CO_3^+$ fragment measurement (m/z = 81) (b) $LiCO_3^-$ fragment measurement (m/z = 67), normalized to $Li^+$ and $O^-$ signals respectively.

TOFSIMS analysis reveals that a small amount of carbonate is deposited on discharge, in accordance with previous results that TEGDME is relatively (but not completely) stable to superoxide attack. However on the initial charge step to $C_1$, a dramatic thirty-fold increase in the carbonate content on the electrode indicates that electrolyte decomposition commences almost immediately. The normalized intensity of the $Li_3CO_3^+$ fragment is essentially the same when observed for the pure $Li_2CO_3$ (see **Table 4-1**). **Figure 4-12** visualizes this through fragment analysis on the positive electrode surface. Furthermore, we see similar data for the negative ion spectrum characterized by the $LiCO_3^-$

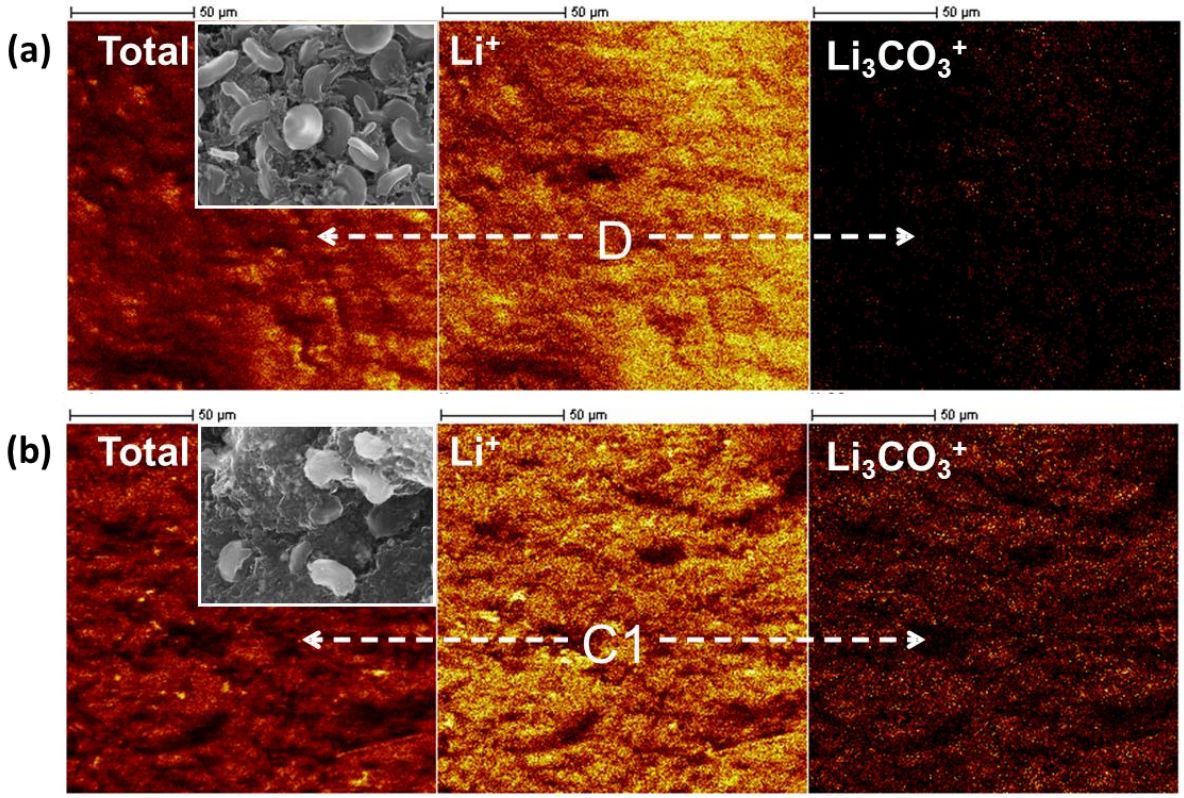


**Figure 4-12 -** Visual summary of the positive TOFSIMS spectral images for electrodes either discharged (position D in **Figure 4-9**): (a) total positive ion fragments; $Li^+$; $Li_3CO_3^+$ or charged (position C1 in **Figure 4-9**): (b) total positive ion fragments; $Li^+$; $Li_3CO_3^+$. The significant contribution of $Li_3CO_3$ + arising from $Li_2CO_3$ deposition is evident in the charged electrode, but not in the discharged electrode.

fragment (mass = 67). The negative ion results are shown in **Figure 4-11b**. The observed reactivity is in full accord with the findings of McCloskey *et. al*, who have used differential electrochemical mass spectroscopy to demonstrate that $Li_2O_2$ reacts with both the carbon surface and the electrolyte to produce a passivation layer of $Li_2CO_3$.[15 **]**

The $Co_3O_4$/RGO may moderate that reactivity by limiting the degree of $Li_2O_2$/C interaction, but the results here do not provide concrete evidence that this is the case. The reaction of the electrolyte with liberated oxygen must also be considered. Regardless of whether peroxide oxidation proceeds via a direct $2e^-$ oxidation ($Li_2O_2 \rightarrow O_2 + 2Li^+ + 2e^-$) or a two-step oxidation process, ( $Li_2O_2 \rightarrow LiO_2 + Li^+ + e^-$; $LiO_2 \rightarrow Li^+ + e^- + O_2$ ) the nascent $O_2$ that is released at the surface of the $Li_2O_2$ nanocrystallites can readily react with the electrolyte. The oxidation of $H_2O_2$ results in the highly reactive singlet $O_2$ ($^1\Delta_g$) in an excited state with a lifetime ranging from seconds to microseconds; the oxidation of $Li_2O_2$ may also produce singlet oxygen. Singlet oxygen is produced by the dismutase reaction of superoxide in acetonitrile ($2HO_2^{\bullet} \rightarrow H_2O_2 + {}^1O_2$).[16,17,18] This species is 0.98 eV higher in energy than the ground state triplet (paramagnetic) $O_2$ and its reactivity with organics is well established. While the evolution of singlet oxygen may not account for this enhanced reactivity, as speculated by McCloskey *et. al.*[19], the TOFSIMS spectra at point $C_1$ shows that the organic lithium carbonates formed *via* a reaction between the peroxide and/or released oxygen with the electrolyte deposit on the surface of the lithium peroxide nanocrystallites. Sudden loss of the peroxide-peroxide interfacial interaction would result in disintegration of the toroidal aggregate structure, coincident with the onset of oxidation as observed.

**Table 4-1 -** Raw TOFSIMS data of standard $Li_2CO_3$ and discharge/charged $Co_3O_4$/RGO electrodes. The numbers presented represent the intensity corresponding to the as mentioned peaks of $Li_2CO_3$ fragments. The normalized fragment intensity (with respect to $Li^+$) implies the amount of $Li_3CO_3^+$ is much greater on charged electrodes compared to the discharged electrode. The high amount of $Li_3CO_3^+$ for C1 charged electrode implies the almost immediate decomposition of electrolyte. The increase of carbonate fragments towards the end of charge is the oxidation of the carbon surface due to reaction with $Li_2O_2$.

| | $^7Li_3CO_3^+$ | $^7Li_2{}^6LiCO_3+$ | | $Li_3CO_3^+/Li^+$ |
|---|---|---|---|---|
| **m/z (ratio)** | **81** | **80** | **(80/81)** | **(81/7)** |
| **$Li_2CO_3$ (standard)** | 14925 | 3590 | 0.241 | 0.057 |
| **D** | 1413 | 300 | 0.212 | 0.005 |
| **C1** | 35940 | 8809 | 0.245 | 0.076 |
| **C2** | 11610 | 2830 | 0.244 | 0.007 |
| **C3** | 13920 | 3510 | 0.252 | 0.036 |
| | | **Theoretical** | **0.243** | |

### 4.4.2 – Degradation Reactions and Cycling Limitations

The carbonate residuals have profound impact on cycling, which is mediated by the presence of $Co_3O_4$/RGO. Poor capacity retention on cycling results from clogging of the porous membrane surface and/or pores with large amounts of $Li_2O_2$ or $Li_2CO_3$.[3] In order to minimize these effects on cycling and study the effect of the metal oxide promoter in full-cell systems, the discharge and charge capacity was limited to 6,000 mAh/$g_c$ (approximately half of the full capacity).The $Co_3O_4$/RGO/KB electrode achieved a charge capacity of 6,000 mAh/$g_c$ for over 7 cycles shown in **Figure 4-13a**, but the KB electrode displayed poorer rechargeability and sharp capacity fading. This was also evident at a capacity limitation of 2,000 mAh/$g_c$ as shown in **Figure 4-13b**. The $Co_3O_4$/RGO promoter exhibits improved cycling, with a capacity retention increase by approximately 25%.

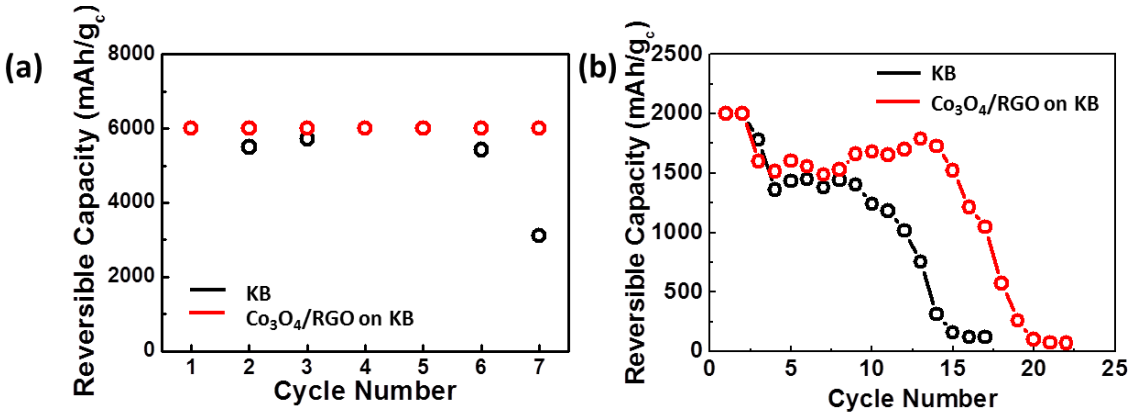


**Figure 4-13** - Cycling characteristics of $Co_3O_4$/RGO catalyst vs. pure KB positive electrode with a capacity limitation of (a) 6,000 mAh/$g_c$ and (b) 2,000 mAh/$g_c$. The capacity failures occur sooner for the KB than for the $Co_3O_4$/RGO on KB electrode.

SEM was used to examine the morphology of the product formed after the 1$^{st}$, 3$^{rd}$, and 18$^{th}$ discharge corresponding to the electrochemical curves shown in **Figure 4-14a**. SEM micrographs taken after discharge of 2,000 mAh/$g_c$ (**Figure 4-14b)** show an abundance of well-defined toroids. Compared to a discharge capacity of 6,000 mAh/$g_c$ shown previously in **Figure 4-6**, these toroids are smaller in size and cover less of the electrode surface. Toroids are also observed for an electrode that has been cycled twice and then stopped at a third 2,000 mAh/$g_c$ discharge (**Figure 4-14c**). However, while the toroid morphology is quite similar to the first discharge, the toroids are accompanied by a film that covers the entire electrode surface. Upon further cycling to the same capacity limitation on the 18$^{th}$ discharge (**Figure 4-14d)**, $Li_2O_2$ toroids are barely visible and a film now dominates the electrode surface along with obvious electrolyte decomposition products. These findings are in agreement with reports that cycling in TEGDME to maximum discharge results in the disappearance of crystalline $Li_2O_2$ from the XRD pattern after 5 cycles.[20]

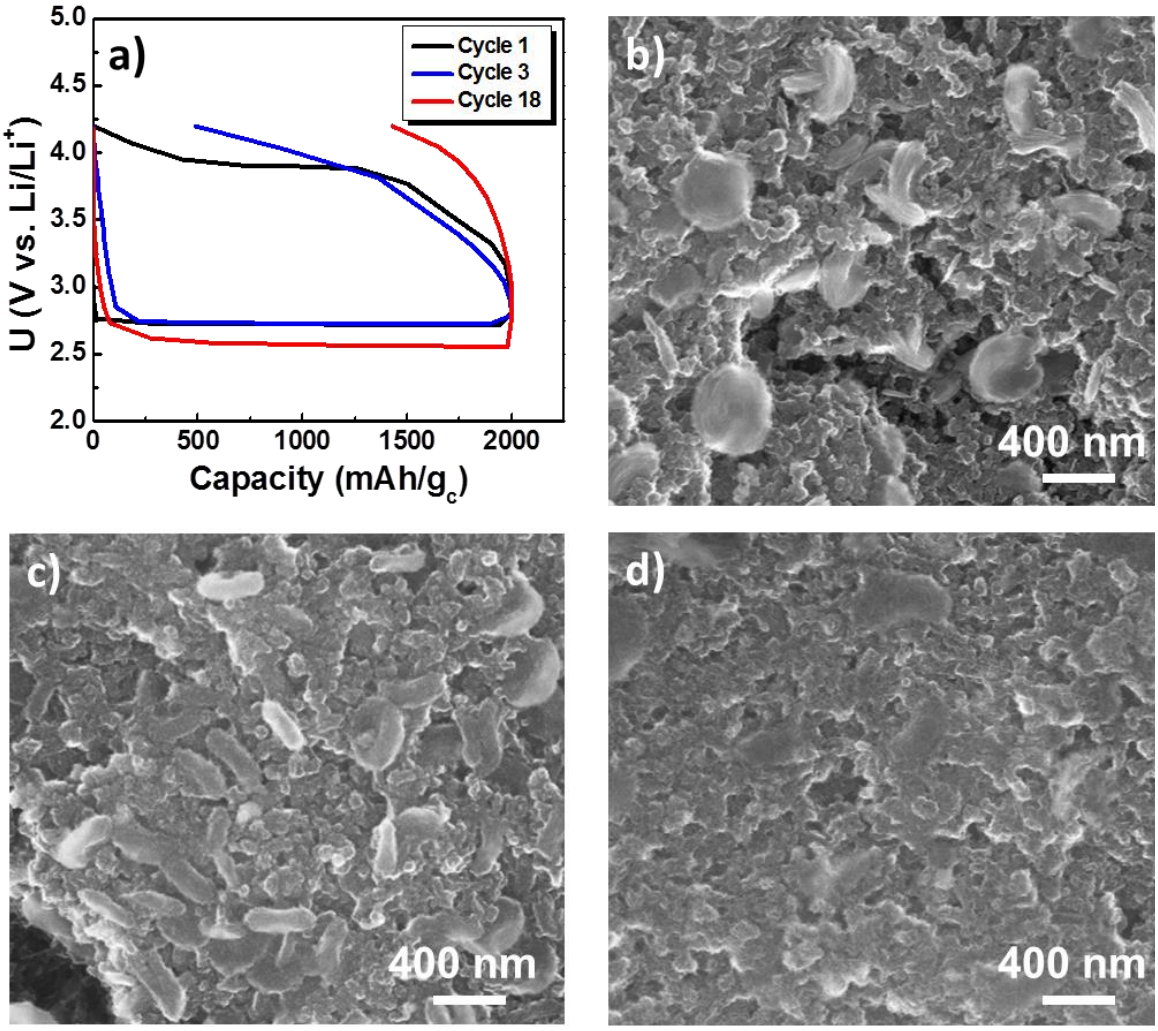


**Figure 4-14 -** (a) Cycling profile for the $Co_3O_4$/RGO on KB electrode with a capacity limitation of 2,000 mAh/$g_c$. The amount of recoverable capacity within the upper voltage limitation of 4.25 V diminishes on each cycle. The corresponding SEM images corresponding to the end of discharge step on (b) 1st discharge, (c) 3rd discharge, and (d) 18th discharge show growth of an increasing impedance layer of Li-carboxylate species.

An overall picture of the Li-$O_2$ cell on cycling and the effect of the $CO_3O_4$/RGO can thus be proposed as follows. Oxygen reduction catalyzed at the carbon surface produces superoxide, whose surface mobility is promoted by the presence of $Co_3O_4$/RGO, thus enhancing the kinetics of formation of $Li_2O_2$. At the immediate onset of the subsequent charge at ~ 3.3V, the reaction of the electrolyte with peroxide deposits organic carbonates on

the nanocrystalline peroxide surface. Disintegration of the toroidal aggregates and loss of peroxide crystallinity results in the collapse of the peroxide/carbonate to form a layer that coats the carbon surface. The $Co_3O_4$/RGO may aid in lowering the OER voltage by facilitating the mobility of $Li_xO_2$ species released on oxidation, and/or by decreasing the reactivity of the nascent $O_2$ that is released (potentially, by catalyzing the conversion of singlet oxygen to triplet oxygen and thus lowering the oxidation potential. This is purely speculation). On the first cycle, in the presence of $Co_3O_4$/RGO, the oxidation potential remains below 3.8 V, whereas it increases above 4.2 V in its absence. Nonetheless, towards the end of charge, there is a second, albeit smaller, increase in carbonate formation indicated from the TOFSIMS data (**Figure 4-11)**. The increase in $CO_2$ production above 4.3 V observed by others using mass spectrometry analysis is ascribed to oxidation of Li-carboxylates from the carbon surface produced via reaction with $Li_2O_2$.[19] Also note, any $CO_2$ released into solution will react with superoxide produced by ORR on the subsequent discharge, to form yet more ”inorganic” $Li_2CO_3$.[21] Its deposition further blocks active sites for ORR on the carbon surface. Hence, after multiple cycles of the Li-$O_2$ cell, the continuous build-up of carbonates on the positive electrode surface terminates the cell activity.

## 4.5 – Conclusions and Final Thoughts

The above studies, as well as identified supplementary reports, support the conclusion that there are advantages to the use of $Co_3O_4$/RGO as positive electrode components for the Li-$O_2$ cell. Improvements in both ORR and OER are clear in the presented electrochemical studies. However, for catalytic materials to impact the Li-$O_2$ chemistry over the entire cell lifetime, the formation of decomposition products during cell operation must be prevented.

Specifically, the oxidation of the aprotic media creates insulating solid materials that deposit onto the positive electrode surface. This causes termination of the catalyst material's active sites, and hence any improvement in ORR/OER activity only occurs for the first few cycles.

Since completion of this work, various studies have further investigated the catalytic activity of different $Co_3O_4$ active sites, and support the ideas and concepts presented in this section. It has been shown that specific $Co_3O_4$ surface facets improve OER capabilities through the lowering of the $O_2$ desorption barrier.[22] In these theoretical studies, oxygen-rich $Co_3O_4$ (111) surfaces strongly attract electrons from $Li_2O_2$ on the surface, which in turn lowers the energy required for $Li^+$ and $O_2$ desorption. Doping of the $Co_3O_4$ can further lower the $O_2$ desorption barrier to further improve the catalyst's OER capabilities. A similar study has proven this concept experimentally with the synthesis of faceted $Co_3O_4$ octahedrons and cubes.[23]. The octahedrons, having oxygen-rich (111) facets, displayed lower charge overpotential and improved OER capabilities compared to the cube (001) surface. This was concluded to be a result of a lower $O_2$ energy desorption barrier which is in agreement with the work presented here, where it is speculated that the observed OER activity is a result of improved mobility of the $O_2/LiO_2$ species that can easily desorb from the positive electrode surface. This leads to the observed voltage efficiency improvement.

However, the deactivation of these active sites over extended cycling is still a problematic issue. Clever engineering of the positive electrode surface to more effectively accommodate these decomposition products, while still maintaining active sites for $O_2$ reduction, is an appealing option to mitigate the effect of this decomposition. The more promising alternative is the development of new, non-aqueous electrolytes that are stable to $O_2^-/Li_2O_2$ attack. However, this may be unrealistic, given the multitude of other electrolyte

properties that must also be present (low viscosity, salt solubility, high oxygen dissolution). Prevention of electrolyte decomposition should allow for the catalytic activity to be maintained during the entirety of the cell lifetime. While TOFSIMS has proven a valuable technique to monitor and identify the decomposition products on the positive electrode surface, it is not ideal for quantification, and does not provide on-line information of the cell chemistry because it is a destructive, off-line technique. Other more sensitive techniques, such as mass spectrometry, are much more useful, as will be discussed in the next section.

Future work within the area of catalyst materials for Li-$O_2$ batteries should not focus entirely on the development of new and expensive oxides, as has been far too common in the literature. Instead, focus should be first towards the development of new stable electrolytes that possess the necessary properties (ionic conductivity, viscosity etc.) for use in a Li-$O_2$ battery. While catalyst materials will be necessary in the future, currently the major "bottle-neck" of Li-$O_2$ battery development is the electrolyte.

# 5.0 - Mass Spectrometry to Determine Electrode Activity

## 5.1 - Introduction and Motivation

One technique that has proven invaluable in understanding the oxidation efficiency and degree of parasitic reactions of metal-air batteries is on-line electrochemical mass spectrometry (OEMS). In my opinion, the use of mass spectrometry is necessary to fully understand and evaluate the chemical processes that occur during battery operation, as will be demonstrated in subsequent sections. For *in-situ* analysis of various metal-$O_2$ batteries, the mass spectrometer must be designed to meet stringent specifications. It must be interfaced with a metal-$O_2$ cell so as to not interfere with normal metal-$O_2$ cell operation, and be capable of quantitatively measuring the evolved gases. The following sections will outline the design and implementation of a mass spectrometer that is capable of *in-situ* gas analysis of electrochemical cells. I will outline the design process, and elaborate on the vital design considerations that are necessary to improve instrument sensitivity and validate the gas quantification. The quantification of gas evolution from the oxidation of $Li_2O_2$ on various positive electrode materials will be presented as a means to demonstrate the necessity of mass spectrometry as an analytical tool. Gas quantification, and its correlation to the observed electrochemistry, will provide insight into the critical factors that affect cell performance. The work presented here stresses the necessity for quantitative analysis of metal-$O_2$ chemistry, for parasitic reactions can be masked as "good" electrochemistry which hides the true nature of the positive electrode/electrolyte activity.

### 5.1.1 – Metal-$O_2$ Cell Interface

In order to perform *in-situ* gas analysis of a metal-$O_2$ battery, a gas capture interface between the electrochemical cell and the mass spectrometer analysis chamber is required.

This is a challenge because all metal-$O_2$ applications are run at atmospheric pressure (or slightly positive), and must be open to the mass spectrometer analysis chamber that operates at ultra-high vacuum (UHV). Furthermore, the presence of this UHV must not interfere with the metal-$O_2$ operation, which typically makes use of volatile aprotic electrolytes. Thus, the following design requirements needed to be met:

- The pressure inside the mass spectrometer must be kept below a threshold of 6.7 x $10^4$ Pa to maintain "linear operation". Below this threshold pressure, intermolecular collisions are minimized to eliminate background noise. This allows for a direct correlation between the gas partial pressure and the ion current measured at the detector, which is necessary for quantification.
- The gas evolution during cell operation must travel from the cell (atmospheric pressure) to the mass spectrometer chamber (ideally 6.7 x $10^{-4}$ Pa) in a concentration that is quantifiable.
- The electrolyte vapours that enter the mass spectrometer must be kept to a minimum, for contamination of the chamber can greatly limit the lifetime of the ionizer and detector, and therefore give erroneous results for gas quantification.
- Operation must not interfere with the Li-$O_2$ cell chemistry.

To address these requirements, a sketch of the entrance chamber is shown in **Figure 5-1**. This design has three main components. *a*) the use of a carrier gas to expel the gases from the cell headspace, *b)* the cell construction itself, and *c)* a micrometer thin capillary at the interface between the mass spectrometer and the entrance chamber. The following section briefly outlines the rationale behind the proposed system, and how this design addresses the requirements mentioned previously.

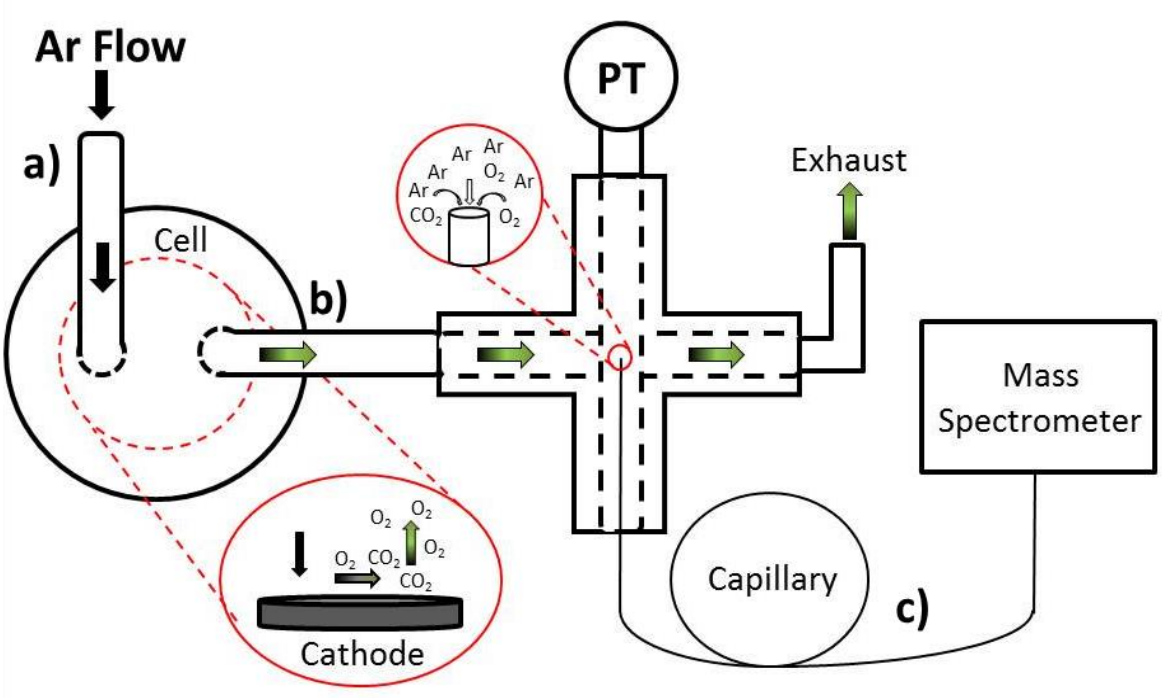


**Figure 5-1 -** Entrance chamber of the mass spectrometer. Ar gas (a) flows over the positive electrode to sweep the gaseous products towards a capillary (b). The capillary, which is attached to the mass spectrometer (c), samples the flow of gas and injects them into the mass spectrometer chamber, where the analysis of gas composition occurs.

One of the main challenges for the on-line measurement of evolved gases is the pressure requirement of the mass spectrometer to ionize, filter, and detect the gas molecules. To analyze the gases with a high degree of resolution, the pressure within the analysis chamber must be below 6.7 x $10^{-3}$ Pa, and ideally less than 6.7 x $10^{-4}$ Pa for quantitative analysis. Given that most cells operate at (or above) atmospheric pressure, the mass spectrometer entrance chamber must maintain a pressure difference between 1 atm (101325 Pa - atmospheric pressure) and the desired UHV while the gaseous products are continuously swept into the chamber. This is accomplished with the use of a 50 μm diameter x 10 cm length fused silica capillary positioned directly from the cell (~101325 Pa) to the mass spectrometer (~6.7 x $10^{-4}$ Pa). The decision to use a 50 μm diameter capillary is discussed in

subsequent chapters. This mass spectrometer design is a modified concept from Tsiouvaras *et.al*. who makes use of a crimped capillary of much smaller length (~10 mm) to control the "leak" of the gas into the mass spectrometer.[1] With the use of a μm-sized capillary, the large pressure difference is able to be maintained, with a final measured chamber pressure of $3.6 \times 10^{-4}$ Pa during operation. There is one issue, however, that arises with the use of a thin capillary; electrolyte condensation. This makes highly volatile, low boiling point solvents such as a DME or acetonitrile difficult to use for residual gas analysis.

To ensure proper gas collection during cell operation, an inert carrier gas is used to carry the evolved gas from the electrochemical cell to the mass spectrometer analysis chamber. Ultra-pure (5.0) Ar is the chosen carrier gas due to its chemical inertness, as well as its easily identifiable and non-interfering fragmentation patterns. In order to properly quantify the gases of interest, it is crucial to control the flow rate of the gaseous products leaving the electrochemical cell. Using a Bronkhorst EL-FLOW mass flow controller, the flow rate of Ar can be controlled within a measured error of 0.0055 mL/min. During cell operation, the argon flows over the positive electrode and sweeps the generated gases past the capillary that joins the electrochemical cell and the analysis chamber. The gas is then sampled at the tip of the capillary and carried into the analysis chamber where it undergoes rapid expansion, filling the analysis chamber. This type of operation makes the Li-$O_2$ cell an open system, and the flow of Ar through the cell causes solvent evaporation. This can lead to contamination of the analysis chamber, as well as the possibility that the cell becomes dry during operation. While some solvents are not volatile enough to cause concern (eg. dimethyl sulfoxide (DMSO), high-order glymes), some will most definitely cause issues (DME). This can be mitigated by the use of two separate streams of Ar. One stream acts as the carrier gas,

and the second stream acts as a dilution gas to reduce the concentration of solvent that enters the capillary. Thus, with the use of two separate, configurable flows of Ar, along with the narrow capillary interface, the evolved gases from the electrochemical cell enter the mass spectrometer in real time with minimal contamination of the instrument.

**Figure 5-2** is a low-level diagram that outlines the necessary hardware and software to operate the system. An Arbin galvanostat/potentiostat controls the electrochemical cell, and the Labview software (National Instruments) provided by Stanford Research Systems (SRS) is used to interface the user with the mass spectrometer. The mass spectrometer instrument is an RGA 200 from SRS. The Ar flow is controlled via the program Flow Read, which controls the flow controller itself (Bronkhurst EL-FLOW). The integration of all three

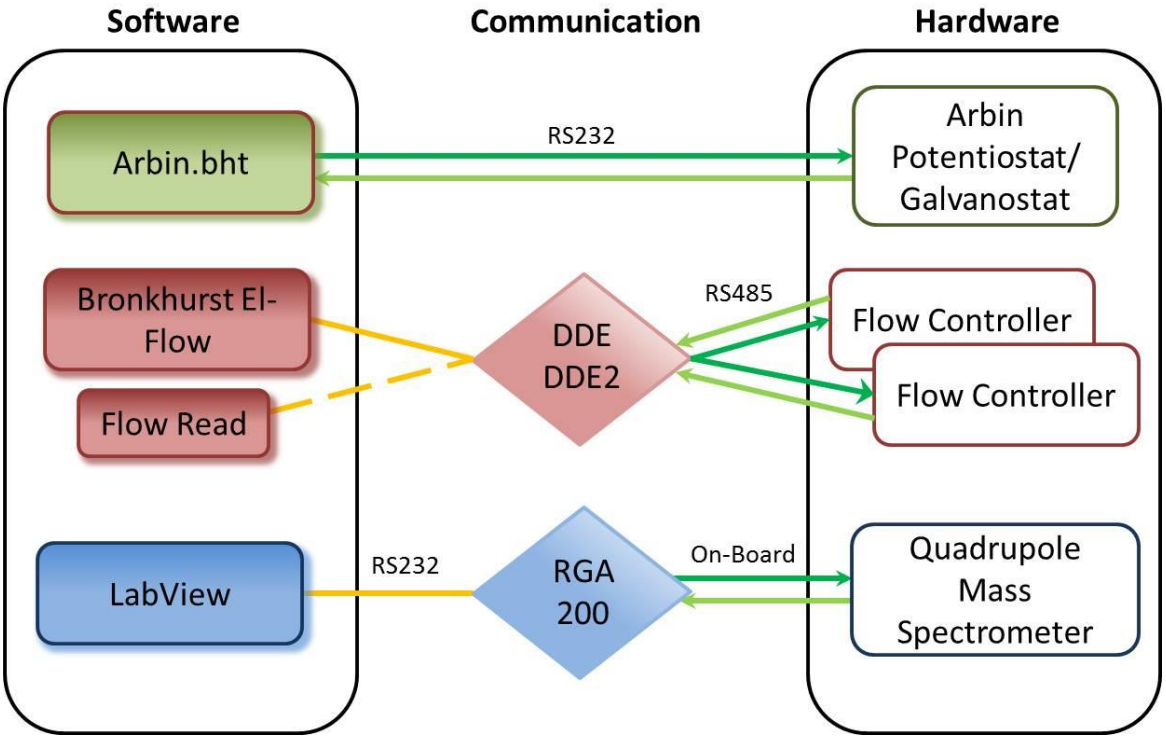


**Figure 5- 2 -** Software and hardware map for the operation of the mass spectrometer.

of these components is necessary for data collection. Post-processing and quantification of the data is performed with a self-created Mathworks® MATLAB script. This script can be found in **Appendix A**

### 5.1.2 – Calibration for Gas Quantification

The above design requirements allow for gas collection from an electrochemical cell, and quantification of the gas for direct relation to the electrochemistry. During operation, gases enter the mass spectrometer analysis chamber and ionize to a variety of fragments. These fragments reach the CDEM detector and produce ion currents corresponding to specific *m/z* values. Through the identification of primary molecular fragments and the various sister fragments, the identity of the original gas molecule is confirmed. A comment about different fragmentation patterns is made in subsequent sections. In order to convert ion current into useable units (for example, gas concentration), the data must undergo a transformation with the aid of calibration data. The importance of a base pressure below 6.7 x $10^{-4}$ Pa is so that the system operates in "linear" mode. That is, the ion current and the concentration of the target gas in the mass spectrometer chamber exhibits a linear relationship according to *equation* 5-1:

$$\boldsymbol{I_m = B_m + S_m[\mathrm{G}]} \qquad (equation\ 5-1)$$

Where $I_m$ is the measured intensity in units of ion current (A), $B_m$ the background (A), $S_m$ the calibration factor (A/ppm), and *[G]* the concentration of gas. Calibration curves with known gas concentrations are used to determine the values of $B_m$ and $S_m$, which allows the equation to be solved for values of *[G]*. An example of this calibration process is shown in **Figure 5-3** below. The two primary gases of interest in metal-$O_2$ systems are $O_2$ and $CO_2$; both are very

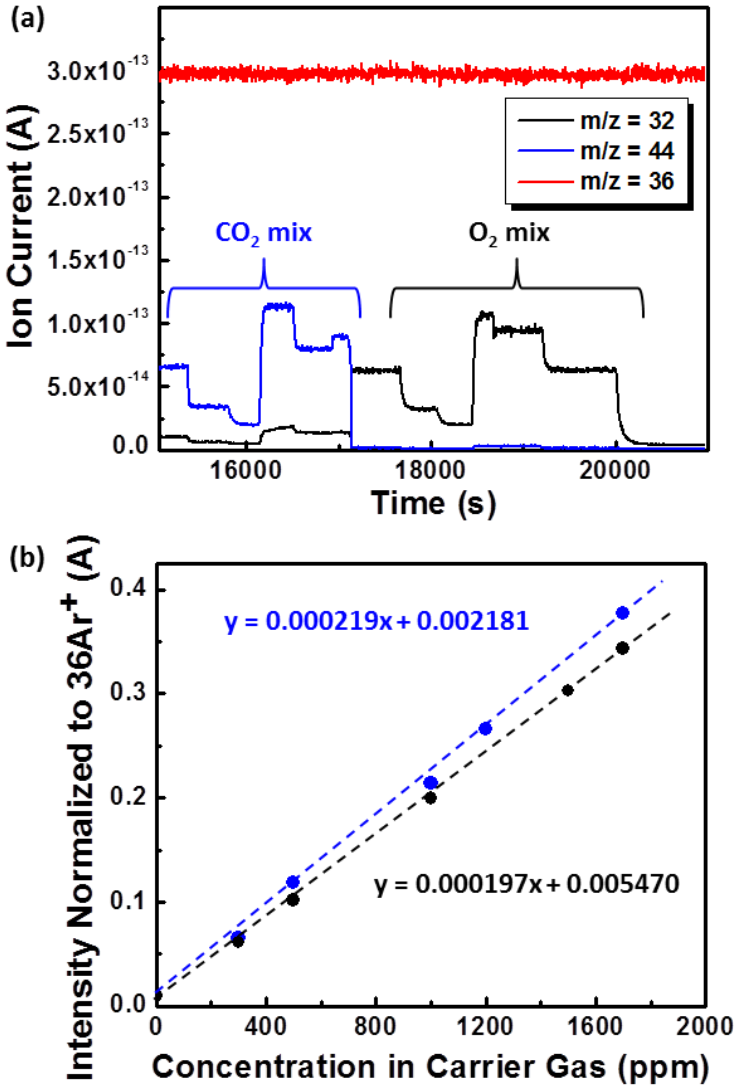


**Figure 5-3 –** Raw ion current values for known concentrations of $O_2$ (m/z = 32) and $CO_2$ (m/z = 44) (a). The plateaus correspond to different gas mixtures of 0-2000 ppm (w/ Ar balance). The ion current corresponding to each plateau is normalized to the Ar isotope background (m/z = 36) and plotted as a function of concentration (b) (blue = $CO_2$, black = $O_2$). The data is linearly fitted to obtain the calibration factors $S_m$.

important to determine the efficiency of metal-$O_2$ chemistry. Known mixtures of 2000 ppm $O_2$ (or $CO_2$) in Ar were used as calibration standards. One flow controller adjusted the flow of the calibration gas, while the second controller adjusted the flow of pure Ar. This allows

for alteration of the target gas concentration. The fraction of target gas in a known concentration produced a specific ion current once steady state was reached, (**Figure 5-3a)**. Typically, four to six different concentrations are collected. These known concentration values are then plotted with respect to ion current, as shown in **Figure 5-3b.** The concentration of target gas is linearly proportional to the measured ion current. All ion current values obtained are normalized to the m/z = 36 of Ar (a tertiary fragment of isotope Ar that is in similar abundance to the target gases of interest). This is to normalize the target gas values to global changes of total pressure within the mass spectrometer as a result of temperature, non-uniform vacuum levels etc., that can occur during measurement. From this linear relationship, the slope can be determined, which corresponds to the calibration factor $S_m$. The ion current produced as a function of time, along with the flow rate of the carrier gas ($Q_{Ar}$), is used to determine the gas evolution rate from the metal-$O_2$ cell, and ultimately the total volume of evolved gas. This is determined with the use of *equations 5-2* and *5-3*:

$$\frac{\mathbf{dG}}{\mathbf{dt}} = \frac{[\boldsymbol{G}]\ (\boldsymbol{ppm})}{\mathbf{1}\ \boldsymbol{x}\ \mathbf{10^{6}}} * \mathbf{4.09}\ \boldsymbol{x}\ \mathbf{10^{-5}} \left(\frac{\boldsymbol{mol}}{\boldsymbol{mL}}\boldsymbol{Ar}\right) * \boldsymbol{Q_{Ar}}\ (\boldsymbol{mL\ Ar/min}) \quad (equation\ 5-2)$$

$$\int_{ti}^{tf} \frac{\boldsymbol{dG}}{\boldsymbol{dt}}\boldsymbol{dt} = \boldsymbol{O_2(mols)} \quad (equation\ 5-3)$$

where *[G]* refers to the concentration of gas, and *dG/dt* is the gas flow rate.

A comment should be made about the fragmentation of gas molecules. Upon ionization, gas molecules fragment into a variety of charged species (m/z values). Each molecule gives rise to a specific fragmentation pattern, and the fraction of specific m/z values is well known and documented.[2] While the calibration procedure discussed above utilizes only a single m/z value per gas molecule generated (the primary, most abundant fragment),

tracking the ion signals of secondary and tertiary fragments allows for validation of the identity of the gas being analyzed. For example, $O_2$ fragments into m/z values of 32, 16, 34, in a molar abundance of 89.2 %, 10.4%, and 0.35% respectively.[2] Thus, when monitoring the $O_2$ evolution from a cell, the m/z = 32 value used for quantification is first compared to the m/z = 16 value to ensure the proper ratio of ~90:10 is met. If this ratio strays during operation, this indicates that another gas is contributing to the m/z = 32 ion current. These can occur from hydrocarbon fragments as a result of electrolyte evaporation, and or air leaks during operation. Hence, during calibration and cell operation, numerous fragmentation patterns are monitored as a means to validate the identity of the target gas. Corrections are made where appropriate to remove any excess signal that may arise during operation.

For Li-$O_2$ cells, I want to observe both the consumption and evolution of gases during Li-$O_2$ cell operation. The above procedure focuses on the quantification of $O_2$ and $CO_2$ during cell charge. This is important as it correlates the value of oxygen to the cell electrochemistry, providing a metric of oxidation efficiency. However, the mass spectrometer is also capable of monitoring the oxygen consumption during cell discharge, which allows for determination of the efficiency of ORR. To monitor $O_2$ consumption, a small amount of $O_2$ in Ar (max 5% vol) flows over the cell. The drop in the oxygen level overtime is monitored and quantified, and correlated to the electrochemistry to determine the efficiency of cell ORR.

This mass spectrometer, of the design outlined above, is an excellent diagnostic tool to determine both the ORR and OER capabilities of various positive electrode materials and electrolyte combinations. The flexibility in both the design of the experiments and the

acquisition of the data allows for a broad range of analysis that can provide a wealth of information about the critical stages of Li-$O_2$ cell operation.

### 5.1.3 – Effect of Capillary Diameter

As stated previously, in order to properly quantify the volume of gas and ensure the CDEM detector life-time is not prematurely shortened, the pressure within the analysis chamber must be kept below 6.7 x $10^{-4}$ Pa. Thus, a thin capillary is utilized to maintain this pressure difference from the entrance chamber to the analysis chamber, while still allowing efficient collection of the generated gas species. A compromise must be made between the sampling rate of the gas and the base pressure of the analysis chamber. To determine the proper capillary size, three different capillaries of the same length (30 cm) but different inner diameter sizes (50 μm, 100 μm, and 150 μm) were evaluated based on the pressure difference they could maintain (ΔP) and the maximum sampling rate of the gases evolved from the Li-$O_2$ cell ($Q_{in}$). To determine these values, each capillary was dried prior to installation at 100 °C, and was left attached to the mass spectrometer overnight to equilibrate pressures and ensure no outgassing was coming from the capillary. The base pressure of the analysis chamber was measured with a Bayard-Albert ionization gauge. $Q_{in}$ was determined through the use of a silicon oil balance. A small vial of silicon oil was added to one end of the gas exit port and connected with clear tubing to make an entirely closed system. When the Ar flow ($Q_{Ar}$) was set to 0 mL/min, the vacuum would displace the oil at a specific rate equal to that of the sampling rate of the capillary. This sampling rate, deemed $Q_{in}$, is entirely a function of the analysis chamber vacuum and the diameter of the capillary. The Ar flow was then empirically set to specific values so that the silicon oil would become stagnant in the center of the tubing. At this point, $Q_{Ar} = Q_{in}$. **Table 5-1** summarizes these results.

**Table 5-1** - Experimental determination of the sampling rate as a function of the capillary diameter, and corresponding base pressure of the analysis chamber when the capillary is attached.

| Inner Diameter (µm) | $P_{Base}$ (Pa) | $Q_{in}$ (mL/min) |
|---|---|---|
| **50 µm** | $2.70 \times 10^{-4}$ | 0.15 |
| **100 µm** | $4.55 \times 10^{-3}$ | 0.75 |
| **150 µm** | $2.70 \times 10^{-2}$ | 3.75 |

It is expected that the data follows very closely with Poiseuille's law (*equation 5-4)*:

$$\Delta P = \frac{128 \mu L Q}{\pi d^4} \qquad (equation\ 5-4)$$

where ΔP is the pressure difference, $L$ is the length of the capillary (30 cm), $\mu$ is the dynamic viscosity, $Q$ is the volumetric flow rate, and $d$ is the diameter of the capillary. Poiseuille's law dictates that the flow rate of a low viscosity fluid through a cylindrical pipe undergoing laminar flow is dependent on two factors: the pressure difference between both ends of the pipe, and the viscous resistance. The viscous resistance is inversely related to the inner diameter of the capillary to the fourth power. Thus, for our purposes, since the length $L$ and the dynamic viscosity $\mu$ are constant for the different capillaries tested, the following linear relationship applies:

$$d^4 \propto \frac{Q}{\Delta P} \qquad (equation\ 5-5)$$

A plot of $d^4$ vs. Q/ΔP exhibits the expected linear relationship (**Figure 5-4**). Based on the defined limits of maintaining a base pressure of $6.7 \times 10^{-4}$ Pa, this would

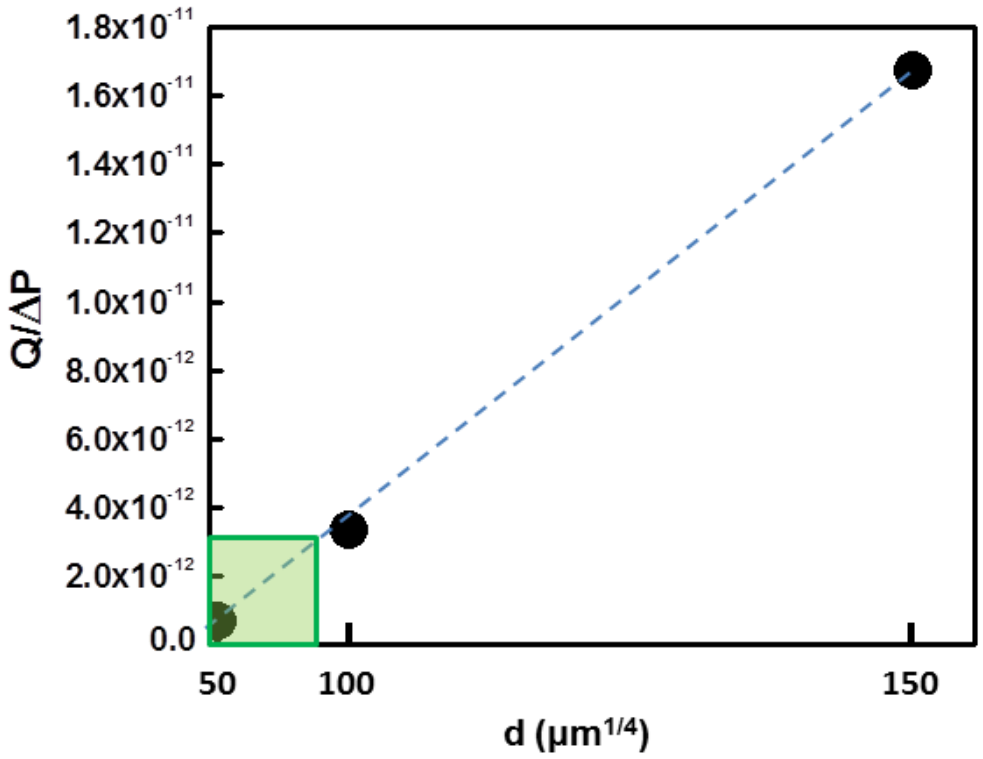


**Figure 5-4 -** Plot of Q/ΔP vs. the capillary diameter ($d^4$). The linear relationship observed between these values indicates that the gas flows within a laminar flow regime and follows Poiseulle's Law. The green box shows the maximum tolerance acceptable for proper quantification of the evolved gases (d < 87 μm).

require an inner diameter of d < 87 μm. From the commercially available capillaries that fall within the required tolerance, a capillary of inner diameter d = 50 μm was chosen for use in the system.

### 5.1.4 – Time Lag and Pressure Stabilization

Apart from the necessary equipment parameters to maintain the required base pressure and ensure gas quantification, one must also be aware of the time lag that occurs between the evolution of the gas at the cell, and the time it takes for the gas to reach the ion detector. The main source of this time lag is the flow rate chosen to sweep the gases from the

cell to the mass spectrometer. Not taking this lag into account during experiments produces quantification errors. In order to investigate this time lag, the oxygen was flowed through the mass spectrometer at a known concentration. The concentration of oxygen was then changed and left to equilibrate with Ar until a constant flow rate was reached. The time it takes for the signal to reach equilibrium (as evident through a flat plateau) is the lag constant τ. The lag constant was collected for various concentrations in order to obtain an average. The total flow rate for this measurement was kept to a maximum (10 mL/min) to ensure that any lag observed is a result of the time it takes for the analysis chamber concentration to reach equilibrium. The results are shown in **Figure 5-5** below. The results of this collection are

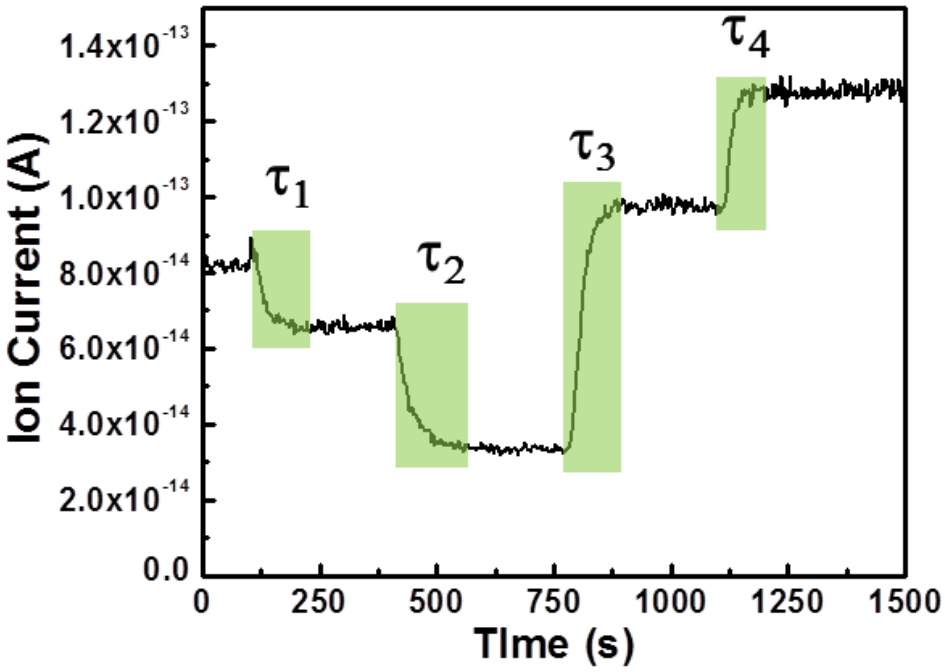


**Figure 5-5 -** Variation of oxygen concentration with respect to time. The time constants, denoted as τ, represent the time it takes for oxygen equilibrium to be reached as a result of the oxygen concentration change at the gas collection point.

$\tau_1$ = 125 s, $\tau_2$ = 145 s, $\tau_3$ = 120 s and $\tau_4$ = 110 s. Based on the visible increases and decreases of the $O_2$ level, there is clearly some asymmetry to the changes of the $O_2$ partial pressure in the analysis chamber. Specifically, more time lag occurs to lower the partial pressure of oxygen than to increase the partial pressure of oxygen. Furthermore, the lag is clearly a function of the change magnitude, for smaller changes in $O_2$ partial pressure require less time for the chamber to reach equilibrium.

This issue of asymmetry does not play a significant role in the error of the oxygen evolution over the course of an actual cell measurement. To understand the impact this time lag has on the accuracy of the measurement, a maximum loss scenario must be investigated. Assume a Li-$O_2$ cell is charged at 500 uA (the upper limit of current rate for most Li-$O_2$ studies presented here), and assume a time lag of 180 s (a greater value than was determined experimentally). This equates to a total of 0.046 μmol of $O_2$ that would not be detected (assuming a perfect 2 $e^-/O_2$ oxidation of $Li_2O_2$). If this occurs in a cell that has been charged to 0.5 mAh, the loss in oxygen would equate to approximately 5% of the total measured oxygen. This is a maximum loss scenario, and in most situations, including the work presented in *Section 5.2* and *Section 6.1*, the cells would be charged for longer periods of time, and the oxidation current would be smaller. On average, the loss in oxygen is only between 0.5 – 1.5% of the total value. This value is insignificant, and can be easily corrected, as has been done so for results that have been published.

### 4.2.1 – Electrochemical Studies

The electrodes used in this study were prepared from a slurry which contained Ketjen black (KB - carbon powder): catalyst ($Co_3O_4$/RGO): Li-Nafion: DBP in a 1:0.5:1.5:3.3 mass ratio. The Li-Nafion was added using a solution of 3.43 wt% Li-Nafion in NMP. An

additional 0.5 mL of NMP was added to the slurry after all constituents were added, and then the slurry was then left to stir overnight to ensure homogeneity. The contents were cast onto a Celgard 2500 separator and left to dry at 60 °C for 3 hours. The film was then punched into 0.636 $cm^2$ discs, and dried at 100 °C under vacuum overnight to ensure all moisture was removed from the electrode. The total mass of the electrode active material was between 0.1 mg – 0.2 mg. The conductivity of the dried electrodes was measured using a 4-point probe technique with an applied current equal to that applied in Li-$O_2$ cells. The average sheet resistance for KB electrodes was 5,000 Ω/sq, and 15,000 Ω/sq for the $Co_3O_4$/RGO on KB electrode.

Catalyst inks were prepared by homogeneously dispersing the prepared $Co_3O_4$/graphene catalyst and/or KB carbon in 1 mL of NMP solution containing Li-Nafion. Dispersions were prepared with a Li-Nafion:carbon mass ratio of 1:2. A glassy carbon electrode (Pine Instruments Co., 0.196 $cm^2$) was coated with the ink and dried at 100 °C for 24 hours to obtain coating loads of 125 μg carbon/$cm^2$. The electrochemical experiments were performed in an Ar-filled glovebox, with a three-electrode cell gas-flow enabled setup consisting of the coated glassy carbon electrode functioning as the working electrode and Li foil as both the counter and reference electrodes. Chronoamperometry (CA) and linear sweep voltammetry (LSV) experiments were controlled with a VMP3 potentiostat and EC-Lab® software (Bio-Logic Science Instruments). The electrolyte used was 0.1 M $LiPF_6$/TEGDME in all cases, and all experiments were performed at room temperature.

Non-aqueous electrochemical experiments were performed in a Li–$O_2$ cell of modified Swagelok design with 1M $LiPF_6$ (battery grade, dry, 99.99% trace metals basis, Techno Semichem, Korea) in distilled TEGDME (<5 ppm $H_2O$) as the electrolyte. Cells

were assembled in an Ar filled glovebox with a lithium metal negative electrode, three porous separators (millipore glass fibre), and a porous carbon-based membrane supported on an aluminum mesh current collector which served as the positive electrode. The separators were presoaked in electrolyte, and an additional 80 μL of electrolyte was added during cell assembly. The cells were encased in a glass housing, and purged for 30 minutes with $O_2$ (99.994% pure $O_2$, Airgas, $H_2O$ < 2 ppm) and subsequently sealed to the ambient atmosphere. The amount of oxygen available to the $O_2$ electrode in the Li–$O_2$ cells within the 270 ml glass housing was at least 50 fold higher than that required for discharging to a capacity of 5000 mA h $g^{-1}$. The cells were rested at open circuit for 6h before testing. The Li–$O_2$ cells were tested galvanostatically using a current density of 140 mA $g^{-1}$ (normalized to the weight of the carbon) upon discharge from open circuit to a lower voltage cut-off of 2.0 V vs. $Li/Li^+$.

## 5.2 – Positive Electrode Activity

### 5.2.1 – Pre-Filled Positive Electrodes

This section will focus on the use of mass spectrometry to determine the oxidation activity of various positive electrode materials towards $Li_2O_2$ oxidation. As stated in previous sections, there are a great deal of electrode and electrolyte degradation reactions during cell discharge/charge. One metric that represents the $Li_2O_2$ charge efficiency and the degree of side reactions is the $e^-/O_2$ ratio. In a 100% efficient reaction, the charge efficiency of the Li-$O_2$ cell is expected to be 2.0 $e^-/O_2$. Alteration from this value indicates parasitic reactions. I use electrodes loaded with non-electrochemically formed $Li_2O_2$ to evaluate the oxidation activity of the various positive electrode materials. This removes any degradation reactions that may arise during electrochemical discharge, and allows for isolation of the oxidation process. These decomposition products that form on discharge create complications on cell

charge, primarily due to the potential required to oxidize these products. These reactions ultimately effect charge efficiency, and negatively impact the $e^-/O_2$ ratio. In this section, I will demonstrate how mass spectrometry can be used to identify oxidation activity of three different positive electrode materials (Carbon, TiC, and $Mo_2C$).

#### 5.2.1.1 – Pre-Filled Positive Electrode Preparation

To prepare positive electrodes filled with $Li_2O_2$, a known amount of $Li_2O_2$ was measured and mixed with a powder of the desired active material in a ratio between 1:4 and 1:8 mass amounts $Li_2O_2$:active material. This mass fraction is dependent on the molar mass of the active materials because the mechanical integrity of the electrode was an issue with high mass (eq. TiC) materials and large fractions of $Li_2O_2$. The contents were ground with a mortar and pestle in a non-aggressive manner so as to not induce a spontaneous combustion caused by the strong oxidizing nature of the $Li_2O_2$. A suspension of 20 mg per 500 μL of PTFE in isopropanol was added to the ground powder mixture to make a thick slurry. This slurry was mechanically pressed onto a stainless steel current collector, and dried under vacuum overnight to remove the isopropanol. The positive electrode was weighed to determine the mass of $Li_2O_2$ that comprised each individual electrode.

#### 5.2.1.2 – Carbon Prefilled Positive Electrode

Carbon is an ideal positive electrode material for the Li-$O_2$ battery. Its high surface area, low cost, and low mass make it ideal for maximizing the gravimetric energy density of the cell while minimizing financial costs. A carbon electrode was prepared with a known amount of $Li_2O_2$, and charged at a current rate of 150 uA (75 uA/$cm^2$) in 1M LiTFSI/TEGDME electrolyte. The electrochemical curve and corresponding gas evolution is shown in **Figure 5-6** below. The capacity of the cell is normalized to the expected capacity

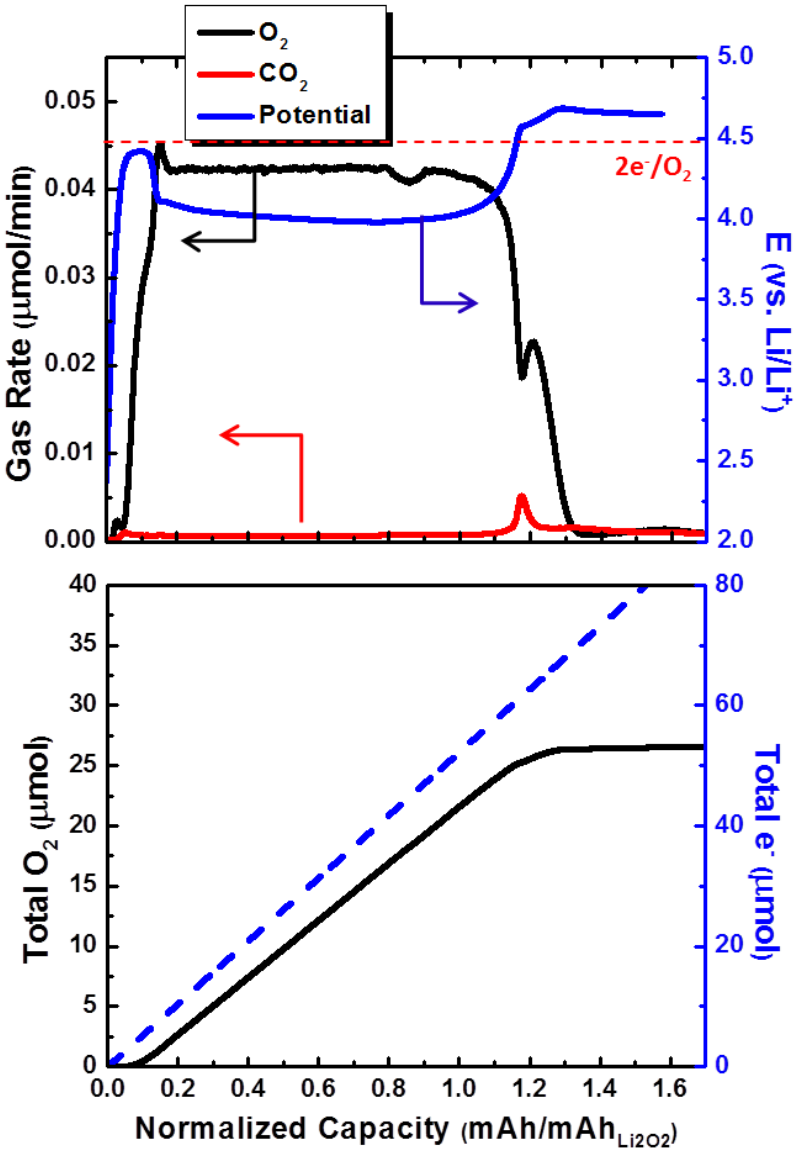


**Figure 5-6 -** (a) Oxidation profile and gas evolution as a function of capacity, and (b) total accumulated oxygen for $Li_2O_2$/carbon electrode composite.

based on complete oxidation of the known quantity of $Li_2O_2$. Thus, a normalized capacity of 1 mAh/mAh$_{Li2O2}$ corresponds to the capacity expected of a 2 $e^-/O_2$ oxidation of $Li_2O_2$. Both the $O_2$ and $CO_2$ gas evolution were monitored during the entirety of cell charge. The voltage profile for the oxidation of $Li_2O_2$ has three clearly defined regions. The first region is the

initial plateau at ~ 4.4 V, which accounts for 15% of the oxidation capacity. No $O_2$ or $CO_2$ accompanies this initial plateau. Following this, the voltage decreases to ~3.9 V, and continues at this voltage for a majority of oxidation. This plateau is accompanied by a spike in the $O_2$ evolution, followed by a plateau at a rate averaging 0.042 μmol/min. This is very close to the expected 0.046 μmol/min for the oxidation of $Li_2O_2$ via a 2 $e^-/O_2$ process. Finally, the oxidation of $Li_2O_2$ concludes with a sharp rise in the voltage at a capacity beyond that expected from the mass of $Li_2O_2$ (~1.2 $mAh/mAh_{Li2O2}$). This is accompanied by a sharp decrease in the $O_2$ evolution rate, along with a small amount of $CO_2$ evolution. At 4.7 V clear electrolyte oxidation occurs with no gas evolution. The total moles of $O_2$ evolved in this

cell equates to 26.1 μmol, which is 88% of the expected 29.8 μmol of $O_2$ based on the mass of $Li_2O_2$. The total $e^-/O_2$ ratio for the entire charge process is 2.45.

This result indicates that the oxidation of the commercial $Li_2O_2$ is rather facile, and is relatively efficient in terms of oxygen evolved per molecule of $Li_2O_2$. However, for two reasons, the voltage profile of $Li_2O_2$ oxidation warrants further discussion. First, the initial charge overpotential is peculiar. Consider that prior to $Li_2O_2$ oxidation, the oxidation of an unknown species must occur to give rise to this ~4.4 V initial voltage. This species not only requires a large overpotential to oxidize, but it must also be oxidized before any $Li_2O_2$ oxidation occurs, evidenced through the $O_2$ evolution onset after this initial charge plateau. There are two possible sources of this charge plateau. One is that it stems from the presence of $Li_2CO_3$ that forms at the $Li_2O_2$/carbon interface during positive electrode preparation. This carbon reactivity has been commented on in the literature.[3,4] This $Li_2CO_3$ creates an interfacial layer that requires a large overpotential to initially oxidize, which then allows electrons to reach and oxidize the $Li_2O_2$ at a lower potential. The second possibility is that

this overpotential arises from impurities present in the $Li_2O_2$. Iodometric titration determined that the purity of commercial $Li_2O_2$ was only 88%, with the resulting 12% most likely being contamination from $Li_2CO_3$ or LiOH that resulted from air exposure during manufacturing and storage. These impurities, which would most likely be present on the surface of the $Li_2O_2$, would require a large overpotential to charge before the fresh $Li_2O_2$ underneath can be oxidized. Such impurities can account for the disagreement between the experimental and theoretical $e^-/O_2$ value, for some charge would be lost due to the presence of these impurities. If these contaminates are present, it is expected that the complete oxidation of $Li_2O_2$, being 88% pure, gives rise to 26.1 μmol $O_2$. The observed amount from mass spectrometry is 26.1 μmol. Hence, it appears that complete oxidation of $Li_2O_2$ can be accounted for based on the total $O_2$ evolved (with a high overpotential). However, the 2.45 $e^-/O_2$, and clear presence of $CO_2$ implies $Li_2O_2$ oxidation is not 100% efficient.

If $Li_2CO_3$ is present, one would expect to see $CO_2$ evolution accompanying this initial charge voltage increase. Careful inspection of **Figure 5-6** reveals that a small volume of $CO_2$ is present during this initial charge step. However, it is unknown whether this $CO_2$ arises from $Li_2CO_3$ inherent in the $Li_2O_2$, or is a product of either the $Li_2O_2$/electrolyte, or the $Li_2O_2$ carbon interface. **Figure 5-7** helps to reveal the origin of $CO_2$ evolution for $^{13}C$ pre-filled positive electrodes. This $^{13}C$ electrode allows for the distinction between $CO_2$ generated from the oxidation of decomposition products originating from the electrolyte ($CO_2$, m/z = 44) and from the carbon positive electrode ($^{13}CO_2$, m/z = 45). The cause of these reactions and the formation of $Li_2CO_3$ (and other carboxylate products) has been discussed previously.

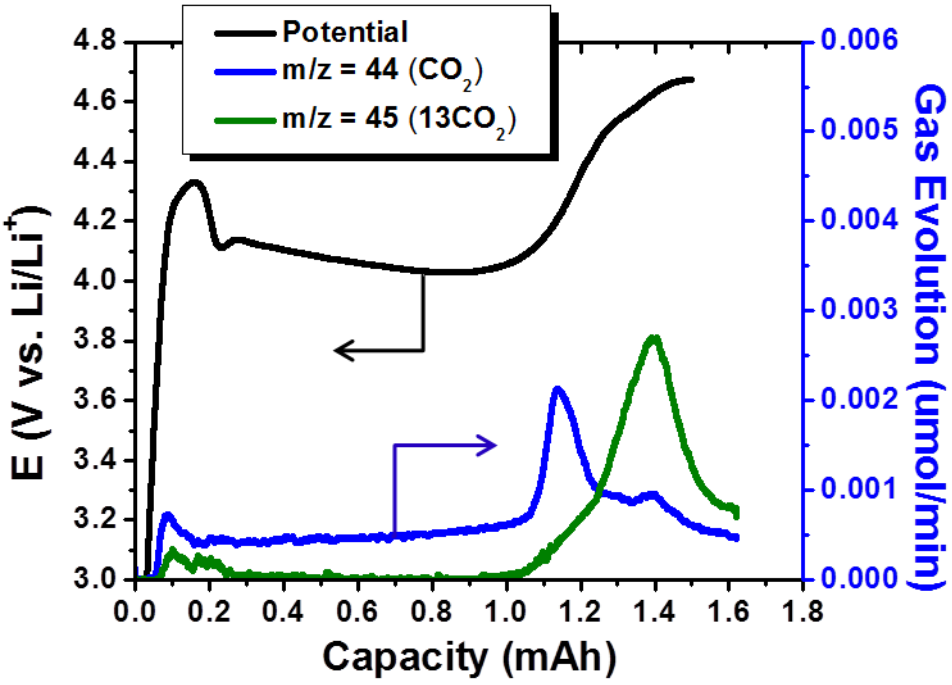


**Figure 5-7** - Oxidation potential profile as well as $CO_2$ gas evolution for a $Li_2O_2/^{13}C$ cathode composite. The two $CO_2$ signals correspond to electrolyte based Li-carboxylates (blue - electrolyte) and $^{13}C$-based Li-carboxylates (green).

Both $CO_2$ and $^{13}CO_2$ evolution is evident upon oxidation of $Li_2O_2$ on $^{13}C$ electrodes in 1M LiTFSI/TEGDME (**Figure 5-7**).

At the initial voltage increase, suspected of being the oxidation of $Li_2O_2$ side products, both $CO_2$ and $^{13}CO_2$ are present. The evolution of $CO_2$ (m/z = 44) results from oxidation of Li-carboxylates from either $Li_2O_2$/electrolyte reactivity, or from the carboxylate present in the impure $Li_2O_2$. The evolution of $^{13}CO_2$ (m/z = 45) is from the oxidation of carbonates at the $Li_2O_2$/carbon interface. Integration of this initial $CO_2$ amount (to a capacity of 0.3 mAh) reveals a $CO_2$:$^{13}CO_2$ ratio of 4:1. Following this initial $CO_2$ spike, there is a lower, but constant, rate of $CO_2$ evolution throughout the entire charge plateau. The $^{13}CO_2$ evolution,

however, completely ceases. It is highly likely that this $CO_2$ evolution is a result of the oxidation of contaminants present within the $Li_2O_2$ itself, which become oxidized in congruence with the oxidation of $Li_2O_2$. In comparison to the evolution rate of $O_2$ shown in **Figure 5-6,** the $CO_2$ evolution is rather minor, implying that a majority of the charge current goes towards oxidation of $Li_2O_2$. Finally, at the end of charge, the rise in cell voltage is accompanied by the evolution of both m/z = 44 and m/z = 45 gases, and thus represents the oxidation of what are most likely carboxylate products that have formed from either the reaction of $Li_2O_2$ with the glyme electrolyte, or from the decomposition products that have formed electrochemically on charge.

#### 5.2.1.3 – TiC Prefilled Positive Electrode

From the results observed with the carbon positive electrode it is clear the stability of the $Li_2O_2$/carbon interface is a negative issue. To investigate the oxygen evolution of $Li_2O_2$ oxidation on a more stable positive electrode surface, TiC was used. TiC is a highly effective positive electrode material for the Li-$O_2$ cell in DMSO-based electrolytes, exhibiting exceptionally low overpotentials and good capacity retention.[5] To confirm this activity, a TiC positive electrode was prepared in a similar manner to that of the carbon positive electrode, and charged under the same conditions in 1M LiTFSI/TEGDME electrolyte. **Figure 5-8** compares the electrochemical charge curve and $O_2$ evolution profile of the TiC to the previous results for the carbon positive electrode. A difference in the electrochemical charge potential is evident (**Figure 5-8a)**. The initial voltage spike observed with the carbon electrode is nearly absent for TiC. I previously attributed this initial charge overpotential to the oxidation of both electrolyte-based and positive electrode-based decomposition products, but this initial charge overpotential is most likely the result of decomposition products that

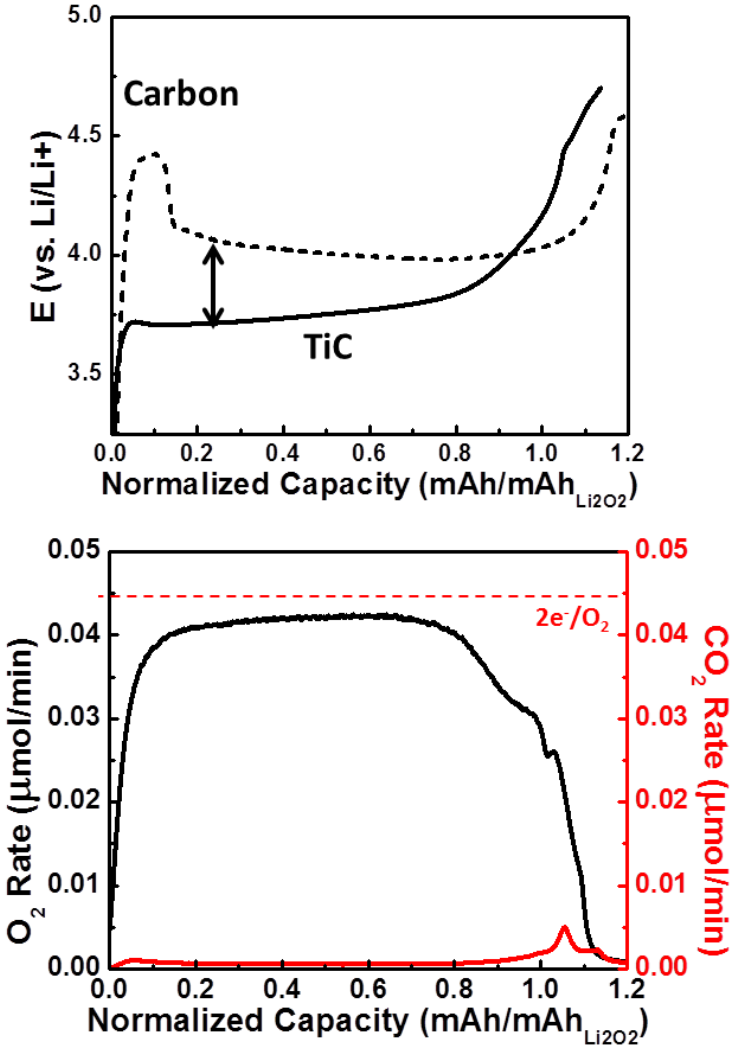


**Figure 5-8 -** (a) Potential oxidation curve for $Li_2O_2$ preloaded onto TiC (solid line), and the $Li_2O_2$ loaded on carbon for comparison (dotted line). The TiC exhibits a much more featureless charge profile, with a clear absence of the initial charge oxidation plateau, as well as lower charge overpotential for $Li_2O_2$ oxidation compared to carbon. (b) $O_2$ and $CO_2$ evolution profile corresponding to the oxidation of $Li_2O_2$ on TiC.

form at the $Li_2O_2$/carbon interface because the reaction that produces $Li_2CO_3$ does not happen on a TiC surface. These observations have been documented in another publication to which I am an author, and expanded upon in greater detail.[6] In this publication, it is shown that TiC reacts with $Li_2O_2$ to form a small interfacial layer of $TiO_{2-x}$. This layer is only a few nanometers thick, which is essential to ensure $e^-$ transfer still occurs on the electrode surface.

Furthermore, this thin $TiO_{2-x}$ surface acts as a passivation layer to prevent further oxidation of the bulk material. Hence, no $Li_2CO_3$ is formed at the interface, and the initial oxidation activity proceeds directly to oxidation of $Li_2O_2$. A similar phenomenon has been observed in other metallic titanium oxide materials, such as $Ti_4O_7$.[7] This can also explain the observed difference in the normalized capacity between carbon and TiC. In the case of carbon, the charge oxidation exceeds 1 $mAh/mAh_{Li2O2}$.. This is due to the initial current oxidizing $Li_2CO_3$, and charge can be considered "wasted" when trying to obtain efficient $Li_2O_2$ removal. In the case of TiC, the oxidation completes very near the expected 1 $mAh/mAh_{Li2O2}$.

Apart from initial charge oxidation, the rest of the $Li_2O_2$ oxidation process appears to be very similar to that of carbon. The $O_2$ evolution of both carbon and TiC positive electrodes is near identical, and gives rise to a flat oxygen evolution profile that equates to 2.45 $e^-/O_2$ on completion of charge (**Figure 5-8b)**. The charge overpotential for TiC, however, is slightly lower than that observed for carbon, with a nominal voltage of 3.7 V observed compared to 4.0 V for the carbon positive electrode. This is most likely due to the absence of an insulating layer of $Li_2CO_3$ at the $Li_2O_2$/TiC interface, and hence the impedance layer is completely absent (or is present as a thinner, more electronically conducting $TiO_{2-x}$ interfacial layer). Furthermore, the $CO_2$ evolution profile is almost identical to that of carbon. That is, there is an initial spike of $CO_2$, followed by a steady evolution of $CO_2$ until the onset of voltage increase. Thus, it is clear that $Li_2CO_3$ present throughout the bulk $Li_2O_2$ undergoes oxidation, with a final $CO_2$ spike most likely from the oxidation of carboxylate products that form on the $Li_2O_2$/C interface. Hence, with mass spectrometry, a clear difference in the positive electrode stability towards $Li_2O_2$ is demonstrated.

The use of TiC with preloaded $Li_2O_2$ also allows us to study the effect of other electrolytes, such as DMSO. The use of DMSO as an electrolyte for the Li-$O_2$ cell is a controversial topic within the metal-$O_2$ battery community. Mentioned previously, DMSO utilizing oxidation resistant positive electrodes such as nanoporous gold (NPG) and TiC exhibits remarkable electrochemical performance with low overpotentials and excellent cycling retention, and to date is one of the best performing electrolyte/positive electrode combinations in terms of charge efficiency and cycling capabilities.[8] However, contrary reports on the stability of DMSO, and the inability to replicate previous results, have made the once exciting results suspect.[9,10]

A simple experiment with preloaded positive electrodes, and a comparison to that of TEGDME, can provide insight into not only the stability of DMSO as an Li-$O_2$ battery electrolyte, but also the necessity of mass spectrometry as an analysis tool to probe the Li-$O_2$ chemistry. **Figure 5-9** below reveals the results for $Li_2O_2$ on TiC charged in DMSO, and a direct comparison to TiC charged in TEGDME. It should be noted that due to the instability of DMSO towards metallic lithium, $LiFePO_4$ was used as the negative electrode. For comparison purposes, the voltage was shifted and represented as vs. $Li/Li^+$ based on the observed potential for lithiation/delithiation of $LiFePO_4$ vs. Li (~ V = 3.45 V). This figure shows the electrochemical charge profile (**Figure 5-9a)** and corresponding integrated values of $O_2$ evolution (**Figure 5-9b)**. The electrochemical charge profile is similar among the two electrolytes, with the DMSO electrolyte exhibiting a slightly higher charge overpotential compared to that of TEGDME. The integrated oxygen evolution profile is shown in **Figure**

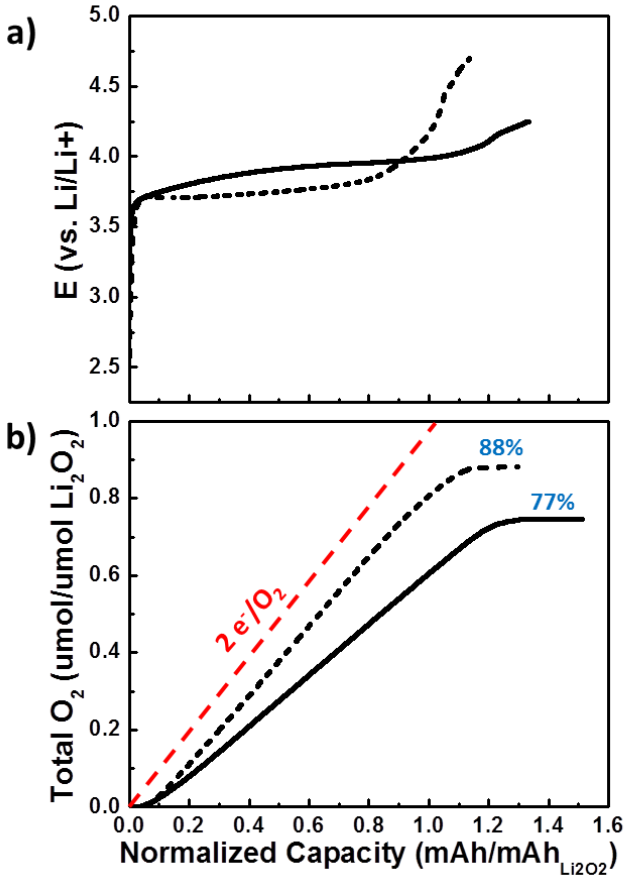


**Figure 5-9** - (a) Oxidation potential of prefilled $Li_2O_2$/TiC cathodes charged in 1M LiTFSI/DMSO electrolyte (solid line) and 1M LiTFSI/TEGDME electrolyte (dotted line). The corresponding accumulation of oxygen on charge is shown in (b), with numerical values indicating the percentage of total oxygen evolution as a function of the theoretical amount based on the total mass of $Li_2O_2$ prior to charge.

**5-9b.** The volume of evolved $O_2$ is significantly less for DMSO than for TEGDME (by ~10%). The rate of $O_2$ evolution is also less, as seen by the shallower slope of the integrated oxygen profiles. Mentioned previously, for TEGDME this value is 2.45 $e^-/O_2$, whereas for DMSO, the $O_2$ evolution rate averages 2.80 $e^-/O_2$.This indicates that on charge, other parasitic reactions must occur that give rise to greater charge inefficiencies. The amount of $CO_2$ evolution generated, which is not shown, is equivalent for both electrolytes in this case.

For DMSO, $Li_2O_2/O_2^-$ reactivity has also been shown to be the source of a large variety of sulphone and sulphoxide based decomposition products.[11,12] While these results demonstrate that DMSO may not be an ideal electrolyte for the Li-$O_2$ battery, it is definitely not completely inadequate as an electrolyte for cell oxidation.

This study, however, fails to recognize the impact that the ORR has on DMSO stability. As mentioned previously, most electrolyte instabilities occur due to the reactivity of $O_2^-$ that forms on cell discharge. Hence, while the study presented here is an ideal tool to investigate the electrolyte stability towards $Li_2O_2$ and the charge oxidation, other reports have demonstrated the extreme instability of DMSO towards $O_2^-$ [10,11] and instabilities against a carbon positive electrode.[9] Hence, combined with the poor oxidation characteristics of DMSO compared to TEGDME presented above, I cannot recommend DMSO be utilized as an electrolyte for future studies in the Li-$O_2$ battery.

### 5.2.2 – Electrochemically Discharged Electrodes

In all of the previous studies discussed thus far, preloaded positive electrodes were used to investigate the activity of specific active materials towards $Li_2O_2$ oxidation, with mass spectrometry demonstrated as an analytical tool to determine the electrode material's OER efficiency. This was done to study the inherent bulk catalysis of large $Li_2O_2$ particles from the positive electrode surface, without any contributions from parasitic reactions that occur during the discharge process. However, while the following studies do provide insight into positive electrode activity and identify critical issues with respect to cell component stability, the impact of the electrochemical discharge process cannot be ignored. A comparison of the charge voltage profile for pre-filled and electrochemically discharged positive electrodes is made in **Figure 5-10**. These results compare the oxidation of

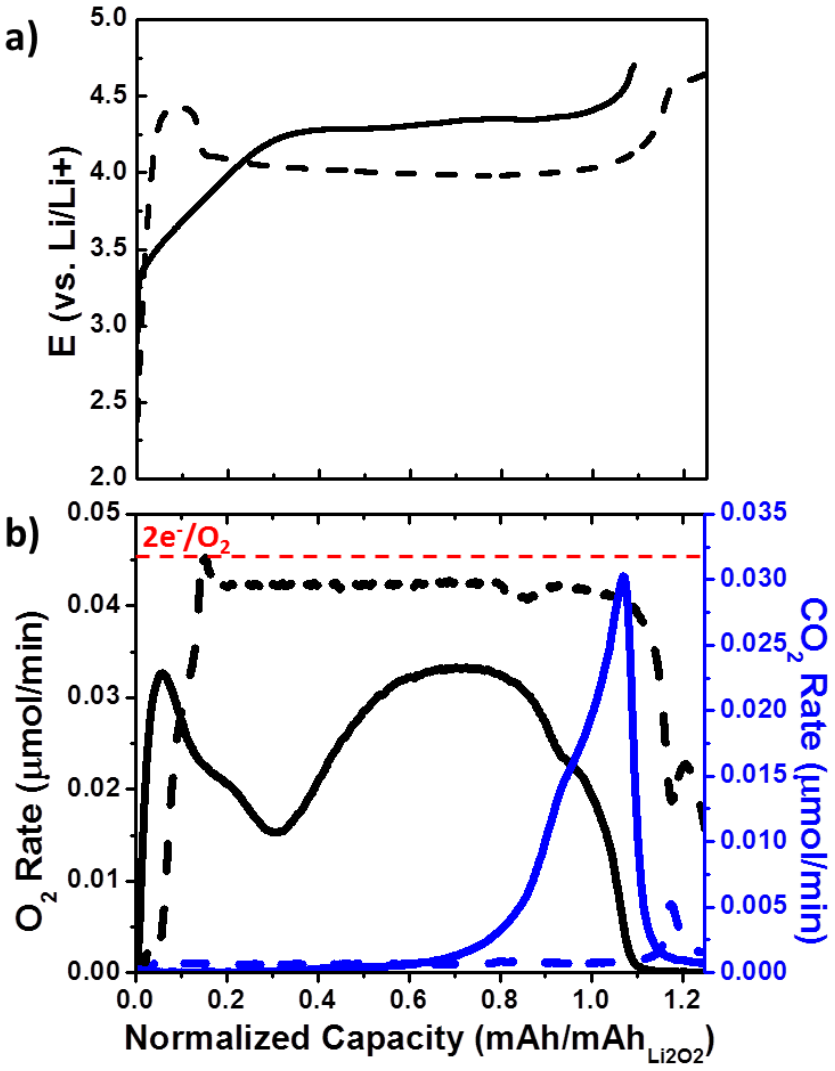


**Figure 5-10 -** Charge potential profiles for electrochemically discharged Vulcan cathode (solid line) and prefilled $Li_2O_2$/Vulcan cathode composite (dotted line), and (b) corresponding $O_2$ (black) and $CO_2$ (blue) evolution profiles. The rate of $O_2$ evolution is significantly less for the discharged Vulcan cathode, and much more $CO_2$ evolution occurs due to the oxidation of much more Li-carboxylate decomposition products.

chemically formed $Li_2O_2$ on preloaded Vulcan carbon positive electrode with that of electrochemically formed $Li_2O_2$ Vulcan carbon positive electrode, both in 1M LiTFSI/TEGDME electrolyte. The positive electrode was discharged at a current rate of 50 µA to a capacity of 1 mAh, and then charged at 150 µA to a voltage limitation of 4.7 V. This

discharge rate was chosen so the deposited $Li_2O_2$ product would be comprised of large (> 600 nm) particles that best resembles the size of $Li_2O_2$ commercial powder particles. The preloaded positive electrode was also charged at 150 μA. The initial voltage rise that was previously discussed with preloaded carbon positive electrodes is completely absent upon oxidation of electrochemically deposited $Li_2O_2$. Instead, the complete absence of this feature is replaced by a low initial charge potential of approximately 3.3 V, which then steadily increases until a plateau is reached at 4.25 V. This plateau remains until complete removal of the $Li_2O_2$ occurs, after which the voltage sharply increases to 4.7 V, which is the onset of electrolyte decomposition. The accompanying oxygen evolution is vastly different than the preloaded positive electrodes. As demonstrated in **Figure 5-10b**, while the oxidation of $Li_2O_2$ for preloaded positive electrode exhibits a constant $O_2$ evolution profile, the discharged positive electrode exhibits a highly variable $O_2$ evolution process throughout the entirety of oxidation. Two "peaks" are observed; $O_2$ evolution that occurs at the initial onset of charge within the sloping region, and $O_2$ evolution that accompanies the flat voltage plateau at 4.3 V. The end of oxidation is accompanied by the evolution of $CO_2$, similar to that of the preloaded positive electrode. However, the total production of $CO_2$ is significantly greater for the discharged positive electrode, implying the oxidation of much more Li-carboxylate decomposition products. Integration of the total $O_2$ amount also shows a drastic contrast, for the discharged positive electrode has an $e^-/O_2$ ratio of ~3.73 $e^-/O_2$, a significantly higher value in comparison to the preloaded positive electrode of 2.45 $e^-/O_2$. This value, accompanied with the greater amount of $CO_2$ evolution, indicates that the parasitic reactions that occur on discharge play a significant role in affecting the efficiency of $Li_2O_2$ oxidation on charge.

### 5.2.3 – Effect of Current Rate on Gas Evolution

A comment must be made about the effect that the discharge/charge rate has on the efficiency of $Li_2O_2$ oxidation. The total amount of $O_2$ evolution for TiC positive electrodes discharged/charged at different rates in 1M LiTFSI/TEGDME electrolyte is shown in **Figure 5-11**. Each electrode was discharged to a capacity of 1 mAh prior to oxidation. The influence

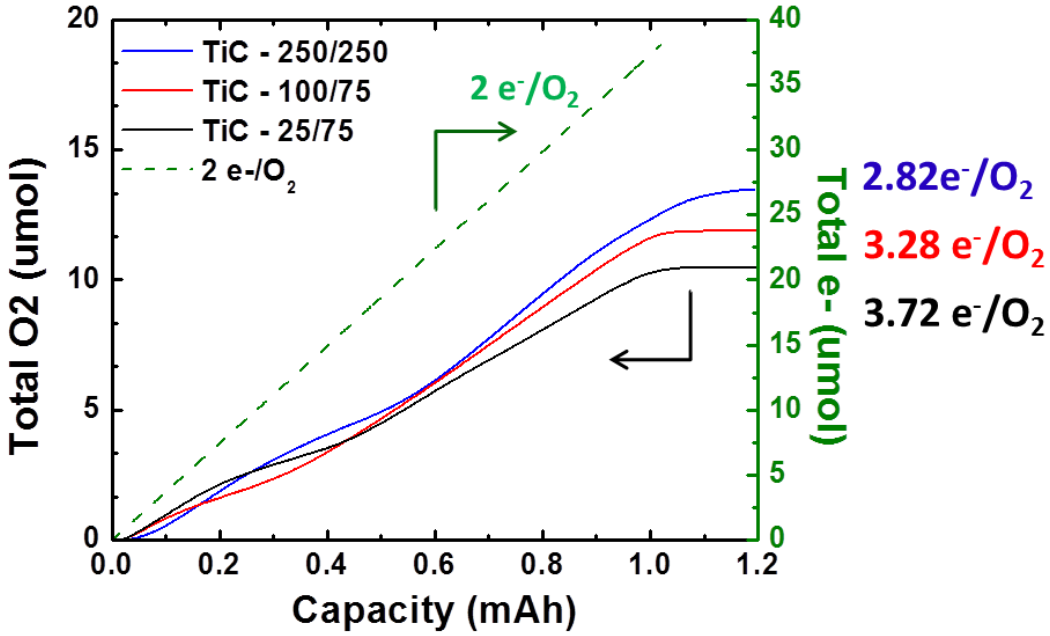


**Figure 5-11** - Total oxygen evolution amount for TiC cathodes in 1M LiTFSI/TEGDME discharged to a capacity of 1 mAh at various current rates, and then charged at different currents. In the legend, the first number is the discharge current, and the second number the charge current (both in $mA/cm^2$)

of the discharge rate on $Li_2O_2$ morphology and corresponding change in charge overpotential as a result of these morphological differences is detailed in other literature in which I am a contributing author.[13] The lower charge overpotential on oxidation that is exhibited by cells discharged at fast rates is due to the difference between $Li_2O_2$ toroids vs, $Li_2O_2$ film. From **Figure 1-4** *(In Section 1)* where this concept was first introduced, the formation of

thin-film $Li_2O_2$ results from fast current rates. With mass spectrometry, it is clear that the discharge and charge rates also have a drastic influence on the degree of oxygen evolution. When the same oxidation current is applied to two different positive electrodes that have been discharged at different rates (25 $\mu A/cm^2$ and 100 $\mu A/cm^2$), the efficiency of oxygen evolution during $Li_2O_2$ oxidation is drastically increased. The abundance of $O_2$ formed at the end of charge is improved from 3.72 $e^-/O_2$ to 3.28 $e^-/O_2$. The most optimal performance occurs when the cell is operated with both a fast discharge and charge current. This is evident when the gas evolution is monitored from a cell that has been discharged and charged at a current rate of 250 $\mu A/cm^2$. Here, the oxygen evolution rate is 2.82 $e^-/O_2$, which is in close agreement the best oxygen evolution efficiencies found in the literature.[9,14] In these reports, fast discharge/charge current rates are also used.

Apart from the change in the morphology of the discharge product, the importance of operating the cell under fast conditions is primarily an issue of cell stability. It has been mentioned previously that the electrolyte is not stable towards $O_2^-$ attack, and forms decomposition products that hinder cell performance. However, $Li_2O_2$ is also a strong nucleophile, and can cause decomposition products to form at the $Li_2O_2$/electrolyte interface after extended periods of exposure. Operation of the cell at high current rates is the most efficient way to reduce the degree of decomposition product formation. This is indicated through the presented mass spectrometry studies. Other efficiency penalties can arise if the cell is operated at high current rates, however, such as issues of mass transport and/or IR resistance negatively affecting the discharge/charge overpotential, which in turn can induce further parasitic reactions. Hence, the most optimized cell conditions are highly dependent on the electrode architecture and morphology, and will vary on a per-system basis. Presented

here was solely a quantitative demonstration of how the oxygen evolution efficiency varies as a function of current rate, and is by no means a definitive suggestion for the rates Li-$O_2$ cells should be operated.

## 5.3 – Study on $Mo_2C$

As a conclusion to this section, I would like to demonstrate the importance of mass spectrometry as a tool to identify cell inefficiencies that are not obvious through basic galvanostatic cycling. In many of the previous results, oxidation efficiency could be inferred from the observed electrochemistry. However, excellent voltage profiles can result in very poor ORR/OER efficiency, masking the true nature of the positive electrode material. In a study performed by Kwak *et. al*, they report on the excellent OER capabilities of $Mo_2C$ in a Li-$O_2$ cell.[15] $Mo_2C$ exhibits a low $Li_2O_2$ oxidation potential and excellent cycling capabilities. They correlate this electrochemical activity with efficient $Li_2O_2$ production and oxidation, and hence claim that $Mo_2C$ is an excellent positive electrode for the Li-$O_2$ cell. There is, however, a necessity for complete characterization of the oxidation activity, or else erroneous conclusions can be drawn with regards to the electrochemical profile representing Li-$O_2$ electrochemistry.

Transition metal carbides possess high electrical conductivity and excellent surface physiochemical properties arising from population of their d-orbital states near the Fermi level that resemble noble metals.[16,17] $Mo_2C$ has shown to be a highly active material for the catalysis of hydrodeoxygenation,[18] hydrogen evolution,[19] and $CO_2$ conversion.[20] To study the effect of $Mo_2C$ as a catalyst material, $Mo_2C$ was synthesized in a nanowire form as shown in **Figure 5-12a**. The $Mo_2C$ is synthesized in its β-$Mo_2C$ form, evident from X-ray diffraction (**Figure 5-12b**). This nanowire morphology is ideal for the Li-$O_2$ cell, considering

that the high surface area allows for the presence of many active sites for ORR and OER. Furthermore, the nanowire morphology and the adequate spacing between bundles of nanowires allows for facile $O_2$ transport throughout the entire positive electrode volume. This is ideal for accommodation of the discharge product $Li_2O_2$, and necessary to obtain a large capacity. The final nanowire products are bundles of stacked nanofibers approximately 100 nm in diameter, as shown in **Figure 5-12a inset**. The surface of $Mo_2C$ is always contaminated with Mo-oxide species, which, in this case, are formed during controlled passivation of the as-synthesized nanowires.[21,22] This was confirmed with the Mo 3d XPS spectra, revealing an average oxidation state of $Mo^{4.1+}$. The metallic properties of the $Mo_2C$ and Mo sub-oxides make the active surface of this "catalyst" material highly conductive.[23]

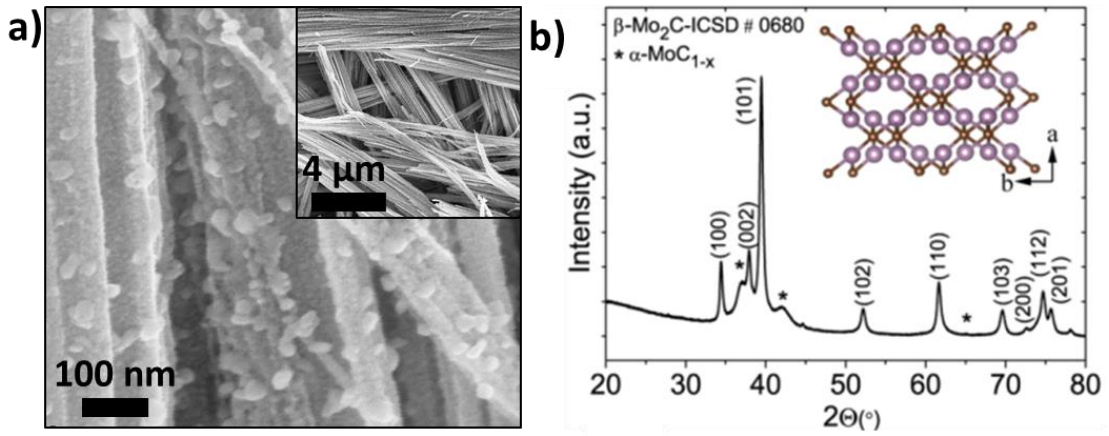


**Figure 5-12 -** (a) SEM micrographs of the as prepared $Mo_2C$ cathode. The nanowires measure 20 nm in diameter. Notice the surface of the $Mo_2C$ is passivated with a rough oxide layer of $MoO_{2+\delta}$ to prevent the instantaneous oxidation of the $Mo_2C$ with the atmosphere during preparation. The crystallites that comprise the nanowire structure are of the β-$Mo_2C$ phase as shown in (b).

**Appendix B** outlines a detailed synthesis of these $Mo_2C$ nanowires, and provides a summary of the Mo3d XPS spectra.

The electrochemical performance of $Mo_2C$ as the positive electrode material is shown in **Figure 5-13a**. This cell was run against metallic lithium as the negative electrode, and 1M LiTFSI/TEGDME as the electrolyte. $Mo_2C$ exhibits a voltage plateau on electrochemical discharge at ~ 2.7 V, similar to that of previously discussed positive electrode materials. The discharge product is primarily $Li_2O_2$, as indicated from the Li 1s XPS spectrum in **Figure 5-13b inset**. Powder X-ray diffraction cannot be used to identify the discharge product due to

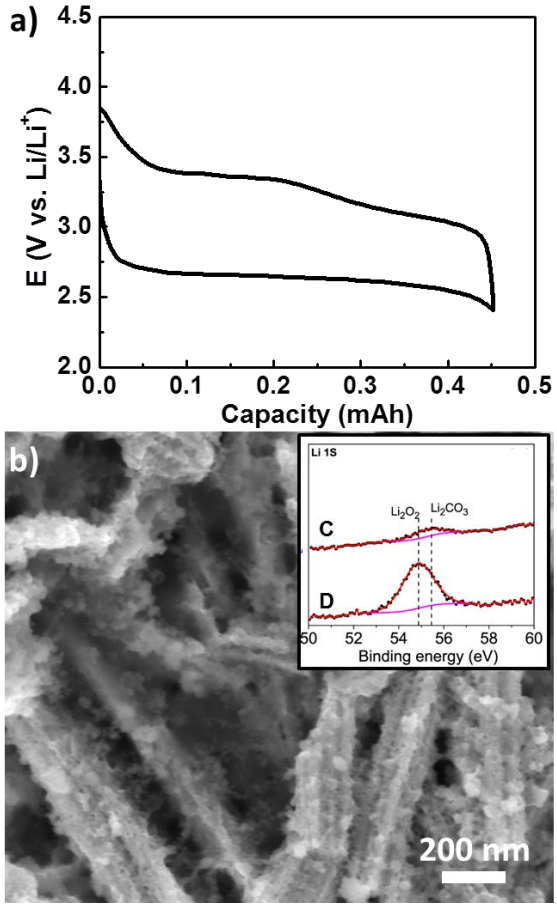


**Figure 5-13 -** (a) Electrochemical discharge/charge profile of the first cycle of $Mo_2C$ electrode run in 1M LiTFSI/TEGDME, and (b) corresponding discharge product $Li_2O_2$ on the $Mo_2C$ surface. The inset in (b) shows the Li 1s spectra for both the discharged (D) and charged (C) $Mo_2C$ cathode. As can be seen, on discharge the primary product is $Li_2O_2$, and on charge a majority of the $Li_2O_2$ is removed, with a small amount of $Li_2CO_3$ present.

interfering peaks of $Mo_2C$, as well as the apparent low crystallinity of the discharge product as determined from the SEM micrograph (**Figure 5-13b)**. The deposited $Li_2O_2$ is present as a thin film, and not the normal crystalline, toroidal shape that is characteristic of electrochemically deposited $Li_2O_2$. The high ORR activity/strong $O_2$ coordination of the $Mo_2C$ surface may contribute to this surface reaction The exact relationship between the electrode surface and $Li_2O_2$ morphology is an area worth further investigation, but is beyond the scope of this section.

$Mo_2C$ exhibits a gently sloping charge profile that originates at 3.25 V. The voltage slowly rises over the course of $Li_2O_2$ oxidation to 3.5 V, where a sudden spike to 4.0 V occurs. This sudden increase in voltage is an indication that the species being oxidized, $Li_2O_2$, is removed. The near complete removal of $Li_2O_2$ is confirmed from the Li 1s XPS spectrum in **Figure 5-13b inset.** There is a small amount of $Li_2CO_3$ on the positive electrode surface at the end of charge, most likely due to the reactivity of $Li_2O_2$ with the ether-based electrolyte.[24] This charge overpotential is remarkably low, and is one of the lowest observed charge voltages to date. To ensure that the discharge and charge voltage profile is a result of the generation and oxidation of $Li_2O_2$, the oxygen consumption and evolution on discharge and charge was determined.

To study the validity of this low charge overpotential, first, $Mo_2C$ was prefilled with commercial $Li_2O_2$ powder and charged in 1M LiTFSI/TEGDME. As discussed in previous sections, the oxidation of a positive electrode prefilled with $Li_2O_2$ removes any influence of the discharge chemistry. A remarkably low overpotential is observed, with a charge plateau at approximately 3.35 V (**Figure 5-14a**). This overpotential is much lower than the charge profile exhibited by carbon and TiC, shown previously in **Figure 5-6** and **Figure 5-8**

respectively. Keep in mind that unlike the $Li_2O_2$ film formed on discharge, the prefilled positive electrodes are comprised of large $Li_2O_2$ particles. Hence, the low charge overpotential is not merely a result of the $Li_2O_2$ morphology. The $O_2/CO_2$ evolution corresponding to the charge of the prefilled $Mo_2C$ electrode is shown in **Figure 5-14b**. In contrast to both TiC and carbon, the amount of $O_2$ generated is significantly less. While the onset of oxygen evolution occurs upon immediate $Li_2O_2$ oxidation, overall the oxygen evolution rate is extremely small. This is a curious result. Integration of this oxygen evolution curve at the end of charge corresponds to a total oxygen evolution fraction of 14%

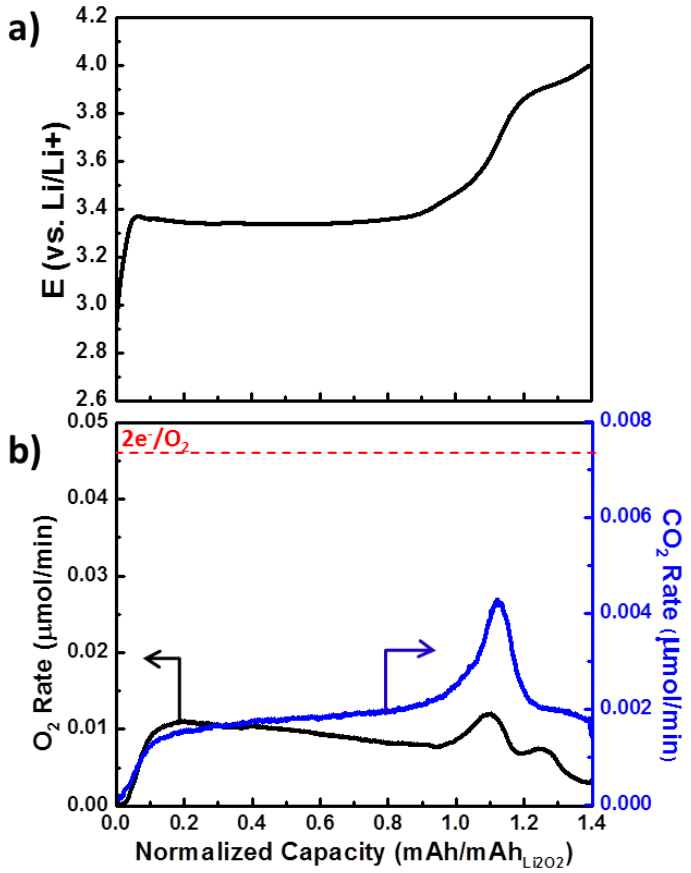


**Figure 5-14 – (**a) Electrochemical charge curve of pre-loaded $Mo_2C$ cathode with $Li_2O_2$ in 1M LiTFSI/TEGDME and (b) corresponding $O_2$ and $CO_2$ gas evolution curve.

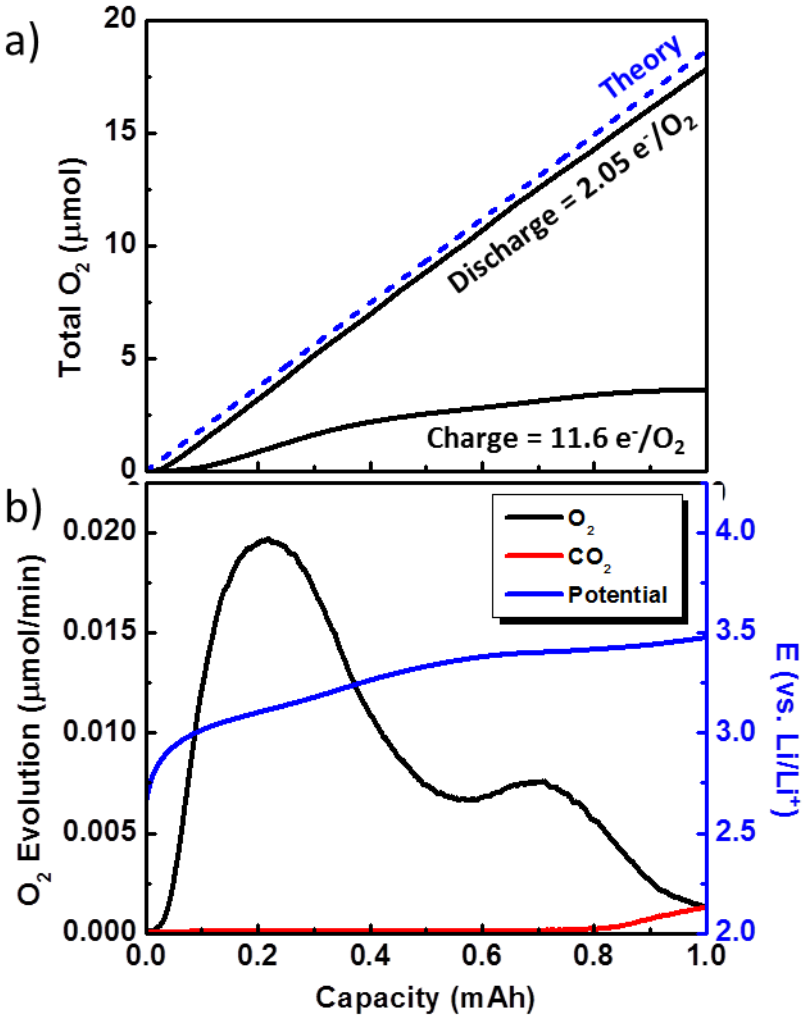


**Figure 5-15 – (**a) Total oxygen consumed (2.05 $e^-/O_2$) on discharge and evolved (11.6 $e^-/O_2$) on charge, and (b) corresponding $O_2/CO_2$ evolution on cell charge. The theoretical rate of $O_2$ evolution should be 0.062 μmol/min based on a charge current of 200 μA.

of what would be expected based on the mass of preloaded $Li_2O_2$ (assuming a 2 $e^-/O_2$ oxidation). Furthermore, the $O_2$ evolution equates to ~11.2 $e^-/O_2$, indicating that a highly inefficient oxidation process results from the low voltage profile. At no point during oxidation does this $O_2$ amount significantly increase. In comparison, the $CO_2$ evolution is similar to that of carbon and TiC positive electrodes. If the lack of oxygen evolution was a

result of enhanced electrolyte decomposition at the $Mo_2C$ surface, a larger fraction of $CO_2$ evolution would be expected. To better determine the cause of this inefficiency and validate this result, further analysis was performed on this positive electrode under real cell operating conditions.

To ensure the production of $Li_2O_2$ agrees with the observed electrochemistry, the oxygen consumption on cell discharge was determined (**Figure 5-15)**. The oxygen consumption was 2.05 $e^-/O_2$ over a capacity of 1 mAh. This is very near the expected 2 $e^-/O_2$ given the reaction $O_2 + 2e^- + 2Li^+ \rightarrow Li_2O_2$. This near perfect agreement demonstrates that the production of $O_2^-$ is unimpeded on the $Mo_2C$ surface. Clearly, oxygen reduction is the main discharge process, followed by the production of $Li_2O_2$ as confirmed previously. To determine if there are differences in the $O_2$ evolution profile among the electrochemically and chemically formed $Li_2O_2$, the oxygen evolution (and $CO_2$ evolution) was monitored for oxidation of a $Mo_2C$ electrode after being discharged to a fixed  decomposition products, the oxidation of $Li_2O_2$ on $Mo_2C$ shows a very large 11.6 $e^-/O_2$ **(Figure 5-15a)**. This is an extremely inefficient charge process, and it is clear that a majority of $O_2$ consumed on discharge is not recovered on charge. Hence, the low charge overpotential is not truly $Li_2O_2$ oxidation as both the electrochemistry and post-mortem analysis of the discharge product would dictate.

The key to these observations of poor $O_2$ evolution lies in the reaction of $Li_2O_2$ with the $Mo_2C$, and the fate of the resultant product on electrochemical charge. The first stage of discharge is the production of $Li_2O_2$, as confirmed by the 2 $e^-/O_2$ reduction step and XPS identification of $Li_2O_2$. However, upon contact with $Li_2O_2$, the surface of $MoO_{2+\delta}$ undergoes the following reaction (*equation 5-6)*:

$$x/2\ Li_2O_2 + MoO_{2+\delta} \rightarrow Li_xMoO_3 \qquad (equation\ 5\text{-}6)$$

This reaction is confirmed through analysis of the Mo 3d XPS spectra (**Figure B-2, Appendix B**), which shows a change in the Mo oxidation state from $Mo^{4.1+}$ to $Mo^{5.5+}$ after cell discharge (x = 0.5).

This reaction is thermodynamically driven by a negative $\Delta G_f$, as is known to occur with $Li_2O_2$ reacts with other surfaces such as carbon, as discussed previously.[25] This reaction creates surface layers of $Li_xMoO_3$. The bulk $Mo_2C$ material is unaffected, but this reaction consumes the $Li_2O_2$. Upon formation of $Li_xMoO_3$, the material forms a colloidal dispersion in the polar aprotic media (TEGDME), giving a metallic blue colour.[26] Such a deep blue colour is easily observed after multiple cell cycles, demonstrated in **Figure 5-16**. Upon cell oxidation, there is a competition between the oxidation of the $Li_2O_2$ and the

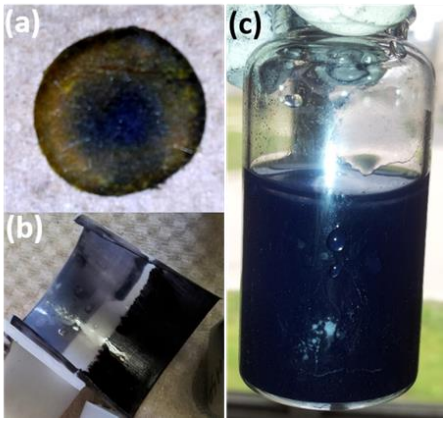


**Figure 5-16 -** (a) Picture of the glass fiber separator after cycling the cell until cell failure (b) electrolyte-soaked Swagelok cell liner (the bottom dark blue section was in direct contact with the electrolyte) after electrochemical cycling of the Mo2C cathode in a Li-$O_2$ cells (c) colloidal solution of chemically lithiated $MoO_3$ in TEGDME. The chemical lithiation was performed by stirring $MoO_3$ with lithium iodide in a 1:0.35 molar ratio in n-hexane for 24 h. The lithiated $MoO_3$ was centrifuged and tested for dispersibility in TEGDME.

$Li_xMoO_3$, resulting in a low charge overpotential, but does not result in a sufficient amount of recovered oxygen. A majority of the oxygen consumed during discharge remains in the solution as $MoO_3$. The $Li_xMoO_3$, and thus dissolves in the electrolyte, which is a method of "self-cleaning" the electrode surface. This causes retention of catalytically active sites that were originally terminated with $Li_2O_2$ to become active once again on charge

and allows for sustained low ORR/OER overpotentials over multiple cycles as shown in **Figure 5-17**. This is further confirmed by the Mo 3d XPS spectrum of a charged positive electrode, where the $Mo^{5.5+}$ signature is absent, and the original $MoO_{2+\delta}$ is restored (**Appendix B**). Eventually, without a method to remove the $MoO_3$ from solution, saturation of the glyme electrolyte and an increase in the electrolyte viscosity leads to cell failure.

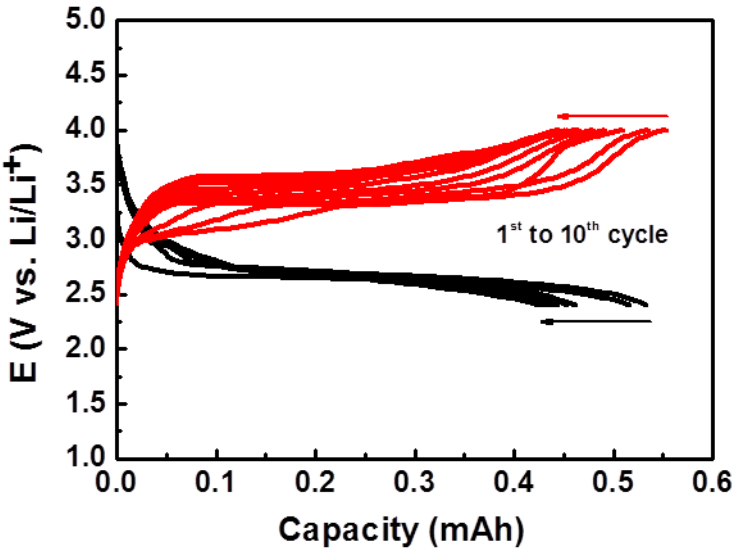


**Figure 5-17 -** Cycling profile of $Mo_2C$ over 10 cycles, with a voltage limitation of 2.5 V – 4.0 V in 1M LiTFSI/TEGDME.

This study proved to be a valuable lesson in the nature of positive electrode surfaces for the Li-$O_2$ cell, for prior to this study the method of "self-cleaning" to regenerate

ORR/OER active sites was unknown. Furthermore, this study demonstrates the importance of mass spectrometry as an analysis tool for Li-$O_2$ chemistry. Without proper quantification of both the $O_2$ consumption and $O_2$ oxidation, the true fate of the $Li_2O_2$ can be masked by other electrochemical processes that show "exciting" oxygen chemistry. In the report by Kwak *et. al,* the electrochemical results are very similar to what has been presented here.[10] While the authors present an overall valuable study, as well as hint at the surface oxidation of $Mo_2C$ during cell operation, they fail to recognize the complete consumption of the electrode material due to reactivity of the $Li_2O_2$, and eventual formation of lithiated $MoO_3$ species that are soluble in the electrolyte. As demonstrated above, this is not apparent through the electrochemistry itself, and without the use of mass spectrometry to quantify the oxidation of $Li_2O_2$ and observe the poor $O_2$ evolution, they fail to recognize the complete consumption of the electrode material due to reactivity with the $Li_2O_2$, and eventual formation of a lithiated $MoO_3$ species. Hence, the excellent electrochemistry is interpreted erroneously and the inefficiencies on cell charge are not realized. Similar conclusions from other reports complimenting the study I presented above further demonstrates the instability of $Mo_2C$ as an electrode material. Yao *et. al*. explores the use of transition metal oxide materials as "solid-state promoters" of enhanced $Li_2O_2$ oxidation kinetics.[27] These promoters are examined to determine the enthalpies for conversion reactions between $Li_2O_2$ and the transition metal oxide to produce lithiated oxides (as was observed for the $Mo_2C$). The lithiated oxides are oxidized at a lower potential than $Li_2O_2 \rightarrow 2Li^+ + O_2$ to liberate gaseous oxygen and $Li^+$ (leaving behind a metal-oxide). They demonstrate that the direct reaction of $Li_2O_2$ with Mo gives rise to $Li_2MoO_4$, which is soluble in the DME electrolyte, and hence is a major issue as the positive electrode is consumed during the OER process. This provides great insight into

how “catalysts” can function to improve the efficiency of $Li_2O_2$ oxidation, and even though Mo-based carbides and oxide dissolution occurs, the investigation of other more stable solid state promoters is an area worthy of investigation.

## 5.4 – Conclusions and Final Thoughts

In conclusion, the importance of mass spectrometry as an analytic tool to evaluate positive electrode activity for $Li_2O_2$ oxidation cannot be stressed enough. The presented discussion on this topic has demonstrated the importance and necessity of an analytic tool that can directly probe the formation/oxidation of $Li_2O_2$ without relying solely on the electrochemistry, for many parasitic reactions occur in the Li-$O_2$ battery that are not electrochemical in nature. Specifically, the high reactivity of the intermediate products during Li-$O_2$ formation (namely $O_2^-$/$HO_2$) are capable of electrolyte decomposition (as well as decomposition of other cell components, as discussed in more detail in *Section 3*), which produce a variety of Li-carboxylate decomposition products. These decomposition products have a significant impact on the efficiency of $Li_2O_2$ oxidation, as is evident from analysis of the residual gases and total $O_2$ evolution. As was shown with the use of preloaded positive electrodes, the oxidation of $Li_2O_2$ itself can be rather facile, and the choice of a positive electrode that does not undergo partial or complete oxidation with the $Li_2O_2$ product (such is the case with $Mo_2C$) can lead to near complete removal of $Li_2O_2$ with only minimal side reactions. While other positive electrodes mentioned show superior electrochemistry, it was through the use of mass spectrometry that their true electrochemical nature was revealed.

In terms of the current mass spectrometer design, future improvements can be made for more efficient quantification as well as improve the user-interface to offer a wide array of characterization possibilities. Currently, the mass spectrometer is capable of testing low

volatility solvents in-real time through the use of a sample-inlet capillary system. Highly volatile solvents pose a serious problem. Specifically, the in-line flow design is not ideal for highly volatile solvents due to evaporation of the electrolyte over long periods of testing, as well as the potential clogging of the thin capillary due to condensation of the electrolyte. This limits the range of analysis to low volatility solvents, such as TEGDME, DMSO, and PC. Furthermore, even with the low-volatile solvents, the evaporation of solvent vapours into the mass spectrometer analysis chamber is not desired due to the high signal background that these vapours generate, as well as the degradation of filament and detector life-time in the presence of hydrocarbons. To mitigate these issues and allow for high-volatile solvent capabilities, one area for future improvement would be the utilization of a $N_2$-cold trap at the outlet of the cell to prevent vapours from reaching the mass spectrometer. A small liquid-$N_2$ trap at the outlet of the cell, before the sampling point of the capillary, would allow for the travel of the $O_2$ and $CO_2$ (and other gases of interest) into the mass spectrometer, while removing the organic vapours prior to reaching the entrance chamber. This would aid a great deal in extending the life-time of the filament/detector as well as allow for the use of highly volatile solvents such as DME, acetonitrile, and others.

# 6.0 – Instabilities of Ether Solvent-Based Na-$O_2$ Batteries

## 6.1 – Introduction

As mentioned in *Section 1.3*, the benefits of the Na-$O_2$ battery compared to the Li-$O_2$ battery are clear. Li-$O_2$ batteries are appealing due to their high theoretical gravimetric energy density (3,505 Wh/kg with respect to the mass of $Li_2O_2$) based on a two-electron reduction process ($Li^+ + O_2 + 2\ e^- \leftrightarrows Li_2O_2$) at a potential of 2.96 V, and low mass reactants (Li metal and gaseous $O_2$).[1,2,3] However, achieving a practical battery has proven difficult due to numerous drawbacks: low rate capability, [4,5] poor cycle life,[6,7] and a high charge overpotential.[8] One solution to this issue lies in the Na-$O_2$ battery. Na-$O_2$ batteries exhibit much lower charge overpotentials (~ 0.1 V vs. 1 V), higher rate capabilities, and improved capacity retention on cycling. [9,10] Although the theoretical energy density of the Na-$O_2$ battery (~1100 Wh/Kg) is much lower than that of the Li-$O_2$ battery, its improved performance may make the Na-$O_2$ battery more appropriate for commercialization.[11] The superior reversibility of the Na-$O_2$ battery is thought to be due to the "cleaner" chemistry associated with the oxygen reduction/evolution (ORR/OER) reactions, at least on the first cycle.[12] Nonetheless, given the high reactivity of superoxide ($NaO_2$) and the strong nucleophilic nature of the $O_2^-$ ions and the $HO_2$ radical, electrolyte degradation is expected.

Sodium-oxygen cells to date have employed ether-based electrolytes, typically diethylene glycol diethyl ether (diglyme/DEGDME). Glymes are the mainstay for many Li-$O_2$ battery electrolytes due to their quasi-stability to superoxide attack, even though mass spectrometry,[13,14] NMR,[15] and XPS[16] spectroscopic studies have shown that they react to produce a wide variety of Li-carboxylate decomposition products that block catalytic surface sites for oxidation,[17] which greatly inhibits cell cycling capabilities. No electrolyte

has been reported that is both stable to $O_2^-$/$Li_2O_2$ in the aprotic metal-oxygen cell, while also possessing low viscosity and high ionic conductivity. The carbon positive electrode is also susceptible to oxidation in the Li-$O_2$ battery, especially during charge.[18,19] Attempts have been made to alleviate positive electrode decomposition through the use of alternative non-carbon or passivated carbon positive electrodes with some success, as discussed throughout this dissertation.[20,21,22] The low mass of carbon and its high surface area are still unmatched with respect to overall gravimetric energy density and cost.

In the following section, I explore the chemistry of Na-$O_2$ batteries in diglyme electrolytes. It is known that decomposition in the Li-$O_2$ battery is in part due to the nucleophilic character of the $O_2^-$ and $Li_2O_2$.[6,14,16,23] This leads to a question: To what extent do these products ($O_2^-$ and $NaO_2$) cause decomposition in the Na-$O_2$ battery, and how does this affect performance? To answer this, the origin and precise nature of side products in the cell are defined and quantified, and a mechanism proposed for their formation. The Na-$O_2$ battery benefits from a very low overpotential on charge owing to the solubility of $NaO_2$/$HO_2$, which facilitates its oxidation and thus exhibits better cycling performance than Li-$O_2$ cells.[24] Nonetheless, analysis shows that formation of decomposition products on discharge – which are largely not removed on charge – are more problematic than previously thought. This leads to an understanding of the origins of the rise in charge potential. Furthermore, resting the cell at open circuit potential in the presence of $NaO_2$ results in dramatic consumption of the superoxide *via* reaction with diglyme. Very significant fractions of carboxylate side products are formed. Evidence shows that the main source of degradation stems from the strong nucleophilic character of the discharge product, $NaO_2$, as well as the reactivity of the $O_2^-$/$HO_2$ radical.

## 6.2 – Experimental

### 6.2.1 – Positive electrode/Cell Preparation and Measurements

For positive electrode preparation, 0.78 $cm^2$ (100 x 100 mesh) stainless steel meshes were sonicated in ethanol and dried prior to use. A slurry of ground $^{13}C$ carbon (Sigma-Aldrich) and PTFE (from a 20 mg/500 μL isopropanol stock solution) was prepared in an 85:15 mass ratio. After it was mixed for 1 minute, the slurry was pressed onto the stainless steel mesh and dried in air at 60 °C for 1 hour. The positive electrodes were dried at 300 °C under vacuum overnight in a Büchi oven, and transferred to an Ar-filled glovebox.

Positive electrodes were employed in either 2 or 3-electrode modified-PFA Swagelok cells. Each positive electrode was placed in a cell with a sodium metal (Sigma-Aldrich) negative electrode, separated by two glass fibre separators and one Celgard separator (2500). Electrolyte (240 μL) comprised of 0.5M NaOTf and 15 ppm $H_2O$ (prepared in-house[24]) in distilled diethylene glycol dimethyl ether (DEGDME, or diglyme) was added to the cell. The cell was then sealed and pressurized to 1.5 atm in 5.0 research grade oxygen (Praxair). Prior to measurement, the cell pressure was monitored with a pressure transducer (PX409, Omegadyne) to ensure that each cell was hermetically sealed. The electrochemical measurements were performed with an Arbin galvanostat/potentiostat. The current density for all experiments was 130 $\mu A/cm^2$; capacity and voltage limitations are as indicated.

Iodometric titration of the dry positive electrode contents was performed, using a slightly modified version[25] of an already reported method.[26] This method is outlined in *Section 2.7.*

NMR experiments were conducted at room temperature in $D_2O$ on a 300 MHz Bruker Advance spectrometer. $^1H$ NMR spectra were referenced to the residual HOD peak at 4.78

ppm. The fraction of decomposition products was determined by integration of the peak area with respect to a known amount of benzene standard added to the solution. This stock solution was prepared using 100 g of $D_2O$ and 0.2 mL benzene and was allowed to equilibrate for 24 hours prior to analysis. Positive electrodes and separators were removed from the cell and washed with THF. The contents were then left to dry under Ar/vacuum for 12 hours before addition of the $D_2O$/benzene solution. Lastly, 0.8 mL of the stock solution was added to the cell contents, which were then collected for measurement.

The reactivity of $O_2^-$/$NaO_2$ was probed via the $KO_2$ reaction proposed in *Section 3.2*. $KO_2$ (Sigma Aldrich) and 18-crown ether (Sigma Aldrich) were used as received. Diglyme was distilled prior to use, and NaOTf was prepared as indicated above. For each reaction, 0.02g $KO_2$ and 0.13g dicyclohexyl-18-crown-6 (crown ether) were added to 2.5 mL diglyme. The reaction was left to stir for four days. To produce $NaO_2$, 0.10 g NaOTf was added immediately following the addition of $KO_2$ and crown ether. The added NaOTf was twice the molar amount of $KO_2$ to ensure complete reaction of the $O_2^-$ to $NaO_2$. After four days, the solid contents were left to settle and were collected via centrifuge. The contents were washed three times with 15 mL THF, and dried under Ar overnight. $D_2O$ was added directly to the solid contents for NMR analysis.

To measure gas evolution on cell charge, the positive electrodes were first discharged using the same Swagelok design described above. Upon completion of discharge, the cell contents (without the metallic sodium electrode) were immediately transferred to an El-Cell electrochemical cell in an Ar-filled glove box and an additional 50 μL of electrolyte was added. The cells were attached in-line with an RGA 200 (Stanford Research Systems), and a continuous flow of 5.0 Ar (Praxair) was used to sweep the evolved gases during cell charge

across a 50 μm diameter capillary for analysis. Quantification was performed using a calibration curve comprised of different concentrations of $O_2/CO_2$ in Ar (0-2000 ppm).

Positive electrodes were removed from cells immediately after cell completion (***no rest*** unless indicated). The positive electrodes were washed with THF, dried under vacuum and mounted onto SEM stubs with double sided carbon tape in a hermetically sealed Ar-filled box. Transfer from the glovebox to the SEM was performed with minimal (*i.e.*, 1 sec) exposure to the atmosphere upon placement into the SEM load-lock chamber. Analysis was performed with a Zeiss Ultraplus FESEM.

XRD measurements were carried out using a Bruker D-8 Advance diffractometer employing Cu-Ka radiation ($\lambda$ = 1.5406 Å). Samples were mounted on a silicon low-background holder using a moisture-protective barrier.

For iodometric titration, the buffer-catalyst solution was prepared by dissolving 65 mg of $(NH_4)_6Mo_7O_{24} \cdot 4H_2O$ (ammonium heptamolybdate) along with 0.11 mol of $H_2PO_4^-$ and 0.03 mol of $HPO_4^{2-}$ in 500 ml of Millipore water. Adding 67 g of KI to this buffer solution and diluting it to 1 L resulted in the reagent buffer solution, which was freshly prepared before use. For the $NaO_2$ quantification, the discharged/charged positive electrodes were transferred to a glass vial to which 5 ml of Millipore water was added and shaken vigorously. The content of the vial was transferred to a conical flask with an extra 5 ml of water that was used to rinse the vial. To this mixture, 15 ml of water and 25 ml of buffer catalyst solution was added. The mixed solution immediately turned yellow indicating the liberation of iodine, which was titrated with standardized thiosulfate solution until a straw yellow color. The titration was continued after adding starch indicator solution with the end point showing a color change from blue-violet to colorless.

### 6.2.2 – Acid Treatment Cell – Carbonate Analysis

Mentioned previously, $CO_2$ gas evolution during Li-$O_2$ cell operation is indicative of the oxidation of various carboxylate degradation products that form as a result of normal cell operation. Hence, the amount of $CO_2$ evolved on charge should correlate to the amount of decomposition products on the positive electrode surface. However, the $CO_2$ evolution on charge is only generated from decomposition products that can be oxidized within the voltage window of the electrolyte. If the species of interest cannot be electrochemically oxidized, then gas analysis during electrochemical oxidation is not helpful. Thus, another approach must be used in order to properly evaluate (and identify) the various decomposition products. Here I will outline the theory behind the use of acid treatment analysis as a means to more accurately quantify the fraction of carbonate-based decomposition products on the metal-$O_2$ positive electrode.

In a report by Thotiyl *et. al.* [18], a strong acid was utilized to oxidize carbonates that form on the positive electrode surface. When a strong acid is added to $Li_2CO_3$, the following equilibrium reaction occurs *(equation 6-1)*:

$$CO_3^{-2} \leftrightarrow HCO_3^{-} \leftrightarrow CO_2 \qquad (equation\ 6\text{-}1)$$

This reaction, under a low pH, will be pushed greatly to the right. In the case of $H_3PO_4$, the exact reaction of $Li_2CO_3$ and $H_3PO_4$ is:

$$3H_3PO_4 + 3Li_2CO_3 \rightarrow 3CO_2 + 3H_2O + 2Li_3PO_4 \qquad (equation\ 6\text{-}2)$$

The final reaction of $Li_2CO_3$ causes $CO_2$ evolution in a 1:1 molar ratio. Given the low pH of the solution, the solubility of $CO_2$ would be virtually zero, and thus all the $CO_2$ that is produced will evolve and be swept into the mass spectrometer. Therefore, without the need

for electrochemical oxidation, the amount of carbonate formation on the positive electrode surface can be analyzed with this method.

A special reaction chamber (**Figure 6-1**) was designed for this study. This chamber is a glass vial that has been fitted with a gas-inlet and gas-outlet, and a screw cap septum that allows for the injection of liquid through a small needle.

**Figure 6-1 -** Reaction vessel for the acid treatment of electrodes. The two quick connects serve as the gas flow inlet and outlet. The top is fitted with an air-tight septum to allow for injection of the acid with minimal air exposure.

To validate this design and determine the accuracy of this test, the glass cell was loaded with known quantities of $Li_2CO_3$. Theoretically, the amount of $CO_2$ evolution, in mols, should equal the amount of $Li_2CO_3$ given the 1:1 ratio of the reaction. **Figure 6-2** is a typical $CO_2$ evolution curve after injection of $H_3PO_4$. Upon immediate addition of 2M $H_3PO_4$ to ~4.20 mg of $Li_2CO_3$ (56.8 μmol), the total fraction of $CO_2$ evolution is 45.3 μmol,

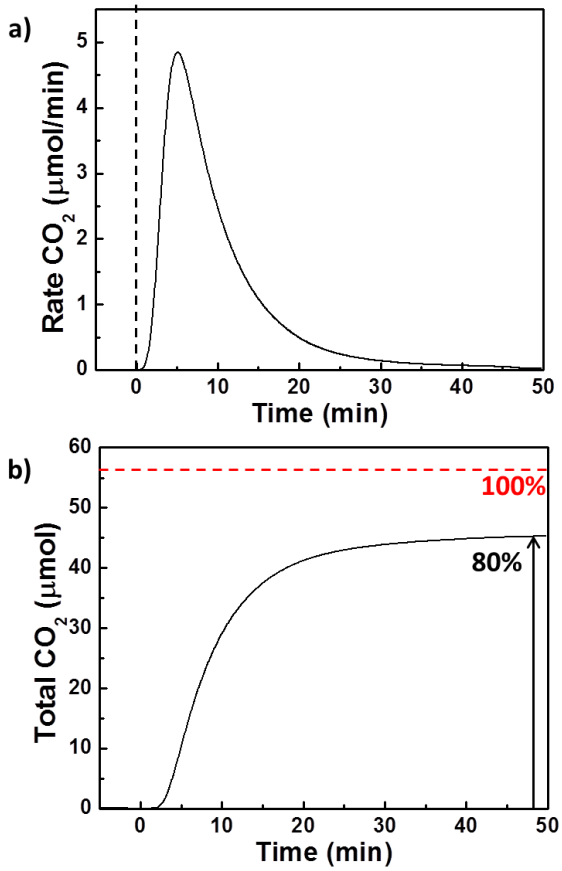


**Figure 6-2** – (a) $CO_2$ evolution curve after injection of 2M $H_3PO_4$ into 4.20 mg of $Li_2CO_3$. (b) Integrated $CO_2$ evolution curve (black) and theoretical $CO_2$ amount (red) based on the total mass of $Li_2CO_3$ analyzed.

approximately 80% of theoretical. There are a few reasons for this value difference. It is highly unlikely that the 20% loss is due to impurities in the $Li_2CO_3$.This compound is completely stable to atmosphere and moisture, so it is unlikely that the product composition changed while in storage. Thus, this 20% loss is most likely due to experimental error. The issue of time lag was mentioned previously in *Section 5.1.4*, and is very likely the cause of $CO_2$ loss during measurement. Given the fast generation and large abundance of $CO_2$, it is highly likely that the $CO_2$ pressure in the analysis chamber does not equilibrate within the timeframe of $CO_2$ generation that is measured at the mass spectrometer inlet. Thus, some

$CO_2$ will be lost. Repeat experiments have shown a similar result of 80% (+/- 2%). Thus, the error in this measurement is systematic. For all results obtained using this method, 20% has been added to the final result to give the true value for the $CO_2$ evolution, and thus the moles of $Li_2CO_3$.

## 6.3 – Ether Solvent Reactivity and Effect on Battery Performance

$^{13}C$-labelled positive electrodes were used to identify the source of decomposition reactions in the Na-$O_2$ cell. This allowed for tracing of the decomposition products to originate from either the reaction of the carbon surface or from the $^{12}C$ diglyme-based electrolyte. To determine the nature of the discharge products, a cell was discharged and charged to a capacity of 1 mAh in 0.5M NaOTf/diglyme. The electrolyte consisted of distilled diglyme, with pure, crystalline NaOTf (synthesized in-house to ensure no contamination from NaOH•$H_2O$ or other species) and 15 ppm $H_2O$ to provide a controlled, albeit very low, fraction of the phase-transfer catalyst necessary to achieve good discharge/charge properties as was previously reported.[24 **Figure 6-3a** shows a typical electrochemical curve for a cell discharged to 1 mAh, and charged to an upper voltage limitation of 4.5 V. The corresponding gas evolution on charge was quantified with an online electrochemical mass spectrometer (OEMS), as has been discussed in extensive detail in *Section 5.1*. The discharge plateau at ~2.1 V and initial charge plateau at ~2.3 V is representative of a typical Na-$O_2$ cell with added $H_2O$ as a proton source and the formation of $NaO_2$ as the discharge product.[9,10,24] The presence of crystalline $NaO_2$ as the sole crystalline discharge product is confirmed in **Figure 6-4**. The three reflections correspond to the (200), (220), and (311) planes of the cubic structure $NaO_2$.[9] A few researchers report on the formation of other discharge products, such as $Na_2O$ and hydrated $Na_2O_2$, while using

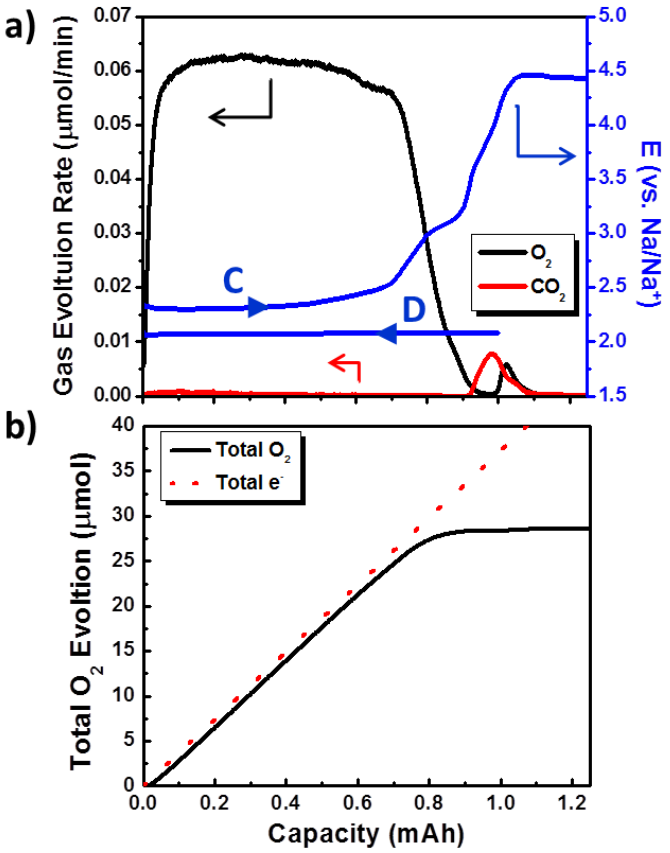


**Figure 6-3 – (**a) Representative discharge (D)/ charge (C) curve for the first cycle of a Na-$O_2$ cell with a $^{13}C$ cathode, and corresponding $O_2$ and $CO_2$ evolution profiles; (b) the integrated values of oxygen evolution (black solid line) compared to theoretical $O_2$ evolution (dashed red line). In the electrochemical profile shown in (a), the onset of the flat profile above 4.4V indicates the onset of electrolyte oxidation.

similar carbon positive electrodes, glyme-based electrolytes, and experimental conditions.[27,28,29,30] These products exhibit poor rechargeability and larger discharge/ charge overpotentials compared to that of $NaO_2$.[27,28] The formation of one product over the other, despite similar experimental conditions, is not known. The formation energies of bulk $NaO_2$ and $Na_2O_2$ are quite close and slightly favour the formation of $Na_2O_2$. However, the lower surface energy of nanoparticulate deposits that initially nucleate on the positive electrode surface favours the formation and growth of $NaO_2$.[31] The added phase transfer

catalyst ($H_2O$) kinetically drives the growth of this nanoparticulate phase upon initial nucleation of the superoxide, as previously discussed in *Section 1.3*.[24]

The electrochemical charge plateau at 2.3 V is accompanied by oxygen evolution, as shown in **Figure 6-3a**. This oxygen evolution is in near agreement with the theoretical 62.2 nmol/min $O_2$ evolution (based on a 100 uA discharge current). This oxygen evolution continues until the voltage rises to 3.0 V, at which point the oxygen evolution rate declines to zero. This suggests an overpotential must be exceeded to complete the process. This is ascribed to an impedance layer, which is discussed below. Integration of this $O_2$ rate (28.6 +/- 0.1 μmol) with respect to the total charge passed at 3.0 V corresponds to 1.10 $e^-/O_2$, as expected given the one-step oxidation of Na-$O_2$ to $Na^+$ and $O_2$. Deviation of this value from the expected 1.00 $e^-/O_2$ agrees closely with other reports that have probed the

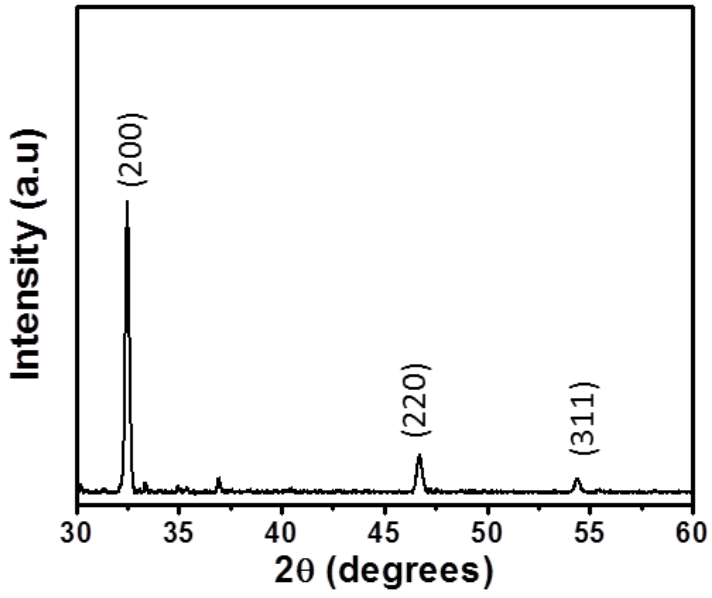


**Figure 6-4 -** Powder x-ray diffraction pattern of a 13C cathode after discharge to 1 mAh in 0.5M NaOTf/15 ppm $H_2O$/diglyme. The pattern is indexed to the cubic phase NaO2.

charge efficiency of the $NaO_2$ cell.[12,24] The loss in charge efficiency is due to electrochemical side reactions that produce degradation products (see below), as well as a small fraction of $NaO_2$ dissolution into the electrolyte. Following the initial charge plateau, there is a stepped voltage profile from 3.0 V to 4.5 V. At 3.2 V, $CO_2$ evolution occurs, followed by the evolution of additional $O_2$ at 3.8 V. This $CO_2$ evolution is ascribed to the oxidation of Na-carboxylates present on the positive electrode surface; a similar observation to that of Li-$O_2$ cells that utilize glyme-based electrolytes.[14] Both the gas evolution of $CO_2$ and $O_2$ appears to be finite, as both cease before electrolyte decomposition occurs at 4.45 V, which is evidenced by the flat voltage profile at this point. The total $NaO_2$ for positive electrodes discharged to 1 mAh was determined to be 33.9 ± 0.5 μmols by iodometric titration, approximately 90% of theoretical (37.7 μmol based on a 100% conversion of $O_2$ to $NaO_2$ via a one electron process). This value agrees with previous reports on $NaO_2$ formation after a single discharge step.[12] Thus, about 10% of the electrons passed cannot be accounted for based solely on the $NaO_2$ present in the cell.

To identify the efficiency of $NaO_2$ oxidation, the fraction of $NaO_2$ that remains on the electrode surface after charging the cell to 3.0 V was determined via iodometric titration. This value was chosen to correspond to the end of the initial $O_2$ evolution profile but before the onset of $CO_2$ evolution. Approximately 1.8 μmol of $NaO_2$ remains, equivalent to 5% of the $NaO_2$ that deposits on cell discharge. This explains the lower-than-ideal capacity measured on charge (~0.85 mAh vs 1 mAh). The capacity on charge can be fully accounted for based on the amount of $NaO_2$ present on discharge (90% of theoretical), less the $NaO_2$ that remains at 3.0 V (5%). This implies that no excess capacity is attributed to the electrochemical formation of decomposition products on the first charge, which will be

discussed in subsequent sections. The second oxygen evolution process in **Figure 6-3a** between 3.8 and 4.4 V corresponds to oxidation of the remaining $NaO_2$, as determined by iodometric analysis of the product at 4.4 V. Only a trace (~ 0.4 μmols of $NaO_2$) remains after this point, indicating that virtually all of the $NaO_2$ is removed prior to the start of electrolyte oxidation at 4.5 V. Given that the removal of $NaO_2$ from 3.0 V to 4.3 V equates to 1.4 μmol, this would be expected to show in the oxygen evolution profile, but integration of the $O_2$ evolution at V > 3.0 V in **Figure 6-3a** reveals only 0.3 μmols of $O_2$ evolves. This discrepancy implies that some of the $NaO_2$ must be consumed during electrochemical charge.

In order to assess and quantify the carboxylate and carbonate products formed on discharge, the $^{13}C$ positive electrode and separators were washed with THF and dried under vacuum. Two techniques were used to identify and quantify the fraction of degradation products. Prepared electrodes were immersed in $D_2O$ to extract the soluble species, providing the $^{1}H$ NMR spectrum shown in **Figure 6-5.** The background peaks of $D_2O$ (solvent) and residual diglyme electrolyte peaks dominate the spectrum. However, the presence of Na-carboxylate decomposition products (Na-formate and Na-acetate) are apparent, as well as the presence of a methoxy (oxo)acetic anhydride. The relative fraction of these products was determined by peak integration and comparison to the integration of the peak corresponding to the internal benzene standard. Mass spectrometry was also used to identify and quantify degradation products. The washed positive electrodes were subjected to acid treatment with 2M $H_3PO_4$, and on-line mass spectrometry quantified the total evolved $CO_2$ ($^{13}CO_2$) gases. The use of a $^{13}C$ carbon allows for the distinction between $CO_2$ (m/z = 44) in the cell. An example $CO_2$ evolution curve is shown in **Figure 6-6**, which shows the acid treatment of a positive electrode discharged to 1 mAh, and charged to 3.0 V. As can be seen, both the

evolution of $CO_2$ and $^{13}CO_2$ occurs, implying that the carbonate formation originates from both the positive electrode and the electrolyte. All experiments were carried out in multiples, and the quantity of side-products determined from the combined analysis. The analysis revealed that a majority of the degradation product is comprised of sodium acetate (~4% of total discharge product), along with equal contributions of sodium formate, methoxy (oxo)acetic anhydride, and $Na_2CO_3$ (~1% each of total discharge product). These data are summarized in **Figure 6-7** and **Table 6-1** and, which express the products as a percentage of the total theoretical $NaO_2$ expected. Only a small fraction of the total decomposition products (~0.5%) originate from the carbon positive electrode as $Na_2{}^{13}CO_3$.

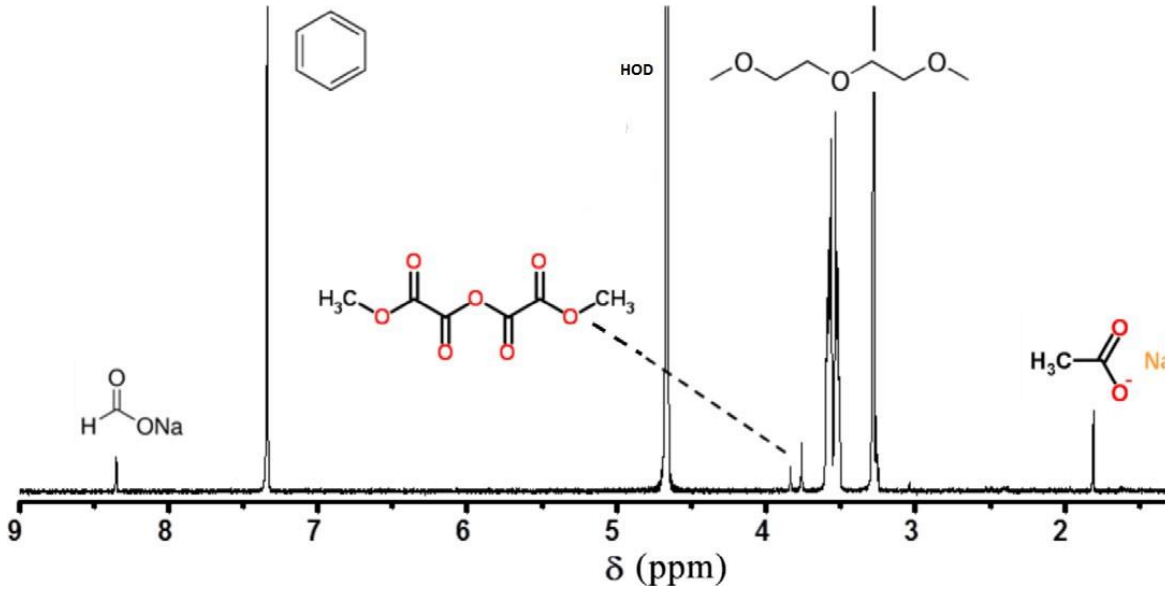


**Figure 6-5** - $^{1}H$ NMR spectrum of a $^{13}C$ cathode discharged to 1 mAh with major compounds identified: sodium formate = 8.4 ppm, sodium acetate = 1.8 ppm, methoxy (oxo)acetic anhydride =3.8 ppm. A known amount of benzene (7.3 ppm) was used as the internal standard

The degree of carboxylate degradation products formed on discharge depends on the positive electrode composition. Comparison of a very low surface area carbon fiber

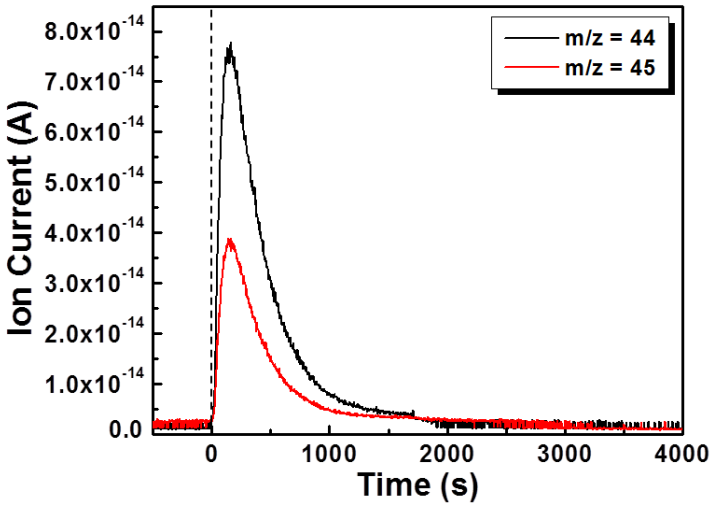


**Figure 6-6 -** The gas evolution profile monitored by on-line mass spectrometry, following 2M $H_3PO_4$ injection into an enclosure containing a $^{13}C$ cathode charged to a voltage of 3.0 V after previous discharge to 1.0 mAh (see Table S1). The gases correspond to $CO_2$ (m/z = 44) and $^{13}CO_2$ (m/z = 45).

positive electrode (Freudenberg GDL, H2315), with a high surface area carbon (Vulcan) (**Table 6-2)** shows that the Freudenberg positive electrode exhibits a much higher fraction of $NaO_2$ formed as a function of current passed (98%). This is reflected in the data by a low fraction of decomposition products, which are also less than those observed by the $^{13}C$ positive electrode. In contrast, the $NaO_2$ and carboxylate fraction exhibited on the Vulcan electrode is similar to that of the $^{13}C$ electrode. These findings agree with a study by Bender *et al*. that reports dramatic differences in the electrochemical performance of different carbon positive electrodes in the Na-$O_2$ cell.[32] They report that the discharge capacity and charge efficiency is dependent on the positive electrode material, with charge efficiencies ranging between 75% to 93%. This wide range is most likely due to variability in the decomposition products, although their nature was not addressed. A comprehensive examination of the role of the carbon is also beyond the scope of the present work. For the study presented here, $^{13}C$

positive electrodes were used in order to distinguish degradation from the positive electrode *vs* the electrolyte.

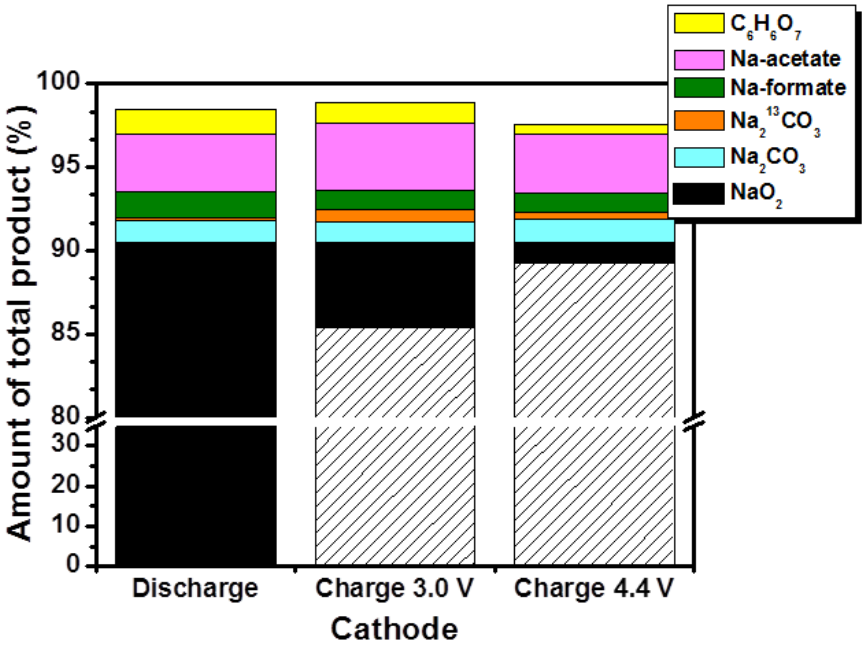


**Figure 6-7 -** Products as a fraction of the total theoretical product (37.7 μmol $NaO_2$) at different stages of cell operation. The $NaO_2$ fraction was determined from iodometric titration; and the identity and amount of sodium acetate, sodium formate, methoxy(oxo)acetic anhydride [$C_6H_6O_7$] and $Na_2CO_3$/$Na_2{}^{13}CO_3$ was determined from a combination of $^1$H NMR spectroscopy and acid treatment to evolve $CO_2$ from the carboxylates/carbonate which was measured by mass spectrometry.

In the Li-$O_2$ system it is known that some decomposition products form on discharge, while the majority of decomposition products are produced on charge due to the high potential to oxidize $Li_2O_2$.[12,13,14] Furthermore, as shown by Thotiyl *et. al.*, the stability of the carbon positive electrode is also a concern, for above 3.5 V the carbon undergoes oxidation in the presence of $Li_2O_2$ to form $Li_2CO_3$.[18] However, given the low charge overpotential of $NaO_2$, the Na-$O_2$ chemistry is reported to be less affected by side-

**Table 6-1 -** Absolute amounts of $NaO_2$ and degradation products formed in the cell at different stages of discharge (to 1 mAh) and charge. The total theoretical product is 37.7 μmol of $NaO_2$. Error in carboxylate/carbonate determination by NMR/acid treatment-mass spectrometry is difficult to estimate owing to the combination of methods used, but is on the order of 10-20%.

| | **Discharge (μmol)** | **Charge 3.0 V (μmol)** | **Charge 4.4 V (μmol)** |
|---|---|---|---|
| **$NaO_2$** | 33.9 (± 0.50) | 1.80 (± 0.20) | 0.37 (± 0.10) |
| **$Na_2CO_3$** | 0.5 | 0.5 | 0.5 |
| **$Na_2{}^{13}CO_3$** | 0.06 (± 0.02) | 0.26 (± 0.06) | 0.17 (± 0.06) |
| **Sodium formate** | 0.6 | 0.4 | 0.4 |
| **Sodium acetate** | 1.3 | 1.5 | 1.3 |
| **Methoxy (oxo)acetic anhydride** | 0.6 | 0.4 | 0.2 |

reactions.[10,12] To confirm that the majority of degradation products are formed on discharge, the decomposition products were analyzed after a cell was charged to 3.0 V prior to a discharge to 1 mAh. This was compared to the degree of decomposition product formation formed after only a single discharge. In agreement with McCloskey *et. al*, the fraction of decomposition products produced on charge is minimal, as shown in **Figure 6-7**.[12] The relative ratio of formate, acetate, carbonate, and anhydride is similar to that of the discharged positive electrode, implying that there is no additional decomposition on charge detectable by the methods used in this study. The only observable difference is that the amount of $Na_2{}^{13}CO_3$ has increased by ~ three folds compared to that of the discharged positive electrodes. Thus, while the charge overpotential for the $NaO_2$ cell is very low (~0.1 V vs. theoretical), it appears that, on charge, the potential is sufficient to promote the oxidation of the carbon surface to form a small fraction of $Na_2{}^{13}CO_3$. The formation of $Na_2{}^{13}CO_3$ could be the result of direct oxidation of the carbon with $NaO_2$, *via* the reaction $5NaO_2 + 2{}^{13}C \rightarrow 2Na_2{}^{13}CO_3 + 2O_2 + Na^+ + e^-$. The amount of $O_2$ that is generated from this reaction is too small to distinguish from the abundance of $O_2$ produced from $NaO_2$ oxidation.

**Table 6-2 -** Absolute amounts in μmols of $NaO_2$ and degradation products after discharge of different carbon electrodes to 1 mAh capacity. The theoretical amount of $NaO_2$ is 37.7 μmols. Error in $NaO_2$ determination by iodometric titration is estimated to be ± 0.50. Error in the other values is difficult to estimate owing to the combination of methods used, but is on the order of 10-20%.

| | **NaO2** | **$Na_2CO_3$** | **Na-formate** | **Na-acetate** | **Methoxy (oxo)acetic anhydride** |
|---|---|---|---|---|---|
| **$^{13}$C-carbon** | 33.9 | 0.5 | 0.6 | 1.3 | 0.6 |
| **Freudenberg** | 36.2 | 0.2 | Trace | 0.3 | Trace |
| **Vulcan** | 32.8 | 0.9 | Trace | 3.9 | 1.1 |

To determine if these carboxylate decomposition products are removed at high voltages and correspond to the $CO_2$ evolution that occurs at ~3.5 V, the products were analyzed by the methods mentioned above after the cell was charged to 4.4 V. Our results in **Figure 6-7** show that all of the carboxylate products remain, but with a small decrease in their total contents. Thus, it is plausible that some of the carboxylate species are oxidized at these potentials, as suggested from the small $CO_2$ evolution (**Figure 6-1a).** In a recent study by fellow colleagues, the electrochemical oxidation of Li-based decomposition products was probed to reveal that on a carbon surface, these decomposition products could not be oxidized at a potential below the stability window of the glyme-based electrolyte.[33] The inability to oxidize carboxylate decomposition products on the carbon surface at a low potential (> 4.7 V vs. $Li/Li^+$) was also confirmed by Meini et. al [34] and Leskes et. al.[15] Thus, either the charge voltage of 4.4 V is below the necessary voltage to charge the decomposition products, or subsequent decomposition occurs as these products are oxidized, as has been stated to occur with the $Li-O_2$ battery.[18] This further supports the conclusion that $NaO_2$ can be oxidized in the presence of non-removable decomposition products in the presence of a proton phase transfer catalyst, which governs the charging process [24]. The oxidation of $Li_2O_2$ does not pass through an $LiO_2$ intermediate,[35] and hence a proton phase

transfer catalyst in the Li-$O_2$ battery has little positive effect on charge.[36] The large overpotential for oxidation of $Li_2O_2$ is also partly due to the presence of surface carboxylates which increase the surface impedance.[37] The oxidation of $NaO_2$ that is solution mediated by a PTC is not impeded by the presence of these degradation products, however, leading to a lower charge overpotential. This is summarized in **Figure 6-8**.

### 6.3.1 – $O_2^-$/$NaO_2$ Oxidation of Diglyme

Hydrogen abstraction from glyme by the highly nucleophilic $O_2^-$ species is a known cause of DME decomposition in Li-$O_2$ cells, which leads to the formation of lithium formate and lithium carbonate on the positive electrode surface.[38,39,40] Recent work also suggests that reactivity of $Li_2O_2$ with water used to determine speciation in NMR experiments may exacerbate carboxylate formation.[41] Much research has been dedicated to the mitigation of electrolyte degradation by exploring alternative solvents, such as sulfones,[42] amides,[43] ionic liquids,[44] and backbone-protected ethers,[38] but no truly stable electrolyte has yet been discovered. In Li-$O_2$ cells another source of reactivity is the surface of $Li_2O_2$. Kumar *et al.* showed that the rate of glyme decomposition is more rapid on the superoxide-terminated ($O_2^-$) surface of $Li_2O_2$ than on that of its peroxide-terminated ($O_2^{2-}$) surface using a combination of computational techniques.[45] It was proposed that the highly reactive superoxide surface of $Li_2O_2$ accelerates the degradation of glyme by a mechanism similar to that of hydrogen abstraction by $O_2^-$. This has implications for the Na-$O_2$ cell, for it suggests that the superoxide $NaO_2$ surface plays a major role in the production of these decomposition products, which is confirmed in subsequent sections.

The formation of sodium formate, sodium acetate, and methoxy(oxo)acetic anhydride products, identified in the cell through NMR analysis enable us to propose a mechanism for

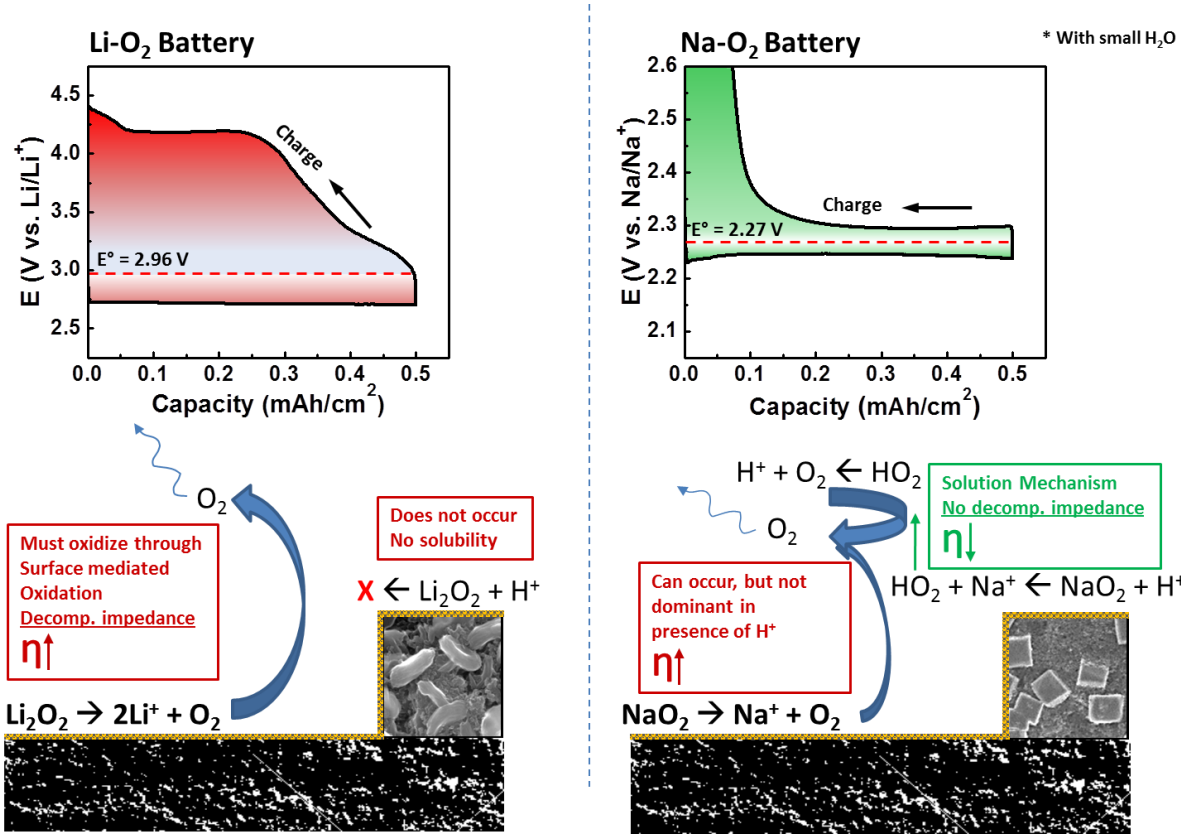


**Figure 6-8** – Schematic detailing the differences in oxidation of $Li_2O_2$ vs. $NaO_2$ in the presence of a PTC (in this case $H_2O$).

the decomposition of diglyme. (see **Figure 6-9**). In this scheme, sodium formate is generated via Path 1, where a methyl hydrogen ($H_\alpha$) abstraction by $O_2^{-\bullet}$ is followed by β-scission of an ether bond to give formaldehyde, which is then oxidized by highly nucleophilic $NaO_2$ to formate. The mechanism by which sodium acetate is generated requires translocation of a hydrogen atom to generate the required methyl-containing two carbon unit of acetate. The most plausible mechanism by which this could occur is an *intra*molecular 1,5-hydrogen abstraction, which conforms to the reactivity profile expected for radical species. A dialkyl ether radical (such as that generated during the initial β-scission of Path 1) would be expected to undergo a 1,5-hydrogen abstraction to give a thermodynamically favoured

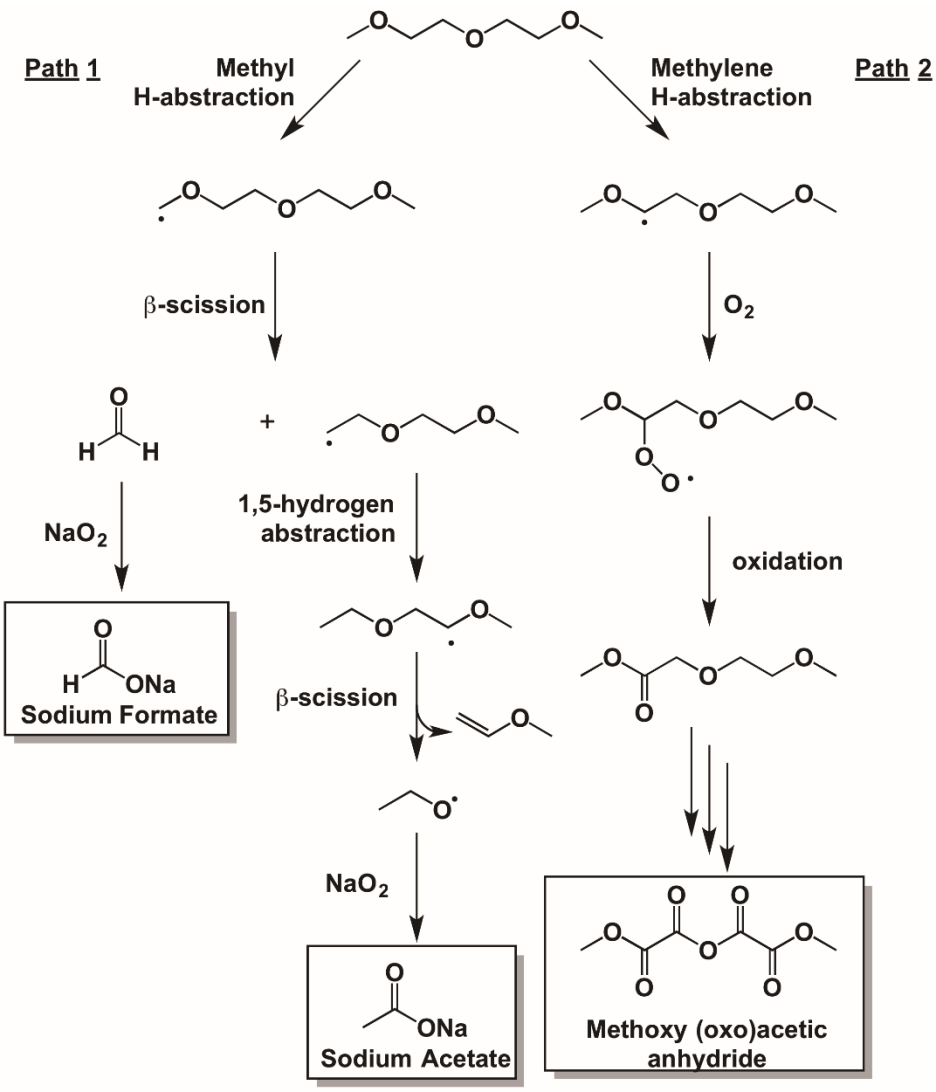


**Figure 6-9 -** Proposed reaction pathway for diglyme degradation. The formation of sodium formate and sodium acetate occurs via Path 1, and is initiated by a methyl hydrogen abstraction from the $O_2^-/NaO_2$. If hydrogen abstraction initially occurs from a methylene hydrogen, as shown in Path 2, the resultant product is methoxy (oxo)acetic anhydride.

oxygen-stabilized secondary radical. β-scission of this secondary radical produces methyl vinyl ether and an ethoxy radical, from which a hydrogen abstraction would lead to acetaldehyde and, upon further oxidation with $NaO_2$, sodium acetate. Whereas only sodium formate is observed for monoglyme, as shown previously in **Figure 1-10,** we note that the

1,5-intermolecular hydrogen abstraction reaction can only occur with higher order glyme electrolytes, explaining why a majority of sodium acetate is a side-product. The formation of methoxy(oxo)acetic anhydride and related compounds are proposed to occur via Path 2, as a result of sequential oxidation events where backbone methylene hydrogens ($H_\beta$) are abstracted by superoxide $O_2^{-\bullet}$ radicals. The predominance of sodium acetate (see below) suggests that hydrogen abstraction from the terminal hydrogen ($H_\alpha$) in diglyme, Path 1, is favored for sodium superoxide. On the other hand, computation[45] and experiment[38] suggests that $H_\beta$ abstraction is slightly more thermodynamically favourable for glyme in the presence of $Li_2O_2$, regardless of whether the surface is $O_2^-$ or $O_2^{2-}$ terminated. Nonetheless, the fact that we observe both Path 1 and Path 2 products in detectable amounts demonstrates the dynamic processes at play.

### 6.3.2 – Impact on Cell Cycling

$NaO_2$ and carboxylate products are not completely removed on charge to a typical 3.0 V, and that has significant implications for cell cycling. The impact of these decomposition products on subsequent cycles is shown in **Figure 6-10** below. **Figure 6-10a** shows a typical electrochemical curve of a cell cycled 4 times with a charge voltage limitation of 3.0 V, followed by a 5$^{th}$ charge with a voltage cut-off of 4.4 V. **Figure 6-10b** shows SEM images of the positive electrode surface at the end of the 5$^{th}$ discharge. The surface is covered with 8 μm x 8 μm $NaO_2$ cubes that possess a relatively clean, smooth surface. **Figure 6-10c** shows the appearance of the positive electrode surface at the end of the 5$^{th}$ charge, with the potential limit of 3.0 V (chosen to correspond to the initial $O_2$ evolution peak in **Figure 6-1a**). The surface is not completely covered with $NaO_2$ cubes, but is mostly populated with smaller cube-shaped structures. These resemble collapsed cubes that appear to have been oxidized

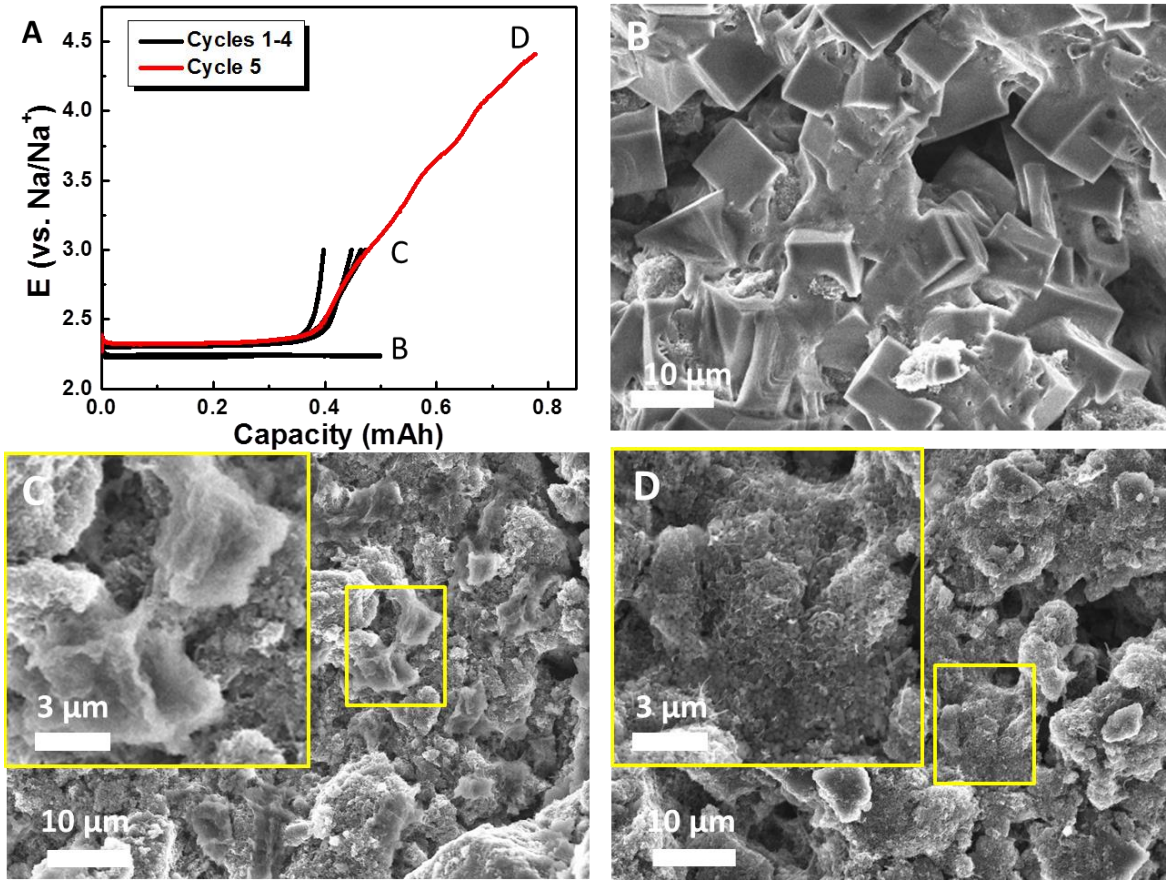


**Figure 6-10 – (**a) Electrochemical discharge/charge profiles of a $^{13}C$ cathode cycled 5 times, with the 5$^{th}$ charge ending at a voltage of 4.4 V. SEM micrographs of the cathode surface at (b) the end of 5$^{th}$ discharge; (c) the end of 5$^{th}$ charge to 3.0 V; (d) the end of 5$^{th}$ charge to 4.4 V.

from the center outwards, leaving behind a roughened shell. This suggests that the inner $NaO_2$ product is oxidized from within the interior of the cubes (*via* PTC in solution), leaving the surface of the cubes covered with sodium carboxylate products, which require a high overpotential for removal. On cycling within a voltage window of 3.0 V, both $NaO_2$ and decomposition products accumulate. This is confirmed by iodometric titration; after 5 cycles with a charge limitation of 3.0 V, 4.48 µmols of $NaO_2$ remain, which is greater than the amount of $NaO_2$ remaining after a single discharge/charge cycle (1.80 µmol, from previous).

To fully remove the remaining species that cannot be oxidized at V < 3.0 V, the positive electrode was charged to 4.4 V on the last cycle. This voltage limitation was selected because it is beyond the point of $CO_2$ and $O_2$ gas evolution, but below that of electrolyte decomposition. The SEM image in **Figure 6-10d** shows a clean positive electrode surface.

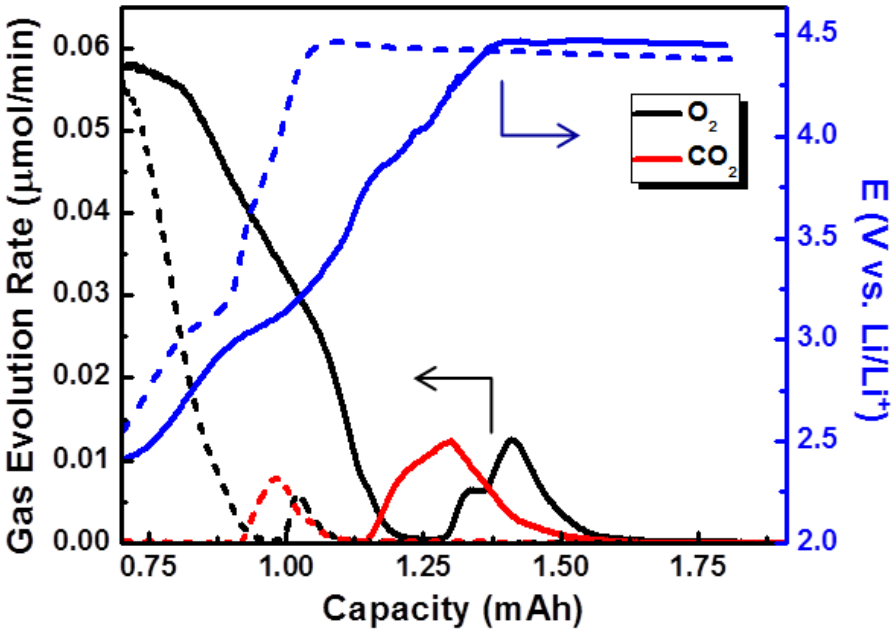


**Figure 6-11 -** Electrochemical profile (blue curve) together with $O_2$ (black curve) and $CO_2$ (red curve) evolution profiles for a cell charged on the 1st cycle (dotted line) and the 5th cycle (solid line). The 5th charge was obtained after 4 cycles with a charge voltage limitation of 3.0 V and a capacity limitation of 1.0 mAh. The fraction of $CO_2$ and $O_2$ generated beyond 3.0 V is greater for the 5th cycle compared to the 1st cycle due to the respective oxidation of accumulated sodium carboxylates, and $NaO_2$ that could not be oxidized at V < 3.0.

The amount of $CO_2$ and $O_2$ that is evolved on the 5th charge process beyond 3.0 V is greater than that of charging beyond 3.0 V for a single discharge process, as shown in **Figure 6-11**. In summary, while the generation and decomposition of $NaO_2$ could occur on cycling in a narrow window if it were the only product, excess charge to higher voltage is necessary in

order to completely remove the remaining $NaO_2$ that is trapped due to the accumulation of carboxylate-based decomposition products. However, cycling a cell with this upper limitation is not an ideal method to improve Na-$O_2$ cell cycling.

As was shown, the complete removal of the $NaO_2$ only occurs when the cell voltage is raised to 4.3 V. The effect of cycling a cell to an upper potential limit of 4.4 V is illustrated by the working electrode profile (**Figure 6-12**). Cycles beyond the first show clear decomposition in the cell, alongside a reduction in obtainable charge capacity. On the subsequent discharge, an overpotential that precedes the normal ORR discharge plateau is ascribed to the reduction of a species generated at high charge potential. Its nature has yet to be identified. In contrast to Hartmann et. al [10], the cell is still able to discharge after it is charged to a high potential. Another difficulty with a high voltage limitation on charge is illustrated in **Figure 6-12b,** by a plot of the working potential of the negative electrode with respect to a sodium metal reference electrode. Charging of a Na-$O_2$ cell to the voltage necessary to remove carboxylates is detrimental to the sodium metal negative electrode. The overpotential required to strip sodium from the negative electrode increases with every cycle, implying the growth of an insulation layer on the sodium metal negative electrode. We speculate that this is due to the accumulation of decomposition products and impedance layers that form on the metallic sodium negative electrode. This is in contrast to a cell operated within the potential window between 1.8 V vs. 3.0 V, where it is shown in **Figure 6-14** that the stripping/plating profile of the negative electrode does not change upon repeated cycling, and that the stripping voltage occurs at a much lower potential. Such a profile is representative of the electrochemical stripping/plating of lithium in glyme-based electrolytes.[46] However, the cell can only achieve < 20 cycles with a charge voltage cut-off

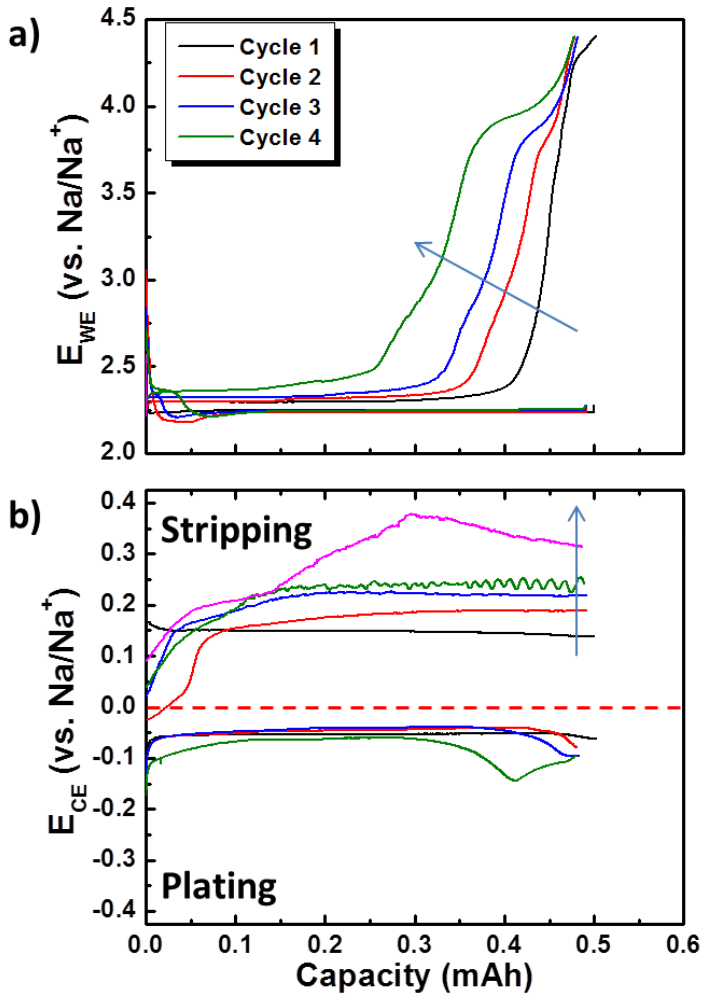


**Figure 6-12 – (**a) Working electrode and (b) counter electrode potential of a Na-$O_2$ cell using a $^{13}C$ cathode cycled 5 times with an upper potential limit of 4.4 V. Plating of sodium onto the anode occurs when the cathode is charged, and stripping of the anode occurs when the cathode is discharged.

of 3.0 V, as shown in **Figure 6-15**. At this point, capacity fading begins, followed by eventual cell termination. It is clear that accumulation of the discharge product is the cause of termination, as evidenced by visual inspection of the positive electrode (**Figure 6-14 inset)**. Other methods are necessary in order to completely oxidize $NaO_2$ since their removal *via* electrochemical charge not only requires a large overpotential, but also accelerates

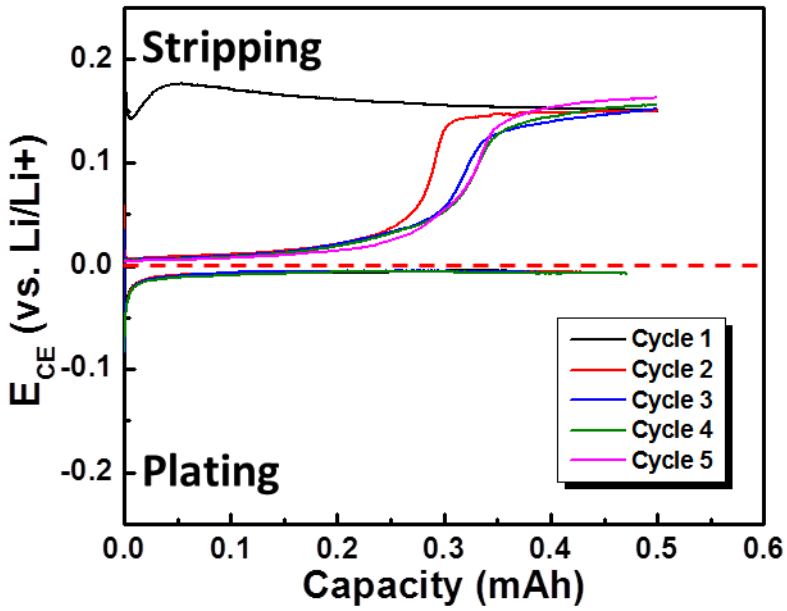


**Figure 6-13 -** The voltage profile of the metallic metal negative electrode (*i.e.,* counter electrode) in a Na-$O_2$ cell cycled with a working electrode ($^{13}C$- carbon) cut-off potential of 3.0 V on charge. The stripping/plating profile shows very little variance from cycle to cycle.

decomposition reactions.

### 6.3.3 – Reactivity of Na-$O_2$ with Diglyme

Reactivity of $NaO_2$ with diglyme can be of concern for the lifetime of Na-$O_2$ cells that utilize this electrolyte (which at the time of this publication, are the majority of reports), as any period of rest in a cell at open circuit voltage (OCV) could induce electrolyte decomposition and consumption of the superoxide. To "mimic" OCV conditions on discharge, diglyme was reacted with $KO_2$ in the presence of crown ether. Superoxide, *i.e.,* "solvated $O_2^-$" was liberated through chelation of $K^+$ ions with dicyclohexyl-18-crown-6 (crown ether).[47] This method was previously utilized to determine electrolyte stability (*Section 3.0).*[6,38,48] For comparison, a second solution was prepared with the same

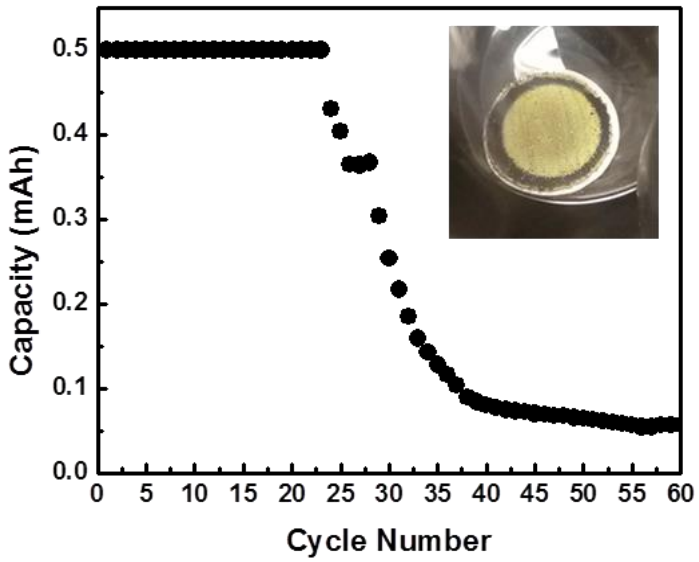


**Figure 6-14** - Discharge capacity as a function of cycle number of a $^{13}C$ cathode in 0.5M NaOTf/15 ppm $H_2O$/diglyme electrolyte. The cell was operated with a capacity limitation of 0.5 mAh, in a voltage window of 1.8 – 3.0 V. Approximately 20 cycles are reached before capacity fade begins, where a rapid decrease in capacity is observed, that eventually leads to cell death. A post-mortem image of the cathode is shown in the inset.

concentration of $KO_2$/crown-ether, except sodium triflate was added to the reaction after 1 hour to immediately trigger precipitation of $NaO_2$. Reactivity of solvated $O_2^-$ can thus be partly distinguished from the reactivity of $NaO_2$, although we recognize that sodium superoxide itself has some, albeit limited, solubility in diglyme.[24] After the solutions were allowed to stir to mimic cell conditions, the solids were recovered and analyzed with $^{`1}H$-NMR. As is shown in **Figure 6-15**, regardless of whether $O_2^-$ or $NaO_2$ is present, acetate and formate are both observed, but approximately 3-5 fold more decomposition products are observed when $NaO_2$ is generated in the solution. The proportion of formate/acetate also varies. In the presence of $O_2^-$, Na-formate is the most abundant product, with only a minimal amount of Na-acetate present (Na-acetate/Na-formate = 0.18). In the presence of $NaO_2$, the

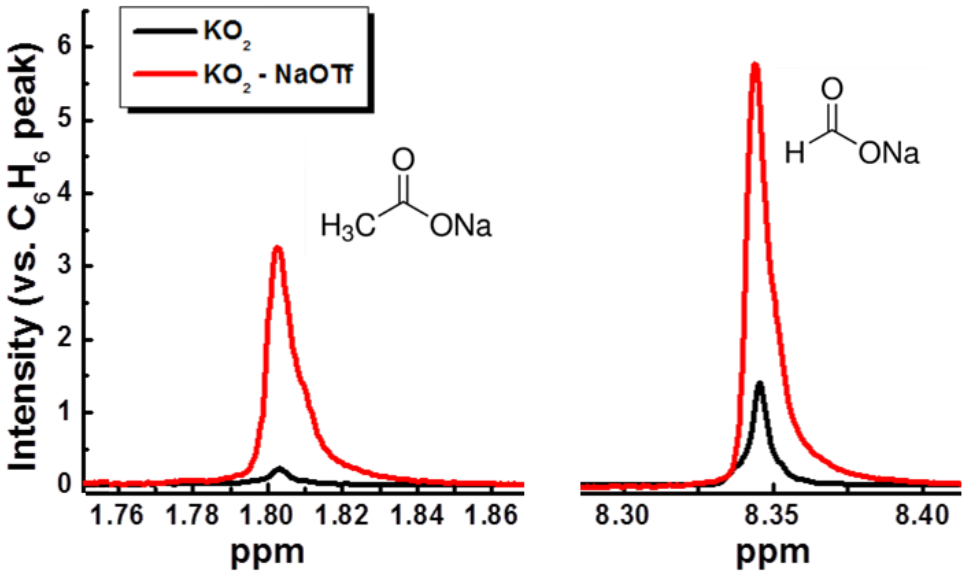


**Figure 6-15 -** $^{1}$H NMR solution spectra of $D_2O$-extracted solid products after exposure of diglyme to chemically generated $O_2^-$ for four days. Each reaction was conducted with 2.5 mL diglyme, 0.02 g $KO_2$, and 0.13 g crown ether (black line). To generate $NaO_2$, 0.1g of NaOTf was introduced into the solution at the same time as $KO_2$/crown ether addition (red line). The spectral peaks are assigned to sodium acetate (left) and sodium formate (right). Both spectra were normalized to an internal benzene standard.

proportion of Na-acetate is nearly three-fold larger (Na-acetate/Na-formate = 0.60). The reason for this difference is not yet understood, but it may result from a surface vs. solution reactivity.

To further confirm reactivity of $NaO_2$ with the electrolyte, $^{13}$C positive electrodes were discharged to a capacity of 1 mAh and held for a period of 100 hours at OCV. The SEM images in **Figure 6-16a** and **6-16b** display the altered $NaO_2$ morphology after extended diglyme exposure. The surface appears to be rough, with clear alteration of the normal cube morphology. A similar phenomenon was observed by Hartmann *et. al*, who noticed a change in the $NaO_2$ morphology as the discharged positive electrode was left to rest while exposed to

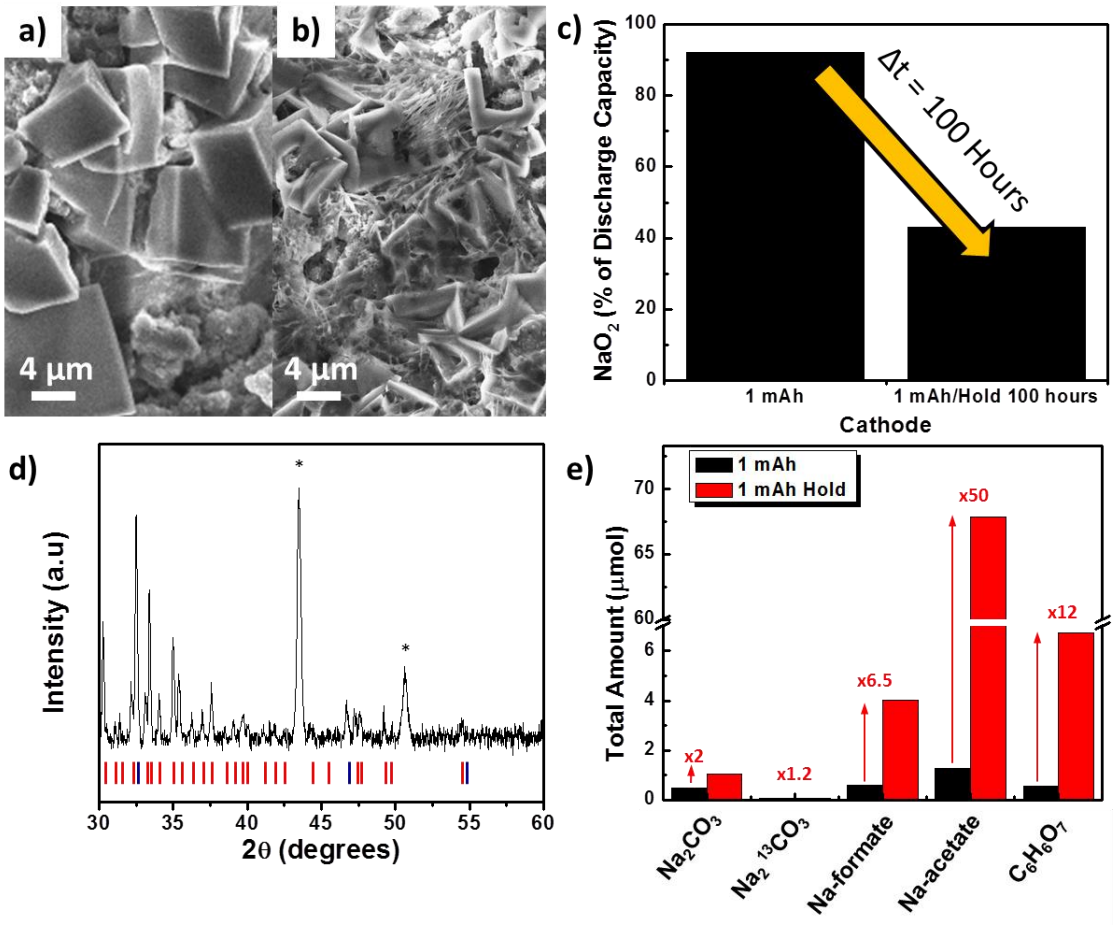


**Figure 6-16** - SEM images of (a) a discharged cathode removed immediately upon completion of discharge; and (b) a discharged cathode rested at open circuit potential in the cell for 100 hours; (c) comparison of the fraction of $NaO_2$ in the product at the end of discharge, and after 100 hours of rest based on the theoretical capacity of 1 mAh (37.7 µmols); (d) X-ray diffraction pattern of the product of cell discharge after rest at open circuit for 100 hours. A mixture of $NaO_2$ (blue ticks) and $Na_2O_2•8H_2O$ (red ticks) is formed, as shown by comparison of the reflections to those in the JCPDS data base; asterisks represent the stainless steel mesh current collector; (e) Decomposition products of the freshly discharged cathode compared to the discharged cathode held at open circuit potential for 100 hours.

the electrolyte.[10] The total amount of $NaO_2$ after 100 hour exposure is 16 µmols, determined by iodometric titration. This is only 43% of the theoretical value, and nearly 50% less than that of the $NaO_2$ amount on a freshly discharged positive electrode (**Figure 6-16c)**. X-ray diffraction analysis of the product, shown in **Figure 6-16d**, reveals a large proportion

of $Na_2O_2$•$8H_2O$. Compared to the freshly discharged positive electrode, it is clear that the reduction in $NaO_x$ purity is associated with a very large increase in the amount of carboxylate-based decomposition products. While the fraction of sodium carbonate doubles during the rest period, the fraction of sodium acetate increases by as much as 50-fold, with a lesser increase in formate. It is clear that the reaction pathway of sodium acetate formation (Figure 4 above) is kinetically favoured compared to the formation of sodium formate. We postulate that, after the initial β-scission, the fragmented anion radical remains on the NaO2 surface (to produce sodium acetate), while the formaldehyde dissolves in solution and thus its conversion to sodium formate is less favored, by comparison. This agrees with the quantification of the reaction products described above, which shows an increased fraction of sodium acetate resulting from contact of diglyme with $NaO_2$. The SEM images (**Figure 6-16a,b)** indicate that the interior of the $NaO_2$ cubes have been etched away in this process, leaving hollow outer shells. This suggests that the outer surface of the $NaO_2$ crystallites react with diglyme to form a passivating layer of Na-carboxylate, and as the cubes crack, dissolution/reaction of the interior superoxide follows. As expected, the fraction of $Na_2{}^{13}CO_3$ remains unaltered, since no new $NaO_2$ contacts the carbon surface during OCV.

## 6.4 – Conclusion and Future Work

This study of the decomposition products formed during operation of a Na-$O_2$ battery shows that on cell discharge solvated $O_2^-$ and $NaO_2$ react with both the carbon positive electrode and the diglyme electrolyte to form a variety of Na-carboxylate decomposition products. On charge, little additional decomposition occurs. The consumption of $NaO_2$ through chemical reactivity with diglyme (to form sodium carboxylates) gives rise to the majority of the capacity loss. Even in the presence of these decomposition products, a large

overpotential is not observed for the oxidation of $NaO_2$, which is in contrast to the oxidation of $Li_2O_2$ in the Li-$O_2$ battery. The key to this is the solution-based oxidation mediated by a proton phase transfer catalyst. However, since both the decomposition products, as well as 100% of the $NaO_2$, cannot be oxidized within this narrow electrochemical window, these products accumulate over many cycles, leading to cell death. This differs from the Li-$O_2$ cell, where electrolyte degradation is exacerbated on charge owing to inherently high overpotentials unless redox mediators are used. In the Li-$O_2$ cell, the rapid conversion of lithium superoxide to lithium peroxide means that superoxide does not aggravate glyme degradation on discharge. Thus, while the low charge overpotential of the Na-$O_2$ cell limits the fraction of decomposition products that form on charge, the highly reactive $O_2^-$ (or $HO_2$), as well as the nucleophilic character of the $NaO_2$ itself, make glyme-based electrolyte degradation in the $NaO_2$ cell a very real concern. This is especially true on storage, because the formation of $Na_2O_2 \cdot 8H_2O$ occurs upon extended exposure to diglyme, and requires a high voltage to oxidize.

Future work in this area must focus on the stability of the organic media. As has been stated throughout this thesis, the formulation of an electrolyte that is stable to $O_2^-/NaO_2$, and exhibits desirable properties is crucial for the long term-success of not only the Na-$O_2$ battery, but metal-$O_2$ batteries in general. Another avenue that has only recently been explored for the Li-$O_2$ battery (and not for the Na-$O_2$ battery) are electrochemical redox mediators.[49,50,51,52] In Li-$O_2$ batteries, these are primarily utilized to chemically oxidize $Li_2O_2$ while limiting the charge voltage to the oxidation potential of the redox mediator itself. While the Na-$O_2$ battery already exhibits a small overpotential, these mediators can be utilized to chemically oxidize $NaO_2$ so that its exposure to the glyme electrolyte is kept to a

minimum. Electrolyte additives can also potentially be utilized to “cap” the surface of $NaO_2$, making it less reactive towards the electrolyte/positive electrode surface. The possibilities are endless when it comes to electrolyte additives, which is the future of the metal-$O_2$ field.

## 7.0 - Final Thoughts and Perspective on the Metal-$O_2$ Battery Field

In *Section 3*, Li-$O_2$ battery materials were screened for chemical stability against $O_2^-$. It was shown that the chemical method of $O_2^-$ generation, *via* the chelation of $KO_2$ with 18-crown-6 ether as a means to generate $O_2^-$ in solution, well represented the chemistry of a Li-$O_2$ battery through the generation of $Li_2O_2$ as the discharge product. This chemical method of $O_2^-$ generation is an ideal tool for screening the reactivity of various cell components with $O_2^-$ as it completely removes the influence of parasitic reactions that are electrochemical in nature. The impact of carbon powder (KB) on the formation of $Li_2O_2$ was discussed. It was concluded that the functional groups on the carbon surface influence the $O_2^-/LiO_2$ binding and affect the final morphology (and crystallinity) of the $Li_2O_2$ product. Popular binder materials, such as PVdF and Li-Nafion were also tested for stability. PVdF is susceptible to hydrogen abstraction by $O_2^-$, causing a defluorination of the polymer backbone, which in turn decomposes the PVdF polymer into parasitic by-products such as $H_2O_2$. In the presence of a catalyst that can promote the oxidation of $H_2O_2$, such as α-$MnO_2$, this leads to the generation of $H_2O$ within the Li-$O_2$ cell and causes the main discharge product to be LiOH, and not $Li_2O_2$.

Apart from positive electrode materials, the chemical generation of $O_2^-$ can also be used to screen for the stability of various solvents used as electrolytes in the Li-$O_2$ cell. Chemically generated $O_2^-$ reacts with PC to form a variety of Li-carboxylates and propylene glycol. With ether based electrolytes, such as TEGDME, $O_2^-$ abstracts the hydrogen atoms on the glyme backbone, leading to the formation of various Li-carboxylates, such as Li-formate and Li-acetate. These are similar to known products that are produced in electrochemical Li-$O_2$ cells. Hence, the severe reactivity of $O_2^-$ towards various Li-$O_2$ cell components is a

pressing concern for long-term cell stability, and the proposed $KO_2$-based screening procedure is an effective tool to diagnose and assess these instabilities with newly developed electrolyte systems. From this study, it is concluded that current Li-$O_2$ materials, in particular ether-based electrolytes, are unsuitable for use in Li-$O_2$ batteries. Hence, further development of $O_2^-$/$LiO_2$ stable electrolytes that will allow for efficient $O_2$ solubility and mass transport are necessary for future progress and commercialization of the Li-$O_2$ battery.

The concept of Li-$O_2$ catalysis and the influence of degradation products was presented and discussed in *Section 4*. This study investigated the use of $Co_3O_4$/RGO as a catalyst material for the Li-$O_2$ battery. The synthesis of $Co_3O_4$/RGO was presented and the material characterized. The activity of $Co_3O_4$/RGO in a Li-$O_2$ battery was determined through full-cell Li-$O_2$ experiments, as well as fundamental electrochemical studies. In a cell with 1M $LiPF_6$/TEGDME as the electrolyte, the $Co_3O_4$/RGO mixed with KB positive electrode exhibits improved voltage efficiency and capacity retention on cycling compared to an electrode comprised of KB alone. However, with the use of cyclic voltammetry, chronoamperommetry, and linear sweep voltammetry, the function of $Co_3O_4$/RGO towards $Li_2O_2$ oxidation is unlike that of traditional electrolcatalysts. Instead, the $Co_3O_4$ acts as a $Li_2O_2$ oxidation promoter and enhances the surface mobility of the $Li_2O_2$/$LiO_2$/$O_2^-$ species to lower the binding energy compared to that of a highly functionalized carbon surface.

This study also highlighted some major issues with catalyst materials in the Li-$O_2$ battery. Specifically, the active sites on a catalyst surface are only active for the first few cycles. This is evident through poor cycling efficiencies and the loss of the catalytic effect on ORR/OER voltages beyond the first cycle. Through analysis via TOFSIMS, it is confirmed that decomposition products form during ORR/OER and cover the positive electrode surface.

These decomposition species, primarily composed of Li-carboxylates, are insulating in nature and require a high voltage to remove; a voltage greater than the electrochemical window of the electrolyte. Hence, after a single cycle, these products cover the electrode surface and diminish any active material activity, eventually leading to cell failure after tens of cycles due to complete deactivation of the electrode surface. This draws us to the major issue with the Li-$O_2$ cell, which is the instability of the electrolyte. Many new electrode materials can be developed and used in a Li-$O_2$ cell that may greatly improve the ORR/OER kinetics. However, the reactivity of the electrolyte with $O_2^-$ and $Li_2O_2$ will ultimately cause the formation of decomposition products that limit the cell cycling stability. This issue is a major set-back for Li-$O_2$ development, for until the electrolyte problem can be solved, the true potential of new positive electrode materials cannot be realized.

In *Section 5* I presented the development of an analytical tool that is crucial to understand the true chemistry that occurs during the ORR/OER processes of a Li-$O_2$ cell. To best suit my lab group need's, the mass spectrometer was designed in a way to allow quantification of gas evolution without interfering with any cell chemistry. The design process was presented, along with analysis of various mass spectrometer components to meet the stringent requirements necessary for quantification. The use of mass spectrometry as an analytical tool is demonstrated with pre-filled $Li_2O_2$/active material composites. The inefficiencies that arise during $Li_2O_2$ oxidation were quantified. The benefits of using non-powder carbon positive electrodes are evident from monitoring the volume of $CO_2$ that evolves as a result of the $Li_2O_2$/carbon interface reactivity. Other materials, such as TiC, are more stable towards reactivity with $Li_2O_2$, and hence should be used as a positive electrode material over carbon powder. The stability of two electrolytes (TEGDME and DMSO) are

also presented in terms of their $O_2$ evolution efficiency for $Li_2O_2$ oxidation. The lack of a 2 $e^-$/$O_2$ evolution ratio indicates parasitic reactions occur during charge. TEGDME appears to be a more suitable electrolyte than DMSO, but neither is truly ideal. Furthermore, the parasitic reactions that occur during cell discharge (electrochemical production of $Li_2O_2$) are shown to have a strong impact on $Li_2O_2$ oxidation. Hence, with the use of mass spectrometry and the studies presented here, it is shown that major inefficiencies in the Li-$O_2$ cell occur as a result of primarily the Li-$O_2$ chemistry. The main product that is formed, $Li_2O_2$, goes through a highly reactive intermediate $O_2^-$ that is the source of cell decomposition.

The importance of analytical tools to directly monitor the gas evolution is presented through a case-study with $Mo_2C$ as a positive electrode material. $Mo_2C$ exhibits a very low charge overpotential compared to other electrode materials, such as carbon and TiC. This is accompanied by the removal of $Li_2O_2$ on the positive electrode surface, as would be expected of an ideal positive electrode material. However, the oxidation of $Li_2O_2$ is very inefficient and produces little $O_2$. Instead, the $Li_2O_2$ reacts with the $Mo_2C$ surface to produce $Li_xMoO_3$. The $Li_xMoO_3$ species dissolves into solution, which cleanses the surface of $Mo_2C$ and frees more ORR/OER active sites, but at the cost of positive electrode consumption. While efficient formation and oxidation of $Li_2O_2$ was presumed from the electrochemistry and product analysis, it is clear this is not the case upon closer inspection of the oxidation efficiency via mass spectrometry. With many more positive electrode materials and electrolytes being tested in Li-$O_2$ cells, I cannot stress enough that it be a requirement that monitoring $O_2$ consumption and evolution be part of future studies as to avoid the misconceptions of efficient $Li_2O_2$ cycling based on the electrochemistry alone.

The final section of this dissertation, *Section 6*, assesses and quantifies the degree of decomposition that occurs during operation of a Na-$O_2$ cell utilizing glyme-based electrolytes. Much like the initial discharge reaction in Li-$O_2$ batteries, the Na-$O_2$ battery produces $O_2^-$ /$NaO_2$ during discharge. Hence, the Na-$O_2$ battery also undergoes a significant degree of decomposition originating from both the electrolyte and the positive electrode. These products are quantified with mass spectrometry, iodometric titration, and $^1$H NMR, and can be directly correlated to the cell voltage characteristics. Unlike the Li-$O_2$ battery, the majority of degradation occurs on cell discharge, with very little decomposition product formation on cell charge. These degradation products are Na-formate, Na-acetate, and oxo(acetic) anhydride. Furthermore, even in the presence of these decomposition products, the Na-$O_2$ battery exhibits a low charge potential. The key to maintaining this low overpotential is the action of a PTC, which promotes the oxidation of $NaO_2$ in solution as opposed to oxidation on the positive electrode surface. Hence, the oxidation of $NaO_2$ can occur within the presence of decomposition products on the surface. The oxidation of the decomposition products, however, is not possible in the operating window of the Na-$O_2$ battery, and hence the degradation products accumulate on cell cycling, and eventually lead to cell death.

It is clear that the $NaO_2/O_2^-$ are the primary culprits for degradation reactions in the Na-$O_2$ battery. This is proven by exposing freshly generated $NaO_2$ to the glyme electrolyte for an extended period of time. The result is the consumption of $NaO_2$ and greatly enhanced degree of electrolyte degradation, as evident through a nearly fifty times increase in the fraction of Na-carboxylate products. The implications of this are catastrophic for the Na-$O_2$ cell, and raises great concerns about the long-term stability of the battery, especially if the product is to ever reach commercialization.

The work presented throughout this thesis clearly identifies the current limitations of aprotic metal-$O_2$ batteries. While new literature that focuses on new and exciting positive electrode materials for metal-$O_2$ batteries is constantly being produced, there are a severe lack of studies address the real issue of metal-$O_2$ batteries – the electrolyte. Unless a stable aprotic electrolyte that is resistant to $O_2^-$ can be produced, the future of aprotic metal-$O_2$ batteries looks grim. What I have presented are methods and tools to help identify the degree of degradation reactions in metal-$O_2$ batteries as a means to better understand where the true problems lie for both the Li-$O_2$ and Na-$O_2$ batteries. These two battery systems operate in a similar manner, but the issues which impede their improvement are fundamentally distinct. Hopefully, the development of new electrolytes with stabilizing additives accelerates so that a more stable metal-$O_2$ system can be realized. Only advancements such as these will create the leap in the metal-$O_2$ battery technology that is necessary to meet today's energy demands and ultimately allow for commercialization of this new technology.

## List of Publications

**R. Black**, A. Shyamsunder, P. Adeli, D. Kundu, G. Murphy, L. F. Nazar. Quantification and Effect of Electrolyte/Positive electrode Decomposition in the Na-$O_2$ Battery. *Accepted – ChemSusChem*, 2016.

D. Kundu, **R. Black**., B. Adams, L. F. Nazar. A Highly Active Low Voltage Redox Mediator for Enhanced Rechargeability of Lithium-Oxygen Batteries, *ACS Central Sci.* 2015, 1, 510-515.

D. Kundu, **R. Black**, B. Adams, K. Harrison, K. Zavadil, L. F. Nazar, Nanostructured Metal Carbides for Aprotic Li-O2 Batteries: New Insights into Interfacial Reactions and Positive electrode Stability, *J. Phys. Chem. Lett.* 2015, 6, 2252-2258.

X. Chun, **R. Black,** R. Fernandez, B. Adams, L. F. Nazar**,** The Critical Role of Phase Transfer Catalysts in Aprotic Sodium Oxygen Batteries, *Nat. Chem.* 2015, 7, 496-501.

V. Duffort, E. Talaie, **R. Black**, L. F. Nazar, Uptake of $CO_2$ in Layered $P_2Na_{0.67}Mn_{0.5}Fe_{0.5}O_2$: Insertion of Carbonate Ions, *Chem. Mat*, 2015, 27 (7), 2515-2524.

D. Kundu, **R. Black**, L. F. Nazar, A Highly Active Nanostructured Metallic Oxide Positive electrode for Aprotic Li-$O_2$ Batteries, *Energy Env. Sci*. 2015, 8 (4), 1292-1298.

B. Adams, **R. Black**, C. Radtke, Z. Williams, L. Medhi, N. Browning, L. F. Nazar, The Importance of Nanometric Passivating Films on Positive electrodes of the Lithium Oxygen Battery, *ACS Nano*, 2014, 8 (12), 12483 – 12493.

M. H. Cho, J. Trottier, C. Gagnon, P. Hovington, D. Clement, A. Vijh, C.S. Kim, A. Guerfi, **R. Black**, L. Nazar, K. Zaghib, The Effects of Moisture Contamination in the Li-$O_2$ Battery, *J. Power Sources*. 2014, 268, 565-574.

B. Adams, **R. Black**, G. Murphy, Z. Williams, R. Fernandes, M. Cuisinier, E. Berg, P. Novak, L. F. Nazar, Towards a Stable Electrolyte for the Lithium Oxygen Battery, *Adv. Energy Mat.* 2015, 5, 1400867.

T. Song, H. Cheng, K. Town, H. Park, **R. Black**, S. Lee, W. Park, Y. Huang, J. Rogers, L.F. Nazar, U. Paik, Electrochemical Properties of Si-Ge Heterostructures as an Negative electrode Material for Lithium Ion Batteries, *Adv. Funct. Mat.* 2013, 1-7.

B. Adams, C. Radtke, **R. Black**, M. Trudeau, K. Zaghib, L.F. Nazar, Current Density Dependence of peroxide Formation in the Li-$O_2$ Battery and its Effect on Charge, *Energy Environ. Sci.* 2013, **6**, 1772-1778.

**R. Black**, Jin-Hyon Lee, B. Adams, C. Mims, and L.F. Nazar, The Role of Catalysts and Peroxide Oxidation in Li-O2 Batteries, *Angew. Chem.* 2012, 52, 392-396 .

S. H. Oh, **R. Black**, E. Pomerantseva, J.H Lee and L.F. Nazar, Synthesis of Nano-Metallic/Porous Oxides as Catalysts for the Li-Air Battery, *Nat. Chem*. 2012, 4, 1004-1010.

J.H. Lee, **R. Black**, E. Pomerantseva, S.H. Oh, G. Botton, F. Nan, and L. F. Nazar, 2012, Na0.44MnO2 Nanowire Catalyzed Lithium-Air Batteries, *Energy Environ. Sci*. 2012, 5 (11), 9558 - 9565.

**R. Black**, B. Adams, and L.F. Nazar, 2012, Non-Aqueous and Hybrid Li-O2 Batteries, *Adv. Energy Mater*. 2012, (7) 801-815.

A. Kim, **R. Black**, Y-J. Hyun, L.F. Nazar, E. Prouzet, Monolithic Mesoporous Silica and Carbon Synthesized in Sponge-like Swollen Liquid Crystals, *Chem. Comm*, 2012, 48, 4335-4337.

**R. Black**, S. Oh, T. Yim, J.H. Lee, B. Adams, and L.F. Nazar, Screening for Superoxide Reactivity in Li-O2 Batteries, *J. Am. Chem. Soc*. 2012, 134 (6), 2902–2905.

X. Ji, S. Evers, **R. Black**, and L.F. Nazar, Stabilizing Lithium-Sulphur Positive electrodes Using Polysulphide Reservoirs, *Nat. Comm*, 2011, 2, 325-3

# References

## Section 1 References


[1] P. G. Bruce, S. A. Freunberger, L. J. Hardwick, J.M. Tarascon. "Li–$O_2$ and Li–S batteries with high energy storage." *Nature Mater.* vol. 11, pp.19-29, 2012.

[2] N. Imanishi, A. C. Luntz, P. G. Bruce, Eds., *The Lithium Air Battery: Fundamentals.* New York, NY: Springer Science + Business Media, 2014.

[3] IBM (2012). *The Battery 500 Project* [Online]. Available at http://www.ibm.com/smarter planet/us/en/smart_grid/article/battery500.html

[4] B.D. McCloskey, A. Speidel, R. Scheffler, "On the Mechanism of Nonaqueous Li-$O_2$ Electrochemistry on C and its Kinetic Overpotentials: Some Implications for Li-Air batteries." *J. Phys. Chem. C.*, Vol. 116, no. 45, pp.23897-23905, 2012.

[5] J. Yang, D. Zhai, H.H. Wang, K. C. Lau, J. A. Schlueter, P. Du, D. J. Myers, Y.K. Sun, L. A. Curtiss, K. Amine, "Evidence for Lithium Superoxide-like Species in the Discharge Product of Li-$O_2$ Battery." *Phys. Chem. Chem. Phys.* Vol. 15, pp.3764 – 3771, 2013.

[6] W. Das, K. C. Lau, P. Redfern, L. A. Curtiss, "Structure and Stability of Lithium Superoxide Clusters and Relevance to Li-$O_2$ Batteries." *J. Phys. Chem. Lett.*, vol. 5, pp.813-819, 2014.

[7] Y.C. Lu, H. Gasteiger, M. Parent, V. Chiloyan, Y. Shao-Horn. "The Influence of Catalysts on Discharge and Charge Voltage of Rechargeable Li-Oxygen Batteries." *Electrochemical and Solid State Letters*, vol 13, pp. A69-A72, 2010.

[8] B. Adams, R. Black, C. Radtke, K. Zaghib, M. Trudeau, L. Nazar, “Current Density Dependance of Peroxide Formation in the Li-$O_2$ Battery and its Effect on Charge”, *Energy Environ. Sci*. vol.6, pp.1772-1778, 2013.

[9] S. Lau, L. A. Archer, “Nucleation and Growth of Lithium Peroxide in the Li-$O_2$ Battery”, *Nano Lett.* vol. 15, pp. 5995-6002, 2015.

[10] N. Aetukuri, B. D. McCloskey, J. Garcia, L. Krupp, V. Viswanathan, A. C. Luntz, “Solvating Additives Drive Solution-Mediated Electrochemistry and Enhance Toroid Growth in Non-Aqueous Li-$O_2$ Batteries.” *Nature Chemistry*, vol. 7, pp. 50-56, 2015.

[11] M. Radin, F. Tian, D. Siegal. “Electron Structure of $Li_2O_2$ {0001} Surfaces.” *J. Mater. Sci.,* vol. 47, pp. 7564-7570, 2012.

[12] L. Johnson, C. Li, Z. Liu, Y. Chen, S. A. Freunberger, P. Ashok, B. Praveen, K. Sholakia, J. M. Tarascon, P. G. Bruce. “The Role of $LiO_2$ Solubility in $O_2$ Reduction in Aprotic Solvents and its Consequences for Li-$O_2$ Batteries.” *Nature Chemistry*, vol. 6, pp. 1091-1099, 2014.

[13] V. Viswanathan, J.K. Norskov, A. Speidel, “Li-$O_2$ Kinetic Overpotentials: Tafel Plots from Experiment and First-Principles Theory,” *J. Phys. Chem. Lett*, Vol. 4, no. 4, pp.556-560, 2013.

[14] S. Ganapathy, B. Adams, G. Stenou, M. Anastasaki, K. Goubitz, X. F. Miao, L. F. Nazar, M. Wagemaker. “Nature of $Li_2O_2$ Oxidation in a Li-$O_2$ Battery Revealed by Operando X-Ray Diffraction.” *J. Amer. Chem. Soc.,* vol. 136, pp. 16335-16344, 2014.

[15] Y. Mo, S.P. Ong, G. Ceder, “First-Principles Study of the Oxygen Evolution Reaction of Lithium Peroxide in the Lithium-Air Battery,” *Phys. Rev. B.* Vol. 84, pp. 205446, 2011.

[16] S. Y. Kang, Y. Mo, S.P. Ong, G. Ceder, "A Facile Mechanism for Recharging $Li_2O_2$ in Li–$O_2$ Batteries," *Chem. Mater.*Vol. 25, no. 16, pp.3328-3336, 2013.

[17] P. Albertus, G. Girishkumar, B. McCloskey, R. S. Sanchez-Carrera, B. Kozinskey, J. Christensen, A. C. Luntz, "Identifying Capacity Limitations in the Li/Oxygen Battery Using Experiments and Modeling," *J. Electrochem. Soc*, Vol. 158, no. 3, pp.A343-A351, 2011.

[18] B. McCloskey, A. Speidel, R. Scheffler, D. C. Miller, V. Viswanathan, J. S. Hummelshoj, J. K. Norskov, A. C. Luntz, "Twin Problems of Interfacial Carbonate Formation in Nonaqueous Li-$O_2$ Batteries," *J. Phys. Chem. C.*,Vol. 3, pp. 997-1001, 2012.

[19] Y. Wang, "Modeling Discharge Deposit Formation and its Effect on the Lithium-Air Battery Performance," *Electrochimica Acta,* Vol. 75, pp.239-246, 2012.

[20] V. Viswanathan, K. S. Thygesen, J. S. Hummelshoj, "Electrical Conductivity in $Li_2O_2$ and its Role in Determining Capacity Limitations in Non-Aqueous Li-$O_2$ Batteries", *J. Chem. Phys*. Vol. 135, no. 21, pp. 214704, 2011.

[21] S. D. Beattie, D. M. Manolescu, S. L. Blair, "High-Capacity Lithium-Air Cathodes", *J. Electrochem. Soc.* Vol. 156, no. 1, pp.A44-A47, 2009.

[22] D. M. Itkis, D. A. Semenenko, E. Kataev, A. Belova, V. Neudachina, A. Sirotina, M. Havecker, D. Teschner, A. Knop-Gericke, P. Dudin, A. Barinov, E. A. Goodilin, Y. Shao-Horn, L. V. Yashina, "Reactivity of Carbon in Lithium-Oxygen Battery Positive Electrodes," *Nano. Lett.* Vol. 13, no. 10, pp. 4697-4701, 2013.

[23] M. M. O. Thotiyl, S. A. Freunberger, Z. Peng, P. G. Bruce, "The Carbon Electrode in Non-Aqueous Li-$O_2$ Cells." *J. Amer. Chem. Soc.* Vol. 135, no. 1, pp.494-500, 2012.

[24] S. Meini, N. Tsiouvaras, K. Uta Schwenke, M. Piana, H. Beyer, L. Lange, H. A. Gasteiger. “Rechargeability of Li-air Cathodes Pre-Filled with Discharge Products Using An Ether-Based Electrolyte Solution: Implications for Cycle-Life of Li-Air Cells.” *Phys. Chem. Chem. Phys.*Vol 15, pp.11478-11493, 2013.

[25] S. R. Gowda, A. Brunet, G. M. Wallraff, B. D. McCloskey. “Implications of $CO_2$ Contamination in Rechargeable Nonaqueous Li-$O_2$ Batteries.” *J. Phys. Chem. Lett*. Vol. 4, pp. 276-279, 2013.

[26] B. D. McCloskey, R. Scheffler, A. Speidel, D. S. Bethune, R. M. Shelby, A. C. Luntz, “On the Efficacy of Electrocatalysis in Nonaqueous Li-$O_2$ Batteries.” *J. Am. Chem. Soc.* vol. 133, no.45, pp.18038-18041, 2011.

[27] M. M. O. Thotiyl, S. A. Freunberger, Z. Peng, Y. chen, Z. Liu, P. G. Bruce,”A Stable Cathode for the Aprotic Li-$O_2$ Battery.” *Nat. Mater.* vol. 12, pp. 1050-1056, 2013.

[28] B. Adams, R. Black, C. Radtke, Z. Williams, B. Layla Meldhi, N. Browning, L. F. Nazar. “The Importance of Nanometric Passivating Films on Cathodes for Li-Air Batteries.” *ACS Nano*, vol. 8, pp. 12483-12493, 2014.

[29] Z. Peng, S. A. Freunberger, Y. Chen, P. G. Bruce. “A Reversible and Higher-Rate Li-$O_2$ Battery.” *Science*, vol. 337, pp. 563-566, 2012.

[30] S. H. Oh, B. Adams, B. Lee, L. F. Nazar. “Direct, Soft Chemical Route to Mesoporous Metallic Lead Ruthenium Pyrochlore and Investigation of its Electrochemical Properties.” *Chem. Mater.*, vol. 27, pp. 2322-2331, 2015.

[31] D. Kundu, R. Black, B. Adams, K. Harrison, K. Zavadil, L. F. Nazar. “Nanostructured Metal Carbides for Aprotic Li-$O_2$ Batteries: New Insights into Interfacial Reactions and Cathode Stability.” *J. Phys. Chem. Lett*. vol. 6, pp. 2252 – 2258, 2015.

[32] W. J. Kwak, K. C. Lau, C. D. Shin, K. Amine, L. A. Curtiss, Y. K. Sun. "A $Mo_2C$/Carbon Nanotube Composite Cathode for Lithium-Oxygen Batteries with High Energy Efficiency and Long Cycle Life." *ACS Nano*, vol. 9, pp. 4129-4137, 2015.

[33] S. S. Zhang. "A Review on Electrolyte Additives for Lithium-Ion Batteries." *J. Pow. Sources*, vol. 162, pp. 1379-1394, 2006.

[34] A. Debart, A. J. Paterson, J. Bao, P. G. Bruce. "α-$MnO_2$ Nanowires: A Catalyst for the $O_2$ Electrode in Rechargeable Lithium Batteries." vol. 120, no. 24, pp. 4597-4600, 2008.

[35] S. S. Zhang, D. Foster, J. Read. "Discharge Characteristics of a Non-Aqueous Electrolyte Li/$O_2$ Battery." vol. 195, no. 4, pp. 1236-1240, 2010.

[36] S. A. Freunberger, Y. Chen, Z. Peng, J. M. Griffen, L. J. Hardwick, F. Barde, P. Novak, P.G. Bruce. "Reactions in the Rechargeable Lithium-$O_2$ Battery with Alkyl Carbonate Electrolytes." vol. 133, no. 20, pp.8040-8047, 2011.

[37] H. Mizuno, F.; Nakanishi, S.; Kotani, Y.; Yokoishi, S.; Iba. "Rechargeable Li-$O_2$ Batteries with Carbonate-Based Liquid Electrolytes." *Electrochemistry*, vol. 78, no. 5, pp. 403-405, 2010.

[38] C. O'Laire, S. Mukerjee, K. M. Abraham. "Influence of Nonaqueous Solvents on the Electrochemistry of Oxygen in the Rechargeable Lithium-Air Battery." *J. Phys. Chem. C.* vol. 114, pp. 9178-9186, 2010.

[39] S. A. Freunberger, Y. Chen, N. Drewett, L. J. Hardwick, F. Barde, P.G. Bruce. "The Lithium-Oxygen Battery with Ether-Based Electrolytes." *Angew. Chem. Int. Ed.* Vol. 50, no. 37, pp.8609-8613, 2011.

[40] B. D. McCloskey, D. S. Bethune, R. M. Shelby, G. Girishkumar, A. C. Luntz. "Solvents' Critical Role in Nonaqueous Lithium-Oxygen Battery Electrochemistry." *J. Phys. Chem. Lett.* vol. 2, no. 10, pp.1161-1166, 2011.

[41] N. Kumar, M. Radin, B. Wood, T. Ogitsu, D. Siegel. "Surface-Mediated Solvent Decomposition in Li-Air Batteries: Impact of Peroxide and Superoxide Surface Terminations." *J. Phys. Chem. C*. vol. 119, pp. 9050-9060, 2015.

[42] Z. Zhang, J. Lu, R. S. Assary, P. Du, H. H. Wang, Y. K. Sun, Y. Qin, K. Lau, J. Greeley, P. Redfern, H. Iddir, L. Curtiss, K. Amine. "Increased Stability Toward Oxygen Reduction Products for Lithium-Air Batteries with Oligoether-Functionalized Silane Electrolytes." *J. Phys. Chem. C.* vol. 115, no. 51, pp.25535-25541, 2011.

[43] B. Adams, R. Black, Z. Williams, R. Fernandes, M. Cuisinier, E. Jaemstorp Berg, P. Novak, G. Murphy, L. F. Nazar. "Towards a Stable Organic Electrolyte for the Lithium Oxygen Battery." *Adv. Energy Mat.* vol. 5, pp. 1400867, 2015.

[44] B. D. McCloskey, A. Valery, A. C. Luntz, S. R. Giwda, G. M. Wallraff, J. M. Garcia, T. Mori, L. E. Krupp. "Combining accurate $O_2$ and $Li_2O_2$ assays to separate discharge and charge stability limitations in nonaqueous Li-$O_2$ batteries. vol. 4, pp. 2989-2993, 2013.

[45] D. Kwabi, T. Batcho, C. Amanchukwull, N. Ortiz-Vitoriano, P. Hammond, C. V. Thompson, Y. Shao-Horn. "Chemical Instability of Dimethyl Sulfoxide in Lithium-Air Batteries." *J. Phys. Chem. Lett.* vol. 5, pp. 2850-2856, 2014.

[46] Sharon, M. Afri, M. Noked, A. Garsuch, A. A. Frimer, D. Aurbach. "Oxidation of Dimethyl Sulfoxide Solutions by Electrochemical Reduction of Oxygen." *J. Phys. Chem. Lett*. vol. 4, pp.3315-2219, 2013.

[47] W. Walker, V. Giordani, J. Uddin, V. S. Bryantsev, G. Chase, D. Addison, "A Rechargeable Li-$O_2$ Battery Using a Lithium Nitrate/N,N-Dimethylacetamide Electrolyte", *J. Am. Chem. Soc.* Vol. 135, no. 6, pp.2076-2079, 2013.

[48] F. Barde, Y. Chen, L. Johnson, S. Schaltin, J. Fransaer, P. G. Bruce, "Sulfone-Based Electrolytes for Nonaqueous Li-$O_2$ Batteries." *J. Phys. Chem. C*. vol. 118,pp. 18892-18898, 2012.

[49] H. Nakamoto, Y. Suzuki, T. Shiotsuki, F. Mizuno, S. Higashi, K. Takechi, T. Asaoka, H. Nishikoori, H. Iba, "Ether-functionalized Ionic Liquid Electrolyte for Lithium-Air Batteries", *J. Power. Sour*, Vol. 243, pp.19-23, 2013.

[50] S. Das, J. Hojberg, K. B. Knudsen, R. Younsei, P. Johansson, P. Norby, T. Vegge. "Instability of Ionic Liquid-Based Electrolytes in Li-$O_2$ Batteries", *J. Phys. Chem. C.* Vol. 119, pp.18084-18090, 2015.

[51] S. K. Das, S. Xu, A. H. Emwas, Y. Y. Lu, S. Srivastava, L. A. Archer. "High Energy Lithium-Oxygen Batteries- Transport Barriers and Thermodynamics", *Energy Environ. Sci.* vol. 5, pp. 8927, 2012.

[52] V. Bryantsev, V. Giordani, W. Walker, M. Blanco, S. Zecevic, K. Sasaki, J. Uddin, D. Addison, G. Chase. "Predicting Solvent Stability in Aprotic Electrolyte Li-Air Batteries: Nucleophilic Substitution by the Superoxide Anion Radical (O2-)." *J. Phys. Chem. A.* vol. 115, pp. 12399-12409, 2011.

[53] G. M. Veith, J. Nanda, L. Delman, N. Dudney. "Influence of Lithium Salts on the Discharge Chemistry of Li-Air Cells." *J. Phys. Chem. Lett*. Vol. 3, no. 10, pp.1242-1247, 2012.

[54] S. R. Gowda, A. Brunet, G. M. Wallraff, B. D. McCloskey. "Implications of $CO_2$ Contamination in Rechargeable Nonaqueous Li-$O_2$ Batteries." *J. Phys. Chem. Lett*. Vol. 4, pp. 276-279, 2013.

[55] K. G. Gallagher, S. Goebel, T. Greszler, M. Mathias, W. Oelerich, D. Eroglu, V. Srinivasan. “Quantifying the Promise of Lithium-Air Batteries for Electric Vehicle.” *Energy Environ. Sci.* vol. 7, pp. 1555-1563, 2014.

[56] E. Peled, D. Golodnitsky, H. Mazor, M. Goor, S. Avshalomov. “Parameter Analysis of A Practical Lithium- and Sodium-Air Electrical Vehicle Battery.” *J. Power Sources* vol. 196, pp. 6835- 6840 (2011).

[57] P. Hartmann, C. L. Bender, M.Vracar, A. K. Durr, A. Garsuch, J. Janek, P. Adelhelm. 7“A Rechargeable Room-Temperature Sodium Superoxide ($NaO_2$) Battery**.”** *Nature Mater.,* vol.12, pp. 228−232, 2013.

[58] S. Y. Kang, Y. Mo, S. P. Ong, G. Ceder. “Nanoscale Stabilization of Sodium Oxides: Implications for Na-$O_2$ Batteries.” *Nano Lett.,* vol.14, pp.1016-1020, 2013.

[59] H. Yadegari. Y. Li, M. Norouzi Banis, X. Li, B. Wang, Q. Sun, R. Li, T. S. Sham, X Cui, X. Sun. “On Rechargeability and Reaction Kinetic of Sodium-Air Batteries. “ *Energy Environ. Sci.*,vol. 7, pp. 3747-3757, 2014.

[60] W. Liu, Q. Sun, Y. Yang, J. Y. Xie, Z. W. Fu. “An Enhanced Electrochemical Performance of a Sodium-Air Battery with Graphene Nanosheets as Air Electrode Catalysts.” Chem. Comm., vol. 49. pp.1951-1953, 2013.

[61] J. Kim, H. D. Lim, H. Gwon, K. Kang. “Sodium-Oxygen Batteries with Alkyl Carbonate and Ether Based Electrolytes.” *Phys. Chem. Chem. Phys.* vol. 15, pp. 3623-3629, 2013.

[62] P. Hartmann, C. Bender, J. Sann, A. Durr, M. Jansen, J. Janek, P. Adelhelm. “A Comprehensive Study on the Cell Chemistry of the Sodium Superoxide (NaO2) Battery.” *Phys. Chem. Chem. Phys.* vol. 15, pp. 11661-11672, 2013.

[63] B.D. McCloskey, G. Jeannette, A. C. Luntz. “Chemical and electrochemical differences in nonaqueous Li-O2 and Na-O2 batteries.” *J. Phys. Chem. Lett.* vol. 5, pp. 1230-1235, 2014.

[64] M. Fleischer. *Recent Estimates of the Abundance of the Elements in the Earth’s Crust*. Washington, D.C: Geological Circular Survey 285, 1953, pp. 1-6.

[65] C. Xia, R. Black, R. Fernandes, B. Adams, L. F. Nazar. “The Critical Role of Phase-Transfer Catalysis in Aprotic Sodium Oxygen Batteries.” *Nature Chemistry.* vol. 7, pp. 496-501, 2015.

[66] C. Bender, B. Jache, P. Adelhelm, J. Janek. “Sodiated Carbon: A Reversible Anode for Sodium-Oxygen Batteries and Route for the Chemical Synthesis of Sodium Superoxide (NaO2). “ *J. Mater. Chem. A.*, vol. 3, pp. 20633-20641, 2015.

## Section 2 References

[1] S. I. Pyun, H. C. Shin, J. W. Lee, J. Y. Goo, “Electrochemical Methods,” in *Electrochemistry of Insertion Materials for Hydrogen and Lithium,* 1st ed. Heidelberg, Germany: Springer, 2012, pp. 16-20.

[2] B. McCloskey, A. Speidel, R. Scheffler, D. C. Miller, V. Viswanathan, J. S. Hummelshoj, J. K. Norskov, A. C. Luntz, “Twin Problems of Interfacial Carbonate Formation in Nonaqueous Li-$O_2$ Batteries,” *J. Phys. Chem. C.*,Vol. 3, pp. 997-1001, 2012.

[3] J. F. Shackelford, “X-Ray Diffraction,” *Chapter 3.7* in *Materials Science for Engineers,* 6th ed. Upper Saddle River, New Jersey: Pearson Prentice Hall, 2005, pp. 104-112.

[4] R. Sodhi, Time-of-Flight Secondary Ion Mass Spectrometry (TOF-SIMS): Versatility in Chemical and Imaging Surface Analysis, *Analyst*, Vol. 129, pp.483-487 (2004).

[5] Models RGA100, RGA200, and RGA300 Residual Gas Analyzer, Rev. 1.8, Standford Research Systems, Sunnyvale, CA, 2009.

## Section 3 References

[1] C. O'Laire, S. Mukerjee, K. M. Abraham, E. Plitcha, M. Hendrickson. "Elucidating the Mechanism of Oxygen Reduction for Lithium-Air Battery Applications." *J. Phys. Chem. C*, vol. 113, pp. 20127-20134, 2009.

[2] C. O'Laire, S. Mukerjee, E. Plitcha, M. Hendrickson, K. M. Abraham. "Rechargeable Lithium/TEGDME-$LiPF_6/O_2$ Battery." *J. Electrochem. Soc.*,vol. 158, pp. A302-A308, 20011.

[3] F. Mizuno, S. Nakanishi, Y. Kotani, S. Yokoishi, H. Iba. "Rechargeable Li-Air Batteries with Carbonate-Based Liquid Electrolytes." *Electrochemistry*, vol. 78, pp. 403-405, 2010.

[4] B. D. McCloskey, D. S. Bethune, R. M. Shelby, G. Girishkumar, A. C. Luntz. "Solvents' Critical Role in Nonaqeuous Lithium-Oxygen Battery Electrochemistry." *J. Phys. Chem. Lett.* Vol. 2, no. 10, pp.1161-1166, 2011.

[5] W. Xu, V. Viswanathan, D. Wang, S. Towne, J. Xiao, Z. Nie, D. Hu, H. G. Zhang, "Investigation on the Charging Process of $Li_2O_2$-Based Air Electrodes in Li-$O_2$ Batteries with Organic Carbonate Electrolytes." *J. Power Sources*, vol. 196, pp. 3894-3899, 2011.

[6] G. Veith, N. Dudney, J. Howe, J. Nanda. “Spectroscopic Characterization of Solid Discharge Products in Li-Air Cells with Aprotic Carbonate Electrolytes.” *J. Phys. Chem. C*. vol. 115, pp. 14325 – 14333, 2011.

[7] S. A Freunberger, Y. Chen, Z. Peng, J. Griffin, L. Hardwick, F. Barde, P. Novak, P. G. Bruce. “Reactions in the Rechargeable Lithium-$O_2$ Battery with Alkyl Carbonate Electrolytes.” *J. Amer. Chem. Soc.* vol. 133, pp. 8040-8047, 2011.

[8] S.H. Oh, T.E. Yim, E. Pomerantseva and L.F. Nazar. “Decomposition Reaction of Lithium Bis(oxalato)borate in the Rechargeable Lithium-Oxygen Cell.” *Electrochem. Solid-State Lett.*, vol. 14, pp. A185-A188, 2011.

[9] G. M. Veith, J. Nanda, L. Delman, N. Dudney. “Influence of Lithium Salts on the Discharge Chemistry of Li-Air Cells.” *J. Phys. Chem. Lett*. Vol. 3, no. 10, pp.1242-1247, 2012.

[10] S. A. Freunberger, Y. Chen, N. Drewett, L. J. Hardwick, F. Barde, P.G. Bruce. ”The Lithium-Oxygen Battery with Ether-Based Electrolytes.” *Angew. Chem. Int. Ed.* Vol. 50, no. 37, pp.8609-8613, 2011.

[11] M. M. O. Thotiyl, S. A. Freunberger, Z. Peng, Y. Chen, Z. Liu, P. G. Bruce, “A Stable Cathode for the Li-$O_2$ Battery,” *Nature Materials*, Vol. 12, pp. 1050-1056, 2013.

[12] Z. Peng, S. A. Freunberger, Y. Chen, P. G. Bruce. “A Reversible Higher Rate Li-$O_2$ Battery,” *Science*, Vol. 337, pp. 563-566, 2012.

[13] B. D. McCloskey, A. Valery, A. C. Luntz, S. R. Gowda, G. M. Wallraff, J. Garcia, T. Mori, L. E. Krupp, “Combining Accurate $O_2$ and $Li_2O_2$ Assays to Separate Discharge and Charge Stability Limitations in Nonaqueous Li-$O_2$ Batteries.” *J. Phys. Chem. Lett.*, Vol. 4, no. 17, pp.2989-2993, 2013.

[14] D. Sharon, M. Afri, M. Noked, A. Garsuch, A. A. Frimer, D. Aurbach. “Oxidation of Dimethyl Sulfoxide Solutions by Electrochemical Reduction of Oxygen.” *J. Phys. Chem. Lett*. Vol. 4, pp.3315-2219, 2013.

[15] W. Walker, V. Giordani, J. Uddin, V. S. Bryantsev, G. Chase, D. Addison. “A Rechargeable Li-$O_2$ Battery Using a Lithium Nitrate/N,N-Dimethylacetamide Electrolyte.” *J. Am. Chem. Soc.* Vol. 135, no. 6, pp.2076-2079, 2013.

[16] Z. Zhang, J. Lu, R. S. Assary, P. Du, H. H. Wang, Y. K. Sun, Y. Qin, K. Lau, J. Greeley, P. Redfern, H. Iddir, L. Curtiss, K. Amine. “Increased Stability Toward Oxygen Reduction Products for Lithium-Air Batteries with Oligoether-Functionalized Silane Electrolytes.” *J. Phys. Chem. C.* Vol. 115, no. 51, pp.25535-25541, 2011.

[17] H. Nakamoto, Y. Suzuki, T. Shiotsuki, F. Mizuno, S. Higashi, K. Takechi, T. Asaoka, H. Nishikoori, H. Iba. “Ether-functionalized Ionic Liquid Electrolyte for Lithium-Air Batteries.” *J. Power. Sour*, Vol. 243, pp.19-23, 2013.

[18] B. McCloskey, A. Speidel, R. Scheffler, D. C. Miller, V. Viswanathan, J. S. Hummelshoj, J. K. Norskov, A. C. Luntz, “Twin Problems of Interfacial Carbonate Formation in Nonaqueous Li-$O_2$ Batteries,” *J. Phys. Chem. C.*,Vol. 3, pp. 997-1001, 2012.

[19] J. S. Filippo Jr., C. I. Chern, J. Valentine. “Reaction of Superoxide with Alkyl Halides and Tosylates.” *J. Org. Chem.* vol. 40, pp. 1678-1680, 1975.

[20] D. Sam, H. E. Simmons. “Crown Ether Chemistry. Substitution Reactions of Potassium Halide and Postassium Hydroxide Complexes of Dicyclohexyl-18-crown-6.” *J. Am. Chem. Soc.* v 96, pp. 2252-2253, 1974.

[21] A. Debart, A. J. Paterson, J. Bao, P. G. Bruce. "α-$MnO_2$ Nanowires: A Catalyst for the $O_2$ Electrode in Rechargeable Lithium Batteries." *Angew. Chemie Int. Ed.* vol.120, pp. 4597-4600, 2008.

[22] Y. Gao, Z. Wang, J. Wan, G. Zou, Y. Qian, "A Facile Route to Synthesize Uniform Single-Crystalline α-$MnO_2$ Nanowires," *J. Crys. Growth*, Vol. 279, pp. 415-419, 2005.

[23] A. S. Arico, V. Antonucci, M. Minutoli, N. Giordano. "The Influence of Functional Groups on the Surface Acid-Base Characteristics of Carbon Blacks." *Carbon*, vol. 27, pp. 337-347, 1989.

[24] Z. Peng, S. Freunberger, L. Hardwick, Y. Chen, V. Giordani, F. Barde, P. Novak, D. Graham, J. M. Tarascon, P. G. Bruce. "Oxygen Reactions in Non-Aqueous $Li^+$ Electrolyte." *Angew. Chem. Int. Ed.* vol. 50, pp. 6351 – 6355, 2011.

[25] M. M. O. Thotiyk, S. A. Freunberger, Z. Peng, P. G. Bruce. "The Carbon Electrode In Nonaqueous Li-$O_2$ Cells." *J. Am. Chem. Soc.* vol. 135, pp. 494-500, 2013.

[26] D. Itkis, D. Semenenko, E. Y. Kataev, A. Belova, V. Neudachina, A. Sirotina, M. Haveckerg, D. Teschners, A. Knop-Gerickej, P. Dudini, A. Barinov, E. Goodilin, Y. Shao-Horn, L. Yashina. "Reactivity of Carbon in Lithium-Oxygen Battery Positive Electrodes." *Nano Lett.* Vol. 13, pp. 4697-4701, 2013.

[27] N. Aetukuri, B. D. McCloskey, J. Garcia, L. Krupp, V. Viswanathan, A. C. Luntz, "Solvating Additives Drive Solution-Mediated Electrochemistry and Enhance Toroid Growth in Non-Aqueous Li-$O_2$ Batteries." *Nature Chemistry*, vol. 7, pp. 50-56, 2015.

[28] R. Mitchell, B. Gallant, Y. Shao-Horn, C. V. Thompson. "Mechanisms of Morphological Evolution of $Li_2O_2$ Particles During Electrochemical Growth." *J. Phys. Chem. Lett.* vol. 4, pp. 1060-1064, 2013.

[29] S. Lau, L.A Archer, "Nucleation and Growth of Lithium Peroxide in the Li-O2 Battery." *Nano Lett.* vol. 15, pp. 5995-6002, 2015.

[30] R. Amin-Sanayei, R. Heinze, Advantages of High Molecular Weight PVdF Binder in Lithium Ion Cells, *NASA Aeropace Battery Workshop*, 2009.

[31] J. Marchand-Brynaert, N. Jongen, J. L. Dewez. "Surface Hydroxylation of Poly(vinylidene fluoride)(PVDF) Film." *J. Polym. Sci. A.* vol. 35, pp. 1227-1235, 1997.

[32] P. Maccone, G. Brinati, V. Arcella. "Environmental Stress Cracking of Poly(vinylidene fluoride) in Sodium Hydroxide. Effect of Chain Regularity." *Polymer Eng. & Sci.* vol. 40, pp. 761-767, 2000.

[33] D. Sawyer, J. Valentine. " How Super is Superoxide." *Acc. Chem. Res.* Vol. 14, pp. 393-400, 1981.

[34] T. Danks, R. Slade, J. Varcoe. "Alkaline Anion-Exchange Radiation-Grafted Membranes for Possible Electrochemical Application in Fuel Cells." *J. Mater. Chem.* vol. 13, pp. 712-721, 2003.

[35] S. Zulifiqar, M. Zulifiqar, M. Rizvi, A. Munir. "Study of the Thermal Degradation of Polychlorotrufluoroethylene, poly(vinylidene fluoride) and Copolymers of Chlorotrifluoroethylene and Vinylidene Fluoride." *Polym. Degrad. Stab.* vol. 43, pp. 423-430, 1994.

[36] A. Sorge, M. Turco, G. Pilone, G. Bagnasco. "Decomposition of Hydrogen Peroxide on $MnO_2/TiO_2$ Catalysts." *J. Prop. Pow.* vol.20, pp. 1069-1075, 2004.

[37] R. Younesi, M. Hahlin, F. Bjorefors, P. Johansson, K. Edstrom. "Li-$O_2$ Battery Degradation by Lithium Peroxide ($Li_2O_2$): A Model Study." *Chem. Mater*, vol. 25, no. 1, pp.77-84, 2012.

[38] A. Debart, A. J. Paterson, J. Bao, P. G. Bruce. "α-$MnO_2$ Nanowires: A Catalyst for the $O_2$ Electrode in Rechargeable Lithium Batteries." vol. 120, no. 24, pp. 4597-4600, 2008.

[39] E. M. Benbow, S. P. Kelly, L. Zhao, J. W. Reutenauer, S. L. Suib. "Oxygen Reduction Properties of Bifunctional α-Manganese Oxide Electrocatalysts in Aqueous and Organic Electrolytes." *J. Phys. Chem. C.* vol. 115, pp. 22009-22017, 2011.

[40] S. Meini, N. Tsiouvaras, K. Uta Schwenke, M. Piana, H. Beyer, L. Lange, H. A. Gasteiger. "Rechargeability of Li-air Cathodes Pre-Filled with Discharge Products Using An Ether-Based Electrolyte Solution: Implications for Cycle-Life of Li-Air Cells." *Phys. Chem. Chem. Phys.*Vol 15, pp.11478-11493, 2013.

[41] K. Takechi, S. Higashi, F. Mizuno, H. Nishikoori, H. Iba, T. Shiga. "Stability of Solvents Against Superoxide Radical Species for the Electrolyte of Lithium-Air Battery." *ECS Electrochem. Lett.* vol. 1, pp. A27-A29, 2012.

[42] K. Uta Schwenke, S. Meini, X. Wu, H. A. Gasteiger, M. Piana. "Stability of Superoxide Radicals in Glyme Solvents for Non-Aqueous Li-$O_2$ Battery Electrolytes." *Phys. Chem. Chem. Phys.* vol. 15, pp. 11830-11839, 2013.

## Section 4 References

[1] G. Girishkumar, B. McCloskey, A.C. Luntz, S. Swanson and W. Wilcke. "Lithium-Air Battery:Promise and Challenges." *J. Phys. Chem. Lett.*vol. 1, pp. 2193-2203, 2010.

[2] A. Debart, J. Bao, . Armstrong, P. G. Bruce. "An $O_2$ Cathode for Rechargeable Lithium Batteries: The Effect Of a Catalyst." *J. Pow. Sources.* vol. 174, pp. 1177-1182, 2007.

[3] A. Debart, A. J. Paterson, J. Bao, P. G. Bruce. "α-$MnO_2$ Nanowires: A Catalyst for the O2 Electrode in Rechargeable Lithium Batteries." *Angew. Chemie. Int. Ed.* vol. 120, no. 24, pp. 4597-4600, 2008.

[4] Y. C. Lu, Z. Xu, H. A. Gasteiger, S. Chen, K. Hamad-Schifferli, Y. Shao-Horn. "Platinum-Gold Nanoparticles: A Highly Active Bifunctional Electrocatalyst for Rechargeable Lithium-Air Batteries." *J. Am. Chem. Soc.* vol. 132, pp. 12170-12171, 2010.

[5] L. Wang, X. Zhao, Y. Lu, M. Xu, D. Zhang, R.S. Ruoff, K.J. Stevenson, J.B. Goodenough, "$CoMn_2O_4$ Spinel Nanoparticles Grown on Graphene as Bifunctional Catalyst for Lithium-Air Batteries." *J. Electrochem. Soc.* vol. 158, pp. A1379-A1382, 2011.

[6] Y. Liang, Y. Li, H. Wang, J. Zhou, J. Wang, T. Regier, H. Dai. "$Co_3O_4$ Nanocrystals on Graphene as a Synergistic Catalyst for Oxygen Reduction Reaction." *Nat. Mater.*, vol. 10, pp. 780-786, 2011.

[7] B. D. McCloskey, R. Scheffler, A. Speidel, D. S. Bethune, R. M. Shelby, A. C. Luntz, "On the Efficacy of Electrocatalysis in Nonaqueous Li-$O_2$ Batteries." *J. Am. Chem. Soc.* vol. 133, no.45, pp.18038-18041, 2011.

[8] S. Yang, G. Cui, S. Pang, Q. Cao, U. Kolb, X. Feng, J. Maier, K. Mullen. "Fabrication of Cobalt and Cobalt Oxide/Graphene Composites: Towards High-Performance Anode Materials for Lithium Ion Batteries." *Chem. Sus. Chem.*, vol. 3, pp. 236-239, 2010.

[9] J. Xiao, D. Mei, X. Li, W. Xu, D. Wang, G. Graff, W. Bennett, Z. Nie, L. Saraf, I. Aksay, J. Liu, J. G. Zhang. “Hierarchically Porous Graphene as a Lithium-Air Battery Electrode.” *Nano Lett.,* vol. 11, pp. 5071-5078, 2011.

[10] K. Abraham, Z. Jiang. “A Polymer Electrolyte-Based Rechargeable Lithium/Oxygen Battery.” *J. Elec. Chem. Soc.* vol. 143, pp. 1-5, 1996.

[11] R. Black, S. H. Oh, J. H. Lee, T. Yim, B. Adams, L. F. Nazar. “Screening for Superoxide Reactivity in Li-$O_2$ Batteries: Effect on $Li_2O_2$/LiOH Crystallization.” *J. Am. Chem. Soc.* vol. 134, pp. 2902-2905, 2012.

---

[12] L.F. Liotta, M. Ousmane, G. DiCarlo, G. Pantaleo, G. Deganello, G. Marci, A. Giroir-Fendler.” Total Oxidation of Propene at Low Temperature Over $Co_3O_4$-$CeO_2$ Mixed Oxides: Role of Surface Oxygen Vacancies and Bulk Oxygen Mobility in the Catalytic Activity.” *Appl. Catal. A.*, vol. 347, pp. 81-88, 2008.

[13] B. D. McCloskey, D. S. Bethune, R. M. Shelby, G. Girishkumar, A. C. Luntz. “Solvents’ Critical Role in Nonaqueous Lithium-Oxygen Battery Electrochemistry.” *J. Phys. Chem. Lett.* vol. 2, pp. 1161, 2011.

[14] A. D. Shaw, M. M. Cortez, A. K. Gianotto,A. D. Applehans, J. E. Olson, C. Karahan, R. Avci, G. S. Groenewold. :Static SIMS Analysis of Carbonate on Basic Alkali-Bearing Surfaces.” *Surf. Interface Anal.,* vol. 35, pp. 310-317, 2003.

[15] B. McCloskey, A. Speidel, R. Scheffler, D. C. Miller, V. Viswanathan, J. S. Hummelshoj, J. K. Norskov, A. C. Luntz, “Twin Problems of Interfacial Carbonate Formation in Nonaqueous Li-$O_2$ Batteries,” *J. Phys. Chem. C.*,Vol. 3, pp. 997-1001, 2012.

[16] J. Hassoun, F. Croce, M. Armand, B. Scrosati. :Investigation of the O2 Electrochemistry in a Polymer Electrolyte Solid-State Cell." *Angew. Chem. Int. Ed*. vol. 50, pp. 2999-3002, 2011.

[17] M. Kasha, A. Ullah Khan. "The Physics, Chemistry, and Biology of Singlet Molecular Oxygen." *Annals of the New York Academy of Sciences.* vol. 171, pp. 5-23, 1970.

[18] E. Mayeda, A. J. Bard. "Singlet Oxygen. The Suppression of its Production in Dismutation of Superoxide Ion By Superoxide Dismutase." *J. Am. Chem. Soc.* vol. 96, pp. 4023-4024, 1974.

[19] B. D. McCloskey, D. S. Bethune, R. M. Shelby, T. Mori, R. Scheffler, A. Speifel, M. Sherwood, A. C. Luntz. "Limitations in Rechargeability of Li-$O_2$ Batteries And Possible Origins." *J. Phys. Chem. Lett.* vol. 3, pp. 3043-3047, 2012.

[20] S. A. Freunberger, Y. Chen, N. Drewett, L. J. Hardwick, F. Barde, P.G. Bruce. "The Lithium-Oxygen Battery with Ether-Based Electrolytes." *Angew. Chem. Int. Ed.* Vol. 50, no. 37, pp.8609-8613, 2011.

[21] S. R. Gowda, A. Brunet, G. M. Wallraff, B. D. McCloskey. "Implications of $CO_2$ Contamination in Rechargeable Nonaqueous Li-$O_2$ Batteries." *J. Phys. Chem. Lett*. Vol. 4, pp. 276-279, 2013.

[22] J. Zhu, X. Ren, J. Liu, W. Zhang, Z. Wen. "Unraveling the Catalytic Mechanism of $Co_3O_4$ for the Oxygen Evolution Reaction in a Li-O2 Battery." *ACS Catalysis*, vol. 5, pp. 73-81, 2015.

[23] R. Gao, J. Zhu, X. Xiao, Z. Hu, J. Liu, X. Liu. "Facet-Dependent Electrocatalytic Performance of $Co_3O_4$ for Rechargeable Li-$O_2$ Battery." *J. Phys. Chem.* C., vol. 119, pp. 4516-4523, 2015.

## Section 5 References


[1] N. Tsiouvaras, S. Meini, I. Buchberger, H. A. Gasteiger, "Novel On-Line Mass Spectrometer Design for the Study of Multiple Charging Cycles of a Li-O2 Battery", *J. Electrochem. Soc.* Vol. 160, no. 3, pp. A471 – A477, 2013

[2] Stanford Research Systems (SRS), Sunnyvale, CA. RGA Labview Software: Gas Fragmentation Library [In Software], Revision 1.8, Updated May 2009.

[3] B. McCloskey, A. Speidel, R. Scheffler, D. C. Miller, V. Viswanathan, J. S. Hummelshoj, J. K. Norskov, A. C. Luntz, "Twin Problems of Interfacial Carbonate Formation in Nonaqueous Li-$O_2$ Batteries," *J. Phys. Chem. C.*,Vol. 3, pp. 997-1001, 2012.

[4] S. Meini, S. Solchenback, M. Piana, H. Gasteiger. "The Role fo Electrolyte Solvent Stability and Electrolyte Impurities in the Electrooxidation of $Li_2O_2$ in Li-$O_2$ Batteries." *J. Electrochem. Soc.* vol. 161, pp. A1306-1314, 2014.

[5] M. M. O. Thotiyl, S. A. Freunberger, Z. Peng, Y. Chen, Z. Liu, P. G. Bruce. "A Stable Cathode for the Aprotic Li-$O_2$ Battery." *Nat. Mat.* vol. 12, pp. 1050-1056, 2013.

[6] B. Adams, R. Black, C. Radtke, Z. Williams, L. Mehdi, N. Browning, L. F. Nazar. "The Importance of Nanometric Passivating Films on Cathode for Li-Air Batteries." *ACS Nano*, vol. 8, pp. 12483-12493, 2014.

[7] D. Kundu, R. Black, E. J. Berg, L. F. Nazar. "A Highly Active Nanostructured Metallic Oxide Cathode for Aprotic Li-O2 Batteries." *Energy Environ. Sci.* vol. 8, pp. 1292-1298, 2015.

[8] M. M. O. Thotiyl, S. A. Freunberger, Z. Peng, Y. chen, Z. Liu, P. G. Bruce,"A Stable Cathode for the Aprotic Li-O2 Battery." *Nat. Mater.* vol. 12, pp. 1050-1056, 2013.

[9] B. D. McCloskey, D. S. Bethune, R. M. Shelby, T. Mori, R. Scheffler, A. Speifel, M. Sherwood, A. C. Luntz. “Limitations in rechargeability of Li-$O_2$ batteries and possible origins.” *J. Phys. Chem. Lett.* vol. 3, pp. 3043-3047, 2012.

[10] Sharon, M. Afri, M. Noked, A. Garsuch, A. A. Frimer, D. Aurbach. “Oxidation of Dimethyl Sulfoxide Solutions by Electrochemical Reduction of Oxygen.” *J. Phys. Chem. Lett*. vol. 4, pp.3315-2219, 2013.

[11] D. Kwabi, T. Batcho, C. Amanchukwu, N. Ortiz-Vitoriano, P. Hammond, C. Thompson, Y. Shao-Horn. “Chemical Instability of Dimethyl Sulfoxide in Lithium-Air Batteries.” *J. Phys. Chem. Lett.* vol. 5, pp. 2850-2856, 2014.

[12] D. Sharon, M. Afri, M. Noked, A. Garsuch, A. Frimer, D. Aurbach. “Oxidation of Dimethyl Sulfoxide Solutions by Electrochemical Reduction of Oxygen.” *J. Phys. Chem. Lett.* vol. 4, pp. 3115-3119, 2013.

[13] B. Adams, C. Radtke, R. Black, M. Trudeau, K. Zaghib, L. F. Nazar. “Current Density Dependence of Peroxide Formation in the Li-$O_2$ Battery and its Effect on Charge.” *Energy & Env. Sci.* vol. 6, pp. 1772-1778, 2014.

[14] H. Beyer, S. Meini, N. Tsiouvaras, M. Piana, H. A. Gasteiger. “Thermal and Electrochemical Decomposition of Lithium Peroxide in Non-Catalyzed Carbon Cathodes for Li–Air Batteries.” *Phys. Chem. Chem. Phys.* vol. 15, pp. 11025-11037, 2013.

[15] W. J. Kwak, K. C. Lau, C. D. Shin, K. Amine, L. Curtiss, Y. K. Sun. “A $Mo_2C$/Carbon Nanotube Composite Cathode for Lithium-Oxygen Batteries with High Energy Efficiency and Long Cycle Life.” *ACS Nano*, Vol. 4. No. 9, pp.4129-4137, 2015.

[16] C. Wan, Y. N. Regmi, B. M. Leonard. “Multiple Phases of Molybdenum Carbide as Electrocatalysts for the Hydrogen Evolution Reaction.” *Angew. Chem. Int. Ed*. vol. 53, pp. 6407-6410, 2014.

[17] Z. Li, C. Chen, E. Zhan, N. Ta, Y. Li, W. Shen. “Crystal-Phase Control of Molybdenum Carbide Nanobelts for Dehydrogenation of Benzyl Alcohol.” *Chem. Commun.* vol. 50, pp. 4469-4471, 2014.

[18] H. Ren, W. Yu, M. Salciccioli, Y. Chen, Y. Huang, K. Xiong, D. G. Vlachos, J. G. Chen. “Selective Hydrodeoxygenation of Biomass-Derived Oxygenates to Unsaturated Hydrocarbons using Molybdenum Carbide Catalysts.” *ChemSusChem.* vol. 6, 798-801, 2013.

[19] Wan, C.; Regmi, Y. N.; Leonard, B. M. “Multiple Phases of Molybdenum Carbide as Electrocatalysts for the Hydrogen Evolution Reaction.” *Angew. Chem. Int. Ed*. vol. 53, pp. 6407-6410, 2014.

[20] M. D. Porosoff, M. D, X. Yang, J. A. Boscoboinik, J. G. Chen. “Molybdenum Carbide as Alternative Catalysts to Precious Metals for Highly Selective Reduction of CO2 to CO.” *Angew. Chem. Int. Ed.* vol. 53, pp. 6705-6709, 2014.

[21] C. Wan, Y. N. Regmi, B. M. Leonard. “Multiple Phases of Molybdenum Carbide as Electrocatalysts for the Hydrogen Evolution Reaction.” *Angew. Chem. Int. Ed.* vol. 53, pp. 6407-6410, 2014.

[22] Li, Z.; Chen, C.; Zhan, E.; Ta, N.; Li Y. ; Shen, W. “Crystal-Phase Control of Molybdenum Carbide Nanobelts for Dehydrogenation of Benzyl Alcohol.” *Chem. Commun.* vol. 50, pp. 4469-4471, 2014.

[23] Li, Z.; Schram, T.; Witters, T.; Cho, H.J.; O’Sullivan, B.; Yamada, N.; Takaaki, T.; Hooker, J. Gendt, S.D.; Meyera, K.D. “Investigation on Molybdenum and Its

Conductive Oxides as p-Type Metal Gate Candidates." *J. Electrochem. Soc.* vol. 7, pp. H481-H484, 2008.

[24] N. Kumar, M. Radin, B. Wood, T. Ogitsu, D. Siegel. "Surface-Mediated Solvent Decomposition in Li-Air Batteries: Impact of Peroxide and Superoxide Surface Terminations." *J. Phys. Chem. C*. vol. 119, pp. 9050-9060, 2015.

[25] B. McCloskey, A. Speidel, R. Scheffler, D. C. Miller, V. Viswanathan, J. S. Hummelshoj, J. K. Norskov, A. C. Luntz, "Twin Problems of Interfacial Carbonate Formation in Nonaqueous Li-$O_2$ Batteries," *J. Phys. Chem. C.*,Vol. 3, pp. 997-1001, 2012.

[26] J. W. Bullard, R. L. Smith. "Structural Evolution of the MoO3 (010) Surface During Lithium Intercalation.**"** *Solid State Ionics*, vol. 160, pp. 335-349, 2003.

[27] K. Yao, M. Risch, S. Y. Sayed, Y. Lee, J. Harding, A. Grimaud, N. Pour, Z. Xu, J. Zhou, A. Mansour, F. Barde, Y. Shao-Horn. "Solid-State Activation of Li2O2 Oxidation Kinetics and Implications for Li-O2 Batteries." *Energy Environ. Sci*. vol. 8, pp. 2417-2426, 2015.

## Section 6 References

[1] J. S. Lee, S. Tai Kim, R. Cao, N. S. Choi, M. Liu, T. Lee, J. Cho. "Metal-air batteries with high energy density: Li-air versus Zn-air." *Adv. Energy Mater.* vol. 1, pp. 34-50, 2011.

[2] P. G. Bruce, S. A. Freunberger, L. J. Hardwick, J. M. Tarascon. "Li-$O_2$ and Li-S batteries with high energy storage." *Nature Mater*. vol. 11, pp. 19-29, 2012.

[3] Y. C. Lu, B. M. Gallant, D. Kwabi, J. Harding, R. Mitchell, M. S. Whittingham, Y. Shao-Horn. "Lithium-oxygen batteries: bridging mechanistic understanding and battery performance." *Energy Environ. Sci*. vol. 6, pp. 750-768, 2013.

[4] B. Adams, C. Radtke, R. Black, M. Trudeau, K. Zaghib, L. F. Nazar. "Current density dependence of peroxide formation in the Li-$O_2$ battery and its effect on charge. *Energy Environ. Sci.*vol. 6, pp. 1772-1778, 2013.

[5] Y. C. Lu, D. Kwabi, K. Yao, J. Harding, J. Zhou, L. Zuin, Y. Shao-Horn. "The discharge rate capability of rechargeable Li-$O_2$ batteries" *Energy Environ. Sci.* vol. 4, pp. 2999-3007, 2011.

[6] K. U. Schwenke, S. Meini, X. Wu, H. A. Gasteiger, M. Piana. "Stability of superoxide radicals in glyme solvents for non-aqueous Li-$O_2$ battery electrolytes." *Phys. Chem. Chem. Phys.* vol. 15, pp. 11830-11839, 2013.

[7] H. G. Jung, J. Hassoun, J. B. Park, Y. K. Sun, B. Scrosati. "An improved high-performance lithium-air battery." *Nature Chem.* vol. 4, pp. 579-585, 2012.

[8] Y. C. Lu, Y. Shao-Horn. "Probing the reaction kinetics of the charge reactions of nonaqueous Li-$O_2$ batteries." *J. Phys. Chem. Lett*. vol. 4, pp. 93-99, 2013.

[9] P. Hartmann, C. Bender, M. Vracar, A. K. Durr, A. Garusch, J. Janek. P. A. Adelhelm. "Rechargeable room-temperature sodium superoxide ($NaO_2$) battery." *Nature Mater.* vol. 12, pp. 228-232, 2013.

[10] P. Hartmann, C. Bender, J. Sann, A. K. Durr, M. Jansen, J. Janek, P. A. Adelhelm. "A Comprehensive study on the cell chemistry of the sodium superoxide ($NaO_2$) battery." *Phys. Chem. Chem. Phys*. vol. 15, pp. 11661-11672, 2013.

[11] S. Das, S. Lau, L. A. Archer. “Sodium-oxygen batteries: a new class of metal-air batteries.” *J. Mater. Chem. A.* vol. 2, pp. 12623-12629, 2014.

[12] B.D. McCloskey, G. Jeannette, A. C. Luntz. “Chemical and electrochemical differences in nonaqueous Li-$O_2$ and Na-$O_2$ batteries.” *J. Phys. Chem. Lett.* vol. 5, pp. 1230-1235, 2014.

[13] B. D. McCloskey, D. S. Bethune, R. M. Shelby, G. Girishkumar, A. C. Luntz. “Solvents’ critical role in nonaqueous lithium-oxygen battery electrochemistry.” *J. Phys. Chem. Lett*. vol. 2, pp. 1161-1166, 2011.

[14] B. D. McCloskey, D. S. Bethune, R. M. Shelby, T. Mori, R. Scheffler, A. Speifel, M. Sherwood, A. C. Luntz. “Limitations in rechargeability of Li-$O_2$ batteries and possible origins.” *J. Phys. Chem. Lett.* vol. 3, pp. 3043-3047, 2012.

[15] M. Leskes, A. J. Moore, G. Goward, C. P. Grey. “Monitoring the electrochemical processes in the lithium-air battery by solid state NMR spectroscopy.” *J. Phys. Chem. C.* vol. 117, pp. 26929-26939, 2013.

[16] Y. C. Lu, E. Crumlin, G. Veith, J. Harding, E. Mutoro, L. Maggetto, N. Dudney, Z. Liu, Y. Shao-Horn. “*In situ* ambient pressure X-ray photoelectron spectroscopy studies of lithium-oxygen redox reactions.” *Scientific Reports*. vol. 2, pp. 715, 2012.

[17] R. Black, J. H. Lee, B. Adams, C. Mims, L. F. Nazar. “The role of catalysts and peroxide oxidation in lithium-oxygen batteries.” *J. Am. Chem. Soc.* Vol. 135, pp. 494-500, 2013.

[18] M. O. Thotiyl, S. Freunberger, Z. Peng, P. G. Bruce. “The carbon electrode in nonaqueous Li-$O_2$ cells.” *J. Am. Chem. Soc.* vol. 135, pp. 494-500, 2013.

[19] D. M. Itkis, D. Semenenko, E. Kataev, A. Belova, V. Neudachina, A. Sirotina, M. Hevecker, D. Teschner, A. Knop-Gericke, P. Dudin, A. Barinov, E. A. Goodilin, Y. Shao-Horn, L. V. Yashina. "Reactivity of carbon in lithium-oxygen battery positive electrodes." *Nano Lett.* vol. 13, pp. 4697-4701, 2013.

[20] M. O. Thotiyl, S. Freunberger, Z. Peng, Y. Chen, Z. Liu, P. G. Bruce. "A stable cathode for the aprotic Li-$O_2$ battery." *Nature Mater.* vol. 12, pp. 1050-1056, 2013.

[21] D. Kundu, R. Black, E. Jaemstorp Berg, L. F. Nazar. "A highly active nanostructured metallic oxide cathode for aprotic Li-$O_2$ batteries." *Energy Environ. Sci.* vol. 8, pp. 1292-1298, 2015.

[22] J. Lu, Y. Lei, K. C. Lau, X. Luo, P. Du, J. Wen, R. S. Assary, U. Das, D. Miller, J. Elam, H. Albishri, S. Abd El-Hady, Y. K. Sun, L. Curtiss, K. A. Amine. "Nanostructured cathode architecture for low charge overpotential in lithium-oxygen batteries." *Nature Comm.* vol. 4, pp. 2383, 2013.

[23] N. Kumar, M. Radin, B. Wood, T. Ogitsu, D. Siegel. "Surface-mediated solvent decomposition in Li-air batteries: impact of peroxide and superoxide surface terminations." *J. Phys. Chem. C.* vol. 119, pp. 9050-9060, 2015.

[24] C. Xia, R. Black, R. Fernandes, B. Adams, L. F. Nazar. "The critical role of phase-transfer catalysis in aprotic sodium oxygen batteries." *Nature Chem.* vol. 7, pp. 496-501, 2015.

[25] B. Adams, R. Black, C. Radtke, L. Mehdi, N. Browning, L. F. Nazar. "The importance of nanometric passivating films on cathodes for Li-air batteries." *ACS Nano.* vol. 8, pp. 12483-12493, 2014.

[26] B. D. McCloskey, A. Valery, A. C. Luntz, S. R. Giwda, G. M. Wallraff, J. M. Garcia, T. Mori, L. E. Krupp. "Combining accurate $O_2$ and $Li_2O_2$ assays to separate discharge

and charge stability limitations in nonaqueous Li-$O_2$ batteries. vol. 4, pp. 2989-2993, 2013.

[27] Z. Jian, Y. Chen, F. Li, T. Zhang, C. Liu, H. J. Zhou. "High capacity Na–$O_2$ batteries with carbon nanotube paper as binder-free air cathode." *J. Power Sources.* vol. 251, pp. 466-469, 2014.

[28] Y. Li, Y. Hossein, X. Li, M. Banis, R. Li, X. Sun. "Superior catalytic activity of nitrogen-doped graphene cathodes for high energy capacity sodium–air batteries. vol. 49, pp. 11731-11733, 2013.

[29] H. Yadegari, Y. L. Li, M. N. Banis, X. Li, B. Wang, Q. Sun, R. Y. Li, T. K. Sham. X. Cuic, X. L. Sun. "On rechargeability and reaction kinetics of sodium–air batteries." *Energy Environ. Sci.* vol. 7, pp. 3747-3757, 2014.

[30] W. Liu, Q. Sun, Y. Yang, J. Y. Xie, Z. W. Fu. "An enhanced electrochemical performance of a sodium-air battery with graphene nanosheets as air electrode catalysts." *Chem. Comm.* vol. 49, pp. 1951-1953, 2013.

[31] S. Y. Kang, Y. Mo, S. P. Ong, G., Cedar. "Nanoscale Stabilization of Sodium Oxides: Implications for Na-$O_2$ Batteries." *Nano Lett.* vol. 14, pp. 1016-1020, 2014.

[32] C. Bender, P. Hartmann, M. Vracar, P. Adelhelm. J. Janek. "On the thermodynamics, the role of the carbon cathode, and the cycle life of the sodium superoxide ($NaO_2$) battery." *Adv. Energy Mater.* vol.4, pp. 1301863, 2014.

[33] S. H. Oh, B. Adams, B. Lee, L. F. Nazar. "Direct Soft Chemical Route to Mesoporous Metallic Lead Ruthenium Pyrochlore and Investigation of its Electrochemical Properties." *Chem. Mater.* vol. 27, pp. 2322-2331, 2015.

[34] S. Meini, N. Tseiouvaras, K. Schwenke, M. Piana, H. Bever, L. Lange, H. A. Gasteger. "Rechargeability of Li-Air Cathodes Pre-Filled with Discharge Products Using an Ether-based Electrolyte Solution: Implications for Cycle-Life of Li-Air Cells." *Phys. Chem. Chem. Phys.* vol. 15, pp. 11478-11493, 2013.

[35] S. Ganapathy, B. Adams, G. Stenou, K. Goubitz, L. F. Nazar, M. Wagemaker. "The nature of $Li_2O_2$ oxidation in a Li-$O_2$ battery revealed by *operando* X-ray diffraction." vol. 136, pp. 15807-15808, 2014.

[36] K. Schwenke, M. Metzger, T. Restle, M. Piana, H. A. Gasteiger. "The influence of water and protons on $Li_2O_2$ crystal growth in aprotic Li-$O_2$ cells." *J. Electrochem. Soc.* vol. 162, pp. A573-A584, 2015.

[37] B. McCloskey, A. Speidel, R. Scheffler, D. C. Miller, V. Viswanathan, J. S. Hummelshoj, J. K. Norskov, A. C. Luntz. "Twin problems of interfacial carbonate formation in the nonaqueous Li-$O_2$ battery." *J. Phys. Chem. C.* vol. 3, pp. 997-1001, 2012.

[38] B. Adams, R. Black, Z. Williams, R. Fernandes, M. Cuisiner, E. Jaemstorp Berg, P. Novak, G. Murphy, L. F. Nazar. "Towards a stable organic electrolyte for the lithium oxygen battery." *Adv. Energy Mat.* vol. 5, pp. 1400867, 2015.

[39] S. A. Freunberger, Y. Chen, N. Drewett, L. Hardwick, F. Barde, P. G. Bruce. "The lithium-oxygen battery with ether-based electrolytes." *Angew. Chem. Int. Ed.* vol. 50, pp. 8609-8613, 2011.

[40] D. Sharon, V. Etacheri, A. Garusch, M. Afri, A. A. Frimer, D. Aurbach. "On the Challenge of Electrolyte Solutions for Li−Air Batteries: Monitoring Oxygen Reduction and Related Reactions in Polyether Solutions by Spectroscopy and EQCM." *J. Phys. Chem. Lett.* vol. 4, pp. 127-133, 2013.

[41] J. M. Garcia, H. W. Horn, J. E. Rice. “Dominant decomposition pathways for ethereal solvents in Li-$O_2$ batteries.” *J. Phys. Chem. Lett.* vol. 6, pp. 1795-1799, 2015.

[42] D. Kwabi, T. Batcho, C. Amanchukwu, N. Ortiz-Vitoriano, P. Hammond, C. Thompson, Y. Shao-Horn. “Chemical instability of dimethyl sulfoxide in lithium-air batteries.” *J. Phys. Chem. Lett.* vol. 5, pp. 2850-2856, 2014.

[43] W. Walker, V. Giordani, J. Uddin, V. Bryantsev, G. Chase, D. A. Addison. “Rechargeable Li-$O_2$ battery using a lithium nitrate/N,N-dimethylacetamide electrolyte.” *J. Am. Chem. Soc* vol. 135, pp. 2076-2079, 2013.

[44] S. Das, J. Hojberg, K. B. Knudsen, R. Younsei, P. Johansson, P. Norby, T. Vegge. “Instability of ionic liquid-based electrolytes in Li-$O_2$ batteries.” *J. Phys. Chem. C.* vol. 119, pp. 18084-18090, 2015.

[45] N. Kumar, M. Radin, B. Wood, T. Ogitsu, D. Siegel. “Surface-mediated solvent decomposition in Li-air batteries: impact of peroxide and superoxide surface terminations.” *J. Phys. Chem. C.* vol. 119, pp. 9050-9060, 2015.

[46] G. Bieket, M. Winter, P. Beiker. “Electrochemical *In Situ* investigations of SEI and dendrite formation on the lithium metal anode.” *Phys. Chem. Chem. Phys.* vol. 17, pp. 8670-8679, 2015.

[47] J. S. Filippo, C. J. Chen, J. S. Valentine. “Reaction of superoxide with alkyl halides and tosylates.” *J. Org. Chem.* vol. 40, pp. 1678-1680, 1975.

[48] R. Black, S. H. Oh, J. H. Lee, T. Yim, B. Adams, L. F. Nazar. “Screening for superoxide reactivity in Li-$O_2$ batteries: Effect on $Li_2O_2$/LiOH crystallization.” *J. Amer. Chem. Soc.* vol.134, pp. 2902-2905, 2012.

[49] Y. Chen, S. A. Freunberger, Z. Peng, O. Fontaine, P. G. Bruce. “Charging a Li-$O_2$ battery using a redox mediator.” *Nature Chem.* vol. 5, pp. 489-494, 2013.

[50] H. D. Lim, H. Song, J. Kim, H. Gwon, Y. Bae, K. Y. Park, J. Hong, H. Kim, T. Kim, Y. H. Kim, X. Lepro, R. Ovalle-Robles, R. H. Baughman, K. Kang. “Superior rechargeability and efficiency of lithium-oxygen batteries: hierarchical air electrode architecture combined with a soluble catalyst.” *Angew. Chem. Int. Ed.* vol. 53, pp. 3926-3931, 2014.

[51] B. J. Bergner, A. Schuermann, K. Peppler, A. Garusch, J. Janek. “TEMPO: A Mobile Catalyst for Rechargeable Li-O2 Batteries.” *J. Am. Chem. Soc.* vol. 136, pp. 15054-15064, 2014.

[52] D. Kundu, R. Black, B. Adams, L. F. Nazar. “A Highly Active Low Voltage Redox Mediator for Enhanced Rechargeability of Lithium-Oxygen Batteries.” *ACS Central Sci.* vol. 1, pp. 510-515, 2015.

# Appendix A – Matlab Script for Mass Spectrometry Post-Processing

```
%Script to convert raw mass spec data into mols
%Based on Parameters:
    %Constant pressure in chamber of 2.03E-6 torr
    %Flow rate of Q mL/min
    %Gain of 500 (x V for m/z = 36)
    %Current O2 Calibration from 14/04/15
    %Current CO2 Calibration from 14/04/15

%Format matlab to have 15 digits + scientific notation output
format shortE
%Read file name and import into matlab as matrix
A = xlsread('rbEE4p4B','Gas'); %Read gas data
B = xlsread('rbEE4p4B','Electrochemistry'); %Read electrochemical data

%For quantification, output in moles
%1          Time            (s)
%2          32.00           Oxygen
%3          44.00           Carbon dioxide
%4          28.00           28
%5          36.00           36Ar
%6          40.00           Ar
%7          14.00           14
%8          16.00           Oxygen2
%9          2.00            Hydrogen
%10         29.00           Methanol?
%11         45.00           Formate
%x(nn)[moles] = (I - B)*S, where I = Intensity (Amps), B = Background
%(Amps), and S = Senstivity (moles/amps)
%Set Time coloumn as x, in min
x = [A(:,1)]./60; %Time conversion from seconds to minutes
%nV = 1.66124E-4; %moles gas in cell headspace
SO2 = 0.21092E-3; %Calibration factor for O2/36Ar per ppm --> June23
ySO2 = 0.00229; %y-intercept of calibration --> June23
EySO2 = 0.008512; %error in ySO2 due to calibration gas error --> June23
SCO2 = 0.2500E-3; %Calibration factor for CO2/36Ar per ppm --> June23
ySCO2 = 0.0182; %y-intercept of calibration for CO2 --> June23
BO2 = 0.00990483; %Baseline O2/36Ar
BCO2 = 5.326E-3; %Baseline CO2/36Ar
SCCO2 = 0.2378E-3;
ySCCO2 = 0.009939;
BCCO2 = 5.326E-3;
Q = 0.5; %Flow Rate carrier gas mL/min
EO2 = A(:,9);  %Voltage, used only for plotting purposes
Ig = 100E-3; %Current used, only for calculation of capacity w.r.t. time,
units mA


%****For Electrochemistry***
%Currently based on columns of 1 = Time (s), 2 = Voltage (V), 3 = Current
%(A), 4 = Capacity (mAh)
x2 = [B(:,1)]; %Taking column of time (s)
E = [B(:,2)]; %Taking column of voltage (V)
I = [B(:,3)]; %Taking column of current (A)
```

```
Capacity = [B(:,4)]; %Taking column of capacity (mAh) *is cumulative w.r.t
time*
cmole = Capacity./1000.*3600.*6.241E18./6.022E23*1E6; %Total moles e-
passed, umol


%****FOR O2 QUANTIFICATION***
O2Ar = (A(:,2)./A(:,5));%-BO2; %Ratio O2/36Ar
O2ppm = (O2Ar-ySO2)./SO2; %S corresponds ONLY to conditions above
O2 = (((O2ppm)*4.0894E-5).*Q)-.00165; %O2 in umol/min %Note: Last number
(if applicable) is background correction to zero graph
O2s = smooth(O2,40);%Smooth data, needed for differentiation
%dO2s = diff(O2s)./diff(x); %derivative (slope) of each interval
%dx = x(1:end-1);%Needed to make the derivative to x-values, uses forward
difference method
%molO2 = (O2ppm.*1E-6).*nV;%Moles O2 based on volume of resevoir and ppm
of gas
cmolO2 = cumtrapz(x,O2.'); %Integration of O2 umol/min data
%cO2ppm = cumsum(molO2);
%cmolO2 = integral(molO2,min[A(:,1)],max[A(:,1)]);%Integrate moles O2
CapacityO2 = cmolO2.*1E-6.*2.*6.022E23./6.241E18.*1000./3600; %total O2 to
mAh
diffO2s = diff(O2s); %Derivative curve of smoothed O2 evolution rate

%Plot of relevant O2 data
figure
subplot(2,3,1) %(nrows,ncol,plot num)
plot(x2./60,E) %plot 1 = Time vs. Voltage
    xlabel('Time (min)')
    ylabel('E (vs. Li/Li+)')
    title('Electrochemistry')
    axis ([0 400 2 5])
subplot(2,3,2)
[haxes,hline1,hline2] = plotyy(x,O2s, x2./60, E); %plot 2 = time vs. O2
(umol/min in Ar)
    xlabel('Time (min)')
    axes(haxes(1)) %Axis of first set of data
       ylabel('O2 (umol/min)')
       axis ([0 max(x) 0 0.25])
       set(gca,'YTick',[0:0.05:0.25])
    axes(haxes(2)) %Axis of second set of data
       ylabel('E (vs. Li/Li+)')
       axis ([0 max(x2) 2 5]) %axis([xmin xmax ymin ymax])
       set(gca,'YTick',[2:0.5:5])
    title('O2 Evolution')
    set(hline2, 'LineStyle', '--') %Set data line 2 to dash style
subplot(2,3,3) %plot 3 = time vs. cumulative O2 (umols)
[haxes,hline1,hline2] = plotyy(x,cmolO2, x2./60, cmole);
    xlabel('Time (min)')
    axes(haxes(1)) %Axis of first set of data
       ylabel('O2 Evolved (umols)')
       axis ([0 max(x) 0 80])
       set(gca,'YTick',[0:10:80])
    axes(haxes(2)) %Axis of second set of data
       ylabel('e- Passed (umols)')
       set(gca,'YTick',[0:20:160])
```

```
       axis ([0 max(x) 0 160]) %axis([xmin xmax ymin ymax])
    title('Moles O2, e- Generated')
%subplot(2,3,4)
%plot(x,smooth(O2ppm,40)) %plot 4 = time vs. O2 (ppm)
%    xlabel('Time (min)')
%    ylabel('O2 (ppm)')
%    title('Change in O2 w.r.t Time')
%subplot(2,3,5)
%[haxes,hline1,hline2] = plotyy(EO2,CapacityO2, E, Capacity); %plot 5 =
Capacity (actual, theory) vs. V
%    xlabel('E (vs. Li/Li+)')
%    axes(haxes(1)) %Axis of first set of data
%       ylabel('Capacity O2 Evolved (mAh)')
%       axis ([2.8 4.75 0 1])
%    axes(haxes(2)) %Axis of second set of data
%       ylabel('Capacity e- Passed (mAh)')
%       axis ([2.5 4.75 0 1]) %axis([xmin xmax ymin ymax])
%    title('Capacity vs. O2')
    %set(hline2, 'LineStyle', '--') %Set data line 2 to dash style

%****FOR CO2 QUANTIFICATION***
CO2Ar = (A(:,3)./A(:,5)); %Ratio CO2/36Ar - Baseline
CO2ppm = (CO2Ar-ySCO2)./SCO2; %S corresponds ONLY to conditions above
CO2 = ((((CO2ppm)*4.0894E-5).*Q))-3.6E-4; %CO2 in umol/min %Note: Last
number is background correction to zero graph
CO2s = smooth(CO2,40);%Smooth data, needed for differentiation
%dO2s = diff(O2s)./diff(x); %derivative (slope) of each interval
%dx = x(1:end-1);%Needed to make the derivative to x-values, uses forward
difference method
%molO2 = (O2ppm.*1E-6).*nV;%Moles O2 based on volume of resevoir and ppm
of gas
cmolCO2 = cumtrapz(x,CO2.'); %Integration of CO2 umol/min data
%cO2ppm = cumsum(molO2);
%cmolO2 = integral(molO2,min[A(:,1)],max[A(:,1)]);%Integrate moles O2
CapacityCO2 = cmolCO2.*1E-6.*2.*6.022E23./6.241E18.*1000./3600; %total CO2
to mAh
diffCO2s = diff(CO2s); %derivative of smoothed CO2 evolution rate

%Plot of relevant CO2 data
figure
subplot(2,3,1) %(nrows,ncol,plot num)
plot(x2./60,E) %plot 1 = Time vs. Voltage
    xlabel('Time (min)')
    ylabel('E (vs. Li/Li+)')
    title('Electrochemistry')
    axis ([0 400 2 5])
subplot(2,3,2)
[haxes,hline1,hline2] = plotyy(x,CO2s, x2./60, E); %plot 2 = time vs. CO2
(umol/min in Ar)
    xlabel('Time (min)')
    axes(haxes(1)) %Axis of first set of data
       ylabel('CO2 (umol/min)')
       axis ([0 max(x) 0 0.015])
       set(gca,'YTick',[0:0.005:0.015])
    axes(haxes(2)) %Axis of second set of data
       ylabel('E (vs. Li/Li+)')
```

```
       axis ([0 max(x2) 2 5]) %axis([xmin xmax ymin ymax])
       set(gca,'YTick',[2:0.5:5])
    title('CO2 Evolution')
    set(hline2, 'LineStyle', '--') %Set data line 2 to dash style
subplot(2,3,3) %plot 3 = time vs. cumulative O2 (umols)
[haxes,hline1,hline2] = plotyy(x,cmolCO2, x2./60, cmole);
    xlabel('Time (min)')
    axes(haxes(1)) %Axis of first set of data
       ylabel('CO2 Evolved (umols)')
       axis ([0 max(x) 0 4])
       set(gca,'YTick',[0:1:4])
    axes(haxes(2)) %Axis of second set of data
       ylabel('e- Passed (umols)')
       set(gca,'YTick',[0:20:160])
       axis ([0 max(x2) 0 160]) %axis([xmin xmax ymin ymax])
    title('Moles CO2, e- Generated')

%****FOR 13CO2 (m/z = 45) QUANTIFICATION***
CCO2Ar = (A(:,10)./A(:,5))-BCCO2; %Ratio CCO2/36Ar - Baseline
CCO2ppm = (CCO2Ar-ySCCO2)./SCCO2; %S corresponds ONLY to conditions above
CCO2 = ((((CCO2ppm./1E6)*4.0894E-5).*Q)*1E6)+4.108E-4; %CCO2 in
umol/min %Note: Last number is background correction to zero graph
CCO2s = smooth(CCO2,40);%Smooth data, needed for differentiation
%dO2s = diff(O2s)./diff(x); %derivative (slope) of each interval
%dx = x(1:end-1);%Needed to make the derivative to x-values, uses forward
difference method
%molO2 = (O2ppm.*1E-6).*nV;%Moles CCO2 based on volume of resevoir and ppm
of gas
cmolCCO2 = cumtrapz(x,CCO2.'); %Integration of CCO2 umol/min data
%cO2ppm = cumsum(molO2);
%cmolO2 = integral(molO2,min[A(:,1)],max[A(:,1)]);%Integrate moles O2
CapacityCCO2 = cmolCCO2.*1E-6.*2.*6.022E23./6.241E18.*1000./3600; %total
O2 to mAh
diffCCO2s = diff(CCO2s); %Derivative curve of smoothed O2 evolution rate

%Write to .xls spreadsheet, title date_Out.xls

%Raw Data Output
%headerRaw = {'Time (min)' '32 O2 (A)' '44 CO2 (A)' '28 N2 (A)' '36 Ar
(A)' '40 Ar (A)' '14 N2 (A)' '16 O2 (A))' '2 H2 (A)' '45 CHO2 (A)'}
%GasRaw = [

%For Oxygen Amount
headerO2 = {'Time (min)' 'Capacity (mAh)' 'O2 Rate (umol/min)' 'dO2 Rate
(umol/min)' 'Total O2 (umol)'}; %cell array of headers 1 by 5
GasO2 = [x (x./60).*Ig O2s [diffO2s;0] cmolO2']; %Data in columns
xlswrite('rbEE4p4B_Out', headerO2, 'Oxygen') % by defualt starts from A1
xlswrite('rbEE4p4B_Out', GasO2, 'Oxygen','A2') % array under the header,
starting at A2

%For CO2 Amount
headerCO2 = {'Time (min)' 'Capacity (mAh)' 'CO2 Rate (umol/min)' 'dCO2
Rate' 'Total CO2 (umol)'}; %cell array of headers 1 by 5
GasCO2 = [x (x./60).*Ig CO2s [diffCO2s;0] cmolCO2']; %Data in columns
xlswrite('rbEE4p4B_Out', headerCO2, 'Carbon Dioxide') % by defualt starts
from A1
```

```
xlswrite('rbEE4p4B_Out', GasCO2, 'Carbon Dioxide','A2') % array under the
header, starting at A2

%For 13CO2 Amount
headerCCO2 = {'Time (min)' 'Capacity (mAh)' '13CO2 Rate (umol/min)'
'd13CO2 Rate' 'Total 13CO2 (umol)'}; %cell array of headers 1 by 5
GasCCO2 = [x (x./60).*Ig CCO2s [diffCCO2s;0] cmolCCO2']; %Data in columns
xlswrite('rbEE4p4B_Out', headerCCO2, '13 Carbon Dioxide') % by defualt
starts from A1
xlswrite('rbEE4p4B_Out', GasCCO2, '13 Carbon Dioxide','A2') % array under
the header, starting at A2

%For Electrochemistry
headerElec = {'Time (min)' 'Capacity (mAh)' 'Current (A)' 'Voltage (V)'
'e- Total (umol)'};
Elec = [x2./60 Capacity I E cmole];
xlswrite('rbEE4p4B_Out', headerElec, 'Electrochemistry')
xlswrite('rbEE4p4B_Out', Elec, 'Electrochemistry','A2')

'Finished!!!!'
```

## Appendix B – $Mo_2C$ Synthesis and XPS Characterization

As stated in the acknowledgements, the synthesis and XPS characterization was performed by Dr. Dipan Kundu. The work presented in this appendix is not that of my own. The work with $Mo_2C$ is presented in *Section 5*.3 as part of this thesis to exemplify the importance of mass spectrometry, and my main contributions to the $Mo_2C$ work involve electrochemical measurements and mass spectrometry analysis. To review the work in its entirety, please consult: D. Kundu, R. Black, B. Adams, K. Harrison, K. Zavadil, L. F. Nazar. "Nanostructured metal carbides for aprotic Li-$O_2$ batteries: new insights into interfacial reactions and positive electrode stability." *J. Phys. Chem. Lett.* vol. 6, pp. 2252-2258, 2015. **DOI:** 10.1021/acs.jpclett.5b00721

**Synthesis of $Mo_2C$ Nanofibers:**

The anilinium trimolybdate hydrate $(C_6H_5NH_3)_2Mo_3O_{10} \cdot 2H_2O$ precursor was synthesized by dissolving 2 mmol of ammonium molybdate $(NH_4)_6Mo_7O_{24} \cdot 4H_2O$) in 40 ml of distilled water, adding 36 mmol of aniline, and stirring the mixture for 1 h.The pH of the mixture was adjusted to ~ 4 by addition of 1 M HCl and the stirring was continue for 6 h at 50°C. A fluffy white product, $C_6H_5NH_3)2Mo_3O_{10} \cdot 2H_2O$, resulted, which was filtered and thoroughly washed with water and ethanol. The precursor was subjected to thermal decomposition at 800°C under Ar flow for 5 h with a heating ramp of 2°C/min to obtain theMo2C nanofibers, which were first passivated under a 1% $O_2$/balance Ar flow for 4 h prior to exposure to ambient atmosphere.

**XPS Spectra of $Mo_2C$ Nanofibers**

The Mo 3d XPS spectra of the $Mo_2C$ nanofibers were fit with a classic contribution of species ranging from $Mo^0$ to $Mo^{6+}$.[1, 2] The surface Mo-species ($Mo^{2+}$ - $Mo^{6+}$) exhibit an average oxidation state of $Mo^{4.1+}$ (i.e., $MoO_{2+\delta}$) [3] as summarized in the quantitative analysis shown in **Figure B-1** (Pristine). A more detailed analysis of the Mo 3d XPS spectra is available in **Figure B-2**.

**XPS Spectra for Discharged/Charged Positive electrode**

Further revealed from the XPS spectra are what occurs on discharge and charge. As was shown in the body of this thesis, the gas evolution on $Li_2O_2$ charge is extremely poor, owing to the interfacial reaction between $MoO_{2+\delta}$ and $Li_2O_2$. This reaction is evidenced by the increase in the average oxidation of $MoO_{2+\delta}$ to $Mo^{5.5+}$ (from $Mo^{4.1+}$), via the following reaction:

$$x/2\ Li_2O_2 + MoO_{2+\delta} \rightarrow Li_xMoO_3 \quad (\text{where x is} \sim 0.5)$$

On electrochemical oxidation, the original $Mo_2C$ surface is nearly recovered. This indicates loss of the $Mo^{5.5+}$ component, and regeneration of the original $MoO_{2+\delta}$ surface. Hence, this supports the “self-cleaning” mechanism of the surface, and creates electronically conductive, catalytically active redox sites for the next reduction cycle.

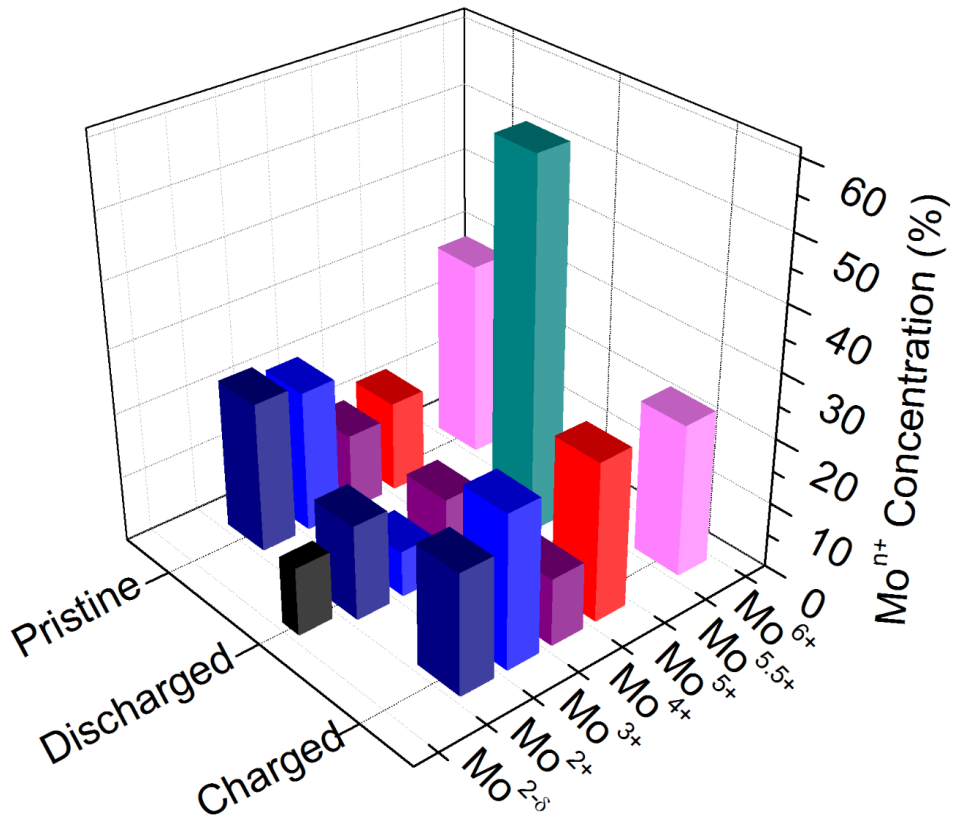


**Figure B-1 -** Quantitative representation of the $Mo_2C$ electrode surface obtained from in-depth XPS studies of the pristine, discharged and charged cathode after galvanostatic discharge/charge in a Li-$O_2$ cell with LiTFSI-TEGDME based electrolyte. The assigned oxidation states of the Mo species are approximated in accord with well-known values from the literature reported for $Mo_2C$,[3] and Mo-oxides as summarized in the XPS Handbook.

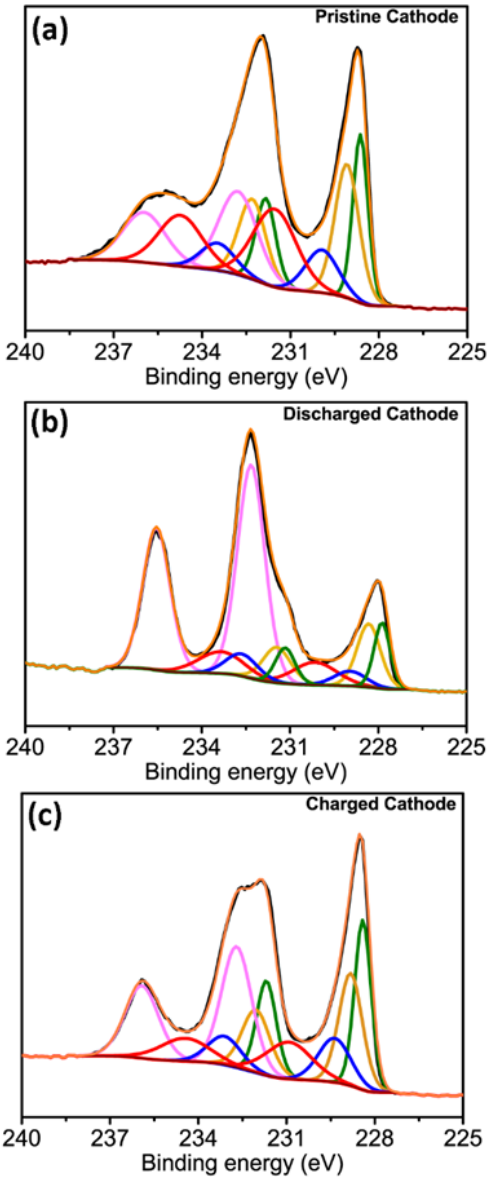


| Sample | Species | Peak positions for Mo3d5/2 & Mo3d3/2 (eV) | FWHM for Mo3d5/2 Mo3d3/2 | Species Percentage (%) |
|---|---|---|---|---|
| (pristine cathode) | $Mo^{2+}$ | 228.63<br>231.84 | 0.60<br>0.79 | 18.49 |
| | $Mo^{3+}$ | 229.08<br>232.30 | 0.97<br>1.08 | 23.64 |
| | $Mo^{4+}$ | 229.94<br>233.47 | 1.31<br>1.37 | 10.21 |
| | $Mo^{5.2+}$ | 231.53<br>234.74 | 1.71<br>1.75 | 24.31 |
| | $Mo^{6+}$ | 232.78<br>235.97 | 1.54<br>1.71 | 23.36 |
| (discharged cathode) | $Mo^{2-\delta}$ | 227.87<br>231.60 | 0.64<br>0.79 | 10.26 |
| | $Mo^{2+}$ | 228.32<br>231.45 | 0.94<br>1.12 | 14.44 |
| | $Mo^{3+}$ | 228.96<br>232.64 | 1.27<br>1.27 | 6.89 |
| | $Mo^{4+}$ | 230.15<br>233.14 | 1.76<br>1.84 | 11.70 |
| | $Mo^{5.5+}$ | 232.32<br>235.54 | 1.095<br>1.098 | 56.75 |
| (charged) | $Mo^{2+}$ | 228.41<br>231.68 | 0.66<br>0.79 | 22.97 |
| | $Mo^{3+}$ | 228.82<br>232.04 | 0.94<br>1.12 | 21.65 |
| | $Mo^{3.5+}$ | 229.37<br>233.11 | 1.29<br>1.33 | 11.67 |
| | $Mo^{5+}$ | 230.92<br>234.44 | 1.83<br>1.96 | 13.77 |
| | $Mo^{6+}$ | 232.70<br>235.92 | 1.21<br>1.35 | 29.92 |

**Figure B-2 -** Mo3d core level XPS spectra for the (a) pristine, (b) discharged, and (c) charged cathode. In the fitted XPS spectra, black line = experimental data, orange line = overall fitted data, other colour lines = fitted individual components ($Mo^{2-\delta}$/$Mo^{2+}$: green, $Mo^{3+}$: golden brown, $Mo^{4+}$: blue, $Mo^{5+}$: red, $Mo^{6+}$: magenta). The oxidation states of the Mo components used in fitting the experimental spectra are best approximated, where their assignment is fully consistent with the literature.[4] The table highlights the peak positions in binding energy, and full width at half maximum (FWHM) for both Mo $3d_{3/2}$ and Mo $3d_{5/2}$ levels along with the percentage of the Mo component obtained by fitting of the XPS spectra collected on pristine, discharged, and charged $Mo_2C$ cathode. Electrochemical discharge/charge was carried out in the 0.5M LiTFSI-TEGDME based electrolyte.

## Appendix B References


[1] Wan, C.; Regmi, Y. N.; Leonard, B. M. Multiple Phases of Molybdenum Carbide as Electrocatalysts for the Hydrogen Evolution Reaction. *Angew. Chem. Int. Ed*. **2014**, *53*, 6407-6410.

[2] Porosoff, M. D.; Yang, X.; Boscoboinik, J. A.; Chen, J. G. Molybdenum Carbide as Alternative Catalysts to Precious Metals for Highly Selective Reduction of $CO_2$ to CO. *Angew. Chem. Int. Ed.* **2014**, *53*, 6705-6709.

[3] Bagus, P. S.; Ilton, E. S.; Nelin, C. J. The Interpretation of XPS Spectra: Insights Into Materials Properties. *Surf. Sci. Rep.* **2013**, *68*, 273–304.

[4] Li, Z.; Chen, C.; Zhan, E.; Ta, N.; Li Y. ; Shen, W. Crystal-Phase Control of Molybdenum Carbide Nanobelts for Dehydrogenation of Benzyl Alcohol. *Chem. Commun.* **2014**, *50*, 4469-4471.

# Appendix C – Inverse Opal Carbon

## Introduction

In this appendix, I will discuss the results of a collaborative project with Dr. Paik at Hanyang University. While the main body of this dissertation focuses on electrolyte issues with metal-$O_2$ batteries and methods to test/screen for stability, it only touches on the importance of the positive electrode material. It was clear from the presented studies that the stability of the positive electrode is of utmost importance when selecting a positive electrode material. However, other considerations are necessary, such as electrode morphology as a means to best house $Li_2O_2$ and obtain the maximum possible energy density. Hence, as part of this collaboration, we investigated the use of an inverse opal carbon (IOC) positive electrode material. In this section, I will demonstrate how the positive electrode architecture has a drastic improvement on the overall energy density of the Li-$O_2$ battery. Through tailored material architecture, the accommodation of the solid discharge product ($Li_2O_2$ and electrolyte decomposition product) is greatly improved. However, as will become apparent, both stability of the carbon surface and decomposition of the electrolyte are major issues that must be overcome before advanced positive electrode architectures can be used in the Li-$O_2$ cell.

As shown in **Figure C-1a** and **Figure C-1c**, an electrode created from active ORR particles with PTFE binding agent can only accommodate a high fraction of discharge product if the entirety of the cathode pore volume is accessible at all stages of cell operation (a high PTFE content, often necessary to create a highly porous and robust cathode, will also block ORR site activity and increase cathode impedance). As will be demonstrated in this section, the specific capacity of the electrode diminishes as the thickness increases due to the

inhibition of reactants to reach the deep-depth active sites. The result is an accumulation of discharge product on the surface of the positive electrode, which results in unfilled void space and a loss in specific energy as the discharge terminates prematurely. Considering that the key advantage of Li-$O_2$ batteries is its high energy density, this issue is critical for practical use. Previous publications have explored the role of carbon morphology and pore structure on Li-$O_2$ performance, but many studies were conducted during the infancy of the Li-$O_2$ battery and employed highly unstable electrolytes,[1, 2] and/or involved the study of micropore (< 2 nm) pore sizes.[3, 4, 5, 6] Theoretical calculations have shown that inhibited oxygen transport due to pore blockage of insoluble discharge product, as well as electronic transport limitations because of the insulating nature of the discharge product, are primary reasons for the termination of discharge.[7,8,9]

The carbon inverse opal electrode was prepared by employing a polystyrene (PS) opal array as a template.[10] In the inverse opal structure derived from a close packed opal array, one large pore has 12 macro-pore channels generated from the contact point with its neighbour PS balls. This inverse opal carbon (IOC) electrode enables efficient electron transport within its 3D network structure, accommodating $Li_2O_2$ formation without pore clogging (**Figure C-1c** and **Figure C-1d**). This provides a discharge capacity of over 8,000 mAh/$g_c$ (> 1000 mAh/$g_{total}$ if one includes the mass of the discharge product, close to the theoretical value of 1158 mAh/$g_{Li2O2}$), regardless of the cathode thickness (within limits).

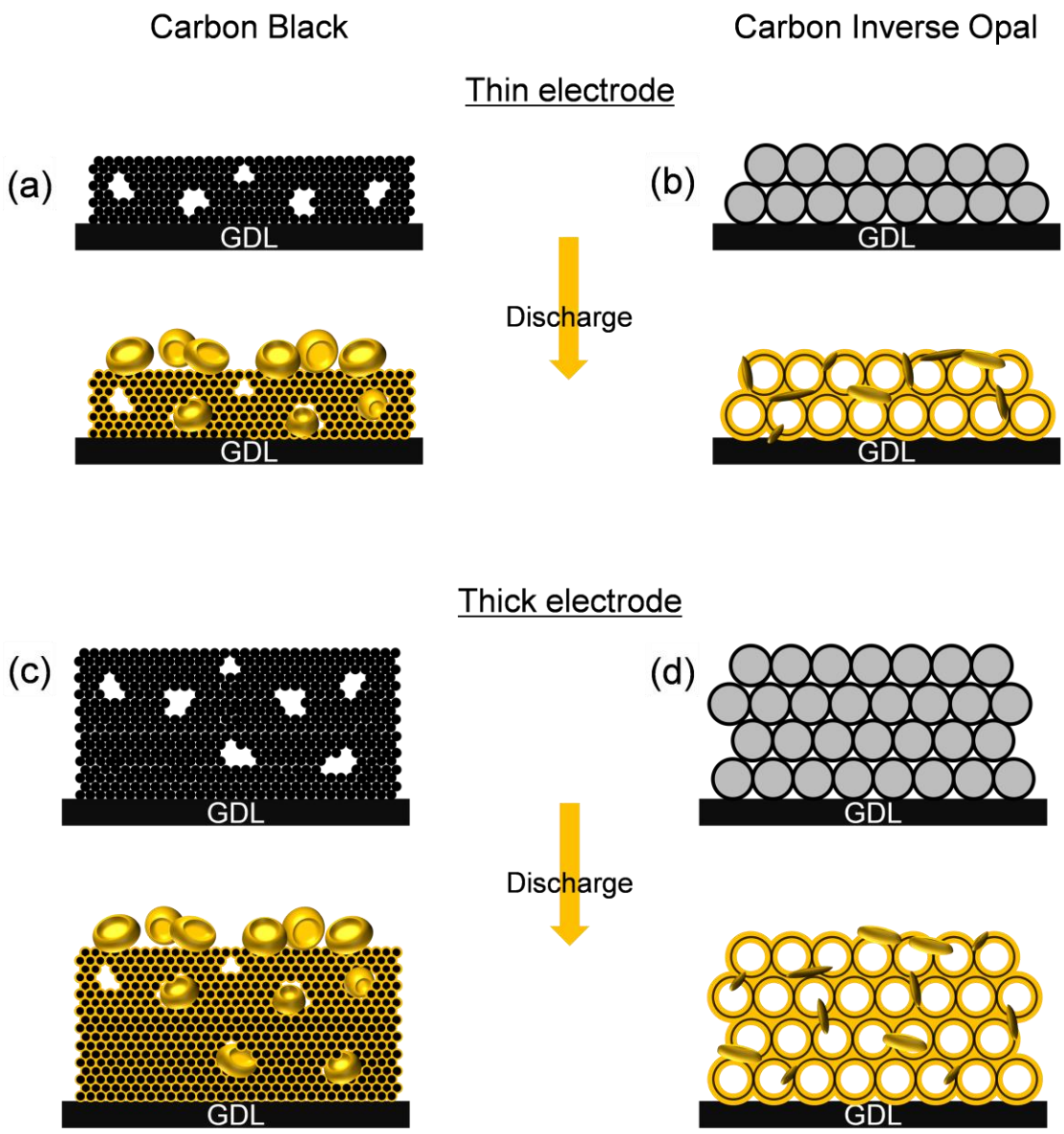


**Figure C - 1** - Illustration for the accumulation of $Li_2O_2$ during discharge of a carbon black/binder composite and free-standing carbon inverse opal electrodes a) thin electrodes and b) thick electrodes.

## Experimental

### Material Synthesis

A polystyrene (PS) opal array - as a sacrificial template - was prepared on a gas diffusion layer (Toray - TGP-H-060) using a convective force driven self-assembly method. PS colloids with a diameter of ~450 nm (3495A, Latex Microsphere Suspensions, Thermo Standards Particles) were used. The thickness of the PS opal array was controlled by adjusting PS concentration in the aqueous suspension from 0.2 wt% to 5 wt%. The PS opal array was impregnated with a 0.2 M glucose solution with 0.5% $H_2SO_4$ (dehydration reagent). The sample was then dried at 80$^o$C for 8 hours and maintained at 170$^o$C overnight. The PS template was removed at 300$^o$C for 2 h and carbonization was carried out at 1400$^o$C for 2 h in an argon atmosphere.

### Characterization

The carbon inverse opal structures were characterized using field emission scanning electron microscopy (FE-SEM, JSM 7600F, JEOL, Japan) and transmission electron microscopy (FE-TEM, JEM-2100F, JEOL, Japan). Raman spectroscopy was performed on a JY LABRAM-HR confocal laser micro-Raman spectrometer using $Ar^+$ laser excitation with a wavelength of 514.5 nm. X-ray diffraction (XRD, Rigaku D/MAX RINT-2000) measurements were performed to study the structural properties with Cu-Kα as the radiation source.

### Electrochemical Measurements

As-prepared carbon inverse opal on GDL was used as an air electrode without any additives or binders. The Ketjen black electrode was prepared by a mixture of Ketjen black carbon and lithiated Nafion™ binder in N-methy-2-pyrrolidone (NMP) with a weight ratio of 9:1. All electrodes were dried at 120 $^{o}$C in vacuum oven overnight. The masses of the carbon inverse opal and carbon black electrodes were measured using a microbalance (Sartorius SE2, resolution 1 μg, Sartorius, Germany). 1 M LiTFSi in tetraethylene glycoldimethyl ether (TEGDME) and lithium metal were used as an electrolyte and an anode, respectively. Cells were assembled in an argon filled glove box by stacking a Li metal negative electrode, a polypropylene separator, and air electrodes between stainless steel rods. The electrochemical performances of the cells were evaluated using a galvanostat/potentiostat (TOSCAT 3000,Toyo Systems, Tokyo, Japan).

## Results and Discussion

**Figure C-2** shows the SEM micrograph of the PS opal array and its carbon inverse opal structure. The PS colloidal opal array was prepared by a confined convective assembly method, and was used as a template for the synthesis of the carbon inverse opal.[11] **Figure C-2a** and **Figure C-2b** show top-view SEM and cross-sectional SEM images of the PS opal array, respectively. The PS colloidal opal array exhibits a close-packed hexagonal arrangement. The carbon inverse opal structure was prepared by infiltration of the carbon precursor solution into the PS array template, followed by the removal of the PS template during the carbonization process to synthesize the final carbon structure. The opal carbon was treated at 1400 $^{o}$C for maximum graphitization in order to minimize the fraction of carbon-oxygen groups while still maintaining the highly porous structure. As shown in **Figure C-2c**, the carbon inverse opal structure has a well-ordered hexagonal network with a

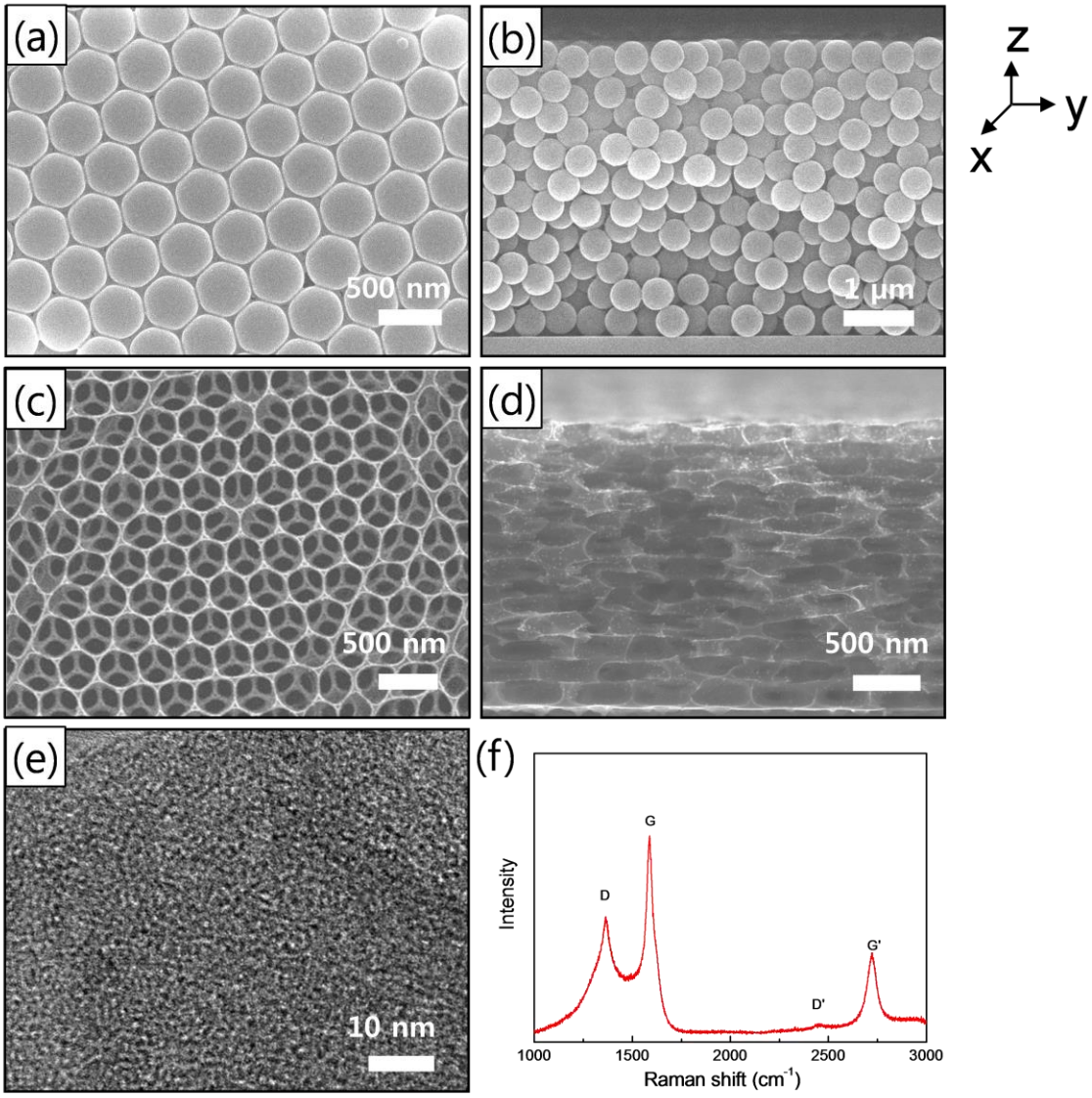


**Figure C - 2 -** (a) Top view and (b) cross sectional SEM images of PS opal array. (c) Top view and (d) cross sectional SEM images of the carbon inverse opal. (e) HR-TEM image and (f) Raman spectrum of the carbon inverse opal.

pore diameter of ~350 nm in the basal plane (i.e., the *xy* plane of the film). On the other hand, the thickness of the carbon inverse opal structure decreased by half with respect to the height of the original PS opal array owing to flattening of the pore structure. This is attributed to the shrinkage of the opal structure during the carbonization process. The microstructure of the carbon inverse opal was also characterized by high resolution transmission electron

microscopy (HRTEM). The carbon inverse opal is comprised of disordered carbon that contains many mesopores, as shown in the high-resolution TEM image (**Figure C-2e**). These mesopores are generated during the polymerization and carbonization of the carbon source.[12] Raman spectroscopy (**Figure C-2f**), two characteristic peaks at 1585 $cm^{-1}$ and 1360 $cm^{-1}$, which correspond to an in-plane carbon stretching mode (G-band) and a disorder-induced vibration mode (D-band), respectively, were observed. The intensity ratio of the D and G bands of the carbon inverse opal ($I_{D/G}$= 0.60) is the same as that ($I_{D/G}$= 0.60) of commercial KB, which provides an opportunity to study electrode geometry dependent electrochemical properties that are independent of the graphitization degree of the carbon electrode.

The 3D network structure and large void space enables efficient oxygen/Li-ion transport within the electrode and easily accommodates the discharge product. The first discharge/charge cycle at current rates of 400, 200, 100 and 50 $mA/g_c$ at a limited discharge capacity of 1000 $mAh/g_c$, showed that the polarization in both ORR and OER increases with increasing current density as expected (**Figure C-3**). The carbon inverse opal exhibits charge behavior similar to that of other carbon-based electrodes in previous reports, and involves the step-wise oxidation of $Li_2O_2$ coupled with Li-carbonate oxidation.[13] This voltage plateau corresponds to the oxidation of both $Li_2O_2$ and cathode/electrolyte decomposition products formed during discharge and charge. Formation of such products is known to occur with the use of glyme-based electrolyte, as thoroughly discussed within the body of this dissertation. Currently, it is known that the electrolyte decomposition plays a major role in the cycling limitation of

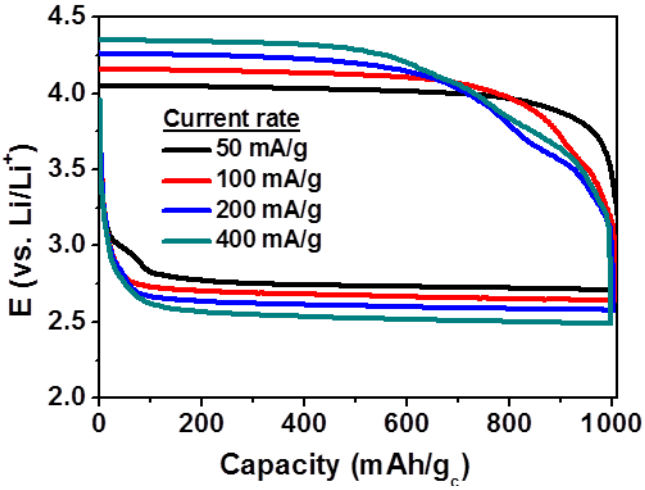


**Figure C - 3 -** (a) Cycle performance of carbon inverse opal electrode at a current density of 50mA/$g_c$. (b) Galvanostatic discharge/charge profiles of carbon inverse opal electrode at various current densities.

aprotic Li-$O_2$ batteries, and attempts to solve this electrolyte issue, either through the use of more stable-organic electrolytes [14] or redox mediators.[15,16,17] are currently underway. Unfortunately, no electrolyte is known to be completely stable to the Li-$O_2$ chemistry, and thus the production of decomposition products is unavoidable until this hurdle is overcome. The main body of this thesis covers this issue extensively.The issue of cathode decomposition is also a concern, for carbon has been shown to decompose electrochemically at charge voltages above 3.5 V on charge, as well as chemically decompose through reaction with the intermediate discharge product $LiO_2$ on discharge.[18, 19] Such an issue has not been addressed within the work presented here, and is a major concern with further development of these advanced electrode architectures. The large surface area and exposed active sites make these decomposition reactions much more prevalent.

The $Li_2O_2$ capacity at different depths of discharge, used as a means to probe the pore filling of the carbon inverse opal electrode, is shown in **Figure C-4** at i) 2000 mAh/$g_c$, ii)

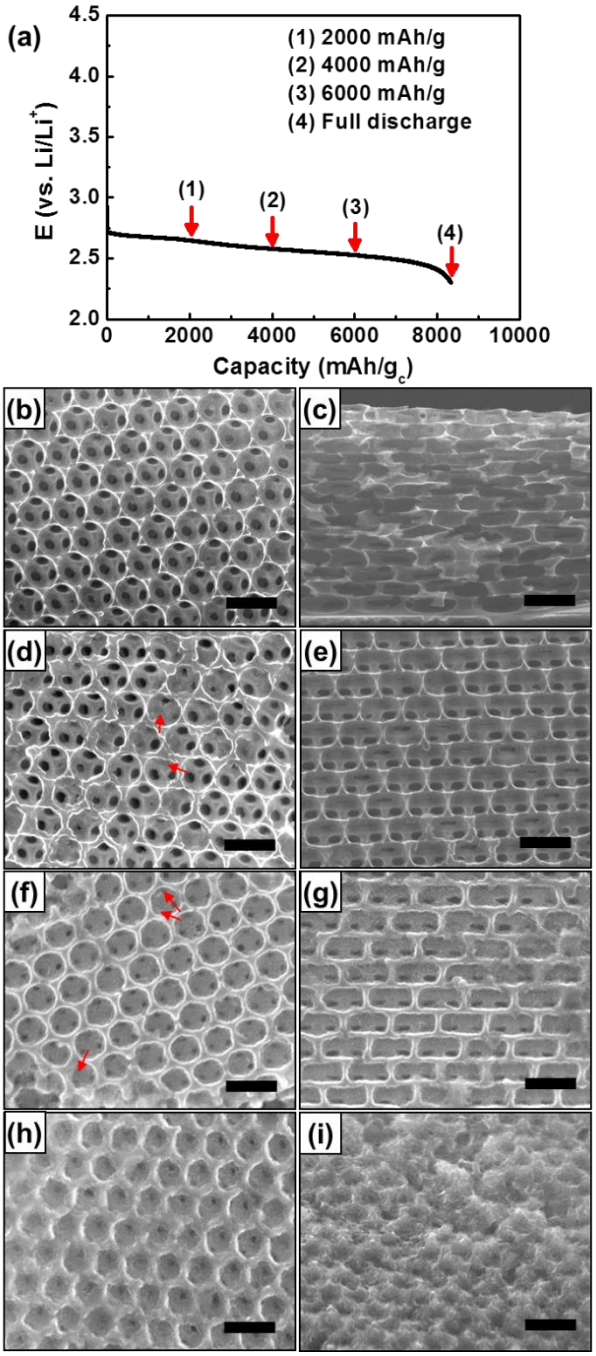


**Figure C - 4 -** Morphological change of carbon inverse opal as a function of the depth of discharge. (a) Discharge profile of the carbon inverse opal electrode with a cutoff voltage of 2.3V. Top-view and cross-sectional SEM images at 2000 mAh/$g_c$ (b-c), 4000 mAh/$g_c$ (d-e), 6000 mAh/$g_c$ (f-g) and after full discharge to 8300 mAh/$g_c$ (h-i). Scale bar is 500 nm.

4000 mAh/$g_c$ iii) 6000 mAh/$g_c$, and iv) end of discharge (cut-off voltage of 2.3 V) where a maximum discharge capacity of 8,300 mAh/$g_c$ (1020 mAh/$g_{cathode}$) is achieved. The inverse opal pore geometry allows for accommodation of the discharge product throughout the entirety of the cathode. **Figure C-4b** shows the top view and cross sectional view SEM images of carbon inverse opal electrode after discharge to 2000 mAh/$g_c$. Although noticeable changes in the overall morphology and dimension compared with pristine carbon inverse opal was not observed, the porous characteristics of the wall, shown in the pristine electrode, vanished as the pores were filled with the discharge product. Upon further discharge to 4,000 and 6,000 mAh/$g_c$, the macro pore channels fill with the discharge products as indicated in **Figure C-4d** and **Figure C-4f**, accompanied by increase of the wall thickness as the discharge product accumulates. At the end of discharge, the entirety of the void space has been filled. The cross sectional view SEM image (**Figure C-4i**) shows this more clearly, implying that the termination of discharge is due to the complete filling of the interior pores of the electrode. The complete pore occlusion by the discharge product prevents the reactants from reaching further catalytic active sites for ORR. The insulating nature of the $Li_2O_2$ also prevents further ORR due to the large increase in the cathode resistance, which has been shown to be a primary cause of discharge termination.[7, 8, 9, 20]

Both KB electrodes (with binder) and carbon inverse opal electrodes (binder free) were fully discharged to investigate the relationship between the electrode configuration and the discharge capacity with electrode thickness. KB is a very high surface area carbon (~1400 $cm^2/g$) comprised primarily of micropores and with a high pore volume (~4.95 $cm^3/g$). In contrast, the IOC has a theoretically smaller pore volume (~1.58 $cm^3/g$), and a much different, more ordered pore structure. **Figure C-5a** and **Figure C-5b** shows the maximum capacity

discharge profiles for KB and IOC electrodes with a thickness of 0.5, 1, 2, 3, 4 µm, respectively. Both exhibit similar discharge plateaus around 2.65 – 2.7 V. KB and IOC electrodes with a thickness of 0.5 µm deliver gravimetric discharge capacities of 6,245 and 8,816 mAh/$g_c$, respectively. However, the IOC electrode maintains a specific discharge capacity over 8,000 mAh/$g_c$ independent of the film thickness. This correlates to a loss in gravimetric capacity of only 6% across all of the film thicknesses studied. The uniform pore density and 3D network pore structure of the carbon inverse opal enable a non-variant specific discharge capacity by accommodating the $Li_2O_2$. The capacity of the KB electrodes

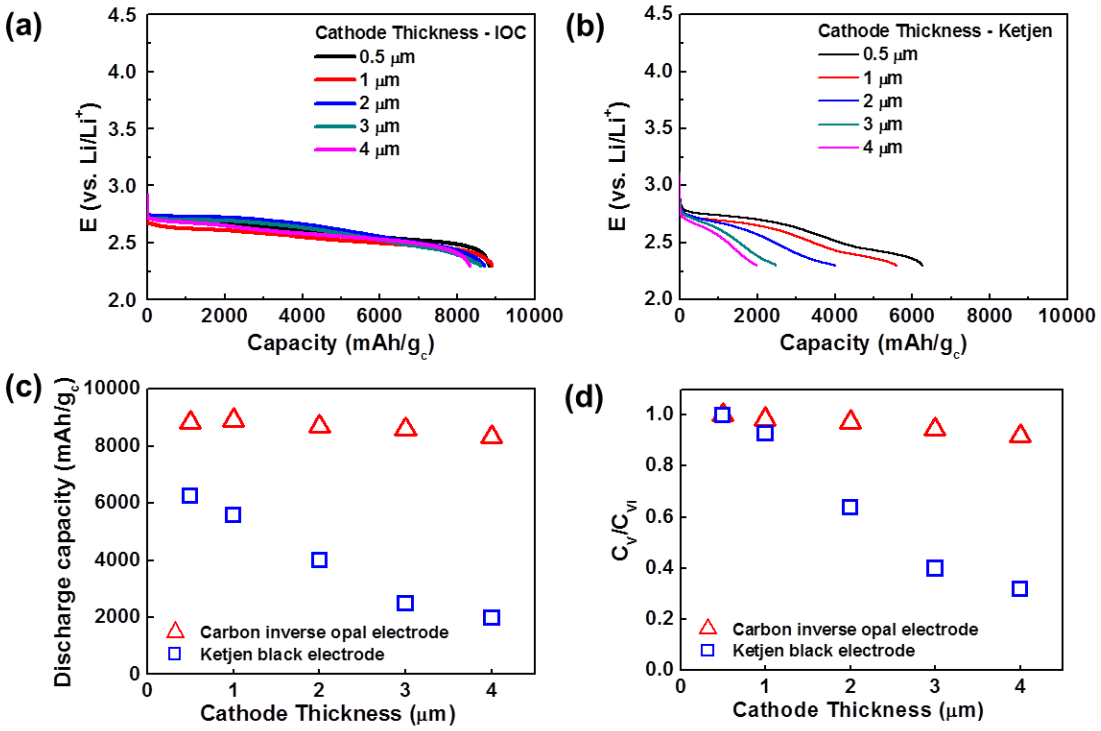


**Figure C - 5 -** Maximum discharge profiles of the (a) carbon inverse opal electrode and (b) Ketjen black/binder electrode of various thicknesses. (c) Plot of specific discharge capacity vs. electrode thickness for the carbon inverse opal and Ketjen black electrodes. (d) Plot of capacity as a function of void volume, normalized to the thinnest electrode studied (0.5 µm).

are significantly decreased with increased electrode thickness: at 4 μm, it delivers a discharge capacity of only 2,070 mAh/$g_c$, a 67% decrease in capacity compared to a cathode thickness of 0.5 μm. The GDL exhibits very low charge/discharge capacities and poor cycle performance, which indicates the contribution of GDL layer on the capacity is negligible. The results obtained here closely compare to other binder-free cathode architectures, such as free-standing carbon fibers reported by Mitchell et. al.[21] Taking into account the total mass of the final discharged cathode and a comparison of the energy density, Mitchell et. al achieves a gravimetric energy density of near 2,500 Wh/$kg_{Dis}$, roughly 75% of the theoretical achievable energy density based on $Li_2O_2$ (~3215 Wh/kg). A similar calculation for the IOC cathodes reveals an energy density between 2682 Wh/$kg_{Dis}$ and 2664 Wh/$kg_{Dis}$, as one increases the cathode thickness from 0.5 um – 4 um (based on a nominal voltage of 2.60 V), which is roughly 83% of the theoretical energy density limit. These results are represented in **Figure C-5c**. As mentioned previously, the obtainable energy density appears to be near independent of the cathode thickness due to the 3D porous structure, which allows for $Li_2O_2$ accomodation during all stages of discharge. In comparison to KB electrodes, at a thickness of 0.5 μm the energy density is 2560 Wh/$kg_{Dis}$, near that of the IOC. However, this energy density diminishes greatly as cathode thickness is increased to 4.0 μm, where an energy density of 1915 Wh/$kg_{Dis}$ is obtained, much lower than both the IOC and other binder-free cathodes reported in the literature.

**Figure C-5d** shows a comparison of the discharge void volume capacity ($C_v$) normalized to the void volume capacity of the thinnest electrode tested (0.5 μm). The inverse opal carbon cathode displays only a minimal decrease in $C_v$ as thickness increases (~8 % from 0.5 μm to 4 μm). A high percentage of the voids are accessible for the Li-$O_2$ chemistry,

regardless of the thickness. In contrast, the KB electrodes show a drastic decrease in $C_v$ as the thickness is increased. Compared to the 0.5 μm electrode, a 4 μm electrode only utilizes ~30% of the available void space. This is attributed to both the limited free space of the electrode for the formation of the discharge product and an earlier onset of channel clogging for mass transport. Thus, while the KB electrode may have a larger surface area and pore volume compared to the inverse opal structure, the pore size and tortuosity greatly limits the accessibility to these pores. In order to achieve Li-$O_2$ batteries with a high energy density in a practical cell system, electrode thickness is critical. These experimental results are supported by theoretical predictions that show that large porosity with limited tortuosity is key to achieving full utilization of the cathode surface during cell discharge.[22] For this to occur, a cathode structure entirely comprised of micropores (or small mesopores) must be avoided (as in the case of KB), and pores large enough to store sufficient discharge product must be present to allow for facile mass transport throughout the entirety of the discharge/charge process.

**Calculation of Void Volume Capacity for Figure C5**

Mentioned in the text, both the size of the pores that comprise the IOC structure (~350 nm) as well as the fragility of the final carbon product make pore analysis utilizing traditional techniques such as $N_2$ isotherm and Hg porosimetry impossible. Thus, the final cathode structure surface area and pore volume was estimated assuming an ordered array of face centered cubic (FCC) spheres based on electron microscopy images.

A perfectly stacked structure of polystyrene spheres in an ordered array would occupy a space of 74% of the total volume, based on an FCC packing structure ($\frac{\pi}{3\sqrt{2}}$). Such a packing

structure of the PS spheres (as subsequent IOC) can be confirmed via the provided electron images. This void volume, corresponding to the volume occupation of the PS spheres, will form the pores of the final carbon structure. Thus, in the inverse opal structure, the carbon walls will theoretically occupy 26% of the total volume. Assuming a carbon density of 1.8 g/cm$^3$ (amorphous carbon), and with the known mass of the cathodes studied at different thicknesses, one can estimate the void volume based on the following equation:

$$V_c = \frac{m_{carbon}}{\rho_{carbon}}$$

$$V_T = V_C * \frac{\pi}{3\sqrt{2}}$$

$$V_v = V_T - V_c$$

Where $V_c$ is the carbon wall volume, $V_T$ the total cathode volume, and $V_v$ the void volume. The corresponding void volume capacity ($C_v$) is determined from the overall capacity divided by this void volume. To determine the void volume of the KB based electrodes, the known pore volume of KB powder (~4.95 cm$^3$/g) was used with the known masses of the cathode. From these values for each individual cathode, the thinnest cathode (in this study, 0.5 um) was taken as the initial volumetric capacity ($C_{vi}$), and other calculated volumetric capacities were normalized to this value, as displayed in **Figure C-5d**.

## Appendix C References


[1] X. Lin, L. Zhou, T. Huang, A. Yu. “Hierarchically porous honeycomb-like carbon as a lithium-oxygen electrode.” *J. Mater. Chem. A.*vol. 1, pp. 1239-1245, 2013.

[2] M. Mirzaeian, P. J. Hall, “Preparation of controlled porosity carbon aerogels for energy storage in rechargeable lithium oxygen batteries.”*Electrochim. Acta* vol. 54, pp. 7444-7451, 2009.

[3] J. Xiao, D. H. Mei, X. L. Li, W. Xu, D. Y. Wang, G. L. Graff, W. D. Bennett, Z. M. Nie, L. V. Saraf, I. A. Aksay, J. Liu, J. G. Zhang, “Hierarchically Porous Graphere as a Lithium-air battery electrode.” *Nano Lett.* vol. 11, pp. 5071-5078, 2011.

[4] S. B. Ma, D. J. Lee, V. Roev, D. Im, S. G. Doo, “Effect of porosity on electrochemical properties of carbon materials for lithium-oxygen battery.” *J Power Sources*. vol. 244, pp. 494-498, 2013.

[5] Y. M. Cui, Z. Y. Wen, S. J. Sun, Y. Lu, J. Jin. “Mesoporous $Co_3O_4$ with different porosities as catalysts for the lithium-oxygen cell.” *Solid State Ionics*. vol. 225, pp. 598-603, 2012.

[6] M. Olivares-Marin, P. Palomino, J. M. Amarilla, E. Enciso, D. Tonti. “Effects of architecture on the electrochemistry of binder-free inverse opal carbons as Li-air cathodes in an ionic liquid-based electrolyte.” *J. Mater. Chem. A.* vol. 1, pp. 14270-14279, 2013.

[7] Y. Wang, “Modeling discharge deposit formation and its effect on lithium-air battery performance.” *Electrochimica Acta* vol. 75, pp. 239-246, 2012.

[8] V. Viswanathan, K. S. Thygesen, J. S. Hummelshoj, J. K. Norskov, G. Girishkumar, B. D. McCloskey, A. C. Luntz. “Electrical conductivity in $Li_2O_2$ and its role in

determining capacity limitations in non-aqueous Li-$O_2$ batteries." *J. Chem. Phys.*vol. 135, pp. 214704, 2011.

[9] P. Albertus, G. Girishkumar, B. McCloskey, R. S. Sanchez-Carrera, B. Kozinsky, J. Christensen, A. C. Luntz. "Identifying capacity limitations in the Li/Oxygen battery using experiments and modeling." *J. Electrochem. Soc.* vol. 158, pp. A343-A351, 2011.

[10] A. Stein. ``Sphere templating methods for periodic porous solids.`` *Micropor.Mesopor. Mat.* vol. 44, pp. 227-239, 2001.

[11] D. K. Yi, J.-H. Lee, J. A. Rogers, U. Paik. "Two-dimensional nanohybridization of gold nanorods and polystyrene colloids." *Appl. Phys. Lett*. vol.94, pp. 84104, 2009.

[12] L. C. Jia, G. P. Mane, C. Anand, D. S. Dhawale, Q. M. Ji, K. Ariga, A. Vinu. "A facile photo-induced synthesis of COOH functonalized meso-macroporous carbon films and their excellent sensing capability for aromatic amines." *Chem. Commun.* vol. 48, pp. 9029-9031, 2012.

[13] Y. C. Lu, Y. Shao-Horn. "Probing the reaction kinetics of the charge reactions of nonaqueous Li-$O_2$ batteries.`" *J. Phys. Chem. Lett.* vol. 4, pp. 93-99, 2013.

[14] B. D. Adams, R. Black, Z. Williams, R. Fernandes, M. Cuisinier, E. J. Berg, P. Novak, G. K. Murphy, L. F. Nazar. "Towards a stable organic electrolyte for the lithium oxygen battery." *Adv. Energy Mater.* vol. 5, pp. 1400867 (11 pages), 2014.

[15] G. V. Chase, S. Zecevic, T. W. Wesley, J. Uddin, K. A. Sasaki, P. G. Vincent, V. Bryantsev, M. Blanco, D. D. Addison, Patent Application US20120028137 A1, 2012.

[16] Y. Chen, S. A. Freunberger, Z. Peng, O. Fontaine, P. G. Bruce. "Charging a Li-$O_2$ battery using a redox mediator." *Nature Chem*. vol. 5, pp. 489-494, 2013.

[17] H.-D. Lim, H. Song, J. Kim, H. Gwon, Y. Bae, K.-Y. Park, J. Hong, H. Kim, T. Kim, Y. H. Kim, X. Lepró, R. Ovalle-Robles, R. H. Baughman, K. Kang. "Superior rechargeability and efficiency of lithium-oxygen batteries: Heirarchical air electrode architecture combined with a soluble catalyst." *Angew. Chem. Int. Ed.* vol. 53, pp. 3926-3931, 2014.

[18] M. M. O. Thotiyl, S. A. Freunberger, Z. Peng, P. G. Bruce. "The carbon electrode in nonaqueous Li-$O_2$ cells." *J. Am. Chem. Soc.* vol. 135, pp. 494-500, 2013.

[19] D. M. Itkis, D. Semenenko, B. Y. Kataev, A. Belova, V. Neudachina, A. Sirotina, M. Havecker, D. Teschner, A. Knop-Gericke, P. Dudin, A. Barinov, E. A. Goodilin, Y. Shao-Horn, L. V. Yashina. "Reactivity of carbon in lithium-oxygen battery positive electrodes." *Nano Lett.* vol. 13, pp. 4697-4701, 2013.

[20] B. D. McCloskey, A. Speidel, R. Scheffler, D. C. Miller, V. Viswanathan, J. S. Hummelshøj, J. K. Nørskov, A. C. Luntz. "Twin problems of interfacial carbonate formation in nonaqueous Li-$O_2$ batteries." *J. Phys. Chem. Lett.* vol. 3, pp. 997-1001, 2012.

[21] R. Mitchell, B. Gallant, C. V. Thompson, Y. Shao-Horn. "All-carbon-nanofiber electrodes for high-energy rechargeable Li-$O_2$ batteries." *Energy Environ. Sci.* vol. 4, pp. 1952-1958, 2011.

[22] Y. Wang, S. C. Cho. "Analysis of air cathode performance for lithium-air batteries." *J. Electrochem. Soc*. vol. 160, pp. A1847-A1855, 2013.